

Development of All-Solid-State Batteries with Sulfide Solid  
Electrolytes

(硫化物固体電解質を用いた全固体電池の開発)

January, 2023

Doctor of Philosophy (Engineering)

Hirotsada Gamo

蒲生浩忠

Toyohashi University of Technology

# Abstract

This thesis reports development of all-solid-state batteries using sulfide-based lithium and sodium solid electrolytes. Rechargeable lithium-ion batteries (LIBs) have been commercially used as power sources for portable electric devices. The LIB technology has been a promise for powering electrical vehicles (EVs) in the past decade. However, in traditional LIBs, the use of organic liquid electrolytes causes some safety issues: leakage and ignition. These safety concerns hinder the market adaption for LIBs, particularly in the EVs sector. In contrast, all-solid-state Li-ion batteries (ASLBs) in which an organic liquid electrolyte is replaced by an inorganic solid electrolyte (SE) show inherently high safety. Thus, ASLBs are a viable option for their application in electric vehicles. The success of ASLBs requires large-scale manufacturing technology for sulfide SEs with high ionic conductivity. Liquid-phase processing is beneficial for achieving ASLBs manufacturing that provides high scalability and low cost. The nature of organic solvents used in the liquid-phase method determines the solubility and chemical stability of lithium thiophosphates. However, there is a lack of leading theory on the solvent effect in the liquid-phase synthesis of  $\text{Li}_7\text{P}_3\text{S}_{11}$  SE, which is representative of highly conducting sulfide material. Chapter 1 constitutes general introduction. In Chapter 2, I provide guidelines for solvent selection for the liquid-phase synthesis of highly conductive crystalline  $\text{Li}_7\text{P}_3\text{S}_{11}$  (Chapter 2.2) and unprecedented solution synthesis method via dynamic sulfur radical anions for the rapid and scalable manufacturing of ASLBs (Chapter 2.3). Using the developed method, the  $\text{Li}_7\text{P}_3\text{S}_{11}$  SEs are prepared in a total time of 2 h through the rapid reaction of 2 min. Additionally, the  $\text{Li}_7\text{P}_3\text{S}_{11}$  SEs show a higher ionic conductivity of  $1.2 \text{ mS cm}^{-1}$  at room temperature than  $\text{Li}_7\text{P}_3\text{S}_{11}$  prepared by ball milling.

The improvement of energy storage devices requires not only the advances of SEs but also active materials. The active material which is conventionally used in traditional LIBs has approached its theoretical capacity limit. The restricted performance motivated the development of next-generation batteries that use active materials with high theoretical capacity. All-solid-state lithium-sulfur batteries (ASLSBs) have received much attention because of their high theoretical capacity. Nevertheless, the utilization of the high theoretical capacity of ASLSBs is limited by the poor electronic and ionic conductivities, and sluggish redox reaction kinetics of cathode materials. In Chapter 3, I report on novel cathode materials with improved electric transport properties and their electrochemical redox behaviors. I describe the structural and electrochemical properties of  $\text{Li}_2\text{S-CaS}$  in Chapter 3.2,  $\text{Li}_2\text{S-CaX}_2$  ( $X = \text{F, Cl, Br, and I}$ ) in Chapter 3.3, and  $\text{Li}_2\text{S-All}_3$  in Chapter 3.4. Comprehensive electrochemical measurements reveal that iodide-ion that involves an oxidation reaction at a slightly higher potential than the

oxidation potential of  $\text{Li}_2\text{S}$  provides desirable redox activity in ASLSBs. The implication of such redox chemistry in the additive is expanded toward understanding the role of sulfide SEs as a redox mediator and the activation mechanism in ASLSBs that is still unclear (Chapter 3.5). The electrochemistry of ASLSBs is governed by electrolyte decomposition behavior in which SEs in the cathode convert into the thiophosphates with the S-S bond in the charge/discharge process. A severe decomposition of electrolytes causes cycle fading instead of increasing the electrochemical redox activity in the early period.  $\text{Li}_2\text{S}/\text{SE}$  interface modification by different rotation speeds in SE mixing allows us to control the decomposition kinetics of electrolytes.

A power system that relies on batteries using Li ions as the conducting species would be insufficient to support the growing demand for electricity because competition for lithium resources is expected to intensify in the future. All-solid-state sodium-ion batteries (ASSBs) using inorganic solid electrolytes are promising candidates for large-scale energy storage applications owing to the natural abundance and low cost of sodium sources. The commercialization of ASSBs requires the development of Na-ion SEs that show high ionic conductivity and air stability.  $\text{Na}_3\text{SbS}_4$  prepared via a solid-phase synthetic method has attracted interest as a potential superionic conductor for ASSBs because it exhibits high conductivity ( $\geq 1.0 \text{ mS cm}^{-1}$  at room temperature) and excellent air stability. In Chapter 4, I describe Cl-doped  $\text{Na}_3\text{SbS}_4$  SEs prepared by the liquid-phase method. The specific crystal structure formed following Cl substitution enables the expansion of bottlenecks for  $\text{Na}^+$  conduction, especially along the c-axis, which leads to the enhanced ionic conductivity of  $\text{Na}_3\text{SbS}_4$ . Additionally, the introduction of NaCl into  $\text{Na}_3\text{SbS}_4$  suppresses the increase in interfacial resistance that accompanies stripping/plating, thereby enhancing the cell's electrochemical stability at 0 V vs.  $\text{Na}/\text{Na}^+$ . Overall conclusions and proposed future work are described in Chapter 5.

The findings obtained in this thesis can provide a viable path toward the development of scalable, low-cost processes for the all-solid-state battery manufacturing, an alternative material for SE and cathode materials with superior performance.

## Table of contents

1	General Introduction .....	1
1.1	Background .....	1
1.2	Lithium-ion batteries .....	1
1.3	All-solid-state lithium-ion batteries .....	3
1.4	Solid electrolytes.....	3
1.4.1	History of ionic conductor materials.....	3
1.4.2	Defect chemistry .....	4
1.4.3	Ion diffusion.....	5
1.4.4	Ion conduction mechanism in crystalline materials.....	6
1.4.5	Manufacturing of sulfide solid electrolytes .....	7
1.5	Liquid-Phase Synthesis.....	8
1.5.1	Solvent effect .....	8
1.5.2	Solvent selection .....	9
1.6	Lithium-sulfur batteries.....	10
1.7	Sodium-ion batteries.....	11
1.8	Objectives.....	12
1.9	Outline .....	12
	References .....	14
2	Liquid-Phase Synthesis of Lithium-Ion Sulfide Solid Electrolyte .....	26
2.1	Background.....	26
2.2	Effect of organic solvent on the reactivity of $\text{Li}_2\text{S-P}_2\text{S}_5$ systems in liquid-phase synthesis.....	27
2.2.1	Introduction.....	27
2.2.2	Experimental methods.....	28
2.2.3	Chemical, structural, and microstructural properties .....	29
2.2.4	Ionic conductivity of $70\text{Li}_2\text{S}\cdot30\text{P}_2\text{S}_5$ systems .....	31
2.2.5	Conclusions.....	32
	References.....	34
2.3	Solution synthesis method via dynamic sulfur radical anions.....	44
2.3.1	Introduction.....	44
2.3.2	Experimental methods.....	45
2.3.3	Solution processing technology via polysulfides.....	47
2.3.4	Structural and electrochemical properties .....	49
2.3.5	Cell performance.....	51
2.3.6	Conclusions.....	53



	References.....	54
3	<b>All-Solid-State Lithium Sulfur Batteries</b> .....	72
3.1	Background .....	72
3.2	Lithium sulfide-calcium sulfide cathode nanocomposites .....	73
3.2.1	Introduction.....	73
3.2.2	Experimental methods.....	74
3.2.3	Structural characterization .....	76
3.2.4	Complex impedance spectroscopy .....	76
3.2.5	Electric modulus analysis .....	78
3.2.6	Electrochemical redox reaction.....	79
3.2.7	Conclusions .....	80
	References .....	82
3.3	Lithium sulfide with dual-doping calcium halide.....	96
3.3.1	Introduction.....	96
3.3.2	Experimental methods.....	97
3.3.3	Structural characterization .....	98
3.3.4	Electrochemical impedance spectroscopy .....	98
3.3.5	Cell performance.....	99
3.3.6	Conclusions .....	101
	References .....	102
3.4	Lithium sulfide cathode materials doped with aluminum iodide .....	113
3.4.1	Introduction.....	113
3.4.2	Experimental methods.....	114
3.4.3	Structural characterization .....	115
3.4.4	Electric conductivity .....	116
3.4.5	Cell performance.....	117
3.4.6	Conclusions .....	118
	References .....	119
3.5	Understanding Decomposition of Electrolytes in All-Solid-State Lithium-Sulfur Batteries .....	127
3.5.1	Introduction.....	127
3.5.2	Experimental methods.....	128
3.5.3	Structural properties of pulverized SEs .....	130
3.5.4	Decomposition Behavior of SEs .....	130

3.5.5	Impact of the Li <sub>2</sub> S/LPS Interface on Battery Performance .....	131
3.5.6	Reaction Chemistry of ASLSBs .....	133
3.5.7	Electrochemical Impedance Spectroscopy of ASLSBs .....	135
3.5.8	Conclusions.....	137
References.....		138
4	Sodium-Ion Solid Electrolyte for All-Solid-State Sodium-Ion Batteries .....	155
4.1	Background.....	155
4.2	Na <sub>3</sub> SbS <sub>4</sub> substituted with Cl solid electrolytes .....	155
4.2.1	Introduction.....	156
4.2.2	Experimental methods.....	157
4.2.3	Structural characterization .....	158
4.2.4	Ionic conductivity properties .....	159
4.2.5	Ionic conduction pathways .....	160
4.2.6	Anode stability .....	161
4.2.7	Conclusions .....	162
References .....		164
5	General Conclusions and Future works .....	176
	List of Publications .....	178
	Acknowledgements.....	179

# Nomenclature

## Abbreviations

3D	Three dimensional
ACN	Acetonitrile
ASLBs	All-solid-state lithium-ion batteries
ASLSBs	All-solid-state lithium-sulfur batteries
ASSBs	All-solid-state sodium-ion batteries
BM	Ball milling method
BVS	Bond valence sum
CL	Conventional liquid phase method
CPE	Constant phase element
CS	Carbon disulfide
CV	Cyclic voltammetry
DC	Direct current
DN	Donor number
DME	1,2-dimethoxyethane
Dox	1,4-dioxane
EC	Ethylene carbonate
EES	Electric energy storage
EIS	Electrochemical impedance spectroscopy
EDS	Energy dispersive X-ray spectroscopy
EtOH	Ethanol
EV	Electric vehicle
FF	Furfural
HSAB	Hard and soft acid/base
KB	Ketjen black
LIB	Lithium-ion battery
LiPON	Lithium phosphorus oxynitride
LISICON	Lithium superionic conductor
Li-S	Lithium-sulfur
LPS	Li <sub>3</sub> PS <sub>4</sub>
NASICON	Sodium superionic conductor
NM	Nitromethane
NMR	Magic-angle spinning-nuclear magnetic resonance
PEEK	Polyether ether ketone
SE	Solid electrolyte

SEI	Solid electrolyte interphase
SEM	Scanning electron microscopy
SHE	Standard hydrogen electrode
SN	Succinonitrile
TG-DTA	Thermogravimetry-differential thermal analysis
THF	Tetrahydrofuran
THP	Tetrahydropyran
UV-Vis	Ultraviolet-visible
VGCF	Vapor grown carbon fiber
XPS	X-ray photoelectron spectroscopy
XRD	X-ray diffraction

### Roman symbols

$A$	Contact area [ $\text{cm}^2$ ]
$a_0$	Jump distance [cm]
$B_{\text{iso}}$	Atomic displacement parameter [ $\text{nm}^2$ ]
$C_{\text{Li}}$	Li concentration of electrode [ $\text{mol cm}^{-3}$ ]
$D$	Crystallite size [nm]
$D_{\text{Li}}$	Lithium-ion diffusion coefficient [ $\text{cm}^2 \text{s}^{-1}$ ]
$D^{\text{T}}$	Trace ion diffusion coefficient [ $\text{cm}^2 \text{s}^{-1}$ ]
$D^{\sigma}$	Ion diffusion coefficient related to Nernst-Einstein relationship [ $\text{cm}^2 \text{s}^{-1}$ ]
$d$	Density of pellet [ $\text{cm}^{-3}$ ]
$E_a$	Activation energy [ $\text{J mol}^{-1}$ ]
$F$	Faraday constant [ $\text{C mol}^{-1}$ ]
$g$	Occupancy
$G$	Gibbs free energy [J]
$H$	Standard enthalpy [J]
$f_{\text{max}}$	Relaxation frequency [ $\text{s}^{-1}$ ]
$I_p$	Peak current for redox reaction [A]
$j$	Imaginary number
$H_R$	Haven ratio
$k_B$	Boltzmann constant [ $\text{J K}^{-1}$ ]
$l$	Thickness [cm]
$n$	Total density of charge carriers [ $\text{C cm}^{-3}$ ]
$M^*$	Complex electric modulus
$M'$	Real part of complex electric modulus

$M''$	Imaginary part of complex electric modulus
$Q$	Capacity [ $\text{mAh g}^{-1}$ ]
$q$	Charge of the mobile ion
$R$	Gas constant [ $\text{J K}^{-1} \text{mol}^{-1}$ ]
$S$	Entropy [ $\text{J K}^{-1}$ ]
$T$	Temperature [K]
$V$	Voltage [V]
$v$	Scan rate [ $\text{mV s}^{-1}$ ]
$Z^*$	Complex impedance [ $\Omega$ ]
$Z'$	Real part of complex impedance [ $\Omega$ ]
$Z''$	Imaginary part of complex impedance [ $\Omega$ ]

### Greek symbols

$\beta$	Integral breadth
$\Delta$	Differential
$\varepsilon$	Microstrain
$\varepsilon_0$	Permittivity of free space [ $\text{F m}^{-1}$ ]
$\gamma$	Fraction of charge carriers
$\theta$	Diffraction angle [degrees]
$\lambda$	Wavenumber of X-rays [nm]
$\nu$	Frequency [ $\text{s}^{-1}$ ]
$\nu_0$	Jump vibrational frequency [ $\text{s}^{-1}$ ]
$\sigma$	Conductivity [ $\text{S cm}^{-1}$ ]
$\sigma_0$	Pre-exponential factor [ $\text{K} \cdot \text{S cm}^{-1}$ ]
$\sigma^*$	Complex conductivity [ $\text{S cm}^{-1}$ ]
$\sigma'$	Real part of complex conductivity [ $\text{S cm}^{-1}$ ]
$\sigma''$	Imaginary part of complex conductivity [ $\text{S cm}^{-1}$ ]
$\tau$	Relaxation time [ $\text{s}^{-1}$ ]
$\omega$	Radical frequency [ $\text{s}^{-1}$ ]

# Chapter 1

## General introduction

### 1.1 Background

Electricity sustains the standard living for humans in modern society. Electric power demand is growing with the development of advanced science and technology, and population growth every year. The majority of today's electrical energy is supplied from fossil fuels, particularly coal, which has been the dominant source of electricity generation in the world.<sup>1</sup> Burning coal emits an average 1000 g lifecycle CO<sub>2</sub>, which is considered to cause environmental pollution and global warming.<sup>2</sup> To reduce greenhouse gas emissions, there is a global imperative to shift toward a sustained energy system that encourages the use of renewable energy technologies. As a sustainable energy system, the smart grid has been proposed, which integrates a significant amount of renewable energy resources.<sup>3</sup> Renewable energy is classified into the solar, wind, hydraulic power, geothermal, solar heat, biomass energy, etc. Solar and wind energy are promising as renewable energy because of their abundance and readily available.<sup>3</sup> These energy systems are accounted for ~5% of global electricity production in 2016; this number is expected to increase by over 10% until the year 2040.<sup>1</sup> However, such sources offer intermittent energy, which requires advanced electrical energy storage technologies. The electric energy storage (EES) technologies have held promise as electrical power for electric vehicles (EVs) in the past decade and are undergoing a turning point.<sup>4</sup> The progress of hybrid electric vehicles, plug-in hybrid electric vehicles, and purely EVs will further reduce dependence on fossil fuels. Lithium-ion batteries (LIBs) are regarded as the battery of choice for powering the next generation of hybrid electric vehicles as well as plug-in hybrids.

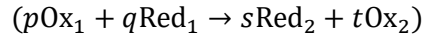
### 1.2 Lithium-ion batteries

Rechargeable lithium-ion batteries can store through the exchange of electrons between two redox couples (i.e., the electrode reactions) as a result of reversible insertion/desertion of the Li-ion into the host electrode material. LIBs consist of three components: two electrodes (cathode and anode) and an electrolyte. The nature of the electrodes and their surface area are of importance in determining the kinetics of redox processes. Additionally, the difference between the equilibrium potential of the cathode and anode determines the cell voltage. The cell voltage,  $\Delta E$ , can be expressed as described in Eq. (1.2.1)

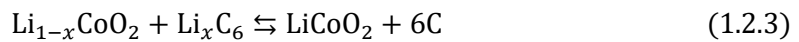
$$\Delta E = \Delta\phi_{\text{cathode}} - \Delta\phi_{\text{anode}} \quad (1.2.1)$$

where,  $\Delta\phi_{\text{cathode}}$  and  $\Delta\phi_{\text{anode}}$  are potential at equilibrium generated cathode and anode, respectively. The resulting Eq. (1.2.1) can be formulated as in Eq. (1.2.2), based on the Nernst equation.

$$\Delta E = \Delta\phi_{\text{cathode}} - \Delta\phi_{\text{anode}} = \Delta E^{\circ} - \frac{RT}{nF} \ln \frac{a_{\text{Red}_1}^s a_{\text{Ox}_2}^t}{a_{\text{Red}_2}^q a_{\text{Ox}_1}^p} \quad (1.2.2)$$



$F$  is the Faraday constant, that is, the charge of a mole of electrons ( $96485 \text{ C mol}^{-1}$ ).  $E^{\circ}$  is the standard potential,  $R$  is the gas constant,  $T$  is temperature,  $n$  is the number of electrons between the electrodes, and  $a$  is the activity of the redox couples.  $\text{Ox}_1$  and  $\text{Red}_1$  belong to the stronger couple (higher potential) and  $\text{Ox}_2$  and  $\text{Red}_2$  belong to the weaker couple (lower potential). Additionally, the electrolyte supplies the ion conduction between the electrodes. In the case of LIBs, Li ions that are mobile ion species flow toward regions of opposite charge by the action of the electric field applied between a cathode and an anode. The common electrolytes have been made by a solution of  $\text{Li}^+$  salt in a mixture of polar aprotic organic solvents. Li-ion batteries, carbon//LiCoO<sub>2</sub> cell, have firstly commercialized as energy storage devices in 1991. Figure 1.1 shows a schematic of LIBs using LiCoO<sub>2</sub>, graphite, and liquid organic electrolyte. The battery typically shows a limited energy density of  $90 \text{ Wh kg}^{-1}$ . The charge/discharge processes in commercial LIBs using a graphite anode and LiCoO<sub>2</sub> cathode can be summarized in Eq(1.2.3)



The aforementioned LIBs can reversibly operate in a cell voltage between 3.6 and 4.2 V. The higher  $\Delta E$  values are achieved by a low potential [ $E^{\circ}(\text{Li}^+/\text{Li}) = -3.04 \text{ V vs. SHE}$ ] of Li-ion. Moreover, the outstanding electrochemistry of LIBs is described by the low molecule weight and small ionic radius of Li-ion, which allows for fast ion diffusion.<sup>5</sup> Following the discovery of LiCoO<sub>2</sub> as a cathode in the 1980s, the development of several cathode materials, for example, LiNi<sub>0.8</sub>Co<sub>0.15</sub>Al<sub>0.05</sub>O<sub>2</sub>, LiFePO<sub>4</sub>, Li(Ni,Mn,Co)O<sub>2</sub>, and LiMn<sub>2</sub>O<sub>4</sub>, delivered the increase in an energy density of  $250 \text{ Wh kg}^{-1}$ , which has boosted technological revolutions of EVs.<sup>6</sup> The EV sales, which account for just 2–3% of total passenger vehicles sales in 2020, are expected to increase 10-fold over the next decade.<sup>7</sup> However, the use of flammable organic liquid electrolytes in conventional LIBs causes some safety issues, such as leakage and ignition. These safety issues and concerns about reliability remain major obstacles that hinder the market adaption of LIBs,

particularly in the EV sector. Taking into this consideration, the increasing market for EVs, the community must reconsider the application of LIBs using organic liquid electrolytes into EVs.

### 1.3 All-solid-state lithium-ion batteries

All-solid-state lithium-ion batteries (ASLBs) in which organic liquid electrolyte is replaced by inorganic solid electrolyte (SE) show inherently high safety owing to the use of the non-flammable inorganic SEs (Figure 1.2). The development of ASLBs is inspired by the discovery of fast ionic conduction in solids.<sup>8</sup> However, ASLBs historically have involved the large disadvantage of their low power density. The problem is caused by the electrode/electrolyte interfacial failure between solids and sluggish ionic conduction in solids. The performance of ASLBs is limited by the mechanical, chemical, and electrochemical properties of SEs. Inorganic SEs are becoming of paramount importance for the development of ASLBs to meet the EV sector's demands for safer and greater batteries. In the following sections, I offer an introduction to solid-state electrolytes and describe their ion transport mechanisms and synthesis methods. I then focus on a broad range of battery chemistries, including all-solid-state lithium-sulfur batteries and all-solid-state sodium-ion batteries.

## 1.4 Solid electrolytes

### 1.4.1 History of ionic conductor materials

The history of solid electrolytes initializes in 1833 with Faraday's discovery of the remarkable conductivity property for solid  $\text{Ag}_2\text{S}$  and  $\text{PbF}_2$  in the high-temperature region.<sup>9</sup> In 1914, high-temperature phase silver iodide ( $\alpha$ -AgI), a fast ionic conductor, was found.<sup>10</sup> Following, in the 1960s, the term 'solid-state ionics' originates with the discovery of  $\beta$ -alumina<sup>11</sup> as a sodium ion conductor and  $\text{RbAg}_4\text{I}_5$ <sup>12</sup> as a silver ion conductor.  $\alpha$ -AgI prepared by a melt-quenching technique exhibits fast ionic conduction behavior at room temperature as if in a liquid.<sup>13</sup> Fast Li-ion conduction in solids was originally reported for  $\text{Li}_3\text{N}$  in 1977.<sup>14</sup> Studies on Li ionic conductor mainly focused on oxides, for example, LISICON (Li superionic conductor)<sup>15</sup>, NASICON (Na superionic conductor)<sup>16</sup>, and LiPON (Li phosphorus oxynitride)<sup>17</sup> systems. In parallel with these studies,  $\text{Li}_2\text{S-P}_2\text{S}_5\text{-LiI}$ <sup>18</sup> and  $\text{LiI-Li}_2\text{S-B}_2\text{S}_3$ <sup>19</sup> glasses were found to deliver an ionic conductivity of the order of  $10^{-3} \text{ S cm}^{-1}$  at room temperature in the early 1980s. Such glasses have the advantage of isotropic conductivity and lack of grain boundaries. In addition, sulfide materials are beneficial for fast ionic conduction because the high polarizability of  $\text{S}^{2-}$  weakens the electrostatic interaction between the anions and cations. The study on highly conducting



crystalline materials met the advanced progress, and discovered  $\text{Li}_7\text{P}_3\text{S}_{11}$ <sup>20</sup>, a highly conducting crystalline phase in the  $70\text{Li}_2\text{S}\cdot 30\text{P}_2\text{S}_5$  system, and  $\text{Li}_{10}\text{GeP}_2\text{S}_{12}$ <sup>21</sup>, the thio-LISICON family; these materials exhibit an ionic conductivity of the order of  $10^{-2} \text{ S cm}^{-1}$  at room temperature comparable with those of liquid electrolytes. The discovery has largely increased the feasibility of the sulfide based ASLB application. It has been of great scientific interest to understand the ion conduction mechanism of these superionic conductors, to enable a rational design guideline for a superionic conductor. In the subsequent section, I will discuss the ion conduction mechanism in solids based on the defect chemistry and crystallographic perspective.

### 1.4.2 Defect chemistry

The effective design of fast ion conductors requires an understanding of defect chemistry.<sup>22-25</sup> Crystalline solids contain defects a variety of defects at finite temperatures, from inherent point defects and extrinsic impurities to grain boundaries, and no perfectly crystalline material exists. The simplest notion of a defect is a mistake at an atom site in a crystal and these are called point defects, including vacancies, self-interstitials, substitutional impurities, and interstitial impurities. Additionally, the defect is classified into two defect models: Schottky defect and Frenkel defect, as shown in Figure 1.3. Schottky defect means the balanced populations of vacancies on both the cation and anion sites in a crystal. Frenkel defect means the paired point defects consisting of a population of vacancies on one subset of atoms generated by displacing some atoms into normally unoccupied interstitial sites. In the Schottky defect, cation and anion vacancies are paired, and in the Frenkel defect, cation vacancy and interstitial are paired. If there is no interaction between the defects, the equilibrium constant,  $K_S$ , is expressed with concentrations instead of activities in the case of Frenkel defect, as follows:

$$K_S = \left(\frac{n_{cv}}{N}\right) \left(\frac{n_{av}}{N}\right) = \exp\left[\frac{-\Delta G_S}{k_B T}\right] \quad (1.4.1)$$

where  $n_{cv}$  is the number of cation vacancies,  $n_{av}$  is the number of anion vacancies per unit volume,  $N$  is the number of cation or anion sites per unit volume in the crystal,  $\Delta G_S$  is the molar Gibbs energy of formation of the Schottky defects,  $k_B$  is the Boltzmann's constant, and  $T$  is the absolute temperature.  $n_{cv}$  is equal to  $n_{av}$  because the crystal maintains electroneutrality. Thus, the number of Schottky defects present,  $n_S$ :

$$n_{cv} = n_{av} = n_S = N \exp\left[\frac{-\Delta G_S}{2RT}\right] \quad (1.4.2)$$

The Gibbs free energy,  $\Delta G_S$ , is often replaced by the enthalpy of Schottky defect formation,  $\Delta H_S$ .

The Gibbs free energy is defined as follows:

$$G = H - TS \quad (1.4.3)$$

where  $H$  is the standard enthalpy and  $S$  is the entropy. As a result, the equilibrium constant of the Schottky defect is given by

$$K_S = \exp\left[\frac{\Delta S_S}{k_B}\right] \exp\left[\frac{-\Delta H_S}{k_B T}\right] \quad (1.4.4)$$

This equation presents that increasing temperature in the system rapidly increases the thermal equilibrium concentration above a certain temperature. This phenomenon is the same for the Frenkel defect.

### 1.4.3 Ionic conductivity

The temperature dependence of the tracer diffusion coefficient or diffusivity,  $D^T$  is often described by the Arrhenius relation

$$D^T = D_0 \exp\left(-\frac{E_a}{k_B T}\right) \quad (1.4.5)$$

where  $D_0$  is the pre-exponential factor and  $E_a$  is the activation energy for ion migration. Given the microscopic point,  $D^T$  can be defined by the Einstein–Smoluchowski relation<sup>26,27</sup>

$$D^T = \lim_{t \rightarrow \infty} \frac{\langle r^2(t) \rangle}{2dt} \quad (1.4.6)$$

Here,  $\langle r^2(t) \rangle$  is the mean square displacement of the particles after the time  $t$ , and  $d$  is the dimensionality of the diffusion. A mobile cation hops between stable sites through interconnected diffusion channels with the minimum potential landscape in a crystal structure framework. Given that the mean jump time is shorter than the mean relaxation time  $\tau$ , the ion will perform elementary jumps with an average jump length,  $a_0$ . From these microscopic quantities, a diffusion coefficient  $D^{uc}$  for uncorrelated jumps can be expressed by

$$D^{uc} = \frac{a_0^2}{2d\tau} \quad (1.4.7)$$

If the mobile ions hop in 3 dimensions with the jump vibrational frequency ( $\nu_0 = \tau^{-1}$ ), Eq. 1(1.4.5) can be transformed into

$$D^T = \frac{a_0^2 v_0}{6} \exp\left(-\frac{E_a}{k_B T}\right) \quad (1.4.8)$$

The ionic conductivity is based on the Nernst-Einstein relationship using

$$\sigma = \frac{nq^2}{k_B T} D^\sigma \quad (1.4.9)$$

where  $n$  is the total density of charge carriers,  $q$  is the charge of the mobile ion. The diffusion coefficient  $D_\sigma$  obtained from conductivity measurements using the Nernst-Einstein relationship (Eq. 1.4.9) is related to the tracer diffusion coefficient  $D^T$  by

$$D^T = H_R D^\sigma \quad (1.4.10)$$

Given a geometrical factor  $z$  that considers the presence of possible cross-correlation in the diffusion (including the Haven ratio  $H_R$  which is the ratio between the tracer and charge diffusion coefficient), the ionic conductivity,  $\sigma$ , in solids is expressed as follows:

$$\sigma = \frac{nq^2 a_0^2 v_0 z}{6k_B T} \exp\left(-\frac{E_a}{k_B T}\right) = \frac{\sigma_0}{T} \exp\left(-\frac{E_a}{k_B T}\right) \quad (1.4.11)$$

where  $\sigma_0$  is the pre-exponential factor for the ion diffusion. The activation energy,  $E_a$ , is the sum of the enthalpy to create the defect and to overcome the energy barrier for the ion migration. However, the defect formation enthalpy is often neglected in heavily defective material. The design of ion conductors to date has relied on the ion conduction mechanism explained by Eq. (1.4.11). Increasing the pre-exponential factor and decreasing the activation energy for ion transport leads to the enhancement of ionic conductivity.

#### 1.4.4 Ion conduction mechanism in crystalline materials

In the classic diffusion model, mobile ions in solids migrate between stable sites through a high-energy landscape. The high activation energy is the sum of defect formation and migration energies because a defect formation step is necessary for macroscopic ion diffusion. The energy landscape along the diffusion channel is affected by the anionic frameworks, dominating the overall conduction properties. The crystal structure framework consisting of anionic sublattices with body-centered cubic (bcc) like frameworks benefits Li-ion diffusion with a lower activation barrier than in other anionic frameworks.<sup>28</sup> Lithium ions in  $\text{Li}_{10}\text{GeP}_2\text{S}_{12}$ , which exhibits the highest Li-ion conductivity reported so far, diffuse predominantly via a series of channels connecting tetrahedron with the Li site in the center along the  $c$  axis, as shown in Figure 1.4.

These tetrahedral sites with large probability densities were observed experimentally and computationally.  $\text{Li}_7\text{P}_3\text{S}_{11}$  has highly distributed 3D (3-dimensional) Li diffusion networks because of its anionic frameworks with a bcc packing (see Figure 1.5). In contrast to this, argyrodite-type Li-ion conductors, lithium garnet, and NASICON without bcc anion packing still deliver high Li ion conductivity over  $1 \text{ mS cm}^{-1}$  at room temperature (Figure 1.6). In particular, argyrodite-type SEs exhibit extremely high ionic conductivities (up to  $24 \text{ mS cm}^{-1}$  at room temperature to date).<sup>29</sup> The ion diffusion in these materials is based on the concerted migration mechanism. In this mechanism, the mobile ions are affected by Coulombic interactions from nearby other mobile ions, which leads to a redistribution of mobile ions at the high-energy interstitial sites and hence a relatively flat energy landscape with a low barrier, as shown in Figure 1.7.<sup>30</sup>

#### 1.4.5 Manufacturing of sulfide solid electrolytes

The understanding origin of fast ion diffusion in superionic conductors has helped to develop a wide range of superionic conductors. The community is currently interested in sulfide-based ASSB manufacturing technologies involving a level of practical application;<sup>31,32</sup> however, large-scale manufacturing of ASLBs faces many difficulties due to the air sensitivity of sulfide-based SEs and starting materials. Contact of sulfide-SEs with moisture results in the decomposition of SEs and a release of highly toxic hydrogen sulfide. The moisture sensitivity of the sulfide SEs is caused by the higher interaction of the central atom in the tetrahedral units with oxygen than to sulfur based on HSAB theory. The use of  $\text{Sn}^{4+}$  and  $\text{Sb}^{5+}$  as the central cation or dopants might be a potential solution.<sup>33,34</sup> However, such a material design is unfavorable for ion conduction in comparison to a phosphorus substitution. The success of ASLBS requires the development of large-scale synthesis for a superionic conductor, such as  $\text{Li}_3\text{PS}_4$ ,  $\text{Li}_6\text{PS}_5\text{Cl}$ ,  $\text{Li}_7\text{P}_3\text{S}_{11}$ ,  $\text{Li}_{10}\text{GeP}_2\text{S}_{12}$ , and  $\text{Li}_7\text{P}_2\text{S}_8\text{I}$ . The synthesis of sulfide SEs is divided into major three methods: solid-state reaction method, liquid-phase method, and mechanochemical reaction method.

In the solid-state reaction method, the reactants are melted and then quenched or slowly cooled. The reaction in this process undergoes in quartz ampoules at higher temperatures of over  $700 \text{ }^\circ\text{C}$  in comparison with the other methods. The reaction process leads to low scalability because to the use of a special equipment. This method can synthesize the  $\text{Li}_2\text{S-P}_2\text{S}_5$  system, argyrodite-type material, and  $\text{Li}_{10}\text{GeP}_2\text{S}_{12}$  SEs.<sup>35-38</sup>

In the mechanochemical reaction method, the reactants are milled using planetary ball mill equipment. This process is beneficial for the development of amorphous phases.<sup>39,40</sup> After ball milling, the amorphous phases are often crystallized by subsequent heat treatment to form

crystalline SEs with high ionic conductivity. In high-energy treatment, it is necessary to be noted contamination from milling pot and ball components. Over the past decade, a variety of SEs have been developed using this technique.<sup>41</sup> The disordered structure induced ball milling results in unique conductivity properties that are different from those of materials synthesized by the solid-state reaction method.<sup>42,43</sup> However, there is a sparse understanding of the mechanochemical reaction mechanism. To date, it was reported that the mechanochemical ball milling method enables to synthesize the sulfide SEs via the one-pot process.<sup>44</sup> This process consumes much energy and limits manufacturing scale-up owing to the use of special apparatus.

In the liquid-phase method, the raw materials react in an organic solvent to a precursor suspension or solution. After vacuum drying and heat treatment, the sulfide SEs were obtained. The organic solvents are usually selected to be highly soluble, highly polar, and aprotic. This process provides high scalability, low cost, low temperature for the reaction, and low reaction time efficiency. In particular, the solution-based process could be used in manufacturing based on the accumulated expertise of lithium-ion batteries, which would reduce the barrier to industry adoption.<sup>31</sup> However, the solvent remaining in the SEs after vacuum drying leads to a decrease in the ionic conductivity in comparison to the other methods. So far, the liquid-phase synthesis of  $\text{Li}_3\text{PS}_4$ ,  $\text{Li}_7\text{PS}_{11}$ , argyrodite-type material, and  $\text{Li}_{10}\text{GeP}_2\text{S}_{12}$  have been reported.<sup>45-48</sup>

## 1.5 Liquid-Phase Synthesis

The solid-phase method and mechanochemical method are used on a laboratory scale for the discovery and design of novel SEs. Their synthesis processes commonly undergo in a glove box under an inert atmosphere because sulfide SEs and their raw materials react with moisture in the air to generate toxic  $\text{H}_2\text{S}$  gas. Given the low scalability of both methods, more effective and scalable synthesis methods are needed to establish a manufacturing scheme. As mentioned above, the liquid-phase method would be an economically viable technology for ASLBs manufacturing. For the liquid-phase synthesis process of  $\text{Li}_2\text{S}$ - $\text{P}_2\text{S}_5$  system materials, typical sulfide SEs, a mixture of  $\text{Li}_2\text{S}$  and  $\text{P}_2\text{S}_5$  is firstly added in an aprotic polar solvent and then mixed or subjected to a sonication treatment to form a lithium thiophosphate intermediate. The obtained precursor converts to the sulfide SEs by heat treatment to remove the solvent. The structure, morphology, and electrochemical properties of sulfide SEs rely on the nature of the organic solvent.

### 1.5.1 Solvent effect

The nature of solvents determines the reactivity and solubility of lithium thiophosphates in the

wet chemical synthesis. The polarity of organic solvent induces changes in bond properties in the intermediate molecular complexes. The polarity is characterized by a dielectric constant and electric dipole moment. The extent of induced polarization for a given bond relies on the strength of the coordinate bonds with the nucleophile and/or the electrophile. The stronger the coordination interaction, the greater the induced polarization. The liquid-phase synthesis has been difficult; estimation of increasing increments for the nucleophilic and electrophilic contributions, the choice of optimal empirical parameters for the nucleophilic and the electrophilic functions, the understanding of reaction mechanism. Thus, the introduction of empirical parameters regarding the respective nucleophilic and electrophilic properties is required for the effective synthesis of sulfide SEs via the liquid-phase. In 1966, Gutmann proposed the concept of donor number (DN) to express quantitatively the Lewis basicity of solvents. The DN is commonly used as an empirical functional parameter for the nucleophilic properties of a solvent, which is defined as the negative enthalpy for the reaction of complexation with  $\text{SbCl}_5$  in a highly diluted solution of dichloroethane. A broad range of aprotic solvents have poor acceptor properties and thus their DN relates to the extent of charge transfer involved in ion solvation. The reactivity of a solute is greatly affected by the nucleophilic and electrophilic interactions with the solvents. For instance, it may be believed that the use of a solvent with high DN is beneficial for the formation of reactive anions. In fact, the reaction between  $\text{Li}_2\text{S}$  and  $\text{P}_2\text{S}_5$  initiates from the dissociation reaction of the  $\text{P}_2\text{S}_5$  by nucleophilic attack of electron donor, that is a solvent with high DN. The suitable reactivity of the raw materials for sulfide SEs, bond polarity, can be gained by a proper choice of solvents.

### 1.5.2 Solvent selection

Given the reaction pathways of sulfide SEs in solvents, we must note the following points: solubility and chemical stability of reactants, products, and intermediates, coordination environments with solvents and subsequent solvent removal, crystallization process during drying and/or heat-treatment, and industrial concerns. The solubility and chemical stability of the raw materials, intermediates, and end products determine the reaction kinetics of the overall reaction process. A reaction process through the solution is beneficial for rapid synthesis. Additionally, a heterogeneous induced by the low solubility of the precursor may result in decrease of reproducibility and increase of engineering cost. These concerns are critical in the case of the large-scale manufacturing. Given the industrial adoption, the exclusion of the solvent removal process is preferred because of its huge energy consumption. Hence, a synthesis process that undergoes soluble precursors to precipitate the end product is the best scheme. However, solvents with high solubility against  $\text{Li}_2\text{S}$ ,  $\text{P}_2\text{S}_5$ , and intermediates commonly show high solubility even against the reaction product. Tetrahydrofuran, acetonitrile, dimethoxymethane, and ethyl

propionate are effective solvents owing to their moderate solubility and no chemical reactions with raw materials and precursors. Alcohol solvent, which is a protic polar solvent, shows high solubility, whereas chemically reacts with  $P_2S_5$  to occur substitution reactions of O for S in the  $P_2S_5$  molecule. It is believed that Alcohol solvent is unsuitable for the wet-chemical reaction of sulfide materials, but a mixed solvent of alcohol and aprotic solvent can be used as an effective reaction media for  $Li_6PS_5X$  ( $X = Cl, Br, \text{ and } I$ ) and  $Li_3PS_4$ .

It must be noted the boiling point of the solvent and bond strength between lithium thiophosphates and solvents in complexes for achieving high ionic conductivity in the SEs prepared by the liquid-phase method. It is necessary to remove the free solvent and the solvent coordinated to the lithium thiophosphate phase in the precursor. The evaporation temperature of the coordinated solvent shows independence on the boiling point, which is influenced by its polarity. Such confusion arises from a tendency that the higher boiling point, the higher polarity of solvents. Taking economic and environmental concerns into consideration, the solvents with weak bonding to the SEs and low boiling points are favored. However, the weaker the coordination bond, the lower the reactivity. From an academic view, a synthesis process with huge energy consumption for the solvent removal process is explored to date. In contrast, for a seamless shift to the chemical industry, the boiling point and viscosity of the solvent must be taken into account.

## 1.6 Lithium-sulfur batteries

Cathodes are a critical component that largely determines the energy density and 40–50% of the total cell cost in commercial LIBs.<sup>49</sup> Nevertheless, the performance of the commercially available LIBs is approaching their theoretical limit. Many researchers have tried to develop cathode materials with high theoretical capacity for improving battery performance. Lithium-sulfur batteries are one of the most desirable EES technology owing to the low cost and natural abundance of sulfur.<sup>50</sup> Elemental sulfur is generated more than 60 million tons annually. The majority of these are a by-product of the hydrodesulfurization process of sulfur dioxide generated by the combustion of fossil fuels in petroleum refining.<sup>51</sup> The abundance of elemental sulfur provides strong motivation to develop innovative chemistry for its utilization. Thus, the development of Li-S batteries is also important in terms of creating a new demand for sulfur. The promise of a device of greater EES than Li-ion has not yet materialized even though Li-S electrochemistry has been examined since the 1940s.<sup>52</sup> Intrinsic problems in Li-S electrochemistry remain poor rechargeability, limited rate capability, and capacity fading.<sup>53</sup> The capacity fading is caused by a shuttle mechanism in which multiple soluble polysulfide intermediates are formed in the charge/discharge process, leading to a self-discharge through

liquid organic electrolytes. The shuttle effect is inhibited in all-solid-state lithium-sulfur batteries (ASLSBs) that replace liquid electrolytes with fast ion-conducting inorganic SEs. Tatsumisago's group first reported ASLSBs with sulfide SEs.<sup>54</sup> The attempt used the S@CuS cathode composite prepared by mechanical milling, demonstrating a high reversible capacity of 650 mAh g<sup>-1</sup> after 20 cycles.

## 1.7 Sodium-ion batteries

Energy storage for the electrical grid has primarily been focused on lithium-ion. The demand for Li-based EES as a power source in EVs is rapidly increasing<sup>3</sup>, thus and competition for lithium resources would be intensified in the future. However, Li is a limited resource in the Earth's crust and has a geologically uneven distribution.<sup>55</sup> Given the abundance and low cost of sodium sources, sodium-ion batteries are one of the most promising rechargeable electrochemical storages. As described in Chapter 1.4.1, sodium electrochemistry originates from the discovery of the solid sodium ion conductor  $\beta''$ -alumina 60 years ago.  $\beta''$ -alumina is a layer structured fast ion conductor in which the mobile sodium ions are located in conduction planes. The synthesis of  $\beta''$ -alumina requires a high processing temperature of over 1200 °C, which is an obstacle to  $\beta''$ -alumina applications. The discovery leads to the development of two sodium ion batteries: the sodium/sulfur battery<sup>56</sup> and ZEBRA cell, in which solid transition metal halides are used as cathode materials<sup>57</sup>. Na-S batteries were commercialized in Japan and operate near 300 °C. The high operating temperature allows for the high reaction kinetics of sodium and sulfur with their melts, and the high ionic conductivity of  $\beta''$ -alumina. Safety concerns and costly heating requirements in Na-S batteries are inspiring much effort for the development of ion conductors with high ionic conductivity at lower temperatures. Sodium superionic conductors called NASICON have attracted great interest in the research field because of their relatively high ionic conductivity at room temperature, and moderate thermal and chemical stability.<sup>58</sup> Solid electrolytes with a NASICON-type structure ( $\text{Na}_{1+n}\text{Zr}_2\text{Si}_n\text{P}_{3-n}\text{O}_{12}$ ,  $0 \leq n \leq 3$ ) are designed as a superionic conductor with 3D networks based on crystallography.<sup>59</sup> Currently, sulfide-based SEs have attracted much attention owing to their high ionic conductivity and good mechanical properties. These features are derived from the high polarizability of  $\text{S}^{2-}$ . Hayashi et al. reported  $\text{Na}_3\text{PS}_4$  with high ionic conductivity of 0.2 mS cm<sup>-1</sup> prepared by a mechanochemical reaction process.<sup>60</sup> In 2016,  $\text{Na}_3\text{SbS}_4$  that fully substituted P with Sb in  $\text{Na}_3\text{PS}_4$  was developed, showing an ionic conductivity of 1.1 mS cm<sup>-1</sup> with a low activation energy of 0.20 eV at room temperature.<sup>61,62</sup>



## 1.8 Objectives

As mentioned above, several problems must be solved for the commercialization of all-solid-state batteries. In this doctoral thesis, I focused on three studies: (i) the liquid-phase synthesis of sulfide solid electrolytes for all-solid-state Li-ion batteries, (ii) the development of the cathode materials for all-solid-state Li-S batteries, (iii) the development of sulfide solid electrolytes for all-solid-state sodium-ion batteries. The specific aims of this thesis are:

i) to identify the critical effect of solvent on reactivity and solubility of  $\text{Li}_2\text{S-P}_2\text{S}_5$  systems in organic solvent and establish novel solution processing technology of sulfide solid electrolytes that provides high scalability, low cost, and short reaction time scale.

ii) to develop  $\text{Li}_2\text{S}$ -based cathode materials with improved electric conductivity for all-solid-state Li-S batteries, investigate their electrochemical redox reactions, and understand the electrochemical decomposition behavior of solid electrolytes in the cathode.

iii) to develop sodium solid electrolytes for all-solid-state sodium-ion batteries (ASSBs) prepared by liquid-phase synthesis method and investigate the effect of their framework structure on ionic conductivity property using Rietveld analysis.

The fulfillment of the objectives will offer great progress toward the commercialization of the next-generation batteries: ASLBs, ASLSBs, and ASSBs.

## 1.9 Outline

This thesis is divided into six chapters. The above introduction constitutes Chapter 1. Chapters 2 to 5 include the main body of the work. Each chapter is structured into an introduction, experimental methods, results and discussion, and conclusions.

Chapter 2 demonstrates the solvent effect on the reactivity and solubility in the liquid-phase synthesis of  $\text{Li}_7\text{P}_3\text{S}_{11}$  SEs and introduces a novel rapid solution synthesis of  $\text{Li}_7\text{P}_3\text{S}_{11}$  via dynamic sulfur radical anions. The structural and electrochemical properties of  $\text{Li}_7\text{P}_3\text{S}_{11}$  SEs prepared via several organic solvents are analyzed by scanning electron microscopy (SEM), X-ray diffraction (XRD), magic-angle spinning-nuclear magnetic resonance (NMR), and electrochemical impedance spectroscopy (EIS) measurements. The chemical species in the precursor solution are identified based on ultraviolet-visible (UV-Vis) and Raman spectroscopy. Based on these results, the reaction mechanism is proposed.

Chapter 3 introduces novel  $\text{Li}_2\text{S}$ -based cathode materials prepared by high-energy ball milling for

ASLSBs. The material development contributes to the understanding the important role of the additive in ASLSBs. A fundamental analysis using electrochemical measurements and Raman measurement unveil the ASLSBs redox chemistry, a previously unclear mechanism.

Chapter 4 presents the development of sodium ion conductors for ASSBs. The structural and electrochemical properties of  $\text{Na}_{3-x}\text{SbS}_{4-x}\text{Cl}_x$  SEs are examined. The detailed crystal structure of  $\text{Na}_{3-x}\text{SbS}_{4-x}\text{Cl}_x$  is analyzed using the Rietveld method. Bond valence sum (BVS) mapping techniques reveal the Na-ion conduction pathways modified by the introduction of Cl-ion.

Overall conclusions and proposed future work are described in Chapter 5.

## References

- (1) Gür, T. M. Review of Electrical Energy Storage Technologies, Materials and Systems: Challenges and Prospects for Large-Scale Grid Storage. *Energy Environ. Sci.* **2018**, *11*, 2696–2767.
- (2) Arunachalam, V. S.; Fleischer, E. L. The Global Energy Landscape and Materials Innovation. *MRS Bulletin* **2008**, *33*, 264–288.
- (3) Yang, Z.; Zhang, J.; Kintner-Meyer, M. C. W.; Lu, X.; Choi, D.; Lemmon, J. P.; Liu, J. Electrochemical Energy Storage for Green Grid. *Chem. Rev.* **2011**, *111*, 3577–3613.
- (4) Tian, Y.; Zeng, G.; Rutt, A.; Shi, T.; Kim, H.; Wang, J.; Koettgen, J.; Sun, Y.; Ouyang, B.; Chen, T.; Lun, Z.; Rong, Z.; Persson, K.; Ceder, G. Promises and Challenges of Next-Generation “beyond Li-Ion” Batteries for Electric Vehicles and Grid Decarbonization. *Chem. Rev.* **2021**, *121*, 1623–1669.
- (5) Lee, S.; Manthiram, A. Can Cobalt Be Eliminated from Lithium-Ion Batteries? *ACS Energy Lett.* **2022**, *7*, 3058–3063.
- (6) Cano, Z. P.; Banham, D.; Ye, S.; Hintennach, A.; Lu, J.; Fowler, M.; Chen, Z. Batteries and Fuel Cells for Emerging Electric Vehicle Markets. *Nat. Energy* **2018**, *3*, 279–289.
- (7) Woodward, M.; Walton, B.; Hamilton, J.; Alberts, G.; Fullerton-Smith, S.; Day, E.; Ringrow, J. *Electric Vehicles - Setting a Course for 2030; Deloitte Insights*. Viewed on December 19.
- (8) Takada, K. Progress and Prospective of Solid-State Lithium Batteries. *Acta Mater.* **2013**, *61*, 759–770.
- (9) Faraday, M. IV. Experimental Researches in Electricity.—Third Series. *Philos. Trans. Royal Soc. Lond.* **1833**, *123*, 23–54.
- (10) Tubandt, C.; Lorenz, E. Molekularzustand Und Elektrisches Leitvermögen Kristallisierter Salze. *Zeitschrift für Physikalische Chemie* **1914**, *87U*, 513–542.
- (11) Joseph T Kummer; Neill Weber. Thermo-Electric Generator. 458, 1969.
- (12) Owens, B. B.; Argue, G. R. High-Conductivity Solid Electrolytes:  $\text{MgAg}_4\text{I}_5$ . *Science (1979)* **1967**, *157*, 308–310.
- (13) Tatsumisago, M.; Shinkuma, Y.; Minami, T. Stabilization of Superionic  $\alpha$ -AgI at Room Temperature in a Glass Matrix. *Nature* **1991**, *354*, 217–218.
- (14) Alpen, U. v.; Rabenau, A.; Talat, G. H. Ionic Conductivity in  $\text{Li}_3\text{N}$  Single Crystals. *Appl. Phys. Lett.* **1977**, *30*, 621–623.
- (15) Hong, H. Y.-P. Crystal Structure and Ionic Conductivity of  $\text{Li}_{14}\text{Zn}(\text{GeO}_4)_4$  and Other New  $\text{Li}^+$  Superionic Conductors. *Mater. Res. Bull.* **1978**, *13*, 117–124.
- (16) Monchak, M.; Hupfer, T.; Senyshyn, A.; Boysen, H.; Chernyshov, D.; Hansen, T.; Schell, K. G.; Bucharsky, E. C.; Hoffmann, M. J.; Ehrenberg, H. Lithium Diffusion Pathway in

- Li<sub>1.3</sub>Al<sub>0.3</sub>Ti<sub>1.7</sub>(PO<sub>4</sub>)<sub>3</sub>(LTP) Superionic Conductor. *Inorg. Chem.* **2016**, *55*, 2941–2945.
- (17) BATES, J. Electrical Properties of Amorphous Lithium Electrolyte Thin Films. *Solid State Ionics* **1992**, *53–56*, 647–654.
- (18) Mercier, R.; Malugani, J.-P.; Fahys, B.; Robert, G. Superionic conduction in Li<sub>2</sub>S – P<sub>2</sub>S<sub>5</sub> – LiI – glasses. *Solid State Ionics*, **1981**, *5*, 663–666.
- (19) Wada, H.; Menetrier, M.; Levasseur, A.; Hagenmuller, P. Preparation and Ionic Conductivity of New B<sub>2</sub>S<sub>3</sub>-Li<sub>2</sub>S-LiI Glasses. *Mater. Res. Bull.* **1983**, *18*, 189–193.
- (20) Yamane, H.; Shibata, M.; Shimane, Y.; Junke, T.; Seino, Y.; Adams, S.; Minami, K.; Hayashi, A.; Tatsumisago, M. Crystal Structure of a Superionic Conductor, Li<sub>7</sub>P<sub>3</sub>S<sub>11</sub>. *Solid State Ionics* **2007**, *178*, 1163–1167.
- (21) Kamaya, N.; Homma, K.; Yamakawa, Y.; Hirayama, M.; Kanno, R.; Yonemura, M.; Kamiyama, T.; Kato, Y.; Hama, S.; Kawamoto, K.; Mitsui, A. A Lithium Superionic Conductor. *Nat. Mater* **2011**, *10*, 682–686.
- (22) Oh, K.; Chang, D.; Lee, B.; Kim, D. H.; Yoon, G.; Park, I.; Kim, B.; Kang, K. Native Defects in Li<sub>10</sub>GeP<sub>2</sub>S<sub>12</sub> and Their Effect on Lithium Diffusion. *Chem. Mater.* **2018**, *30*, 4995–5004.
- (23) Gorai, P.; Long, H.; Jones, E.; Santhanagopalan, S.; Stevanović, V. Defect Chemistry of Disordered Solid-State Electrolyte Li<sub>10</sub>GeP<sub>2</sub>S<sub>12</sub>. *J. Mater. Chem. A* **2020**, *8*, 3851–3858.
- (24) Lorger, S.; Usiskin, R. E.; Maier, J. Transport and Charge Carrier Chemistry in Lithium Sulfide. *Adv. Funct. Mater.* **2019**, *29*, 1807688–1807698.
- (25) Maier, J. Defect Chemistry and Ion Transport in Nanostructured Materials Part II. Aspects of Nanoionics. *Solid State Ionics* **2003**, *157*, 327–334.
- (26) Einstein, A. Über Die von Der Molekularkinetischen Theorie Der Wärme Geforderte Bewegung von in Ruhenden Flüssigkeiten Suspendierten Teilchen. *Ann. Phys.* **1905**, *322*, 549–560.
- (27) von Smoluchowski, M. Zur Kinetischen Theorie Der Brownschen Molekularbewegung Und Der Suspensionen. *Ann. Phys.* **1906**, *326*, 756–780.
- (28) Wang, Y.; Richards, W. D.; Ong, S. P.; Miara, L. J.; Kim, J. C.; Mo, Y.; Ceder, G. Design Principles for Solid-State Lithium Superionic Conductors. *Nat. Mater* **2015**, *14*, 1026–1031.
- (29) Zhou, L.; Assoud, A.; Zhang, Q.; Wu, X.; Nazar, L. F. New Family of Argyrodite Thioantimonate Lithium Superionic Conductors. *J. Am. Chem. Soc.* **2019**, *141*, 19002–19013.
- (30) He, X.; Zhu, Y.; Mo, Y. Origin of Fast Ion Diffusion in Super-Ionic Conductors. *Nat. Commun.* **2017**, *8*, 15893–15898.
- (31) Lee, J.; Lee, T.; Char, K.; Kim, K. J.; Choi, J. W. Issues and Advances in Scaling up

- Sulfide-Based All-Solid-State Batteries. *Acc. Chem. Res.* **2021**, *54*, 3390–3402.
- (32) Miura, A.; Rosero-Navarro, N. C.; Sakuda, A.; Tadanaga, K.; Phuc, N. H. H.; Matsuda, A.; Machida, N.; Hayashi, A.; Tatsumisago, M. Liquid-Phase Syntheses of Sulfide Electrolytes for All-Solid-State Lithium Battery. *Nat. Rev. Chem.* **2019**, *3*, 189–198.
- (33) Sahu, G.; Lin, Z.; Li, J.; Liu, Z.; Dudney, N.; Liang, C. Air-Stable, High-Conduction Solid Electrolytes of Arsenic-Substituted  $\text{Li}_4\text{SnS}_4$ . *Energy Environ. Sci.* **2014**, *7*, 1053–1058.
- (34) Chen, X.; Guan, Z.; Chu, F.; Xue, Z.; Wu, F.; Yu, Y. Air-Stable Inorganic Solid-State Electrolytes for High Energy Density Lithium Batteries: Challenges, Strategies, and Prospects. *InfoMat* **2022**, *4*, e12248–e12267.
- (35) Homma, K.; Yonemura, M.; Kobayashi, T.; Nagao, M.; Hirayama, M.; Kanno, R. Crystal Structure and Phase Transitions of the Lithium Ionic Conductor  $\text{Li}_3\text{PS}_4$ . *Solid State Ionics* **2011**, *182*, 53–58.
- (36) Deiseroth, H. J.; Kong, S. T.; Eckert, H.; Vannahme, J.; Reiner, C.; Zaiß, T.; Schlosser, M.  $\text{Li}_6\text{PS}_5\text{X}$ : A Class of Crystalline Li-Rich Solids with an Unusually High  $\text{Li}^+$  Mobility. *Angew. Chem.* **2008**, *47*, 755–758.
- (37) Kamaya, N.; Homma, K.; Yamakawa, Y.; Hirayama, M.; Kanno, R.; Yonemura, M.; Kamiyama, T.; Kato, Y.; Hama, S.; Kawamoto, K.; Mitsui, A. A Lithium Superionic Conductor. *Nat. Mater.* **2011**, *10*, 682–686.
- (38) Xu, M.; Song, S.; Daikuhara, S.; Matsui, N.; Hori, S.; Suzuki, K.; Hirayama, M.; Shiotani, S.; Nakanishi, S.; Yonemura, M.; Saito, T.; Kamiyama, T.; Kanno, R.  $\text{Li}_{10}\text{GeP}_2\text{S}_{12}$ -Type Structured Solid Solution Phases in the  $\text{Li}_{9+\delta}\text{P}_{3+\delta}\text{S}_{12-k}\text{O}_k$  System: Controlling Crystallinity by Synthesis to Improve the Air Stability. *Inorg. Chem.* **2022**, *61*, 52–61.
- (39) Tsukasaki, H.; Mori, S.; Shiotani, S.; Yamamura, H. Ionic Conductivity and Crystallization Process in the  $\text{Li}_2\text{S}$ – $\text{P}_2\text{S}_5$  Glass Electrolyte. *Solid State Ionics* **2018**, *317*, 122–126.
- (40) Stöffler, H.; Zinkevich, T.; Yavuz, M.; Hansen, A. L.; Knapp, M.; Bednarčík, J.; Randau, S.; Richter, F. H.; Janek, J.; Ehrenberg, H.; Indris, S. Amorphous versus Crystalline  $\text{Li}_3\text{PS}_4$ : Local Structural Changes during Synthesis and Li Ion Mobility. *J. Phys. Chem. C* **2019**, *123*, 10280–10290.
- (41) Schlem, R.; Burmeister, C. F.; Michalowski, P.; Ohno, S.; Dewald, G. F.; Kwade, A.; Zeier, W. G. Energy Storage Materials for Solid-State Batteries: Design by Mechanochemistry. *Adv. Energy Mater.* **2021**, *11*, 2101022–2101042.
- (42) Hayashi, A.; Noi, K.; Sakuda, A.; Tatsumisago, M. Superionic Glass-Ceramic Electrolytes for Room-Temperature Rechargeable Sodium Batteries. *Nat. Commun.* **2012**, *3*, 856–860.
- (43) Krauskopf, T.; Culver, S. P.; Zeier, W. G. Local Tetragonal Structure of the Cubic Superionic Conductor  $\text{Na}_3\text{PS}_4$ . *Inorg. Chem.* **2018**, *57*, 4739–4744.
- (44) Cronau, M.; Szabo, M.; Roling, B. Single-Step Ball Milling Synthesis of Highly

- Li<sup>+</sup>-conductive Li<sub>5.3</sub>PS<sub>4.3</sub>ClBr<sub>0.7</sub> glass Ceramic Electrolyte Enables Low-Impedance All-Solid-State Batteries. *Mater. Adv.* **2021**, *2*, 7842–7845.
- (45) Teragawa, S.; Aso, K.; Tadanaga, K.; Hayashi, A.; Tatsumisago, M. Liquid-Phase Synthesis of a Li<sub>3</sub>PS<sub>4</sub> Solid Electrolyte Using N-Methylformamide for All-Solid-State Lithium Batteries. *J. Mater. Chem. A* **2014**, *2*, 5095–5099.
- (46) Calpa, M.; Rosero-Navarro, N. C.; Miura, A.; Terai, K.; Utsuno, F.; Tadanaga, K. Formation Mechanism of Thiophosphate Anions in the Liquid-Phase Synthesis of Sulfide Solid Electrolytes Using Polar Aprotic Solvents. *Chem. Mater.* **2020**, *32*, 9627–9632.
- (47) Matsuda, A.; Muto, H.; Phuc, N. H. H. Preparation of Li<sub>3</sub>PS<sub>4</sub> Solid Electrolyte by Liquid-Phase Shaking Using Organic Solvents with Carbonyl Group as Complex Forming Medium. *J. Jpn. Soc. Powder Powder Metallurgy*, **2016**, *63*, 976–980.
- (48) Ghidui, M.; Ruhl, J.; Culver, S. P.; Zeier, W. G. Solution-Based Synthesis of Lithium Thiophosphate Superionic Conductors for Solid-State Batteries: A Chemistry Perspective. *J. Mater. Chem. A* **2019**, *7*, 17735–17753.
- (49) Lee, S.; Manthiram, A. Can Cobalt Be Eliminated from Lithium-Ion Batteries? *ACS Energy Lett.* **2022**, *7*, 3058–3063.
- (50) Chung, W. J.; Griebel, J. J.; Kim, E. T.; Yoon, H.; Simmonds, A. G.; Ji, H. J.; Dirlam, P. T.; Glass, R. S.; Wie, J. J.; Nguyen, N. A.; Guralnick, B. W.; Park, J.; Somogyi, Á.; Theato, P.; Mackay, M. E.; Sung, Y. E.; Char, K.; Pyun, J. The Use of Elemental Sulfur as an Alternative Feedstock for Polymeric Materials. *Nat. Chem.* **2013**, *5*, 518–524.
- (51) Rauchfuss, T. Under Sulfur's Spell. *Nat. Chem.* **2011**, *3*, 648.
- (52) Bruce, P. G.; Freunberger, S. A.; Hardwick, L. J.; Tarascon, J. M. Erratum:Li<sub>2</sub>O and Li<sub>2</sub>S Batteries with High Energy Storage. *Nat. Mater.* **2012**, *11*, 19–29.
- (53) Bruce, P. G.; Hardwick, L. J.; Abraham, K. M. Lithium-Air and Lithium-Sulfur Batteries. *MRS Bull.* **2011**, *36*, 506–512.
- (54) Hayashi, A.; Ohtomo, T.; Mizuno, F.; Tadanaga, K.; Tatsumisago, M. All-Solid-State Li/S Batteries with Highly Conductive Glass-Ceramic Electrolytes. *Electrochem. Commun.* **2003**, *5*, 701–705.
- (55) Yabuuchi, N.; Kubota, K.; Dahbi, M.; Komaba, S. Research Development on Sodium-Ion Batteries. *Chem. Rev.* **2014**, *114*, 11636–11682.
- (56) Oshima, T.; Kajita, M. Development of Sodium-Sulfur Batteries. *Int. Appl. Ceram. Technol.* **2004**, *1*, 269–276.
- (57) Bones, R. J.; Teagle, D. A.; Brooker, S. D.; Cullen, F. L. Development of a Ni<sub>2</sub>NiCl<sub>2</sub> Positive Electrode for a Liquid Sodium (ZEBRA) Battery Cell. *J. Electrochem. Soc.* **1989**, *136*, 1274–1278.
- (58) Nanjundaswamy, K. S.; Padhi, A. K.; Goodenough, J. B.; Okada, S.; Ohtsuka, H.;

- Araib, H.; Yamakib, J. Synthesis, Redox Potential Evaluation and Electrochemical Characteristics of NASICON-Related-3D Framework Compounds. *Solid State Ionics*, **1996**, *92*, 1–10.
- (59) Hong, Y.-P. CRYSTAL STRUCTURES AND CRYSTAL CHEMISTRY IN THE SYSTEM  $\text{Na}_{1+x}\text{Zr}_2\text{Si}_x\text{P}_{3-x}\text{O}_{12}$ . Pergamon Press. Inc. **1976**, *11*, 173–182.
- (60) Hayashi, A.; Noi, K.; Sakuda, A.; Tatsumisago, M. Superionic Glass-Ceramic Electrolytes for Room-Temperature Rechargeable Sodium Batteries. *Nat. Commun.* **2012**, *3*, 856–890.
- (61) Banerjee, A.; Park, K. H.; Heo, J. W.; Nam, Y. J.; Moon, C. K.; Oh, S. M.; Hong, S. T.; Jung, Y. S.  $\text{Na}_3\text{SbS}_4$ : A Solution Processable Sodium Superionic Conductor for All-Solid-State Sodium-Ion Batteries. *Angew. Chem.* **2016**, *55*, 9634–9638.
- (62) Zhang, L.; Zhang, D.; Yang, K.; Yan, X.; Wang, L.; Mi, J.; Xu, B.; Li, Y. Vacancy-Contained Tetragonal  $\text{Na}_3\text{SbS}_4$  Superionic Conductor. *Adv. Sci.* **2016**, *3*, 1600089–1600094.

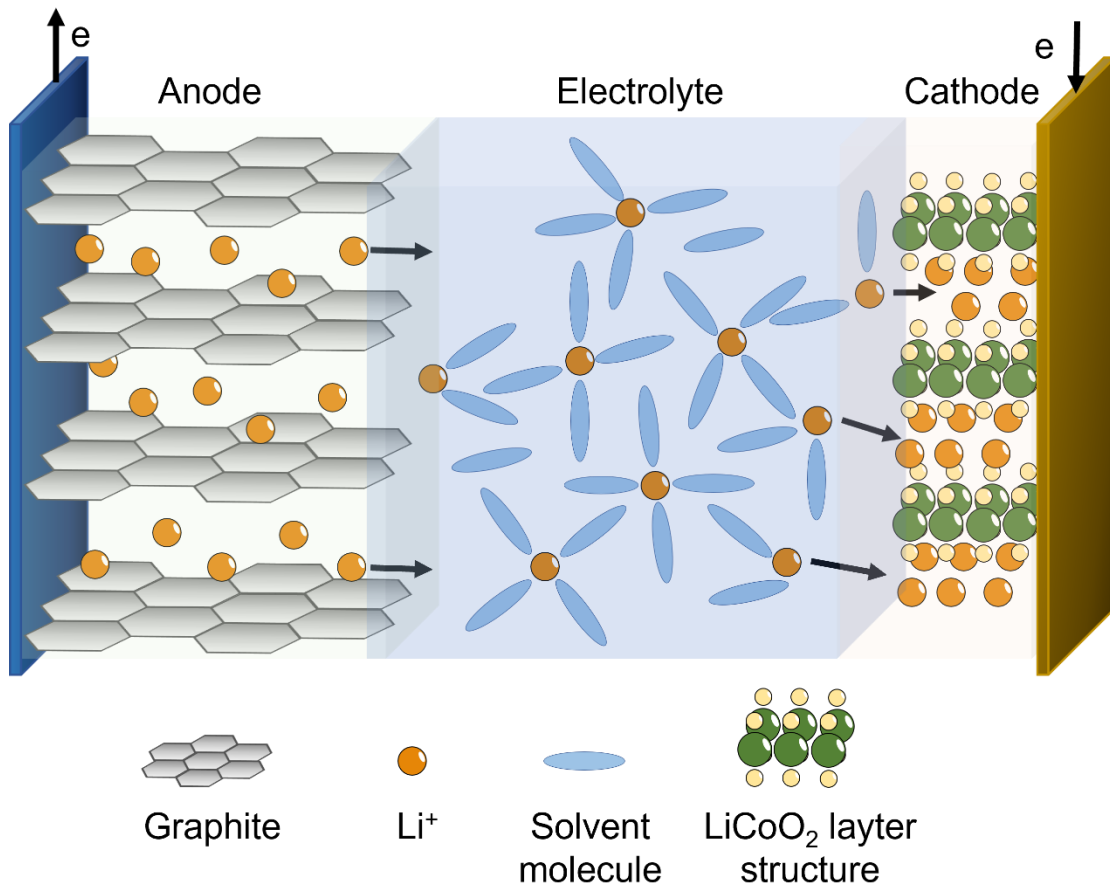


**Figure 1.1.** Schematic of conventional LIBs using graphite as an anode and  $\text{LiCoO}_2$  as a cathode.



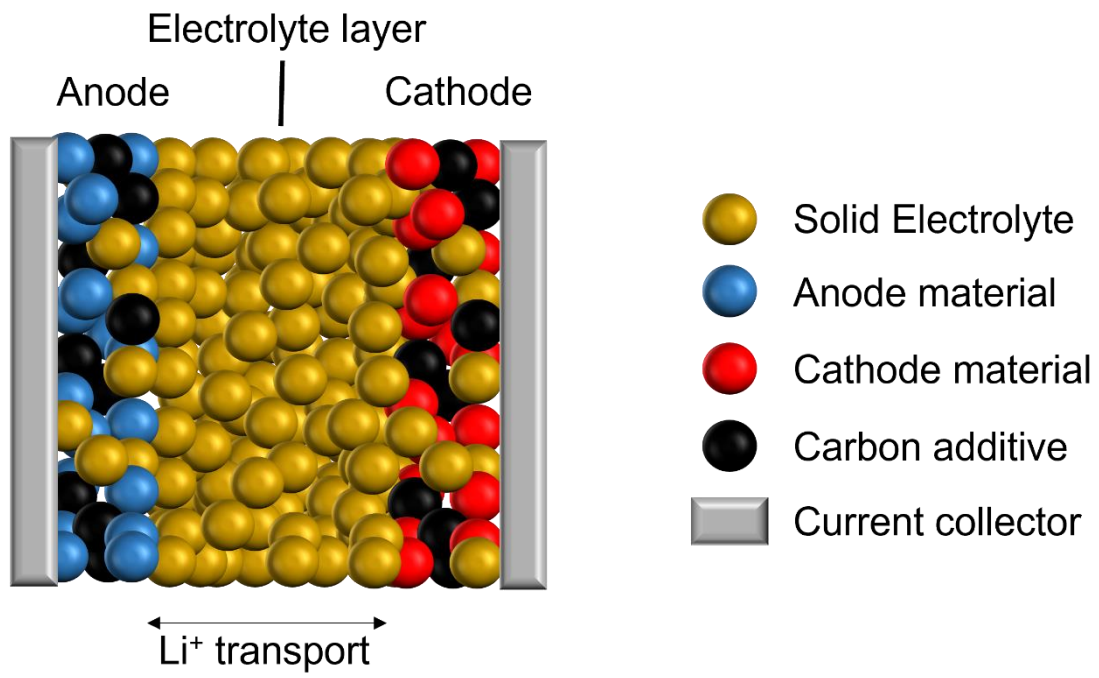


**Figure 1.2.** Schematic of ASLBs in which organic liquid electrolyte is replaced by inorganic SE.

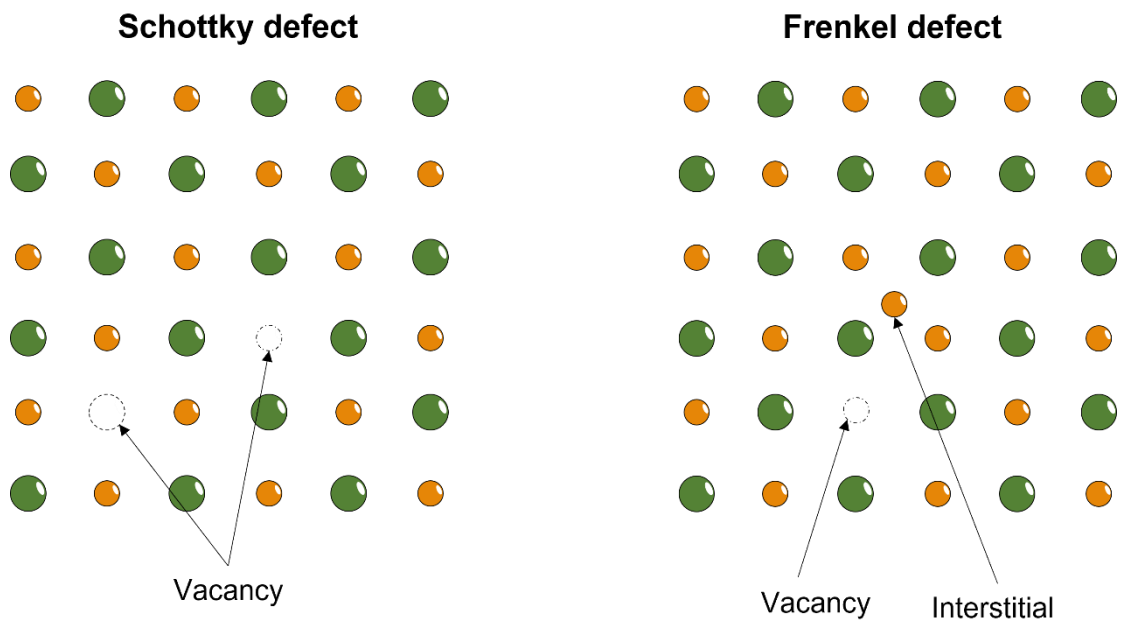


**Figure 1.3.** Idealized representations of intrinsic point defects in an ionic crystal; (a) Schottky defect, (b) Frenkel defect.

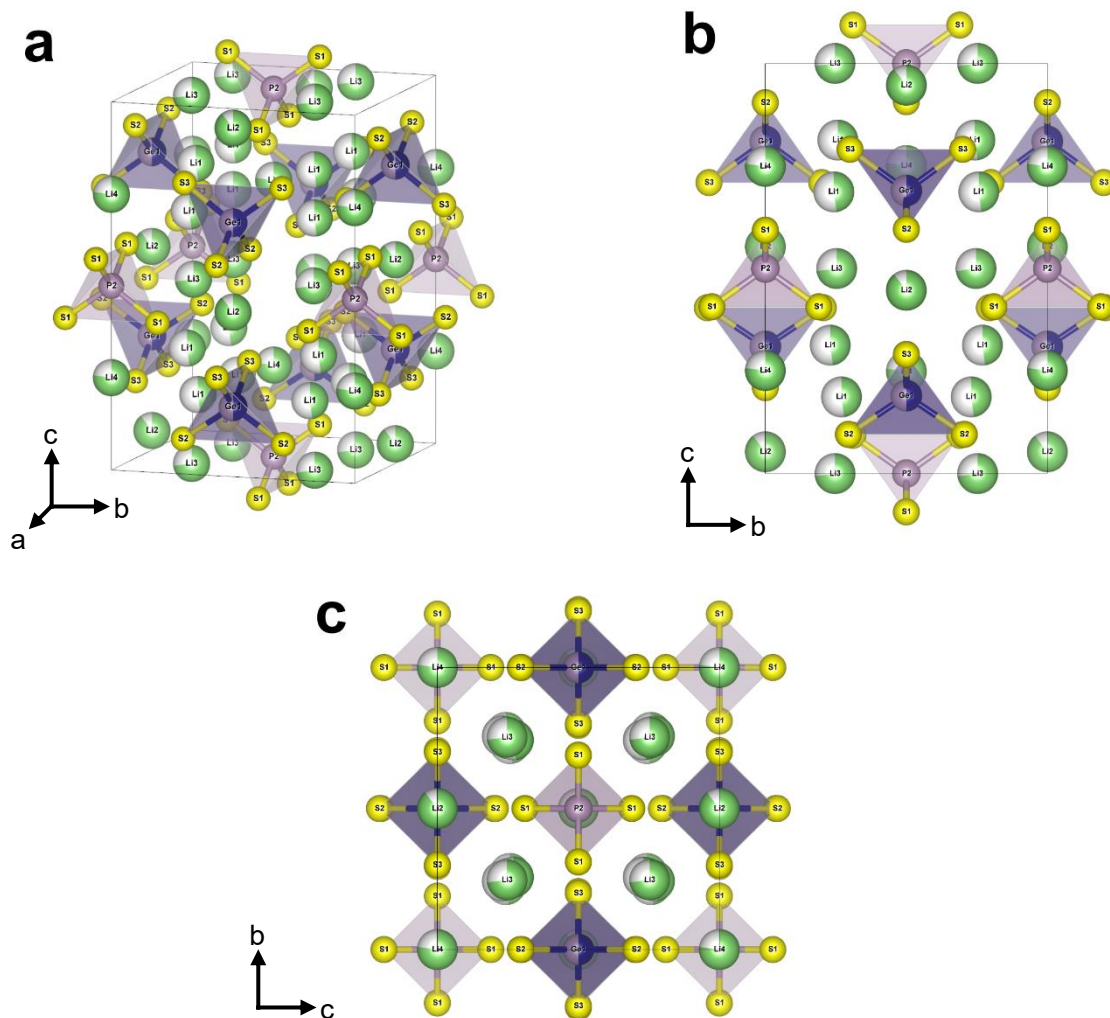


**Figure 1.4.** (a) Crystal structure of  $\text{Li}_{10}\text{GeP}_2\text{S}_{12}$  with a space group of  $P 42/n m c$ , visualized with VESTA software (ICSD no. 7215190). (b) the side view and (c) top view. Lithium atom, sulfur atom, germanium atom, and phosphorus atom are colored green, yellow, blue, purple, respectively. The sulfur anion sublattice is closely located in a bcc framework.

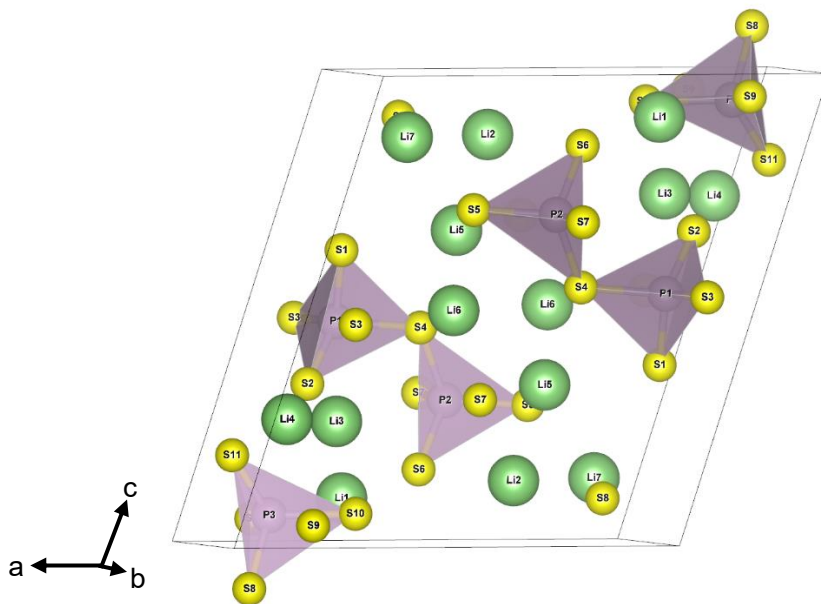


**Figure 1.5.** Crystal structure of  $\text{Li}_7\text{P}_3\text{S}_{11}$  with a space group of  $P-1$ , visualized with VESTA software (ICSD no. 157654). Lithium atom, sulfur atom, and phosphorus atom are colored green, yellow, and purple, respectively.

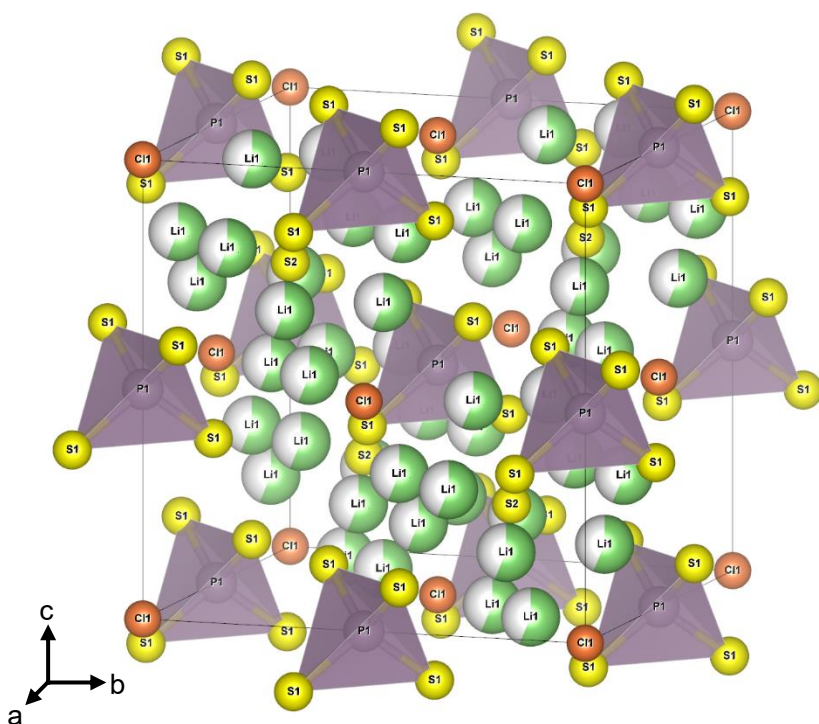
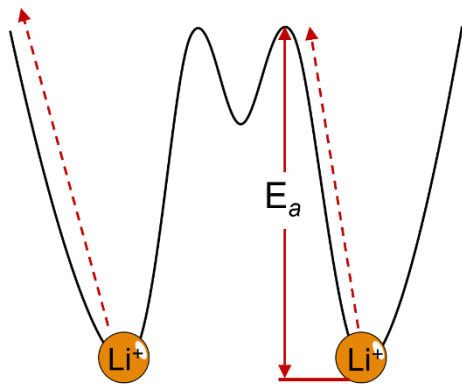


**Figure 1.6.** Crystal structure of  $\text{Li}_6\text{PS}_5\text{Cl}$  with a space group of  $F\bar{4}3m$ , visualized with VESTA software (ICSD no. 1626573). Lithium atom, sulfur atom, phosphorus atom, and chlorine atom are colored green, yellow, purple, and orange, respectively.

### Single ion migration



### Concerted ion migration

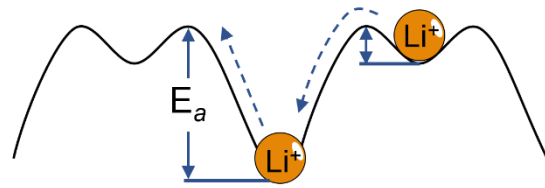


**Figure 1.7.** Proposed ion migration mechanism of (a) traditional vacancy Li ion diffusion and (b) concerted Li ion migration with a flatter energy landscape induced by the Coulombic interactions between the mobile ions.

## Chapter 2

# Liquid-phase synthesis of lithium-ion sulfide solid electrolytes

### 2.1 Background

Rechargeable batteries are a viable option for clean energy storage systems and their application in electric vehicles. The rapid growth of LIBs has raised safety concerns regarding commercial LIBs with liquid electrolytes. In particular, the use of flammable organic liquid electrolytes can cause leakage from and ignition of the electrolytes.<sup>1,2</sup> Replacing the organic liquid electrolyte with SEs will ensure excellent battery safety. Thus, ASLBs using inorganic SEs are considered next-generation ESS devices that provide high intrinsic safety, which is currently of great interest for EV technologies.<sup>2,3</sup> The success of ASLBs is a key for SEs with high ionic conductivity. ASLB studies over the past decades have focused on exploring the rational classes of SEs. Solid electrolytes are classified into oxide, sulfide, and halide materials. Sulfide SEs are a type of SE that offers the potential to realize higher ionic conductivity at room temperature than the others because of the higher polarizability of  $S^{2-}$ .<sup>1</sup> Additionally, sulfide SEs provide intimate contact that can be achieved between solids by directly cold-pressing the sulfide powder instead of the high-sintering needed for oxides. These advantages make sulfide SEs attractive for ASLBs. Previous works have discovered sulfide-based SEs that exhibit ionic conductivities on the order of  $10^{-2}$  S  $cm^{-1}$  at room temperature, for example,  $Li_{10}GeP_2S_{12}$ ,<sup>4</sup>  $Li_7P_3S_{11}$ ,<sup>5</sup> and argyrodite-type SEs,<sup>6</sup> comparable even to those of organic electrolytes. Such SEs are commonly synthesized by solid-state and mechanochemical methods, which consume much energy and limit manufacturing scale-up owing to the use of special apparatus.<sup>7</sup> Moreover, the moisture sensitivity of sulfide-based SEs and starting materials has been a serious obstacle to developing the large-scale manufacturing technologies of ASLBs.<sup>7,8</sup> In contrast, the liquid-phase method is highly scalable and low-cost for the entire manufacturing process and allows the production of composite materials with electrolytes and electrodes in intimate contact.<sup>9,10</sup> The liquid-phase method is classified into suspension, solution, and dissolution-precipitation methods. Among the liquid-phase synthesis, the solution-based process could be used in manufacturing based on the accumulated expertise of lithium-ion batteries, which would reduce the barrier to industry adoption.<sup>8</sup> Given the reactivity of sulfide, aprotic polar solvents are suitable for a reaction medium in the liquid-phase synthesis of sulfide SEs. The nature of organic solvents affects the solubility and chemical stability of lithium thiophosphates in the liquid process. However, there is a lack of leading theory on the solvent effect in the liquid-phase synthesis of the highly conductive crystalline  $Li_7P_3S_{11}$  phase. In

this chapter, I provide guidelines for solvent selection for the liquid-phase synthesis of superionic conductor  $\text{Li}_7\text{P}_3\text{S}_{11}$  (Chapter 2.2) and unprecedented solution synthesis method via dynamic sulfur radical anions for the rapid and scalable manufacturing of ASLBs (Chapter 2.3).

## 2.2 Effect of organic solvent on the reactivity of $\text{Li}_2\text{S-P}_2\text{S}_5$ systems in liquid-phase synthesis

In this chapter, guidelines for solvent selection for the liquid-phase synthesis of  $\text{Li}_7\text{P}_3\text{S}_{11}$  SEs are described through a systematic study on the reactivity and solubility of lithium thiophosphates in organic solvents.  $70\text{Li}_2\text{S}\cdot 30\text{P}_2\text{S}_5$  system, a raw material of  $\text{Li}_7\text{P}_3\text{S}_{11}$ , is treated via a wet-chemical reaction using eight organic solvents with various chemical and physical properties: dielectric constant, molecule structure, and boiling point. I reveal that the solvent's polarity, characterized by the dielectric constant, plays a critical role in the formation of crystalline  $\text{Li}_7\text{P}_3\text{S}_{11}$ . Acetonitrile solvent with a high dielectric constant is found to lead to high-purity crystalline  $\text{Li}_7\text{P}_3\text{S}_{11}$  SEs with high ionic conductivity. Given the high dielectric constant, low boiling point, and linear molecule structure of acetonitrile (ACN), ACN solvent is suitable for the liquid-phase synthesis of a crystalline  $\text{Li}_7\text{P}_3\text{S}_{11}$  SE with high purity.

### 2.2.1 Introduction

The performance of sulfide SEs prepared by the liquid phase method depends on the nature of organic solvents, such as solubility, polarity, and boiling point.<sup>11,12</sup> The solubility and polarity of organic solvents dominate the reactivity of lithium thiophosphates in the organic solvent. The use of aprotic solvents with high solubility and polarity, e.g., tetrahydrofuran (THF) and ACN, is effective for the liquid phase synthesis of  $\beta\text{-Li}_3\text{PS}_4$ , a typical sulfide SE.<sup>13</sup> Phuc et al. proposed that  $\text{Li}_3\text{PS}_4$  was synthesized by a liquid-phase shaking, in which the wet-reaction is assisted by mechanical energy from beads mill.<sup>14</sup> Yamamoto et al. demonstrated the effect of solvent on the ionic conductivity of  $\text{Li}_3\text{PS}_4$  synthesized by a liquid shaking method.<sup>15</sup> The ionic conductivity of  $\text{Li}_3\text{PS}_4$  prepared via a liquid-phase shaking was found to have a strong correlation with the polarity,  $\delta_p$ , of the solvent, reaching  $5.09 \times 10^{-4} \text{ S cm}^{-1}$  at room temperature in the case of butyl acetate with low polarity. This value is consistent with the conductivity of a sample obtained via ball milling. In addition to  $\text{Li}_3\text{PS}_4$ ,  $\text{Li}_7\text{P}_3\text{S}_{11}$  prepared by the liquid-phase method delivers high ionic conductivity and is a promising candidate for easier processing of ASLBs.<sup>7</sup> In 2012,  $\text{Li}_7\text{P}_3\text{S}_{11}$  was synthesized using 1,2-dimethoxyethane solvent, which showed an ionic conductivity of  $2.7 \times 10^{-4} \text{ S cm}^{-1}$  at room temperature.<sup>16</sup> Following this,  $\text{Li}_7\text{P}_3\text{S}_{11}$  was prepared using ACN, THF, and anisole solvents.<sup>17,18</sup> Several research groups have also focused their efforts on the synthesis of



Li<sub>7</sub>P<sub>3</sub>S<sub>11</sub> based on ACN solvent.<sup>19–23</sup> Xu et al. observed differences between Li<sub>7</sub>P<sub>3</sub>S<sub>11</sub> synthesized from THF and ACN solvents and suggested that the steric hindrance (ring or short-chain structure) of these solvent molecules results in the presence of residue molecules in the SE.<sup>17</sup> However, due to the absence of systematic studies, no leading theory on the solvent effect in the liquid-phase synthesis of highly conductive crystalline Li<sub>7</sub>P<sub>3</sub>S<sub>11</sub> phase has been developed.

In this work, I investigated the effect of solvent on reactivity in the formation of Li<sub>7</sub>P<sub>3</sub>S<sub>11</sub> SEs. I employed 1,4-dioxane (Dox), carbon disulfide (CS), tetrahydropyran (THP), nitromethane (NM), ACN, furfural (FF), succinonitrile (SN), and ethylene carbonate (EC) reaction mediums. The use of organic solvents with high dielectric constant leads to high reactivity in the Li<sub>2</sub>S–P<sub>2</sub>S<sub>5</sub> system, being beneficial for the formation of high-purity crystalline Li<sub>7</sub>P<sub>3</sub>S<sub>11</sub> from liquid-phase synthesis. However, all the solvents with a high dielectric constant except for ACN undergo a side reaction with the Li<sub>2</sub>S–P<sub>2</sub>S<sub>5</sub> system. Furthermore, they are not suitable for solvent removal via a drying process because of their high boiling point. Here, we demonstrate that ACN solvent is a suitable solvent for the formation of Li<sub>7</sub>P<sub>3</sub>S<sub>11</sub> SE because of its high dielectric constant, linear structure, and low boiling point.

## 2.2.2 Experimental methods

**Synthesis.** Lithium sulfide (99.9%, Mitsuwa) and P<sub>2</sub>S<sub>5</sub> (99%, Merck) were mixed in a mole ratio of 7:3 and then added into Dox (anhydrous, 99.8%, Aldrich), THP (anhydrous, 99%, Aldrich), CS (anhydrous, ≥99%, Aldrich), ACN (super dehydrated, 99.8%, Fujifilm), FF (99%, Aldrich), NM (98%, TCI), SN (99.0%, TCI), and EC (anhydrous, 99%, Aldrich) solvents, separately. The mass/volume ratio of the powder/solvent was 1:20 g/ml. The resultant mixtures were stirred at 50°C for 3 days, and the obtained suspensions were dried under vacuum at 80°C for 12 h. In the case of FF, SN, and EC, a temperature of 150°C was required during the drying process. After that, the precursor powders were annealed at 270°C for 1 h to obtain the Li<sub>7</sub>P<sub>3</sub>S<sub>11</sub> SEs. The entire Li<sub>7</sub>P<sub>3</sub>S<sub>11</sub> synthesis process was handled under an Ar atmosphere.

**Material characterization.** Powder XRD measurements were carried out under  $2\theta = 10^\circ\text{--}50^\circ$  with a step interval of  $0.02^\circ$  and a scan rate of  $1^\circ \text{min}^{-1}$  using a Rigaku Ultima IV diffractometer. The X-ray beam was generated by CuK $\alpha$  radiation (40 kV, 30 mA). I used an XRD holder with a beryllium window (Rigaku). Scanning electron microscopy characterization was carried out using an SEM (S4800, Hitachi), and Thermogravimetry-Differential Thermal Analysis (TG-DTA; EVO II, Rigaku) was performed under Ar flow with a temperature increase of  $5 \text{ K min}^{-1}$ .

**Electrochemical measurements.** The total conductivities of the SEs were measured through samples cold pressed into pellets with diameters of  $\sim 10.0 \text{ mm}$  under a pressure of 256 MPa. To assemble the cell for EIS measurements, each sample ( $\sim 80 \text{ mg}$ ) was filled into a holder made of

polyether ether ketone (PEEK) with two stainless steel rods as blocking electrodes. EIS measurements were conducted via alternating-current impedance spectroscopy (SI 1260, Solartron) in a frequency range of 1 MHz to 10 Hz under a dry Ar flow at a temperature of 298 K.

### 2.2.3 Chemical, structural, and microstructural properties

Figure 2.2.1 shows the suspensions for  $\text{Li}_7\text{P}_3\text{S}_{11}$  with each organic solvent after stirring at  $50^\circ\text{C}$  for 3 days. The color of the suspension varies depending on the solvent. The suspensions with ACN and THP were milky white and off-white, respectively. Chemical reactivity in organic solvents generally depends on the polarity between solvent molecular and ionic species.<sup>24</sup> In particular, the dielectric constant and DN of the organic solvent are crucial indicators for the formation of a solvating complex. For instance, ACN molecules have stronger interactions with Li ions due to their high dielectric constant, as outlined in Table 2.2.1. In addition, the coordination of ACN with cations (in this case Li ions) is less affected by steric hindrance because of the linear structure.<sup>25</sup> The strong interaction between Li ions and ACN indicates their shorter bond length relative to those between Li ions and other solvents, resulting in the white color of the suspension, which is the typical color of the  $\text{Li}_3\text{PS}_4$  complex. THP solvent also offers a lower dielectric constant and steric hindrance induced by its cyclic structure. These natures lead to a weaker interaction with Li ions. The use of Dox, CS, and NM as the reaction media resulted in a yellowish-white suspension, indicating poorer reactivity to  $\text{Li}_3\text{PS}_4$  than ACN and THP. The mixture of starting materials including FF solvent immediately became discolored (black) after the addition of the solvent, indicating the occurrence of a side reaction between the FF solvent molecules and the  $\text{Li}_2\text{S}-\text{P}_2\text{S}_5$  systems. The suspension with SN solvent gradually became black during stirring, probably resulting in the relatively strong cross-interaction between Li ions and the two CN groups in SN. Figure 2.2.2a and b shows the XRD patterns of the precursors and samples following heat treatment, respectively. The crystal structures of the precursors vary depending on the solvent due to the differences in polarity and structure of the solvent molecules. The XRD pattern of the precursor containing ACN solvent is consistent with that of  $\text{Li}_3\text{PS}_4\cdot\text{ACN}$ , as reported by Calpa et al.<sup>26</sup> The  $\text{Li}_7\text{P}_3\text{S}_{11}$  precursor involves two phases of the  $\text{Li}_2\text{S}\cdot\text{P}_2\text{S}_5$  and  $\text{Li}_3\text{PS}_4$  complexes.<sup>27</sup> According to a recent study, following a drying process at  $100^\circ\text{C}$ ,  $\text{Li}_2\text{S}\cdot\text{P}_2\text{S}_5$  with ACN exhibits a halo-shaped XRD pattern originating from its amorphous structure.<sup>28</sup> Thus, the  $\text{Li}_7\text{P}_3\text{S}_{11}$  precursor with ACN solvent contains crystalline  $\text{Li}_3\text{PS}_4\cdot\text{ACN}$  and amorphous  $\text{Li}_2\text{S}\cdot\text{P}_2\text{S}_5$ . Residue  $\text{Li}_2\text{S}$  is observed in the precursors with ACN, THP, CS, and Dox solvents. The intensity of the peak corresponding to residual  $\text{Li}_2\text{S}$  decreases in relation to increases in the dielectric constant of the solvent. The precursor with EC solvent retains a large amount of unreacted  $\text{Li}_2\text{S}$  without being affected by the high polarity of the EC solvent. Lithium-sulfur

batteries using EC-based liquid electrolytes suppress the dissolution of lithium polysulfides generated during the electrochemical cycling process.<sup>29</sup> This indicates that EC solvent has low solubility for sulfur species, which can be described by the low reactivity of the EC solvents with  $\text{Li}_2\text{S}$  and  $\text{P}_2\text{S}_5$  observed in this study.

$\text{Li}_7\text{P}_3\text{S}_{11}$  crystalline phase was successfully synthesized in the samples with ACN, THP, and Dox solvent following heat treatment. The intensity of the first peak originated from the  $\text{Li}_7\text{P}_3\text{S}_{11}$  crystal phase at 29.7 degrees increases in the order of Dox, THF, and then ACN solvents, which shows the value of 232, 316, and 386, respectively. This observation suggests that the higher dielectric constant of the solvent delivers higher purity of crystalline  $\text{Li}_7\text{P}_3\text{S}_{11}$ . In the samples containing THP and Dox,  $\text{Li}_3\text{PS}_4$  and  $\text{Li}_2\text{P}_2\text{S}_6$  crystalline phases remain following heat treatment. This is consistent with the trend observed in  $\text{Li}_7\text{P}_3\text{S}_{11}$  synthesized from the liquid phase in ACN and THF solvents demonstrated in a previous study.<sup>17</sup> The sample with NM solvent involves an unknown phase. The samples containing FF and SN exhibit amorphous structure before and after heat treatment at 270°C. Given the color of the precursor suspension and the XRD results, the FF and SN solvent molecules may cause a side reaction with the initial materials. The aldehyde is also activated by the action of Lewis acid as a catalyst. FF solvent is an aromatic compound with an aldehyde group, which indicates that the side reaction is caused by the coordinate bond between Li ions and negatively charged oxygen molecules within the carboxyl group. In addition, Li ions attack the oxygen molecules of the cyclic compound within the FF solvent molecules, which is associated with ring opening and a chain of side reactions.

Figure 2.2.3 shows SEM images of  $70\text{Li}_2\text{S}\cdot 30\text{P}_2\text{S}_5$  SEs prepared via each solvent. In all the samples, the secondary particles range in diameter from 50 to 100  $\mu\text{m}$ . The microstructures of the samples prepared using ACN, THP, and Dox exhibit intriguing textures, including one resembling a broccoli crown. The microstructure of the sample prepared via ACN solvent involves uniform pseudo-spherical primary particles of less than 1  $\mu\text{m}$ , and each particle is aggregated and connected with the others. The homogeneous  $\text{Li}_7\text{P}_3\text{S}_{11}$  is produced through a solid reaction between the  $\text{Li}_3\text{PS}_4$  complex and  $\text{Li}_2\text{S}\cdot\text{P}_2\text{S}_5$ . The samples using THP and Dox form primary particles with nonuniform shapes, showing rougher particles than the sample generated via ACN solvent. The microstructures of the samples generated via NM, SN, and EC exhibit a very rough particle surface. Monolithic particles of greater than 50  $\mu\text{m}$  are observed in the samples synthesized via CS and FF. This means that the residue includes coordinated complexes and compounds generated from a side reaction, as shown in the TG-DTA results. Figure 2.2.4a and b displays the TGA and DTA curves, respectively, for the precursors in Dox, THP, and ACN solvents. The precursor powders prepared using ACN and THP both exhibit three steps of weight loss. Several studies have demonstrated that forward DTA scans of  $\text{Li}_3\text{PS}_4$  complexes containing

organic solvent exhibit large endothermic peaks.<sup>13,15</sup> Further, the decomposition reaction of  $\text{Li}_7\text{P}_3\text{S}_{11}$  to  $\text{Li}_4\text{P}_2\text{S}_6$ ,  $\text{Li}_3\text{PS}_4$ , and sulfur occurs at a temperature higher than  $280^\circ\text{C}$ .<sup>30,31</sup> Thus, the first step corresponds to the evaporation of solvent molecules coordinated to  $\text{Li}_2\text{S}-\text{P}_2\text{S}_5$ , the second step corresponds to the evaporation of solvent molecules coordinated to  $\text{Li}_3\text{PS}_4$ , and the third step corresponds to the evaporation of sulfur with the decomposition of  $\text{Li}_7\text{P}_3\text{S}_{11}$ . The heat treatment temperature for the formation of  $\text{Li}_7\text{P}_3\text{S}_{11}$  SEs was determined from the TG-DTA results. The precursors prepared using Dox, THP, and ACN involve the solvent molecule at 3.0wt%, 32.3wt%, and 20.7wt%, respectively. The respective mole ratios of the coordinated solvent molecules of Dox, THP, and ACN in the precursor are 0.17, 2.73, and 3.14 against  $3.5\text{Li}_2\text{S}\cdot 1.5\text{P}_2\text{S}_5$ . The extent of the weight loss is not correlated with the boiling point of the solvent. The precursors prepared using Dox, THP, and ACN solvents exhibit endothermic peaks at  $120^\circ\text{C}$ ,  $150^\circ\text{C}$ , and  $200^\circ\text{C}$ , respectively. These observations indicate that the strength of the chemical interaction between the  $\text{Li}_2\text{S}-\text{P}_2\text{S}_5$  system and solvent molecules increases in the order of Dox, THP, and then ACN. This is related to solvent polarity, characterized by the dielectric constant. In the case of the precursors containing the NM, FF, and SN solvents, continuous weight loss during the annealing process is observed up to  $450^\circ\text{C}$  (Figure 2.2.4c and d). This experimental result indicates that these solvent molecules remain following heat treatment at  $270^\circ\text{C}$ . It should be noted that these observations may be influenced by the evaporation of sulfur within  $70\text{Li}_2\text{S}\cdot 30\text{P}_2\text{S}_5$  during heat treatment.

#### 2.2.4 Ionic conductivity of $70\text{Li}_2\text{S}\cdot 30\text{P}_2\text{S}_5$ systems

Figure 2.2.5a shows Nyquist plots of the  $70\text{Li}_2\text{S}\cdot 30\text{P}_2\text{S}_5$  SEs synthesized using Dox, THP, and ACN. The total resistance, including the bulk and grain boundary contributions, was determined by the real-axis intercept at high frequency. The resistance of SEs decreases in the order of Dox, THP, and then ACN. Figure 2.2.5b shows the calculated conductivities as a function of the solvent's dielectric constant. These results reveal the correlation between the dielectric constant of the solvent and the ionic conductivity of the obtained SEs. The  $70\text{Li}_2\text{S}\cdot 30\text{P}_2\text{S}_5$  SEs synthesized using ACN solvent exhibit the highest ionic conductivity of  $0.8 \text{ mS cm}^{-1}$  at room temperature among the prepared samples. Highly crystallized  $70\text{Li}_2\text{S}\cdot 30\text{P}_2\text{S}_5$  SEs exhibit higher ionic conductivity than the amorphous  $70\text{Li}_2\text{S}\cdot 30\text{P}_2\text{S}_5$ .<sup>32,33</sup> The high ionic conductivity obtained from the sample prepared using ACN can be explained by the formation of high-purity crystalline  $\text{Li}_7\text{P}_3\text{S}_{11}$ , which is caused by the high chemical reactivity of the  $70\text{Li}_2\text{S}\cdot 30\text{P}_2\text{S}_5$  system in ACN solvent. Commonly, the use of high-DN solvents is an effective strategy for the wet-chemical reaction.<sup>34-37</sup> In addition to the dielectric constant, the donor number may also play a role in reactivity. However, the high reactivity of the  $\text{Li}_2\text{S}-\text{P}_2\text{S}_5$  system in low-DN ACN solvent cannot be explained by the DN. In the case of  $\text{Li}_3\text{PS}_4$  synthesized via a solvent, the use of a solvent with

low polarity will lead to higher ionic conductivity since solvents with low polarity are more easily removed and yield a lower crystallinity ratio.<sup>15,38</sup> In contrast, the intrinsic high ionic conductivity of  $\text{Li}_7\text{P}_3\text{S}_{11}$  is caused by a high level of crystallinity.<sup>32</sup> Therefore, a high dielectric constant of the solvent is an essential factor in realizing high conductivity in  $\text{Li}_7\text{P}_3\text{S}_{11}$ . However, the samples using solvents with high dielectric constants other than ACN solvent exhibits ionic insulating properties. The FF, SN, and NM solvents cause a side reaction with the  $\text{Li}_2\text{S}-\text{P}_2\text{S}_5$  system, which is responsible for the solvent molecule residue present following heat treatment. Further, in the case of EC, the reactivity of the  $\text{Li}_2\text{S}-\text{P}_2\text{S}_5$  system is low despite it having the highest dielectric constant among the solvents examined. Given this finding, I believe that differences in the structures of solvent molecules lead to different reactivities with lithium thiophosphates. Additionally, high dielectric solvents typically have an extremely high boiling point, which also limits the choice of solvent for the wet-chemical synthesis of  $\text{Li}_7\text{P}_3\text{S}_{11}$  SEs. Taking into this consideration of the dielectric constant, molecular structure, and boiling point, ACN solvent is the most suitable solvent for the liquid-phase synthesis of  $\text{Li}_7\text{P}_3\text{S}_{11}$  among the investigated solvents.

### 2.2.5 Conclusions

In summary, I undertook a systematic study of the effect of solvent on the reactivity of an  $\text{Li}_2\text{S}-\text{P}_2\text{S}_5$  system during the liquid-phase synthesis of  $\text{Li}_7\text{P}_3\text{S}_{11}$  SEs. The  $\text{Li}_7\text{P}_3\text{S}_{11}$  crystal phase forms through the wet-chemical reaction in ACN, THP, and Dox solvents, vacuum drying, and then heat treatment. In contrast, a side reaction and insufficient reactivity for the synthesis of  $\text{Li}_7\text{P}_3\text{S}_{11}$  are confirmed for the CS, NM, FF, SN, and EC solvents. The microstructures of the samples prepared using ACN, THP, and Dox have notable textures, such as a broccoli crown. Thermophysical properties of the precursor obtained from TG-DTA suggest that the strength of the chemical interaction between the lithium thiophosphates and solvent molecules within the precursor structure increases in the order of Dox, THP, and then ACN. Thus, the use of ACN solvent leads to the high chemical reactivity of the  $70\text{Li}_2\text{S}\cdot 30\text{P}_2\text{S}_5$  system. The ionic conductivities of the samples prepared using Dox, THP, and ACN solvent increase in relation to increases in the solvent's dielectric constant. The sample using ACN solvent shows the highest ionic conductivity of  $0.8 \text{ mS cm}^{-1}$  at room temperature among the samples prepared in this work. The high ionic conductivity of  $\text{Li}_7\text{P}_3\text{S}_{11}$  SEs can result from the formation of high-purity crystalline  $\text{Li}_7\text{P}_3\text{S}_{11}$ . These experimental results indicate that the solvent's polarity, characterized by the dielectric constant, plays an important role in the formation of  $\text{Li}_7\text{P}_3\text{S}_{11}$  using the liquid-phase method. Furthermore, a high boiling point and a ring structure that cause steric hindrance are unfavorable solvent attributes for the wet-chemical synthesis of  $\text{Li}_7\text{P}_3\text{S}_{11}$  SE. Overall, this study has revealed that a solvent's dielectric constant is a significant factor in obtaining the optimal  $\text{Li}_7\text{P}_3\text{S}_{11}$  via wet-chemical reaction. Given the dielectric constant, molecular structure, and boiling point, the ACN

solvent is suitable for the liquid-phase synthesis of  $\text{Li}_7\text{P}_3\text{S}_{11}$ .

## References

- (1) Zhang, Z.; Shao, Y.; Lotsch, B.; Hu, Y. S.; Li, H.; Janek, J.; Nazar, L. F.; Nan, C. W.; Maier, J.; Armand, M.; Chen, L. New Horizons for Inorganic Solid State Ion Conductors. *Energy Environ. Sci.* **2018**, *11*, 1945–1976.
- (2) Takada, K. Progress and Prospective of Solid-State Lithium Batteries. *Acta Mater.* **2013**, *61*, 759–770.
- (3) Chen, S.; Xie, D.; Liu, G.; Mwizerwa, J. P.; Zhang, Q.; Zhao, Y.; Xu, X.; Yao, X. Sulfide Solid Electrolytes for All-Solid-State Lithium Batteries: Structure, Conductivity, Stability and Application. *Energy Storage Mater.* **2018**, *14*, 58–74.
- (4) Kamaya, N.; Homma, K.; Yamakawa, Y.; Hirayama, M.; Kanno, R.; Yonemura, M.; Kamiyama, T.; Kato, Y.; Hama, S.; Kawamoto, K.; Mitsui, A. A Lithium Superionic Conductor. *Nat. Mater.* **2011**, *10*, 682–686.
- (5) Seino, Y.; Ota, T.; Takada, K.; Hayashi, A.; Tatsumisago, M. A Sulphide Lithium Super Ion Conductor Is Superior to Liquid Ion Conductors for Use in Rechargeable Batteries. *Energy Environ. Sci.* **2014**, *7*, 627–631.
- (6) Adeli, P.; Bazak, J. D.; Huq, A.; Goward, G. R.; Nazar, L. F. Influence of Aliovalent Cation Substitution and Mechanical Compression on Li-Ion Conductivity and Diffusivity in Argyrodite Solid Electrolytes. *Chem. Mater.* **2021**, *33*, 146–157.
- (7) Miura, A.; Rosero-Navarro, N. C.; Sakuda, A.; Tadanaga, K.; Phuc, N. H. H.; Matsuda, A.; Machida, N.; Hayashi, A.; Tatsumisago, M. Liquid-Phase Syntheses of Sulfide Electrolytes for All-Solid-State Lithium Battery. *Nat. Rev. Chem.* **2019**, *3*, 189–198.
- (8) Lee, J.; Lee, T.; Char, K.; Kim, K. J.; Choi, J. W. Issues and Advances in Scaling up Sulfide-Based All-Solid-State Batteries. *Acc. Chem. Res.* **2021**, *54*, 3390–3402.
- (9) Tan, D. H. S.; Banerjee, A.; Deng, Z.; Wu, E. A.; Nguyen, H.; Doux, J. M.; Wang, X.; Cheng, J. H.; Ong, S. P.; Meng, Y. S.; Chen, Z. Enabling Thin and Flexible Solid-State Composite Electrolytes by the Scalable Solution Process. *ACS Appl. Energy Mater.* **2019**, *2*, 6542–6550.
- (10) Kim, D. H.; Oh, D. Y.; Park, K. H.; Choi, Y. E.; Nam, Y. J.; Lee, H. A.; Lee, S. M.; Jung, Y. S. Infiltration of Solution-Processable Solid Electrolytes into Conventional Li-Ion-Battery Electrodes for All-Solid-State Li-Ion Batteries. *Nano Lett.* **2017**, *17*, 3013–3020.
- (11) Ruhl, J.; Riegger, L. M.; Ghidui, M.; Zeier, W. G. Impact of Solvent Treatment of the Superionic Argyrodite  $\text{Li}_6\text{PS}_5\text{Cl}$  on Solid-State Battery Performance. *Adv. Energy Sustain. Res.* **2021**, *2*, 2000077–2000086.
- (12) Wang, X.; Ye, L.; Nan, C. W.; Li, X. Effect of Solvents on a  $\text{Li}_{10}\text{GeP}_2\text{S}_{12}$ -Based Composite Electrolyte via Solution Method for Solid-State Battery Applications. *ACS Appl. Mater. Interfaces* **2022**, *14*, 46627–46634.

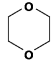
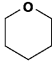
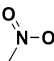
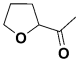
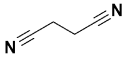
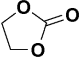
- (13) Liu, Z.; Fu, W.; Payzant, E. A.; Yu, X.; Wu, Z.; Dudney, N. J.; Kiggans, J.; Hong, K.; Rondinone, A. J.; Liang, C. Anomalous High Ionic Conductivity of Nanoporous  $\beta$ -Li<sub>3</sub>PS<sub>4</sub>. *J. Am. Chem. Soc.* **2013**, *135*, 975–978.
- (14) Phuc, N. H. H.; Morikawa, K.; Mitsuhiro, T.; Muto, H.; Matsuda, A. Synthesis of Plate-like Li<sub>3</sub>PS<sub>4</sub> Solid Electrolyte via Liquid-Phase Shaking for All-Solid-State Lithium Batteries. *Ionics* **2017**, *23*, 2061–2067.
- (15) Yamamoto, K.; Yang, S.; Takahashi, M.; Ohara, K.; Uchiyama, T.; Watanabe, T.; Sakuda, A.; Hayashi, A.; Tatsumisago, M.; Muto, H.; Matsuda, A.; Uchimoto, Y. High Ionic Conductivity of Liquid-Phase-Synthesized Li<sub>3</sub>PS<sub>4</sub> Solid Electrolyte, Comparable to That Obtained via Ball Milling. *ACS Appl. Energy Mater.* **2021**, *4*, 2275–2281.
- (16) Ito, S.; Nakakita, M.; Aihara, Y.; Uehara, T.; Machida, N. A Synthesis of Crystalline Li<sub>7</sub>P<sub>3</sub>S<sub>11</sub> Solid Electrolyte from 1,2-Dimethoxyethane Solvent. *J. Power Sources* **2014**, *271*, 342–345.
- (17) Xu, R. C.; Xia, X. H.; Yao, Z. J.; Wang, X. L.; Gu, C. D.; Tu, J. P. Preparation of Li<sub>7</sub>P<sub>3</sub>S<sub>11</sub> Glass-Ceramic Electrolyte by Dissolution-Evaporation Method for All-Solid-State Lithium Ion Batteries. *Electrochim. Acta* **2016**, *219*, 235–240.
- (18) Maniwa, R.; Calpa, M.; Rosero-Navarro, N. C.; Miura, A.; Tadanaga, K. Synthesis of Sulfide Solid Electrolytes from Li<sub>2</sub>S and P<sub>2</sub>S<sub>5</sub> in Anisole. *J. Mater. Chem. A* **2021**, *9*, 400–405.
- (19) Calpa, M.; Rosero-Navarro, N. C.; Miura, A.; Tadanaga, K. Instantaneous Preparation of High Lithium-Ion Conducting Sulfide Solid Electrolyte Li<sub>7</sub>P<sub>3</sub>S<sub>11</sub> by a Liquid Phase Process. *RSC Adv.* **2017**, *7*, 46499–46504.
- (20) Calpa, M.; Rosero-Navarro, N. C.; Miura, A.; Tadanaga, K. Electrochemical Performance of Bulk-Type All-Solid-State Batteries Using Small-Sized Li<sub>7</sub>P<sub>3</sub>S<sub>11</sub> Solid Electrolyte Prepared by Liquid Phase as the Ionic Conductor in the Composite Cathode. *Electrochim. Acta* **2019**, *296*, 473–480.
- (21) Fan, B.; Zhang, Q.; Luo, Z.; Zhang, X.; Ma, H.; Fan, P.; Xue, B. Influence of Precipitate/Supernatant Ratio during Liquid-Phase Synthesis of Solid Electrolyte Li<sub>7</sub>P<sub>3</sub>S<sub>11</sub>. *Solid State Ionics* **2019**, *343*, 115073–115079.
- (22) Cai, L.; Wan, H.; Zhang, Q.; Mwiszerwa, J. P.; Xu, X.; Yao, X. In Situ Coating of Li<sub>7</sub>P<sub>3</sub>S<sub>11</sub> Electrolyte on CuCo<sub>2</sub>S<sub>4</sub>/Graphene Nanocomposite as a High-Performance Cathode for All-Solid-State Lithium Batteries. *ACS Appl. Mater. Interfaces* **2020**, *12*, 33810–33816.
- (23) Shi, J.; Liu, G.; Weng, W.; Cai, L.; Zhang, Q.; Wu, J.; Xu, X.; Yao, X. Co<sub>3</sub>S<sub>4</sub>@ Li<sub>7</sub>P<sub>3</sub>S<sub>11</sub> Hexagonal Platelets as Cathodes with Superior Interfacial Contact for All-Solid-State Lithium Batteries. *ACS Appl. Mater. Interfaces* **2020**, *12*, 14079–14086.
- (24) Gutmann, V. Solvent effects on the reactivities of organometallic compounds *Coord. Chem.*



- Rev.* **1976**, *18*, 225–255.
- (25) Zou, Q.; Lu, Y. C. Solvent-Dictated Lithium Sulfur Redox Reactions: An Operando UV-Vis Spectroscopic Study. *J. Phys. Chem. Lett.* **2016**, *7*, 1518–1525.
- (26) Calpa, M.; Nakajima, H.; Mori, S.; Goto, Y.; Mizuguchi, Y.; Moriyoshi, C.; Kuroiwa, Y.; Rosero-Navarro, N. C.; Miura, A.; Tadanaga, K. Formation Mechanism of  $\beta$ -Li<sub>3</sub>PS<sub>4</sub> through Decomposition of Complexes. *Inorg. Chem.* **2021**, *60*, 6964–6970.
- (27) Wang, Y.; Lu, D.; Bowden, M.; el Khoury, P. Z.; Han, K. S.; Deng, Z. D.; Xiao, J.; Zhang, J. G.; Liu, J. Mechanism of Formation of Li<sub>7</sub>P<sub>3</sub>S<sub>11</sub> Solid Electrolytes through Liquid Phase Synthesis. *Chem. Mater.* **2018**, *30*, 990–997.
- (28) Calpa, M.; Rosero-Navarro, N. C.; Miura, A.; Terai, K.; Utsuno, F.; Tadanaga, K. Formation Mechanism of Thiophosphate Anions in the Liquid-Phase Synthesis of Sulfide Solid Electrolytes Using Polar Aprotic Solvents. *Chem. Mater.* **2020**, *32*, 9627–9632.
- (29) Wu, Z.; Bak, S.-M.; Shadik, Z.; Yu, S.; Hu, E.; Xing, X.; Du, Y.; Yang, X.-Q.; Liu, H.; Liu, P. Understanding the Roles of the Electrode/Electrolyte Interface for Enabling Stable Li // Sulfurized Polyacrylonitrile Batteries. *ACS Appl. Mater. Interfaces* **2021**, *13*, 31733–31740.
- (30) Busche, M. R.; Weber, D. A.; Schneider, Y.; Dietrich, C.; Wenzel, S.; Leichtweiss, T.; Schröder, D.; Zhang, W.; Weigand, H.; Walter, D.; Sedlmaier, S. J.; Houtarde, D.; Nazar, L. F.; Janek, J. In Situ Monitoring of Fast Li-Ion Conductor Li<sub>7</sub>P<sub>3</sub>S<sub>11</sub> Crystallization Inside a Hot-Press Setup. *Chem. Mater.* **2016**, *28*, 6152–6165.
- (31) Dietrich, C.; Weber, D. A.; Sedlmaier, S. J.; Indris, S.; Culver, S. P.; Walter, D.; Janek, J.; Zeier, W. G. Lithium Ion Conductivity in Li<sub>2</sub>S-P<sub>2</sub>S<sub>5</sub> Glasses-Building Units and Local Structure Evolution during the Crystallization of Superionic Conductors Li<sub>3</sub>PS<sub>4</sub>, Li<sub>7</sub>P<sub>3</sub>S<sub>11</sub> and Li<sub>4</sub>P<sub>2</sub>S<sub>7</sub>. *J. Mater. Chem. A* **2017**, *5*, 18111–18119.
- (32) Preefer, M. B.; Grebenkemper, J. H.; Schroeder, F.; Bocarsly, J. D.; Pilar, K.; Cooley, J. A.; Zhang, W.; Hu, J.; Misra, S.; Seeler, F.; Schierle-Arndt, K.; Seshadri, R. Rapid and Tunable Assisted-Microwave Preparation of Glass and Glass-Ceramic Thiophosphate “Li<sub>7</sub>P<sub>3</sub>S<sub>11</sub>” Li-Ion Conductors. *ACS Appl. Mater. Interfaces* **2019**, *11*, 42280–42287.
- (33) Minami, K.; Hayashi, A.; Tatsumisago, M. Crystallization Process for Superionic Li<sub>7</sub>P<sub>3</sub>S<sub>11</sub> Glass-Ceramic Electrolytes. *J. Am. Ceram. Soc.* **2011**, *94* (6), 1779–1783.
- (34) Bieker, G.; Wellmann, J.; Kolek, M.; Jalkanen, K.; Winter, M.; Bieker, P. Influence of Cations in Lithium and Magnesium Polysulphide Solutions: Dependence of the Solvent Chemistry. *Phys. Chem. Chem. Phys.* **2017**, *19*, 11152–11162.
- (35) Zhou, L.; Park, K. H.; Sun, X.; Lalère, F.; Adermann, T.; Hartmann, P.; Nazar, L. F. Solvent-Engineered Design of Argyrodite Li<sub>6</sub>PS<sub>5</sub>X (X = Cl, Br, I) Solid Electrolytes with High Ionic Conductivity. *ACS Energy Lett.* **2019**, *4*, 265–270.

- (36) Yubuchi, S.; Uematsu, M.; Deguchi, M.; Hayashi, A.; Tatsumisago, M. Lithium-Ion-Conducting Argyrodite-Type  $\text{Li}_6\text{PS}_5\text{X}$  ( $\text{X} = \text{Cl}, \text{Br}, \text{I}$ ) Solid Electrolytes Prepared by a Liquid-Phase Technique Using Ethanol as a Solvent. *ACS Appl. Energy Mater.* **2018**, *1*, 3622–3629.
- (37) Teragawa, S.; Aso, K.; Tadanaga, K.; Hayashi, A.; Tatsumisago, M. Liquid-Phase Synthesis of a  $\text{Li}_3\text{PS}_4$  Solid Electrolyte Using N-Methylformamide for All-Solid-State Lithium Batteries. *J. Mater. Chem. A* **2014**, *2*, 5095–5099.
- (38) Takahashi, M.; Yang, S.; Yamamoto, K.; Ohara, K.; Phuc, N. H. H.; Watanabe, T.; Uchiyama, T.; Sakuda, A.; Hayashi, A.; Tatsumisago, M.; Muto, H.; Matsuda, A.; Uchimoto, Y. Improvement of Lithium Ionic Conductivity of  $\text{Li}_3\text{PS}_4$  through Suppression of Crystallization Using Low-Boiling-Point Solvent in Liquid-Phase Synthesis. *Solid State Ionics* **2021**, *361*, 115568–115572.
- (39) Warren, J.; And, W.; Ogg, E. F. *THE DIELECTRIC CONSTANTS OF BINARY MIXTURES. V THE ELECTRIC MOMENTS OF CERTAIN ORGANIC MOLECULES IN CARBON DISULFIDE AND HEXANE SOLUTION.* *J. Am. Chem. Soc.* **1927**, *50*, 94–101.
- (40) Lohr' And, G.; Bywater, S. Anionic Polymerization of Styrene in Oxepane (Hexamethylene Oxide). Counter-Ion, Sodium. *Can. J. Chem.* **1970**, *48*, 2031–2034.
- (41) S. B. Nagy. DIELECTROMETRIC ANALYSIS OF MULTICOMPONENT SYSTEMS. *Acta chim. Acad. Sci. Hung.* **1961**, *27*, 51–64.
- (42) Alarco, P. J.; Abu-Lebdeh, Y.; Abouimrane, A.; Armand, M. The Plastic-Crystalline Phase of Succinonitrile as a Universal Matrix for Solid-State Ionic Conductors. *Nat. Mater.* **2004**, *3*, 476–481.

**Table 2.2.1.** Physical and chemical properties of ACN, THP, Dox, CS, NM, FF, AN, and EC solvents.

Solvent	Structure	Boiling point (°C)	Dielectric constant
Dox		101	2.2 <sup>24</sup>
CS	<b>S=C=S</b>	46	2.63 <sup>39</sup>
THP		88	5.5 <sup>40</sup>
NM		101	35.9 <sup>24</sup>
ACN	<b>—C≡N</b>	82	38 <sup>24</sup>
FF		162	42 <sup>41</sup>
SN		267	55 <sup>42</sup>
EC		248	89.1 <sup>24</sup>

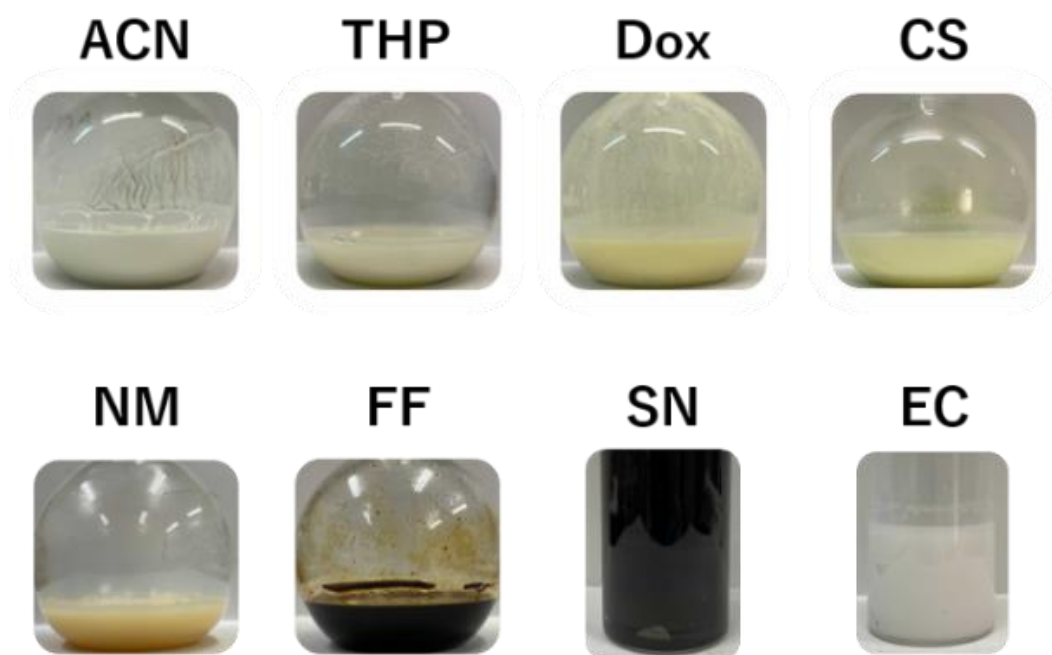


**Figure 2.2.1.** Photographs of 70Li<sub>2</sub>S-30P<sub>2</sub>S<sub>5</sub> mixtures after stirring for 3 days in ACN, THP, Dox, CS, NM, FF, AN, and EC solvents.

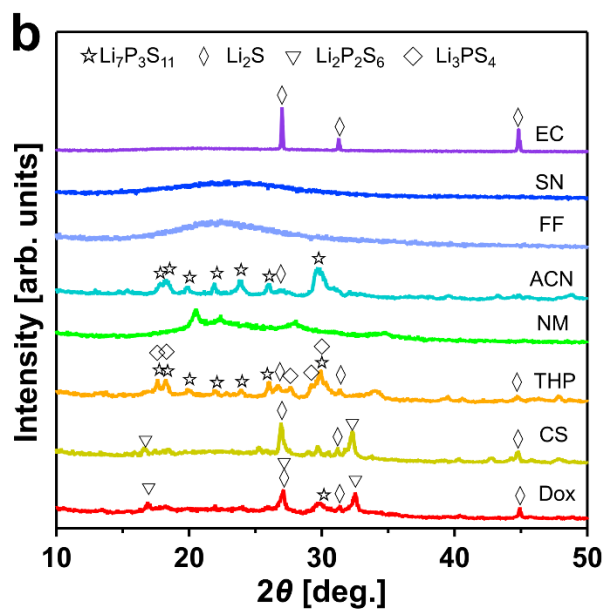
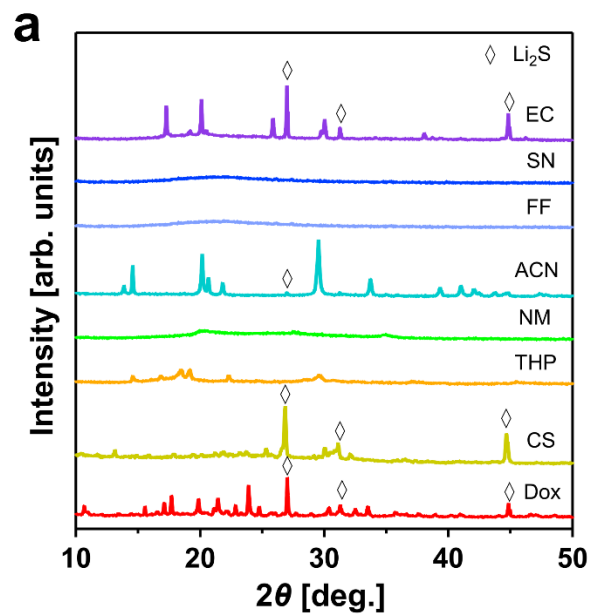


**Figure 2.2.2.** XRD patterns of (a) precursors after drying under vacuum and (b) 70 $\text{Li}_2\text{S}$ –30 $\text{P}_2\text{S}_5$  SEs synthesized using each solvent.

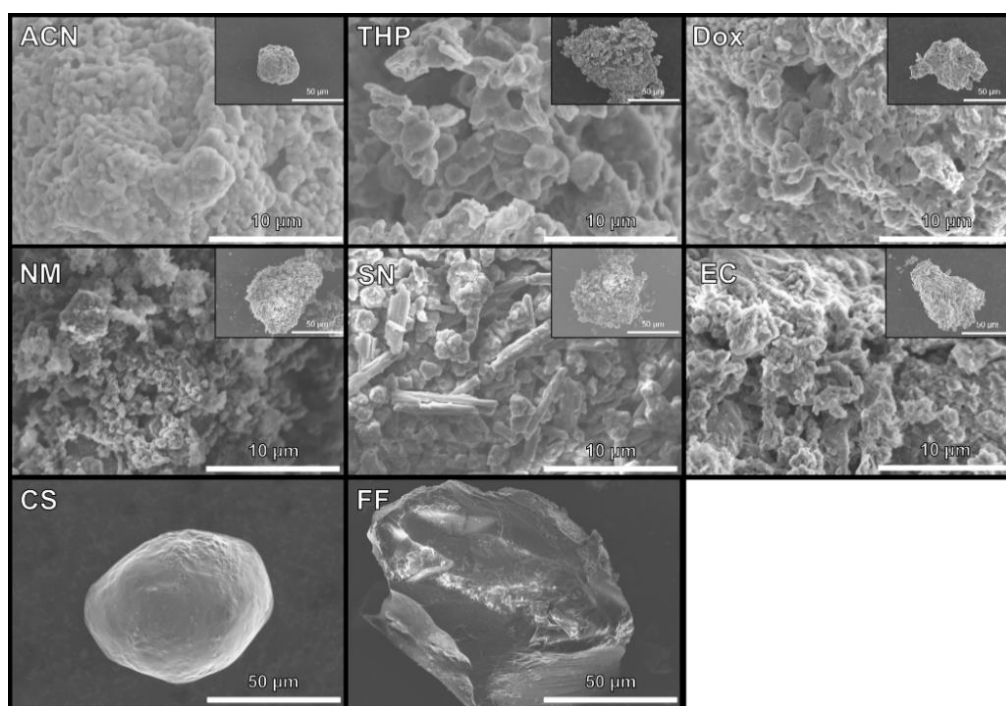


**Figure 2.2.3.** SEM images of  $70\text{Li}_2\text{S}-30\text{P}_2\text{S}_5$  synthesized via ACN, THP, Dox, NM, SN, EC, CS, and FF solvents.

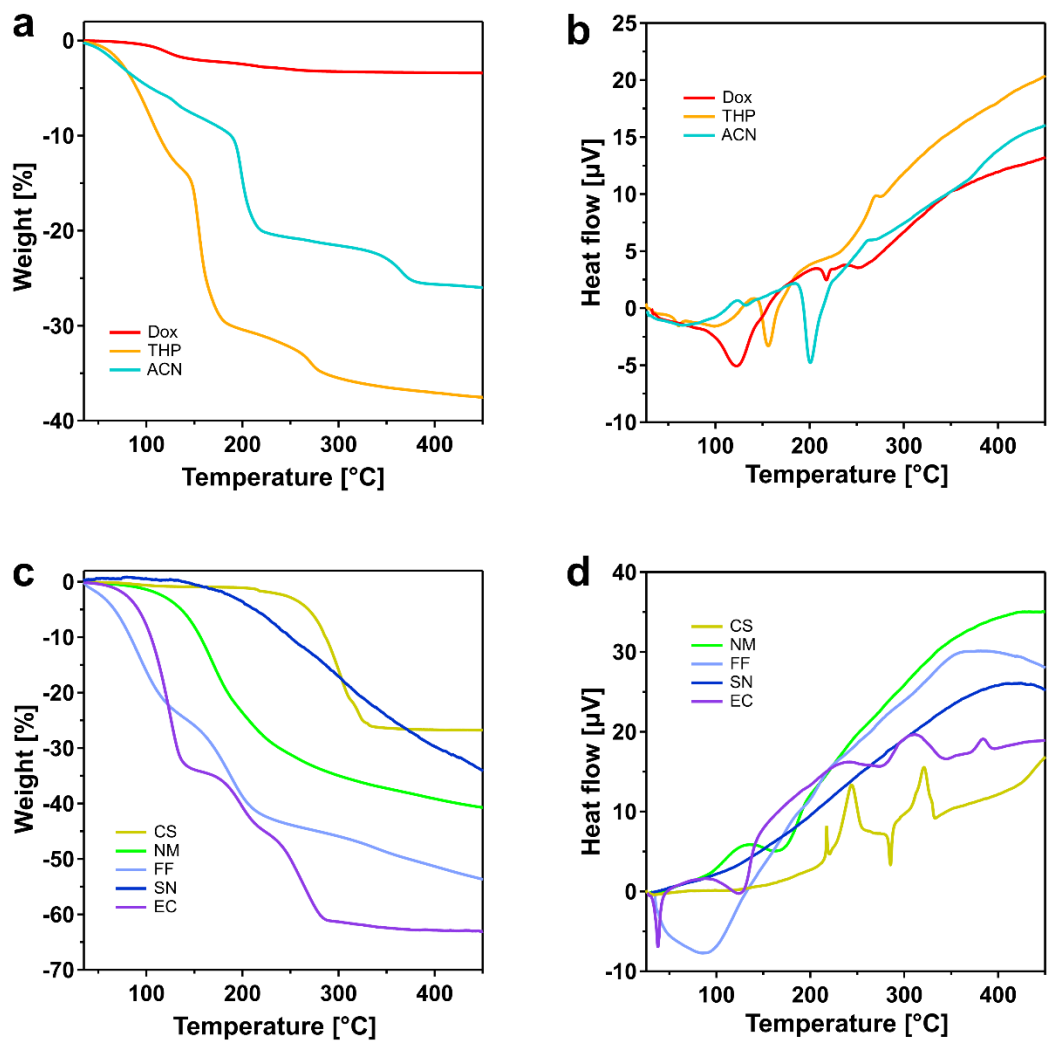


**Figure 2.2.4.** (a) TGA and (b) DTA curves of  $70\text{Li}_2\text{S}-30\text{P}_2\text{S}_5$  precursors synthesized using Dox, THP, and ACN as solvents. (c) TGA and (d) DTA curves of  $70\text{Li}_2\text{S}-30\text{P}_2\text{S}_5$  precursors synthesized using CS, NM, FF, SN, and EC as solvents.

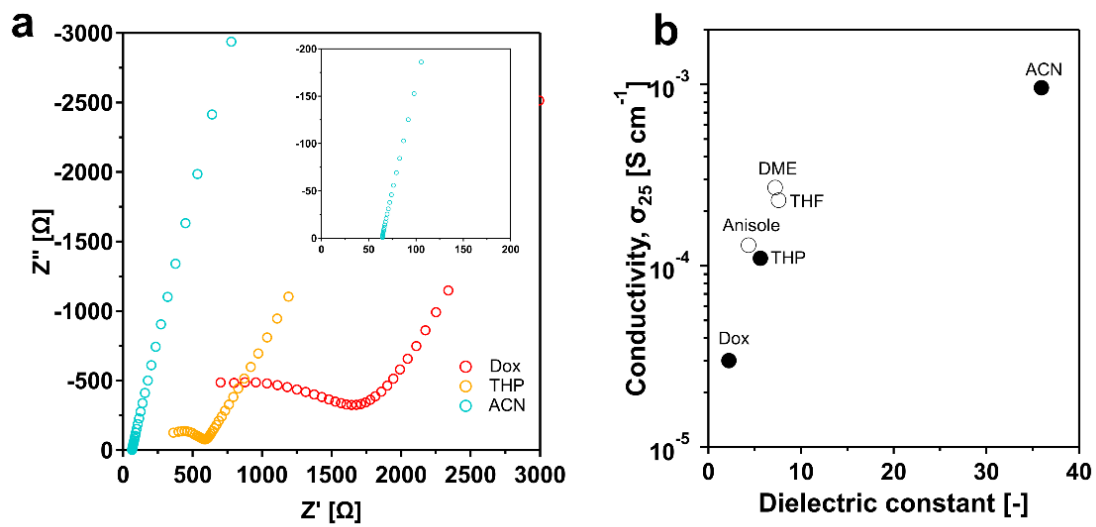


**Figure 2.2.5.** (a) Nyquist plot and (b) ionic conductivity at room temperature for 70Li<sub>2</sub>S–30P<sub>2</sub>S<sub>5</sub> system formed via Dox, THP, and ACN solvents as a function of dielectric constant together with those of 70Li<sub>2</sub>S–30P<sub>2</sub>S<sub>5</sub> system formed via other solvents.<sup>17-19</sup> The white circles indicate reference values.



## 2.3 Solution synthesis method via dynamic sulfur radical anions

In this chapter, I describe the developed solution processing via dynamic sulfide radical anions. A mixture of  $\text{Li}_2\text{S}$ ,  $\text{P}_2\text{S}_5$ , and excess elemental sulfur in a mixed solvent of ACN, THF, and a trace EtOH immediately converts the homogenous precursor solution in which  $\text{S}_3^-$  radical anions exist. The presence of EtOH enhances the chemical stability of  $\text{S}_3^-$ . The resulting sulfide radical anions serve as a mediator with two strategies: the soluble polysulfide formation and activation of  $\text{P}_2\text{S}_5$ , and thus allows the generation of the precursor solution in 2 min. The  $\text{Li}_7\text{P}_3\text{S}_{11}$  SEs are prepared in a total treatment time of 2 h without the need for ball milling or high-energy treatment, showing higher ionic conductivity and excellent cell performance of ASLBs than  $\text{Li}_7\text{P}_3\text{S}_{11}$  prepared by ball milling. This method provides paves the way for accelerated adoption of practical ASLBs manufacturing.

### 2.3.1 Introduction

In Chapter 2.2, I have established the leading theory on the solvent effect on the wet-chemical reaction of  $\text{Li}_7\text{P}_3\text{S}_{11}$  SEs. Acetonitrile as a reaction mediator is suitable for the formation of crystalline  $\text{Li}_7\text{P}_3\text{S}_{11}$  SEs because of its high polarity, as characterized by the dielectric constant. Using ACN solvent, the wet-chemical reaction for the formation of  $\text{Li}_7\text{P}_3\text{S}_{11}$  undergoes a precursor suspension containing the  $\text{Li}_3\text{PS}_4 \cdot \text{ACN}$  (75 $\text{Li}_2\text{S}$ ·25 $\text{P}_2\text{S}_5$  molar ratio) precipitate and the  $\text{Li}_2\text{S} \cdot \text{P}_2\text{S}_5$  (50 $\text{Li}_2\text{S}$ ·50 $\text{P}_2\text{S}_5$  molar ratio) solution.<sup>1,2</sup> The conventional liquid-phase synthesis of the  $\text{Li}_2\text{S}$ - $\text{P}_2\text{S}_5$  system involves the reaction rate-limiting step during the formation of the insoluble  $\text{Li}_3\text{PS}_4$  intermediate in certain organic solvents.<sup>3</sup> A further concern is the difficulty in dissociating  $\text{P}_4\text{S}_{10}$  to the reactive  $\text{P}_2\text{S}_5$  in the initial reaction to the lithium thiophosphate.<sup>4</sup>  $\text{P}_2\text{S}_5$  intrinsically exists as an insoluble dimer  $\text{P}_4\text{S}_{10}$ , although it is commonly reported as  $\text{P}_2\text{S}_5$ . These reaction rate-limiting steps result in a longer reaction time (at least 24 h) for liquid-phase synthesis in the absence of additional energy than the mechanochemical reaction.<sup>5,6</sup> The suspension process of  $\text{Li}_7\text{P}_3\text{S}_{11}$  SEs causes heterogeneity derived from the complicated phase formations, which increases the engineering costs for the large-scale manufacturing of ASLBs. There have been efforts toward solution processing in which SEs synthesized from the solid-state method were dissolved in an organic solvent, but an irreversible reaction occurs in the solvent with high solubility, leading to a decrease in ionic conductivity.<sup>7,8</sup> To overcome the abovementioned issues, Lim et al. proposed solution processing via soluble polysulfide as a manufacturing technology for sulfide-based ASLBs,<sup>9</sup> which was recently applied in the synthesis of  $\text{Li}_6\text{PS}_5\text{Cl}$  SEs.<sup>10</sup> The polysulfides, notably  $\text{S}_3^-$  radical anions, serve as a mediator for the formation of lithium thiophosphates and as an additive for enhanced solubility of the precursor. However, the reported solution processing via

polysulfide still involves a long reaction time of 24 h or more owing to the slow reaction rate of polysulfide formation. The chemical stability of lithium thiophosphates and polysulfides in organic solvents is determined by the nature of the solvent. A reasonable solvent for the effective reaction process, hence, is necessary to develop a solution processing method via soluble polysulfide for sulfide-based ASLB manufacturing technology.

Herein, I report an unprecedented solution processing technology via dynamic sulfide radical anions for the rapid and scalable manufacturing of ASLBs (Figure 2.3.1). The proposed solution processing dramatically reduces the reaction time to produce the precursor solution (or suspension) from 24 to 72 h in the conventional liquid-phase synthesis to ~2 min. I have introduced the  $S_3^-$  radical anion as a mediator with two strategies (the soluble polysulfide formations and activation of  $P_2S_5$ ) to proceed with the reaction quickly. In the presence of excess elemental sulfur, a  $Li_2S$  and  $P_2S_5$  (7:3 molar ratio) solution containing ACN, THF, and trace amounts of ethanol (EtOH) changes from inhomogeneous to a homogenous black solution without additional energy. Trace amounts of EtOH are employed to enhance the chemical stability of multiple stable lithium polysulfides in which the  $S_3^-$  radical anion is the dominant chemical species.  $Li_7P_3S_{11}$  SEs are prepared for a total of 2 h and show a high ionic conductivity of  $1.2 \text{ mS cm}^{-1}$  at room temperature, which is higher in comparison with  $Li_7P_3S_{11}$  SEs prepared by ball milling. The doped excess sulfur evaporates through the melt diffusion process of excess sulfur during the heat-treatment process for the crystallization of  $Li_7P_3S_{11}$ . The melt diffusion in the synthetic procedure is proposed here for fabricating the cathode composites for ASLBs.  $TiS_2$ -SE composites using the  $Li_7P_3S_{11}$  with excess sulfur allow uniformity and tight connection in electrodes and show better cell performance than that of  $TiS_2$ -SE composites using  $Li_7P_3S_{11}$  prepared by ball milling.

### 2.3.2 Experimental methods

**Materials Synthesis.** Lithium sulfide (Mitsuwa Chemical, 99.9%),  $P_2S_5$  (Sigma-Aldrich, 99%), and elemental sulfur (Sigma-Aldrich, 99.98%) were mixed in a molar ratio of 7:3: $x$ . After adding the initial mixture powder (1 g) to a mixed solvent (20 mL) including ACN (Fujifilm Wako, 99.5%), THF (Sigma-Aldrich, 99.9%), and EtOH (Konishi, 99.5%) in a volume ratio of 1:1:0.05, respectively, the resulting solvent mixture was stirred and dissolved for several minutes. The obtained solution was dried at 130 °C under vacuum for 1 h, followed by heat treatment for 1 h on a hot plate to obtain  $xPS-Li_7P_3S_{11}$  SEs ( $x$  is the sulfur content in the  $7Li_2S \cdot 3P_2S_5 \cdot xS$  molar ratio). For comparison,  $Li_7P_3S_{11}$  SEs were synthesized by conventional liquid-phase synthesis and ball milling. First,  $Li_2S$  and  $P_2S_5$  were mixed in a molar ratio of 7:3. After adding ACN (20 mL) to the mixture powder (1 g), the obtained mixture was stirred for 72 h at 50 °C on a hot plate. The resulting suspension was dried at 80 °C under vacuum for 12 h, followed by heat treatment at

270 °C for 1 h on the hot plate to obtain CL-Li<sub>7</sub>P<sub>3</sub>S<sub>11</sub> SEs. The initial mixture powder (2 g) of Li<sub>2</sub>S and P<sub>2</sub>S<sub>5</sub> was put into a zirconia pot (45 mL) with zirconia balls (4 mm in diameter, 60 g). The ball-milling treatment was performed at a rotation speed of 400 rpm for 10 h using a planetary ball mill apparatus (P-7, Fritsch). The resultant precursor powders were heated at 270 °C for 1 h on the hot plate to obtain BM-Li<sub>7</sub>P<sub>3</sub>S<sub>11</sub> SEs. All procedures were conducted under an Ar atmosphere in the glove box.

**Material characterization.** The mean structure of the sample was examined by powder XRD measurements using a Rigaku SmartLab. The X-ray beam was generated by CuK $\alpha$  radiation. Diffraction data were collected under  $2\theta = 10^\circ\text{--}50^\circ$  with a step interval of  $0.02^\circ$  and a scan rate of  $5^\circ \text{ min}^{-1}$ . TGA using EVO II (Rigaku) was conducted under a flow of Ar (industrial gas, 99.997%) with a temperature ramp of  $5 \text{ K min}^{-1}$ . SEM characterization was carried out on a Hitachi-S4800 with an EDS (ULTIM MAX, Oxford Instrument). The local structures of the samples and precursor solutions were investigated by UV–Vis spectrophotometry (Jasco V-670), Laser Raman spectrometry (Jasco, NRS-3100), and solid-state NMR spectrometry (Bruker, AVANCE III 400). The solid-state MAS <sup>31</sup>P NMR measurement was conducted at a rotation speed of 6 kHz.

**Electrochemical measurements.** The overall ionic conductivities of the prepared samples were measured by alternating-current impedance spectroscopy (Hokuto Denko, Hz-pro) in a frequency range of 1 MHz to 10 Hz under an Ar atmosphere. To fabricate the cells for Electrochemical Impedance Spectroscopy measurements, each sample (~80 mg) was filled into a holder made of PEEK with two stainless-steel rods, followed by a uniaxial pressure of 256 MPa to form pellets with diameters of ~10.0 mm at room temperature. To determine the electrical conductivity of the prepared samples, DC polarization measurements were performed on the pellets with applied voltages of 0.1 V, 0.2 V, 0.3 V, and 0.4 V for 30 min each. To fabricate the symmetric Li cell, ~80 mg of Li<sub>7</sub>P<sub>3</sub>S<sub>11</sub> powder was cold pressed under a pressure of 256 MPa in a 10 mm diameter PEEK die. Li metal was loaded into both sides of the Li<sub>7</sub>P<sub>3</sub>S<sub>11</sub> pellets. The DC polarization measurements of the symmetric cells were evaluated by cycling at a current density of  $0.1 \text{ mA cm}^{-2}$  during each 1 h cycle at room temperature using a charge-discharge device (Nagano, BST-2004H).

**Assembly of ASLBs.** Titanium sulfide (Sigma-Aldrich, 99.9%) and the precursor powders for 5PS-Li<sub>7</sub>P<sub>3</sub>S<sub>11</sub> before heat treatment were mixed in an appropriate weight ratio using a mortar, followed by heat treatment at 350 °C for 1 h on a hot plate to obtain the final 50TiS<sub>2</sub>-50(5PS-Li<sub>7</sub>P<sub>3</sub>S<sub>11</sub>) composite (wt%). The additive amount of the precursor powder was determined by a weight loss of up to 350 °C based on the thermogravimetric analysis. For comparison, the 50TiS<sub>2</sub>-50(BM-Li<sub>7</sub>P<sub>3</sub>S<sub>11</sub>) cathode composite was prepared by hand-mixing TiS<sub>2</sub> powder and BM-Li<sub>7</sub>P<sub>3</sub>S<sub>11</sub> in a weight ratio of 50:50. For the galvanostatic cycling tests, the Li-In | 5PS-Li<sub>7</sub>P<sub>3</sub>S<sub>11</sub>-350 |

50TiS<sub>2</sub>-50(5PS-Li<sub>7</sub>P<sub>3</sub>S<sub>11</sub>) and 50TiS<sub>2</sub>-50(BM-Li<sub>7</sub>P<sub>3</sub>S<sub>11</sub>) cells were assembled as follows. First, 80 mg of 5PS-Li<sub>7</sub>P<sub>3</sub>S<sub>11</sub>-350 powder was used to fill a PEEK die with a diameter of 10 mm and pressed under 90 MPa at room temperature. Then, the cathode composites were uniformly spread over one side of the SE layer and pressed under 256 MPa at room temperature. Indium foil (8 mm diameter) and lithium foil (3 mm diameter) were placed on the other side of the SE layer and pressed under 90 MPa at room temperature. The battery cells rested for 1 h before galvanostatic cycling testing. The mass loading of the cathode composites was 14 mg cm<sup>-2</sup>. The theoretical capacity of TiS<sub>2</sub> is 239 mAh g<sup>-1</sup>. The fabricated ASLBs were tested under a current density of 0.167 mA cm<sup>-2</sup> (0.1 C) in a voltage range of 1.0–2.4 V (vs. Li-In) at 30 °C. The galvanostatic cycling tests at a high C-rate (1C) were performed after 1 cycle of pre-operation at 0.1C

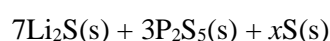
### 2.3.3 Solution processing technology via polysulfides

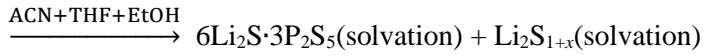
Organic solvents play a significant role in the solubility and chemical stability of lithium thiophosphates in solution processing.<sup>4,11–14</sup> To investigate the effects of solvent on the chemical stability and solubility of lithium thiophosphates, a mixture of Li<sub>2</sub>S and P<sub>2</sub>S<sub>5</sub> at a molar ratio of 7:3 was added to the mixed solvent containing ACN and THF. The mixture was then subjected to sonication treatment for 1 h (Figure 2.3.2a). Most of the 7Li<sub>2</sub>S·3P<sub>2</sub>S<sub>5</sub> dissolve in the mixed solvent (ACN/THF) to form a clear solution with a slight precipitate after sonication treatment. The mixed solvent containing ACN and THF in a 1:1 volume ratio exhibits high solubility against Li<sub>2</sub>S–P<sub>2</sub>S<sub>5</sub> systems. A previous study reported that 50Li<sub>2</sub>S·50P<sub>2</sub>S<sub>5</sub> (mol %) dissolves in ACN<sup>3</sup> and 60Li<sub>2</sub>S·40P<sub>2</sub>S<sub>5</sub> (mol %) dissolves in THF.<sup>15</sup> The high solubility in the ACN/THF solvent mixture should be caused by the solvent effect of ACN and THF with their own high solubility. In the obtained clear solution, peaks corresponding to PS<sub>3</sub><sup>4-</sup>, P<sub>2</sub>S<sub>7</sub><sup>4-</sup>, P<sub>2</sub>S<sub>6</sub><sup>4-</sup>, and P<sub>2</sub>S<sub>6</sub><sup>2-</sup> anion units are observed in the Raman spectra (Figure 2.3.2b).

Figure 2.3.3a shows the solubility of Li<sub>2</sub>S and P<sub>2</sub>S<sub>5</sub> (7:3 molar ratio) with and without excess sulfur in the organic solvent. The precursor suspension of Li<sub>2</sub>S and P<sub>2</sub>S<sub>5</sub> (7:3 molar ratio) in ACN forms a yellowish solution with white precipitate after stirring for 3 days at 50 °C, which is consistent with previous reports.<sup>1,2</sup> Conversely, 7Li<sub>2</sub>S·3P<sub>2</sub>S<sub>5</sub> with excess elemental sulfur rapidly dissolves in the mixed solvent of ACN, THF, and EtOH without additional energy. The obtained black solution (7Li<sub>2</sub>S·3P<sub>2</sub>S<sub>5</sub>·5S solution) forms multiple stable polysulfides and thiophosphate anions containing PS<sub>4</sub><sup>3-</sup>, P<sub>2</sub>S<sub>6</sub><sup>4-</sup>, and P<sub>2</sub>S<sub>7</sub><sup>4-</sup> units (Figure 2.3.3b). Lithium polysulfide solutions are known to form complex equilibria in disproportionation and dissociation reactions.<sup>16,17</sup> A variety of polysulfides, such as dianion S<sub>n</sub><sup>2-</sup> and radical anions S<sub>m</sub><sup>·-</sup>, with different chain lengths, depends on the polysulfide concentration and solvent.<sup>16–20</sup> In the UV–Vis absorption spectra of 7Li<sub>2</sub>S·3P<sub>2</sub>S<sub>5</sub>·5S in the mixed solvent (Figure 2.3.3c), three main peaks are detected at 265 nm, 410 nm, and 610 nm, which are assigned to S<sub>8</sub>, S<sub>4</sub><sup>2-</sup>, and S<sub>3</sub><sup>·-</sup>, respectively, according to the literature.<sup>21</sup>

A weak shoulder corresponding to  $S_6^{2-}$  at approximately  $\sim 350$  nm appears in the 1.0 mM solution. These findings are consistent with the fact that lithium polysulfide stabilizes to  $S_8$  and  $S_4^{2-}$  in THF and  $S_8$ ,  $S_8^{2-}$ ,  $S_6^{2-}$ , and  $S_3^{\cdot-}$  in ACN.<sup>17</sup> The absorbance of the peak corresponding to the  $S_3^{\cdot-}$  radical is independent of the concentration, which suggests that the  $S_3^{\cdot-}$  radical anion is the dominant species among multiple stable polysulfides. In general, the polysulfides including  $S_8^{2-}$ ,  $S_6^{2-}$ ,  $S_4^{2-}$ , and  $S_3^{\cdot-}$  generate slowly in highly polar solvents because their formations are associated with a complex system of equilibria, in which the  $S_3^{\cdot-}$  radical anions are the dominant chemical species.<sup>16,17</sup> Interestingly,  $S_3^{\cdot-}$  formation occurs faster in the mixed solvent containing a trace amount of EtOH compared to the solvent without EtOH (Figure 2.3.4). UV–Vis measurements of the  $Li_2S_6$  polysulfide solution with and without EtOH after stirring 2 days and 5 days were carried out to investigate the effects of EtOH on the chemical stability of polysulfide. All solutions show the spectra corresponding to  $S_8$ ,  $S_8^{2-}$ ,  $S_6^{2-}$ ,  $S_4^{2-}$ , and  $S_3^{\cdot-}$  polysulfides. The UV–Vis spectrum of the polysulfide solution without EtOH after stirring 2 days shows lower absorbance than the other solutions. This indicates that the  $S_3^{\cdot-}$  radical anion, the dominant chemical species in the dissociation equilibria, has low chemical stability without the EtOH molecule. The presence of EtOH in the  $Li_2S_6$  polysulfide solution favors the generation of multiple stable polysulfides over a shorter timescale compared with the absence of EtOH. Lithium polysulfide dynamics rely on the lithium solvation environment in solution, which is of great interest in the electrochemistry of lithium-sulfur batteries.<sup>22</sup> The lithium polysulfide in the electrolyte involves weak  $Li^+ - S_x^{2-}$  bonding because of the multiple electrostatic attraction forces from both the polysulfide and salt anion.<sup>22,23</sup> The competition between the polysulfide dianions and salt anions for the Li cation results in stronger  $Li^+$ –solvent interactions and thus enhances solubility. In the case of lithium polysulfides in highly polar solvents, the solvent bonds strongly to Li-ions, weakening the interaction between Li-ions and polysulfides. This lithium solvation environment brings a dissociation equilibrium, in which  $S_3^{\cdot-}$  radical anions are thermodynamically stable.<sup>9,17</sup> For these reasons, the strong interaction between EtOH and  $Li^+$  enhances the chemical stability of the  $S_3^{\cdot-}$  radical anion. The  $S_3^{\cdot-}$  with an unpaired electron serves as a mediator for the reaction to proceed quickly.

Figure 2.3.5 outlines the proposed reaction pathways of lithium thiophosphates with excess elemental sulfur in the precursor solution. First, lithium ions are strongly coordinated with highly polar EtOH and ACN solvents (Step 1). Next,  $S_3^{\cdot-}$  radical anions are shielded from Li-ions and stabilized (Step 2). Then,  $S_3^{\cdot-}$  radical anions with high reactivity attack the phosphorus moiety on  $P_4S_{10}$  and break the  $P_4S_{10}$  adamantane-like cage structure (Step 3). The chemical formula during this reaction is as follows:





Calpa et al. proposed that the reactive  $\text{P}_2\text{S}_5$  dissociated from  $\text{P}_4\text{S}_{10}$  in ACN solvent rapidly reacts with  $\text{Li}_2\text{S}$  to form highly soluble polymer-like  $\text{PS}_3^-$  chains, which convert into a variety of thiophosphate anions, such as  $\text{P}_2\text{S}_6^{2-}$ ,  $\text{PS}_4^{3-}$ , and  $\text{P}_2\text{S}_7^{4-}$ , via further reactions. The reaction pathway involves two rate-limiting steps: the dissociation of  $\text{P}_4\text{S}_{10}$  into reactive  $\text{P}_2\text{S}_5$  and the formation of  $\text{PS}_4^{3-}$  anion. The insoluble  $\text{PS}_4^{3-}$  anions are slowly formed through a kinetically unfavorable reaction in which  $\text{PS}^{3-}$  chains react with  $\text{Li}_2\text{S}$  to form on the surface of insoluble  $\text{Li}_2\text{S}$  particles. Soluble precursors in the solvent are preferred for the reaction to proceed quickly. However, we should note that lithium thiophosphates decompose faster in high polarity solvents such as *N*-methyl formamide and EtOH because of the low chemical stability in them.<sup>24,25</sup> In this demonstration, adding excess elemental sulfur and a reasonable solvent allow the dissolution of the precursor, which benefits the reaction kinetics for the lithium thiophosphates.<sup>9</sup> Moreover,  $\text{P}_4\text{S}_{10}$  uptakes one electron from the unpaired electron of the  $\text{S}_3^-$  radical anion and dissociates into  $\text{P}_2\text{S}_5$  to initiate reaction. It is noteworthy that the  $\text{Li}_7\text{P}_3\text{S}_{11}$  reaction route proposed here involves no rate-limiting step during the formation of the precursor solution. Solution processing in this study provides an unprecedented reaction route for sulfide-based SEs, which represents great progress toward practical large-scale manufacturing of sulfide-based ASLBs.

### 2.3.4 Structural and electrochemical properties

Figure 2.3.6a shows the XRD patterns of crystalline  $\text{Li}_7\text{P}_3\text{S}_{11}$  SEs prepared by the solution processing method via polysulfides ( $x\text{PS-Li}_7\text{P}_3\text{S}_{11}$ , where  $x$  is the sulfur content in the  $7\text{Li}_2\text{S}\cdot 3\text{P}_2\text{S}_5\cdot x\text{S}$  molar ratio), the conventional liquid-phase method based on ACN (CL- $\text{Li}_7\text{P}_3\text{S}_{11}$ ), and ball milling (BM- $\text{Li}_7\text{P}_3\text{S}_{11}$ ) along with the reference pattern calculated from the  $\text{Li}_7\text{P}_3\text{S}_{11}$ <sup>26</sup> crystal structure data using VESTA software.<sup>27</sup> CL- $\text{Li}_7\text{P}_3\text{S}_{11}$  involves  $\text{Li}_2\text{S}$  and  $\text{Li}_3\text{PS}_4$ , an intermediate for  $\text{Li}_7\text{P}_3\text{S}_{11}$ , whereas both  $x\text{PS-Li}_7\text{P}_3\text{S}_{11}$  ( $x \geq 5$ ) and BM- $\text{Li}_7\text{P}_3\text{S}_{11}$  form crystalline  $\text{Li}_7\text{P}_3\text{S}_{11}$  without impurities. There are no detrimental effects to the synthesis of  $\text{Li}_7\text{P}_3\text{S}_{11}$  SEs with the addition of excess elemental sulfur. In  $3\text{PS-Li}_7\text{P}_3\text{S}_{11}$ , the peak assigned to the  $\text{Li}_2\text{S}$  phase is observed. The relative intensity of the peak corresponding to the  $\text{Li}_7\text{P}_3\text{S}_{11}$  crystal structure at  $\sim 30$  degrees is lower than that of ideal crystalline  $\text{Li}_7\text{P}_3\text{S}_{11}$  in all samples with excess sulfur. It is intriguing that the XRD pattern of  $\text{Li}_7\text{P}_3\text{S}_{11}$  with lower crystallinity reported by Mizuno et al. has a similar feature to that of  $x\text{PS-Li}_7\text{P}_3\text{S}_{11}$ .<sup>28</sup> The total ionic conductivities were calculated from the resistance value determined by the real-axis intercept at high frequency in the Nyquist plot. Figure 2.3.6b shows the ionic conductivity values versus inverse temperature for  $x\text{PS-Li}_7\text{P}_3\text{S}_{11}$  ( $x = 3, 5,$

7). The ionic conductivities at 25 °C range from  $6.0 \times 10^{-4} \text{ S cm}^{-1}$  to  $9.2 \times 10^{-4} \text{ S cm}^{-1}$ , exhibiting the highest value in 5PS-Li<sub>7</sub>P<sub>3</sub>S<sub>11</sub> among all compositions. Adding an EtOH content that exceeded the threshold levels results in a decrease in ionic conductivity (Figure 2.3.6c). No change is detected in the XRD patterns for 5PS-Li<sub>7</sub>P<sub>3</sub>S<sub>11</sub> heated at a temperature range between 270 °C and 350 °C, while 5PS-Li<sub>7</sub>P<sub>3</sub>S<sub>11</sub> heated at 370 °C decomposes into the Li<sub>4</sub>P<sub>2</sub>S<sub>6</sub> phase, as shown in Figure 2.3.7a. The 5PS-Li<sub>7</sub>P<sub>3</sub>S<sub>11</sub> heated at the optimal temperature (350 °C) exhibits an ionic conductivity of  $1.2 \text{ mS cm}^{-1}$ , which is higher than  $0.8 \text{ mS cm}^{-1}$  in CL-Li<sub>7</sub>P<sub>3</sub>S<sub>11</sub> and  $1.0 \text{ mS cm}^{-1}$  in BM-Li<sub>7</sub>P<sub>3</sub>S<sub>11</sub> (Figures 2.3.7b). This is consistent with the finding that the Li<sub>7</sub>P<sub>3</sub>S<sub>11</sub> crystal phase decomposes to thermodynamically stable phases such as Li<sub>4</sub>P<sub>2</sub>S<sub>6</sub>, Li<sub>3</sub>PS<sub>4</sub>, and sulfur.<sup>28,29</sup> On the other hand, the previous study reported that the Li<sub>7</sub>P<sub>3</sub>S<sub>11</sub> crystal phase decomposes at 280 °C.<sup>29</sup> The different decomposition temperatures between the previous and these studies can be explained by the difference in heat treatment methodology (hot-press apparatus vs. hot plate). Figure 2.3.7c shows TG curve of the 5PS-Li<sub>7</sub>P<sub>3</sub>S<sub>11</sub> precursor. The first weight loss steps until approximately 230 °C indicate the evaporation of the solvent and sulfur. Slight weight loss is observed between 230 °C and 370 °C, which should contribute to the removal of some residual solvent molecules or sulfur. The weight of the sample decreases above 370 °C, suggesting the evaporation of sulfur with the decomposition of Li<sub>7</sub>P<sub>3</sub>S<sub>11</sub>.<sup>28,29</sup> The electronic conductivities of Li<sub>7</sub>P<sub>3</sub>S<sub>11</sub> prepared by each method were measured by a DC polarization test at room temperature shown in Figure 2.3.8. The DC electronic conductivities of 5PS-Li<sub>7</sub>P<sub>3</sub>S<sub>11</sub> heated at 270 °C and 350 °C (denoted as 5PS-Li<sub>7</sub>P<sub>3</sub>S<sub>11</sub>-270 and 5PS-Li<sub>7</sub>P<sub>3</sub>S<sub>11</sub>-350) are  $1.3 \times 10^{-10} \text{ S cm}^{-1}$  and  $8.1 \times 10^{-10} \text{ S cm}^{-1}$ , respectively. This difference in the electronic conductivity might be caused by residual solvent molecules or sulfur. These experimental results demonstrate that Li<sub>7</sub>P<sub>3</sub>S<sub>11</sub> SEs synthesized by this solution processing method retain their performance as pure ionic conductors.

To identify the local structure, solid-state <sup>31</sup>P NMR was performed on 5PS-Li<sub>7</sub>P<sub>3</sub>S<sub>11</sub>-350 (Figure 2.3.9). None of the signals associated with P–O bonding appear due to the addition of trace EtOH, which is in agreement with the XRD results. 5PS-Li<sub>7</sub>P<sub>3</sub>S<sub>11</sub>-350 shows two signals at 82.9 and 87.8 ppm, corresponding to the PS<sub>4</sub><sup>3-</sup> and P<sub>2</sub>S<sub>7</sub><sup>4-</sup> anions, respectively. The full width at the half-maximum value of the signals is 0.79 kHz for the PS<sub>4</sub><sup>3-</sup> unit and 1.59 kHz for the P<sub>2</sub>S<sub>7</sub><sup>4-</sup> unit. The P<sub>2</sub>S<sub>7</sub><sup>4-</sup> anion species, which consists of two corner-sharing tetrahedrons, offers flexible motion in the local environment, which should lead to a chemical shift distribution. Indeed, an NMR study of Li<sub>7</sub>P<sub>3</sub>S<sub>11</sub> reported that the asymmetric structure of the P<sub>2</sub>S<sub>7</sub><sup>4-</sup> polyanion with altered bond lengths and angles could induce different isotropic chemical shifts in the NMR spectra.<sup>30</sup> The disordered local structure may be reflected in the peculiar relative peak intensity of the XRD pattern (Figure 2.3.6a), which differs from that of the ideal Li<sub>7</sub>P<sub>3</sub>S<sub>11</sub> crystal phase. Assuming a real Li<sub>7</sub>P<sub>3</sub>S<sub>11</sub> crystal phase, in which PS<sub>4</sub><sup>3-</sup> and P<sub>2</sub>S<sub>7</sub><sup>4-</sup> units coexist in a 1:1 ratio, the peak area ratio of PS<sub>4</sub><sup>3-</sup> and P<sub>2</sub>S<sub>7</sub><sup>4-</sup> based on solid-NMR is 1:2 in the stoichiometry, whereas that of 5PS-

Li<sub>7</sub>P<sub>3</sub>S<sub>11</sub>-350 is 1:1.15. Uchida et al. proposed an analogous Li<sub>7</sub>P<sub>3</sub>S<sub>11</sub> crystal based on NMR spectroscopy, in which P<sub>2</sub>S<sub>7</sub><sup>4-</sup> converts into two PS<sub>4</sub><sup>3-</sup> units.<sup>31</sup> The reaction equation is as follows:



It was reported that the analogous Li<sub>7</sub>P<sub>3</sub>S<sub>11</sub> crystal is formed in Li<sub>7</sub>P<sub>3</sub>S<sub>11</sub> with lower crystallinity and corresponds to the composition of crystalline Li<sub>7</sub>P<sub>3</sub>S<sub>11</sub> with excess sulfur.<sup>31</sup> 5PS-Li<sub>7</sub>P<sub>3</sub>S<sub>11</sub>-350 with excess sulfur should form the analogous Li<sub>7</sub>P<sub>3</sub>S<sub>11</sub> crystal, which can be described by a higher PS<sub>4</sub><sup>3-</sup> content in the structure and lower crystallinity. According to previous experimental and computational studies, it was shown that Li<sub>7</sub>P<sub>3</sub>S<sub>11</sub> SEs exhibit inherently high ionic conductivity because of their crystal structure that favors ion migration.<sup>26,28,32</sup> 5PS-Li<sub>7</sub>P<sub>3</sub>S<sub>11</sub>-350 shows higher ionic conductivity than the highly crystallized BM-Li<sub>7</sub>P<sub>3</sub>S<sub>11</sub>, despite being stoichiometrically inconsistent with the anion units in ideal Li<sub>7</sub>P<sub>3</sub>S<sub>11</sub> and the disordered local environment. The high ionic conductivity of 5PS-Li<sub>7</sub>P<sub>3</sub>S<sub>11</sub>-350 should originate from the expanded Li-ion conduction path induced by the unique anion framework of the analogous Li<sub>7</sub>P<sub>3</sub>S<sub>11</sub> crystal.<sup>31</sup> Moreover, the disordered local environment likely provides desirable structural attributes with higher degrees of freedom for ion movement.<sup>32</sup>

Figure 2.3.10 shows the SEM images of Li<sub>7</sub>P<sub>3</sub>S<sub>11</sub> synthesized by each method. In all samples, the secondary particles range in diameter from 50 to 100 μm. The microstructure of the CL-Li<sub>7</sub>P<sub>3</sub>S<sub>11</sub> exhibits textures resembling a broccoli crown, involving uniform pseudo-spherical primary particles of less than 1 μm, as shown in Chapter 2.2. Meanwhile, 5PS-Li<sub>7</sub>P<sub>3</sub>S<sub>11</sub>-270 and -350 show particle morphologies resembling a monolith with a relatively smooth particle surface, which is produced through the melt diffusion process of sulfur during heat treatment. Table 1 provides a detailed summary of the ionic conductivity and synthetic conditions of Li<sub>7</sub>P<sub>3</sub>S<sub>11</sub> prepared by different liquid-phase methods. The performance of the metastable Li<sub>7</sub>P<sub>3</sub>S<sub>11</sub> prepared by the liquid-phase method depends on various manufacturing conditions, such as solvent selection, reaction treatment, drying process, etc. The ionic conductivity varies by one order of magnitude, even when the manufacturing conditions are only slightly different.<sup>1,2,6,11,33–36</sup> This fact indicates that the conventional methods involve difficulty in achieving intrinsic high conductivity for Li<sub>7</sub>P<sub>3</sub>S<sub>11</sub> during large-scale manufacturing. This solution processing technology dramatically reduces the processing time for the wet-chemical reaction from 24 to 72 h in conventional liquid-phase synthesis to ~2 min, leading to improved producibility, cost, scalability, and performance compared to the SEs produced by conventional methods.

### 2.3.5 Cell performance

Symmetric cells Li || CL-Li<sub>7</sub>P<sub>3</sub>S<sub>11</sub>, BM-Li<sub>7</sub>P<sub>3</sub>S<sub>11</sub>, 5PS-Li<sub>7</sub>P<sub>3</sub>S<sub>11</sub>-270, and 5PS-Li<sub>7</sub>P<sub>3</sub>S<sub>11</sub>-350 || Li were cycled at a current density of 0.1 mA cm<sup>-2</sup> (Figure 2.3.11). The rapid decrease in



overpotential appears within 20 h in cells fabricated using BM-Li<sub>7</sub>P<sub>3</sub>S<sub>11</sub> and 5PS-Li<sub>7</sub>P<sub>3</sub>S<sub>11</sub>-350, indicating a short circuit caused by an unstable interface between the Li metal and SEs (Figure 2.3.11a and b). The cells prepared with CL-Li<sub>7</sub>P<sub>3</sub>S<sub>11</sub> and 5PS-Li<sub>7</sub>P<sub>3</sub>S<sub>11</sub>-270 exhibit increased overpotential as the stripping/plating process is repeated, but interestingly, they operate without a short circuit during 400 h of cycling (Figure 2.3.11c and d). These remarkable improvements may have originated from residual solvents that contain N atoms. I deduce that Li<sub>3</sub>N, which is thermodynamically stable with Li, is generated at the SEs/Li interface.<sup>37</sup> An unstable voltage profile appears in the cell using 5PS-Li<sub>7</sub>P<sub>3</sub>S<sub>11</sub>-270 during the initial period, suggesting the formation of solid electrolyte interphases with interfacial compatibility. In addition, a difference in overpotential between cells with CL-Li<sub>7</sub>P<sub>3</sub>S<sub>11</sub> and 5PS-Li<sub>7</sub>P<sub>3</sub>S<sub>11</sub>-270 gradually becomes evident during long-term cycling. The cell comprising 5PS-Li<sub>7</sub>P<sub>3</sub>S<sub>11</sub>-270 SEs demonstrates a lower overpotential relative to the cell using CL-Li<sub>7</sub>P<sub>3</sub>S<sub>11</sub> SEs after 400 h of cycling (15 mV vs. 34 mV). The decomposition reaction kinetics is affected by the electronic conductivity of the SEs since insertion of lithium requires a supply of both ion and electron to the reaction field.<sup>38-40</sup> From the DC polarization measurements, 5PS-Li<sub>7</sub>P<sub>3</sub>S<sub>11</sub>-270 SEs exhibit a lower electronic conductivity ( $1.3 \times 10^{-10}$  S cm<sup>-1</sup> at room temperature) than CL-Li<sub>7</sub>P<sub>3</sub>S<sub>11</sub> SEs ( $4.7 \times 10^{-10}$  S cm<sup>-1</sup> at room temperature), which very likely results in the difference in electrochemical stability between CL-Li<sub>7</sub>P<sub>3</sub>S<sub>11</sub> and 5PS-Li<sub>7</sub>P<sub>3</sub>S<sub>11</sub>-270 SEs.

To evaluate the electrochemical performance of Li<sub>7</sub>P<sub>3</sub>S<sub>11</sub> SEs prepared by the solution processing technology, I fabricated cathode composites using the Li<sub>7</sub>P<sub>3</sub>S<sub>11</sub> SEs. Coating technologies using a Li<sub>7</sub>P<sub>3</sub>S<sub>11</sub> slurry process have often been adopted for the preparation of cathode composites employing a broad range of metallic sulfides as the cathode active material.<sup>41-45</sup> In my demonstrations, I prepared TiS<sub>2</sub> composites by melt diffusion of excess sulfur in Li<sub>7</sub>P<sub>3</sub>S<sub>11</sub> SEs during the heating process (Figure 2.3.12a). SEM-EDS mapping analysis of the 50TiS<sub>2</sub>-50(BM-Li<sub>7</sub>P<sub>3</sub>S<sub>11</sub>) (wt%) fabricated using a mortar and 50TiS<sub>2</sub>-50(5PS-Li<sub>7</sub>P<sub>3</sub>S<sub>11</sub>) fabricated via melt of excess sulfur are shown in Figure 2.3.12b and c, respectively. In 50TiS<sub>2</sub>-50(BM-Li<sub>7</sub>P<sub>3</sub>S<sub>11</sub>), no obvious SE particles are dispersed on the TiS<sub>2</sub> surface, as shown in the SEM image (Figure 2.3.12b). In contrast, the 50TiS<sub>2</sub>-50(5PS-Li<sub>7</sub>P<sub>3</sub>S<sub>11</sub>) composites show particles containing phosphorus evenly distributed throughout. This suggests that the 5PS-Li<sub>7</sub>P<sub>3</sub>S<sub>11</sub> SEs are uniformly coated on the TiS<sub>2</sub> surface via the melt of excess sulfur. Figure 2.3.13a and b shows the cell performance of Li-In | 5PS-Li<sub>7</sub>P<sub>3</sub>S<sub>11</sub>-350 | TiS<sub>2</sub>-SE ASLB cells using BM-Li<sub>7</sub>P<sub>3</sub>S<sub>11</sub> and 5PS-Li<sub>7</sub>P<sub>3</sub>S<sub>11</sub>. The charge-discharge tests of both cells conducted at 30 °C and a current density of  $\sim 0.167$  mA cm<sup>-2</sup> (corresponding to 0.1C) exhibit high discharge capacities of 226 mAh g<sup>-1</sup> for the TiS<sub>2</sub>-(5PS-Li<sub>7</sub>P<sub>3</sub>S<sub>11</sub>) composite and 218 mAh g<sup>-1</sup> for the TiS<sub>2</sub>-(BM-Li<sub>7</sub>P<sub>3</sub>S<sub>11</sub>) composite at the first discharge (Figure 2.3.13a). In the cell with BM-Li<sub>7</sub>P<sub>3</sub>S<sub>11</sub>, the capacity decreases to 195 mAh g<sup>-1</sup> in the subsequent first charge, whereas the cell with 5PS-Li<sub>7</sub>P<sub>3</sub>S<sub>11</sub> retains the high discharge

capacity ( $222 \text{ mAh g}^{-1}$ ) and shows better reversibility than that of the cell with BM- $\text{Li}_7\text{P}_3\text{S}_{11}$ . The cell with 5PS- $\text{Li}_7\text{P}_3\text{S}_{11}$  exhibits an almost identical discharge capacity ( $\sim 140 \text{ mAh g}^{-1}$ ) as the cell with BM- $\text{Li}_7\text{P}_3\text{S}_{11}$  and a coulombic efficiency of 100%, even after 20 cycles (Figure 2.3.13b). In addition, the  $\text{TiS}_2$ -(5PS- $\text{Li}_7\text{P}_3\text{S}_{11}$ ) composite exhibits higher cell performance at a high C-rate (1C) during 20 cycles than that of the  $\text{TiS}_2$ -(BM- $\text{Li}_7\text{P}_3\text{S}_{11}$ ) composite (Figure 2.3.13.c). The improved cell performance should be attributed to the uniformity and tight connection in the  $\text{TiS}_2$ -SE composites via molten sulfur, as shown in the SEM image (Figure 2.3.12c). In another recent study, Xiao et al. applied  $\text{Li}_{1.9}\text{OHCl}_{0.9}$  SEs with a low melting point ( $\sim 300 \text{ }^\circ\text{C}$ ) to melt-infiltration technology for ASLB manufacturing, such that  $\text{Li}_{1.9}\text{OHCl}_{0.9}$  infiltrated into the electrodes in a liquid state during heating until  $\sim 300 \text{ }^\circ\text{C}$ , and then solidified during cooling.<sup>46</sup> The melt-infiltration process enables the potential scalable and low-cost manufacturing, as well as a homogeneous SE-electrode interface with extremely low porosity. I have demonstrated that SE coating technology via melt of excess sulfur creates a dense SE coating on the electrode.

### 2.3.6 Conclusions

I have developed a promising solution processing technology via dynamic sulfide radical anions for rapid and scalable manufacturing of highly conductive  $\text{Li}_7\text{P}_3\text{S}_{11}$  SEs. The addition of a small amount of EtOH changes the reactive mixture of  $7\text{Li}_2\text{S}\cdot 3\text{P}_2\text{S}_5$  with excess elemental sulfur in a mixed solvent of ACN and THF from an inhomogeneous suspension to a homogeneous black solution. The joint effect of adding excess elemental sulfur and reasonable solvent results in the optimal solution coordination behavior, boosting the intermediate species' solubility. Moreover, the presence of EtOH enhances the chemical stability of  $\text{S}_3^{\cdot -}$  radical anion, which enables the activation of  $\text{P}_2\text{S}_5$  for the quick formation of the precursor solution. The precursor solution containing the  $\text{S}_3^{\cdot -}$  radical anion is kinetically more favorable than the insoluble precursor and intermediate produced using the conventional slurry process. The  $\text{Li}_7\text{P}_3\text{S}_{11}$  precursor solution is obtained in just 2 min in this solution processing. The prepared  $\text{Li}_7\text{P}_3\text{S}_{11}$  exhibits ionic conductivity of  $1.2 \text{ mS cm}^{-1}$  at  $25 \text{ }^\circ\text{C}$ ; this is higher than the  $\text{Li}_7\text{P}_3\text{S}_{11}$  synthesized by ball milling and conventional liquid-phase method based on ACN solvent. This solution processing technology can be applied for the effective fabrication of electrodes densely coated with SEs via molten sulfur. The  $\text{TiS}_2$ -SE composite using the  $\text{Li}_7\text{P}_3\text{S}_{11}$  with excess sulfur shows a high reversible capacity of  $228 \text{ mAh g}^{-1}$  at the first discharge and excellent cell performance compared with cells prepared using  $\text{TiS}_2$ -(BM- $\text{Li}_7\text{P}_3\text{S}_{11}$ ) composite fabricated by a mortar. The solution processing technology reported here provides a rapid synthesis, scalability, low cost, and intimate contacts between the active material/SEs, which opens new opportunities for the advancement of practical ASLB manufacturing.

## References

- (1) Wang, Z.; Jiang, Y.; Wu, J.; Jiang, Y.; Huang, S.; Zhao, B.; Chen, Z.; Zhang, J. Reaction Mechanism of  $\text{Li}_2\text{S-P}_2\text{S}_5$  System in Acetonitrile Based on Wet Chemical Synthesis of  $\text{Li}_7\text{P}_3\text{S}_{11}$  Solid Electrolyte. *Chem. Eng. J.* **2020**, *393*, 124706–124714.
- (2) Wang, Y.; Lu, D.; Bowden, M.; el Khoury, P. Z.; Han, K. S.; Deng, Z. D.; Xiao, J.; Zhang, J. G.; Liu, J. Mechanism of Formation of  $\text{Li}_7\text{P}_3\text{S}_{11}$  Solid Electrolytes through Liquid Phase Synthesis. *Chem. Mater.* **2018**, *30*, 990–997.
- (3) Calpa, M.; Rosero-Navarro, N. C.; Miura, A.; Terai, K.; Utsuno, F.; Tadanaga, K. Formation Mechanism of Thiophosphate Anions in the Liquid-Phase Synthesis of Sulfide Solid Electrolytes Using Polar Aprotic Solvents. *Chem. Mater.* **2020**, *32*, 9627–9632.
- (4) Ghidui, M.; Ruhl, J.; Culver, S. P.; Zeier, W. G. Solution-Based Synthesis of Lithium Thiophosphate Superionic Conductors for Solid-State Batteries: A Chemistry Perspective. *J. Mater. Chem. A.* **2019**, *7*, 17735–17753.
- (5) Zhou, L.; Park, K. H.; Sun, X.; Lalère, F.; Adermann, T.; Hartmann, P.; Nazar, L. F. Solvent-Engineered Design of Argyrodite  $\text{Li}_6\text{PS}_5\text{X}$  (X = Cl, Br, I) Solid Electrolytes with High Ionic Conductivity. *ACS Energy Lett.* **2019**, *4*, 265–270.
- (6) Ito, S.; Nakakita, M.; Aihara, Y.; Uehara, T.; Machida, N. A Synthesis of Crystalline  $\text{Li}_7\text{P}_3\text{S}_{11}$  Solid Electrolyte from 1,2-Dimethoxyethane Solvent. *J. Power Sources* **2014**, *271*, 342–345.
- (7) Tan, D. H. S.; Banerjee, A.; Deng, Z.; Wu, E. A.; Nguyen, H.; Doux, J. M.; Wang, X.; Cheng, J. H.; Ong, S. P.; Meng, Y. S.; Chen, Z. Enabling Thin and Flexible Solid-State Composite Electrolytes by the Scalable Solution Process. *ACS Appl. Energy Mater.* **2019**, *2*, 6542–6550.
- (8) Ruhl, J.; Riegger, L. M.; Ghidui, M.; Zeier, W. G. Impact of Solvent Treatment of the Superionic Argyrodite  $\text{Li}_6\text{PS}_5\text{Cl}$  on Solid-State Battery Performance. *Adv. Energy Sustain. Res.* **2021**, *2*, 2000077–2000086.
- (9) Lim, H. D.; Lim, H. K.; Xing, X.; Lee, B. S.; Liu, H.; Coaty, C.; Kim, H.; Liu, P. Solid Electrolyte Layers by Solution Deposition. *Adv. Mater. Interfaces* **2018**, *5*, 1701328–1701336.
- (10) Kim, M. J.; Choi, I. H.; Jo, S. C.; Kim, B. G.; Ha, Y. C.; Lee, S. M.; Kang, S.; Baeg, K. J.; Park, J. W. A Novel Strategy to Overcome the Hurdle for Commercial All-Solid-State Batteries via Low-Cost Synthesis of Sulfide Solid Electrolytes. *Small Methods* **2021**, *5*, 2100793–2100803.
- (11) Xu, R. C.; Xia, X. H.; Yao, Z. J.; Wang, X. L.; Gu, C. D.; Tu, J. P. Preparation of  $\text{Li}_7\text{P}_3\text{S}_{11}$  Glass-Ceramic Electrolyte by Dissolution-Evaporation Method for All-Solid-State Lithium Ion Batteries. *Electrochim. Acta* **2016**, *219*, 235–240.

- (12) Takahashi, M.; Yang, S.; Yamamoto, K.; Ohara, K.; Phuc, N. H. H.; Watanabe, T.; Uchiyama, T.; Sakuda, A.; Hayashi, A.; Tatsumisago, M.; Muto, H.; Matsuda, A.; Uchimoto, Y. Improvement of Lithium Ionic Conductivity of  $\text{Li}_3\text{PS}_4$  through Suppression of Crystallization Using Low-Boiling-Point Solvent in Liquid-Phase Synthesis. *Solid State Ionics* **2021**, *361*, 115568–115572.
- (13) Yamamoto, K.; Yang, S.; Takahashi, M.; Ohara, K.; Uchiyama, T.; Watanabe, T.; Sakuda, A.; Hayashi, A.; Tatsumisago, M.; Muto, H.; Matsuda, A.; Uchimoto, Y. High Ionic Conductivity of Liquid-Phase-Synthesized  $\text{Li}_3\text{PS}_4$  Solid Electrolyte, Comparable to That Obtained via Ball Milling. *ACS Appl. Energy Mater.* **2021**, *4*, 2275–2281.
- (14) Matsuda, A.; Muto, H.; Phuc, N. H. H. Preparation of  $\text{Li}_3\text{PS}_4$  Solid Electrolyte by Liquid-Phase Shaking Using Organic Solvents with Carbonyl Group as Complex Forming Medium. *J. Jpn. Soc. Powder Metallurgy*, **2016**, *63*, 976–980.
- (15) Lai, C.; Shu, C.; Li, W.; Wang, L.; Wang, X.; Zhang, T.; Yin, X.; Ahmad, I.; Li, M.; Tian, X.; Yang, P.; Tang, W.; Miao, N.; Zheng, G. W. Stabilizing a Lithium Metal Battery by an in Situ  $\text{Li}_2\text{S}$ -Modified Interfacial Layer via Amorphous-Sulfide Composite Solid Electrolyte. *Nano Lett.* **2020**, *20*, 8273–8281.
- (16) Zou, Q.; Lu, Y. C. Solvent-Dictated Lithium Sulfur Redox Reactions: An Operando UV-Vis Spectroscopic Study. *J. Phys. Chem. Lett.* **2016**, *7*, 1518–1525.
- (17) Bieker, G.; Wellmann, J.; Kolek, M.; Jalkanen, K.; Winter, M.; Bieker, P. Influence of Cations in Lithium and Magnesium Polysulphide Solutions: Dependence of the Solvent Chemistry. *Phys. Chem. Chem. Phys.* **2017**, *19*, 11152–11162.
- (18) Lu, Y. C.; He, Q.; Gasteiger, H. A. Probing the Lithium-Sulfur Redox Reactions: A Rotating-Ring Disk Electrode Study. *J. Phys. Chem. C* **2014**, *118*, 5733–5741.
- (19) Cuisinier, M.; Hart, C.; Balasubramanian, M.; Garsuch, A.; Nazar, L. F. Radical or Not Radical: Revisiting Lithium-Sulfur Electrochemistry in Nonaqueous Electrolytes. *Adv. Energy Mater.* **2015**, *5*, 1401801–140186.
- (20) Jin, Q.; Qi, X.; Yang, F.; Jiang, R.; Xie, Y.; Qie, L.; Huang, Y. The Failure Mechanism of Lithium-Sulfur Batteries under Lean-Ether-Electrolyte Conditions. *Energy Storage Mater.* **2021**, *38*, 255–261.
- (21) Rauh, R. D.; Shuker, F. S.; Marston, J. M.; Brummer, S. B. Formation of lithium polysulfides in aprotic media. *J. Inorg. Nucl. Chem.* **1977**, *39*, 1761–1766.
- (22) Rajput, N. N.; Murugesan, V.; Shin, Y.; Han, K. S.; Lau, K. C.; Chen, J.; Liu, J.; Curtiss, L. A.; Mueller, K. T.; Persson, K. A. Elucidating the Solvation Structure and Dynamics of Lithium Polysulfides Resulting from Competitive Salt and Solvent Interactions. *Chem. Mater.* **2017**, *29*, 3375–3379.
- (23) Gupta, A.; Bhargava, A.; Jones, J. P.; Bugga, R. v.; Manthiram, A. Influence of Lithium

- Polysulfide Clustering on the Kinetics of Electrochemical Conversion in Lithium-Sulfur Batteries. *Chem. Mater.* **2020**, *32*, 2070–2077.
- (24) Teragawa, S.; Aso, K.; Tadanaga, K.; Hayashi, A.; Tatsumisago, M. Liquid-Phase Synthesis of a  $\text{Li}_3\text{PS}_4$  Solid Electrolyte Using N-Methylformamide for All-Solid-State Lithium Batteries. *J. Mater. Chem. A* **2014**, *2*, 5095–5099.
- (25) Ito, A.; Kimura, T.; Sakuda, A.; Tatsumisago, M.; Hayashi, A. Liquid-Phase Synthesis of  $\text{Li}_3\text{PS}_4$  Solid Electrolyte Using Ethylenediamine. *J. Solgel Sci. Technol.* **2022**, *101*, 2–7.
- (26) Yamane, H.; Shibata, M.; Shimane, Y.; Junke, T.; Seino, Y.; Adams, S.; Minami, K.; Hayashi, A.; Tatsumisago, M. Crystal Structure of a Superionic Conductor,  $\text{Li}_7\text{P}_3\text{S}_{11}$ . *Solid State Ionics* **2007**, *178*, 1163–1167.
- (27) Momma, K.; Izumi, F. VESTA: A Three-Dimensional Visualization System for Electronic and Structural Analysis. *J. Appl. Crystallogr.* **2008**, *41*, 653–658.
- (28) Mizuno, F.; Hayashi, A.; Tadanaga, K.; Tatsumisago, M. New Lithium-Ion Conducting Crystal Obtained by Crystallization of the  $\text{Li}_2\text{S}-\text{P}_2\text{S}_5$  Glasses. *Electrochem. Solid-State Lett.* **2005**, *8*, A603–A606.
- (29) Busche, M. R.; Weber, D. A.; Schneider, Y.; Dietrich, C.; Wenzel, S.; Leichtweiss, T.; Schröder, D.; Zhang, W.; Weigand, H.; Walter, D.; Sedlmaier, S. J.; Houtarde, D.; Nazar, L. F.; Janek, J. In Situ Monitoring of Fast Li-Ion Conductor  $\text{Li}_7\text{P}_3\text{S}_{11}$  Crystallization Inside a Hot-Press Setup. *Chem. Mater.* **2016**, *28*, 6152–6165.
- (30) Murakami, M.; Shimoda, K.; Shiotani, S.; Mitsui, A.; Ohara, K.; Onodera, Y.; Arai, H.; Uchimoto, Y.; Ogumi, Z. Dynamical Origin of Ionic Conductivity for  $\text{Li}_7\text{P}_3\text{S}_{11}$  Metastable Crystal As Studied by  $^{67}\text{Li}$  and  $^{31}\text{P}$  Solid-State NMR. *J. Phys. Chem. C* **2015**, *119*, 24248–24254.
- (31) Uchida, K.; Ohkubo, T.; Utsuno, F.; Yazawa, K. Modified  $\text{Li}_7\text{P}_3\text{S}_{11}$  Glass-Ceramic Electrolyte and Its Characterization. *ACS Appl. Mater. Interfaces* **2021**, *13*, 37071–37081.
- (32) Chang, D.; Oh, K.; Kim, S. J.; Kang, K. Super-Ionic Conduction in Solid-State  $\text{Li}_7\text{P}_3\text{S}_{11}$ -Type Sulfide Electrolytes. *Chem. Mater.* **2018**, *30*, 8764–8770.
- (33) Calpa, M.; Rosero-Navarro, N. C.; Miura, A.; Tadanaga, K. Instantaneous Preparation of High Lithium-Ion Conducting Sulfide Solid Electrolyte  $\text{Li}_7\text{P}_3\text{S}_{11}$  by a Liquid Phase Process. *RSC Adv.* **2017**, *7*, 46499–46504.
- (34) Yao, X.; Liu, D.; Wang, C.; Long, P.; Peng, G.; Hu, Y. S.; Li, H.; Chen, L.; Xu, X. High-Energy All-Solid-State Lithium Batteries with Ultralong Cycle Life. *Nano Lett.* **2016**, *16*, 7148–7154.
- (35) Fan, B.; Zhang, Q.; Luo, Z.; Zhang, X.; Ma, H.; Fan, P.; Xue, B. Influence of Precipitate/Supernatant Ratio during Liquid-Phase Synthesis of Solid Electrolyte  $\text{Li}_7\text{P}_3\text{S}_{11}$ . *Solid State Ionics* **2019**, *343*, 115073–115079.

- (36) Maniwa, R.; Calpa, M.; Rosero-Navarro, N. C.; Miura, A.; Tadanaga, K. Synthesis of Sulfide Solid Electrolytes from  $\text{Li}_2\text{S}$  and  $\text{P}_2\text{S}_5$  in Anisole. *J. Mater. Chem. A* **2021**, *9*, 400–405.
- (37) Wenzel, S.; Leichtweiss, T.; Krüger, D.; Sann, J.; Janek, J. Interphase Formation on Lithium Solid Electrolytes - An in Situ Approach to Study Interfacial Reactions by Photoelectron Spectroscopy. *Solid State Ionics* **2015**, *278*, 98–105.
- (38) Han, F.; Westover, A. S.; Yue, J.; Fan, X.; Wang, F.; Chi, M.; Leonard, D. N.; Dudney, N. J.; Wang, H.; Wang, C. High Electronic Conductivity as the Origin of Lithium Dendrite Formation within Solid Electrolytes. *Nat. Energy* **2019**, *4*, 187–196.
- (39) Swamy, T.; Chen, X.; Chiang, Y. M. Electrochemical Redox Behavior of Li Ion Conducting Sulfide Solid Electrolytes. *Chem. Mater.* **2019**, *31*, 707–713.
- (40) Wang, S.; Zhang, W.; Chen, X.; Das, D.; Ruess, R.; Gautam, A.; Walther, F.; Ohno, S.; Koerver, R.; Zhang, Q.; Zeier, W. G.; Richter, F. H.; Nan, C. W.; Janek, J. Influence of Crystallinity of Lithium Thiophosphate Solid Electrolytes on the Performance of Solid-State Batteries. *Adv. Energy Mater.* **2021**, *11*.
- (41) Shi, J.; Liu, G.; Weng, W.; Cai, L.; Zhang, Q.; Wu, J.; Xu, X.; Yao, X.  $\text{Co}_3\text{S}_4@\text{Li}_7\text{P}_3\text{S}_{11}$  Hexagonal Platelets as Cathodes with Superior Interfacial Contact for All-Solid-State Lithium Batteries. *ACS Appl. Mater. Interfaces* **2020**, *12*, 14079–14086.
- (42) Ahmad, N.; Zhou, L.; Faheem, M.; Tufail, M. K.; Yang, L.; Chen, R.; Zhou, Y.; Yang, W. Enhanced Air Stability and High Li-Ion Conductivity of  $\text{Li}_{6.988}\text{P}_{2.994}\text{Nb}_{0.2}\text{S}_{10.934}\text{O}_{0.6}$  Glass-Ceramic Electrolyte for All-Solid-State Lithium-Sulfur Batteries. *ACS Appl. Mater. Interfaces* **2020**, *12*, 21548–21558.
- (43) Khurram Tufail, M.; Ahmad, N.; Zhou, L.; Faheem, M.; Yang, L.; Chen, R.; Yang, W. Insight on Air-Induced Degradation Mechanism of  $\text{Li}_7\text{P}_3\text{S}_{11}$  to Design a Chemical-Stable Solid Electrolyte with High  $\text{Li}_2\text{S}$  Utilization in All-Solid-State Li/S Batteries. *Chem. Eng. J.* **2021**, *425*, 130535–130545.
- (44) Xu, R. C.; Xia, X. H.; Wang, X. L.; Xia, Y.; Tu, J. P. Tailored  $\text{Li}_2\text{S}$ - $\text{P}_2\text{S}_5$  Glass-Ceramic Electrolyte by  $\text{MoS}_2$  Doping, Possessing High Ionic Conductivity for All-Solid-State Lithium-Sulfur Batteries. *J. Mater. Chem. A* **2017**, *5*, 2829–2834.
- (45) Tufail, M. K.; Zhou, L.; Ahmad, N.; Chen, R.; Faheem, M.; Yang, L.; Yang, W. A Novel Air-Stable  $\text{Li}_7\text{Sb}_{0.05}\text{P}_{2.95}\text{S}_{10.5}\text{I}_{0.5}$  Superionic Conductor Glass-Ceramics Electrolyte for All-Solid-State Lithium-Sulfur Batteries. *Chem. Eng. J.* **2021**, *407*, 127149–127158.
- (46) Xiao, Y.; Turcheniuk, K.; Narla, A.; Song, A. Y.; Ren, X.; Magasinski, A.; Jain, A.; Huang, S.; Lee, H.; Yushin, G. Electrolyte Melt Infiltration for Scalable Manufacturing of Inorganic All-Solid-State Lithium-Ion Batteries. *Nat. Mater.* **2021**, *20*, 984–990.

**Table 2.3.1** Ionic conductivity and synthetic conditions of  $\text{Li}_7\text{P}_3\text{S}_{11}$  prepared by the liquid-phase method.

Solvent	Synthesis	Reaction time (h)	Drying time (h)	Heat temperature ( $^{\circ}\text{C}$ )	$\sigma$ ( $\text{mS cm}^{-1}$ ) at room temperature	Reference
THF	Stirring at $50^{\circ}\text{C}$	24	–	250	0.24	[12]
ACN	Stirring at $50^{\circ}\text{C}$	24	–	250	0.97	[12]
ACN	Ultrasonication at $60^{\circ}\text{C}$	0.5	3	220	1.0	[34]
ACN	Stirring at $50^{\circ}\text{C}$	24	12	260	1.5	[35]
ACN	Stirring at RT	72	2	250	$\sim 0.3$	[9]
ACN	Stirring at $50^{\circ}\text{C}$	72	–	260	0.87	[2]
ACN	Stirring at $50^{\circ}\text{C}$	120	–	250	0.51	[1]
DME	Stirring	72	–	250	0.27	[36]
Anisole	Microwave at $260^{\circ}\text{C}$	$\sim 0.5$	3	300	0.13	[37]
ACN + THF + EtOH	Lightly stirring at RT	0.03	1	350	1.2	This work

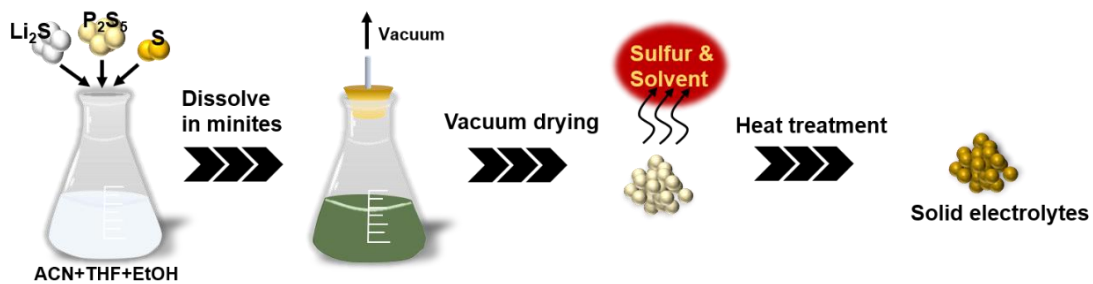


**Figure 2.3.1** Schematics of the novel solution processing technology for sulfide SEs.



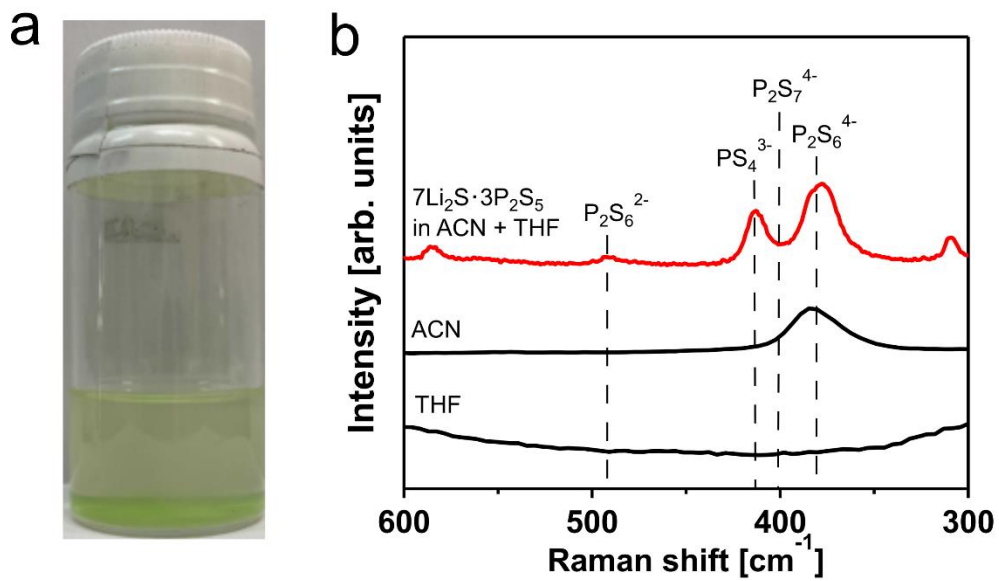


**Figure 2.3.2.** Solubility of lithium phosphates in the organic solvent. (a) Photo and (b) Raman spectra of  $7\text{Li}_2\text{S}\cdot 3\text{P}_2\text{S}_5$  solution in ACN/THF solvent mixture after sonication treatment.

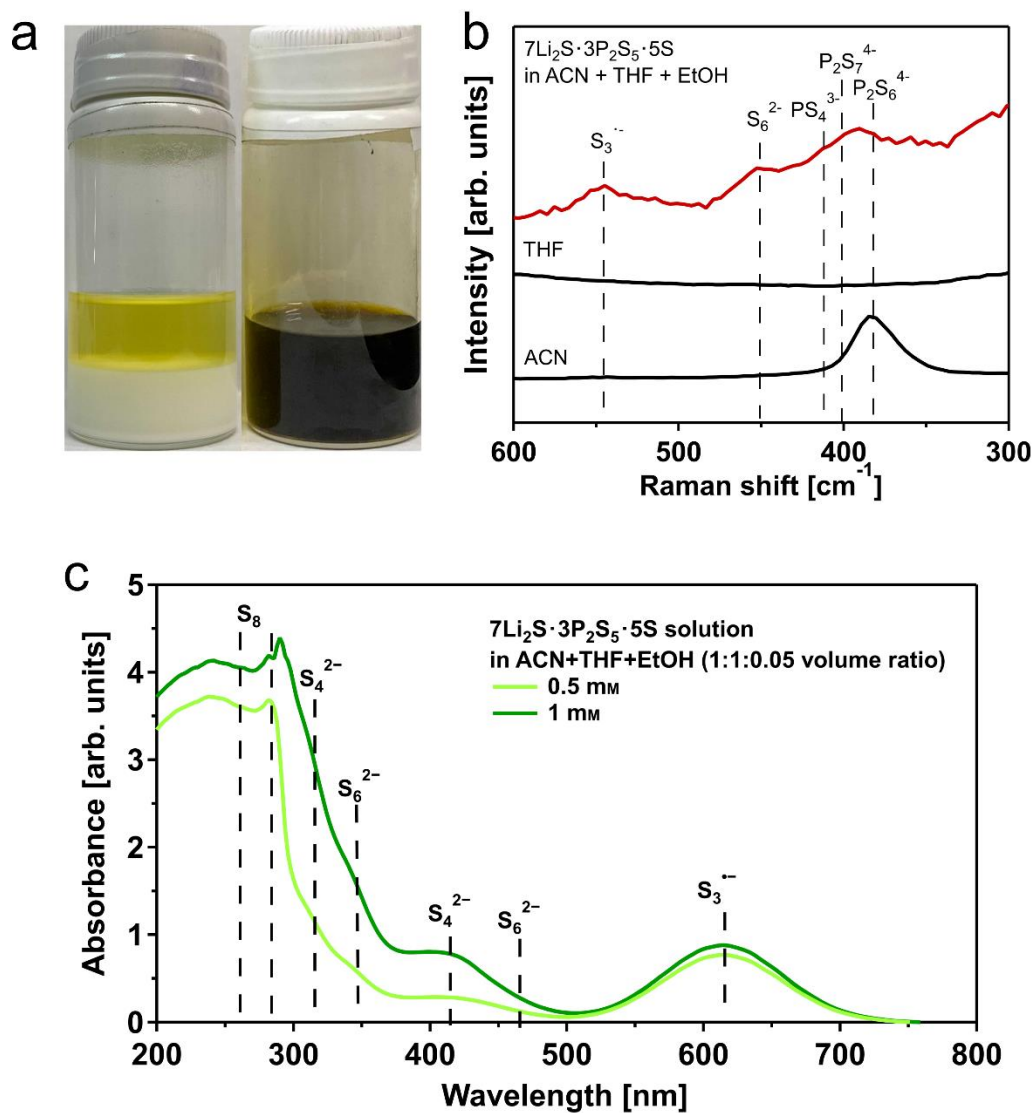


**Figure 2.3.3** (a) Solubility of  $7\text{Li}_2\text{S}\cdot 3\text{P}_2\text{S}_5$  mixtures with and without excess elemental sulfur in the organic solvent. (b) Raman spectra of ACN, THF, and  $7\text{Li}_2\text{S}\cdot 3\text{P}_2\text{S}_5\cdot 5\text{S}$  in the mixed solvent of ACN, THF, and EtOH. (c) UV-Vis spectra of  $7\text{Li}_2\text{S}\cdot 3\text{P}_2\text{S}_5\cdot 5\text{S}$  in the mixed solvent of ACN, THF, and EtOH at 0.5 mM and 1.0 mM.

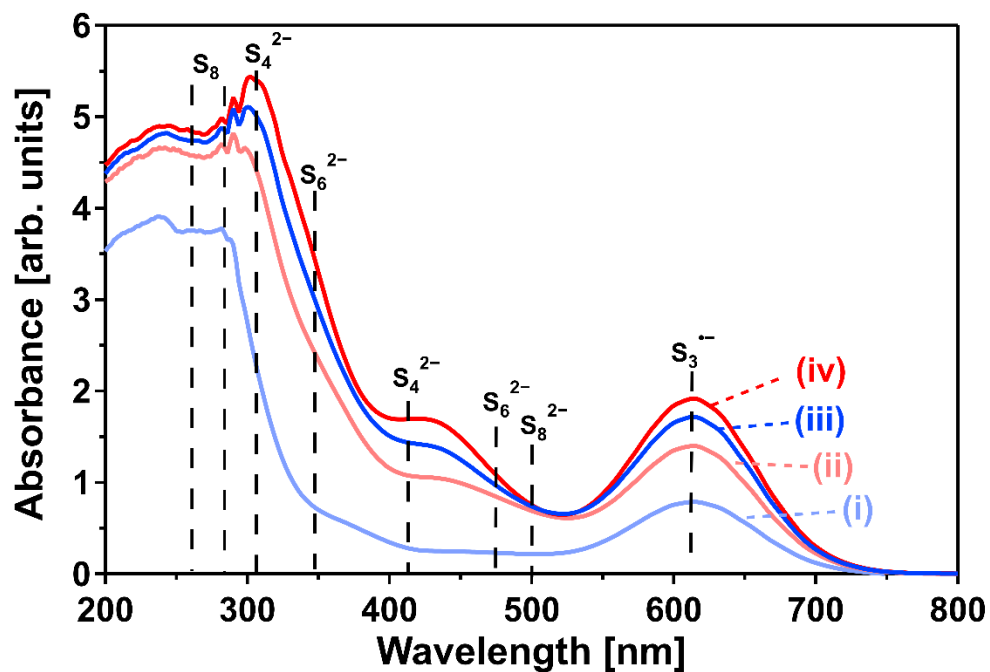


**Figure 2.3.4.** UV–Vis spectra of  $\text{Li}_2\text{S}_6$  (1.0 mM) in the ACN/THF (1:1 volume ratio) solvent mixture after stirring for i) 2 days and iii) 5 days; and in the ACN/THF/EtOH (1:1:0.05 volume ratio) solvent mixture after stirring for ii) 2 days and iv) 5 days.

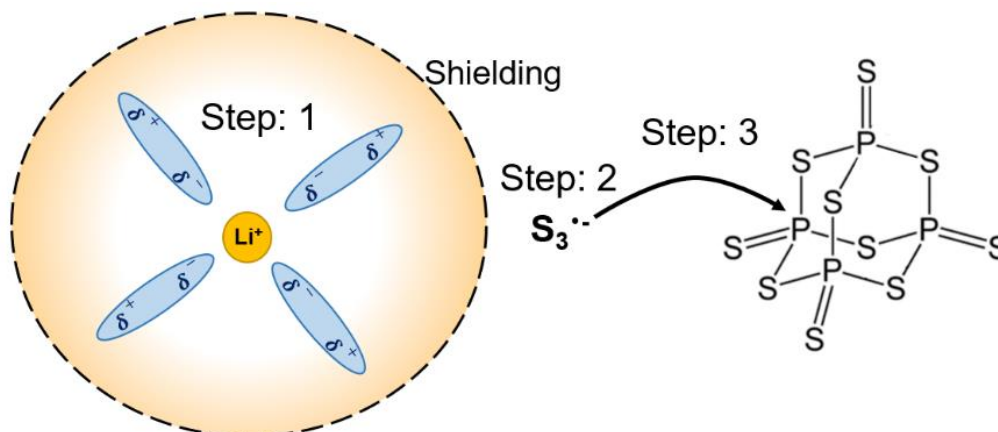


**Figure 2.3.5.** Schematic of proposed reaction with excess sulfur. Step 1: Lithium ions are strongly coordinated with EtOH and ACN molecules with high polarity. Step 2:  $S_3^{\cdot-}$  radical anions are shielded from Li-ions and stabilized. Step 3:  $S_3^{\cdot-}$  with high reactivity attacks the phosphorus on  $P_4S_{10}$  and breaks the  $P_4S_{10}$  cage.

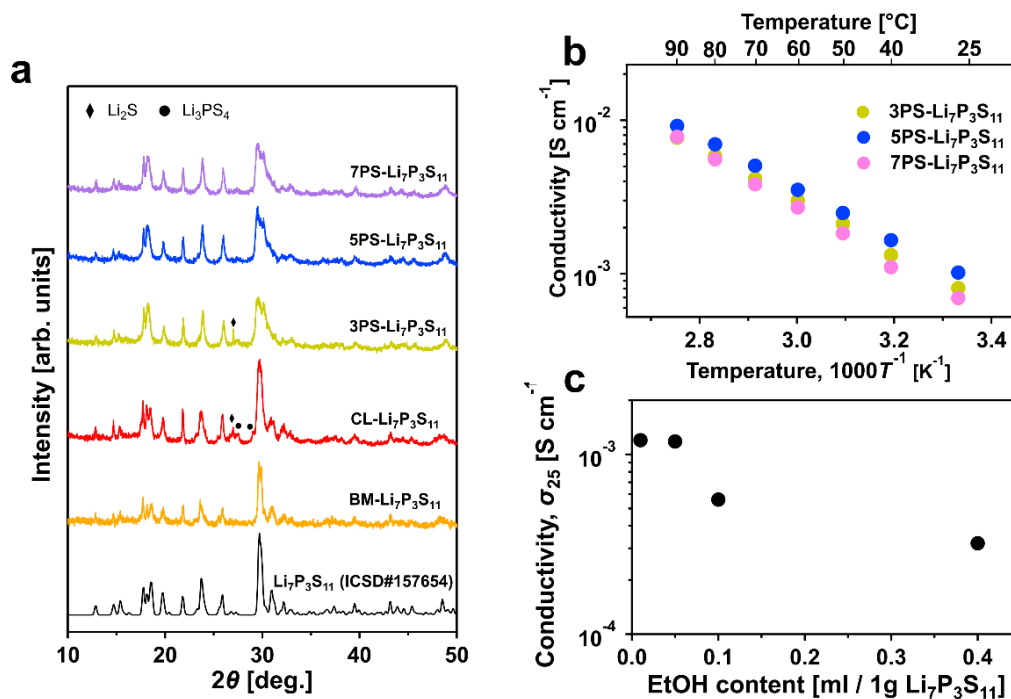


**Figure 2.3.6.** The structural and electrochemical properties of  $x$ PS-Li<sub>7</sub>P<sub>3</sub>S<sub>11</sub> ( $x = 3, 5, 7$ ), CL-Li<sub>7</sub>P<sub>3</sub>S<sub>11</sub>, and BM-Li<sub>7</sub>P<sub>3</sub>S<sub>11</sub>. (a) XRD patterns of  $x$ PS-Li<sub>7</sub>P<sub>3</sub>S<sub>11</sub> ( $x = 3, 5, 7$ ), CL-Li<sub>7</sub>P<sub>3</sub>S<sub>11</sub>, and BM-Li<sub>7</sub>P<sub>3</sub>S<sub>11</sub>. (b) Ionic conductivity versus inverse temperature for  $x$ PS-Li<sub>7</sub>P<sub>3</sub>S<sub>11</sub> ( $x = 3, 5, 7$ ). (c) ionic conductivity of 5PS-Li<sub>7</sub>P<sub>3</sub>S<sub>11</sub> prepared using mixed solvents of ACN/THF/EtOH (1:1: $x$  volume ratio) at room temperature.

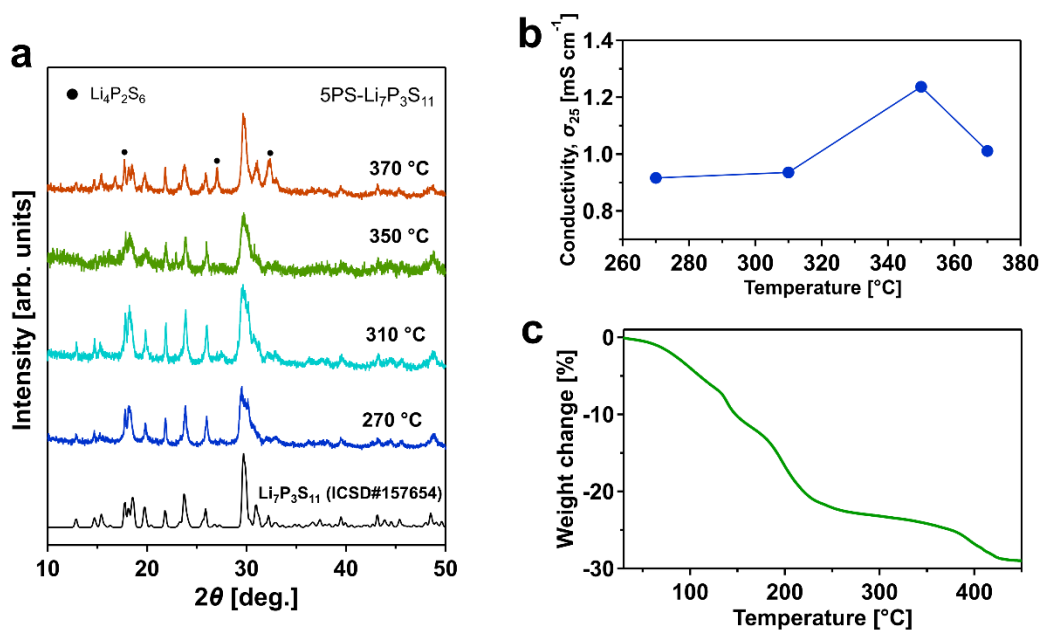


**Figure 2.3.7.** (a) XRD patterns for 5PS- $\text{Li}_7\text{P}_3\text{S}_{11}$  heated at each temperature. (b) Ionic conductivity at 25 °C for 5PS- $\text{Li}_7\text{P}_3\text{S}_{11}$  as a function of heating temperature. (c) TGA curve of 5PS- $\text{Li}_7\text{P}_3\text{S}_{11}$  precursor without heat treatment.

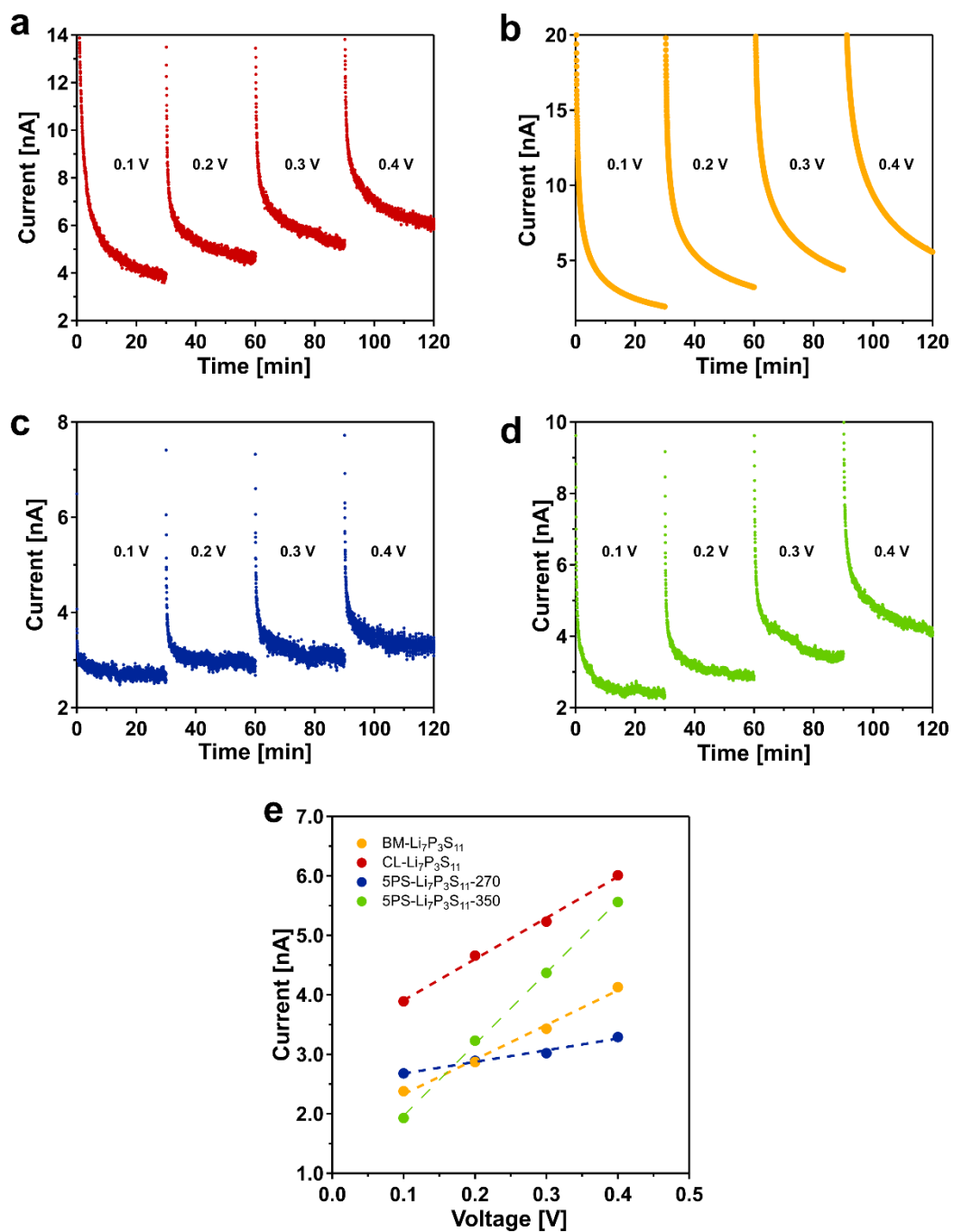


**Figure 2.3.8.** DC polarization of (a) CL-Li<sub>7</sub>P<sub>3</sub>S<sub>11</sub>, (b) BM-Li<sub>7</sub>P<sub>3</sub>S<sub>11</sub>, (c) 5PS-Li<sub>7</sub>P<sub>3</sub>S<sub>11</sub>-270, and (d) 5PS-Li<sub>7</sub>P<sub>3</sub>S<sub>11</sub>-350. (e) The response current of each sample with an applied voltage of 0.2 V, 0.4 V, 0.6 V, and 0.8 V along with the linear fits.

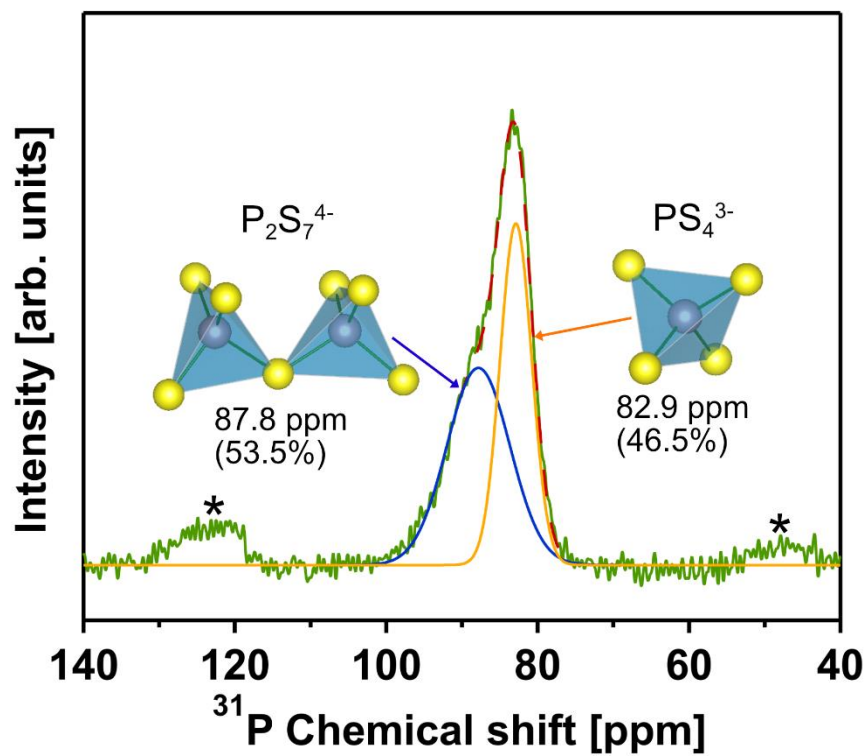


**Figure 2.3.9.** Solid-state  $^{31}\text{P}$  NMR spectra of 5PS-Li $_7$ P $_3$ S $_{11}$ -350. The asterisks indicate spinning sidebands.



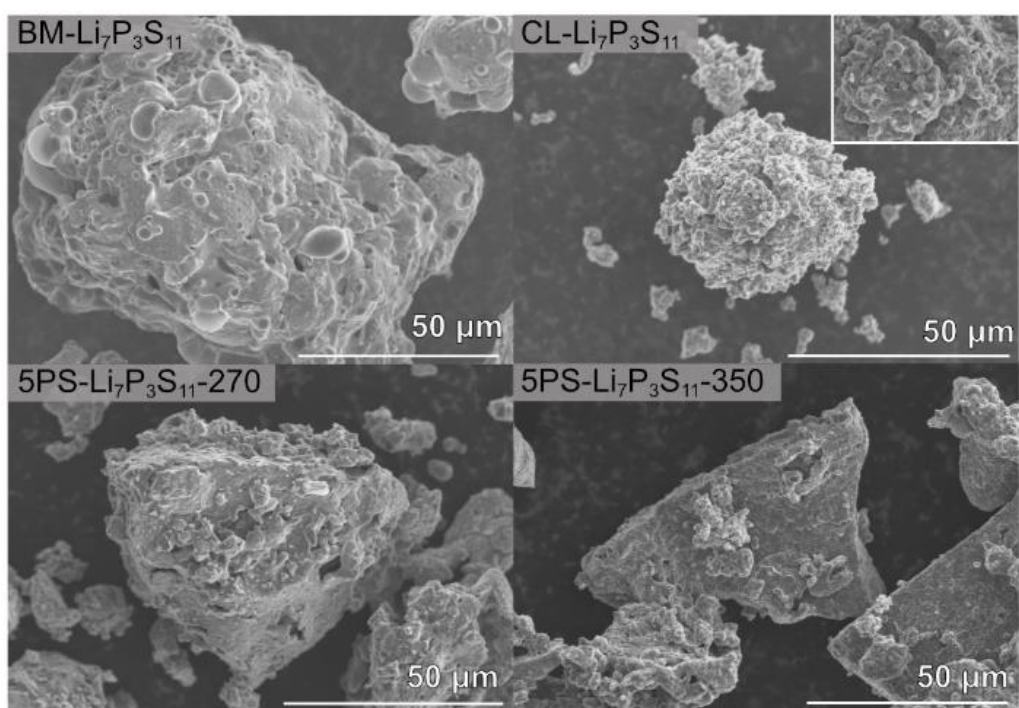


**Figure 2.3.10.** SEM images of  $\text{BM-Li}_7\text{P}_3\text{S}_{11}$ ,  $\text{CL-Li}_7\text{P}_3\text{S}_{11}$ ,  $5\text{PS-Li}_7\text{P}_3\text{S}_{11}\text{-270}$ , and  $5\text{PS-Li}_7\text{P}_3\text{S}_{11}\text{-350}$ .

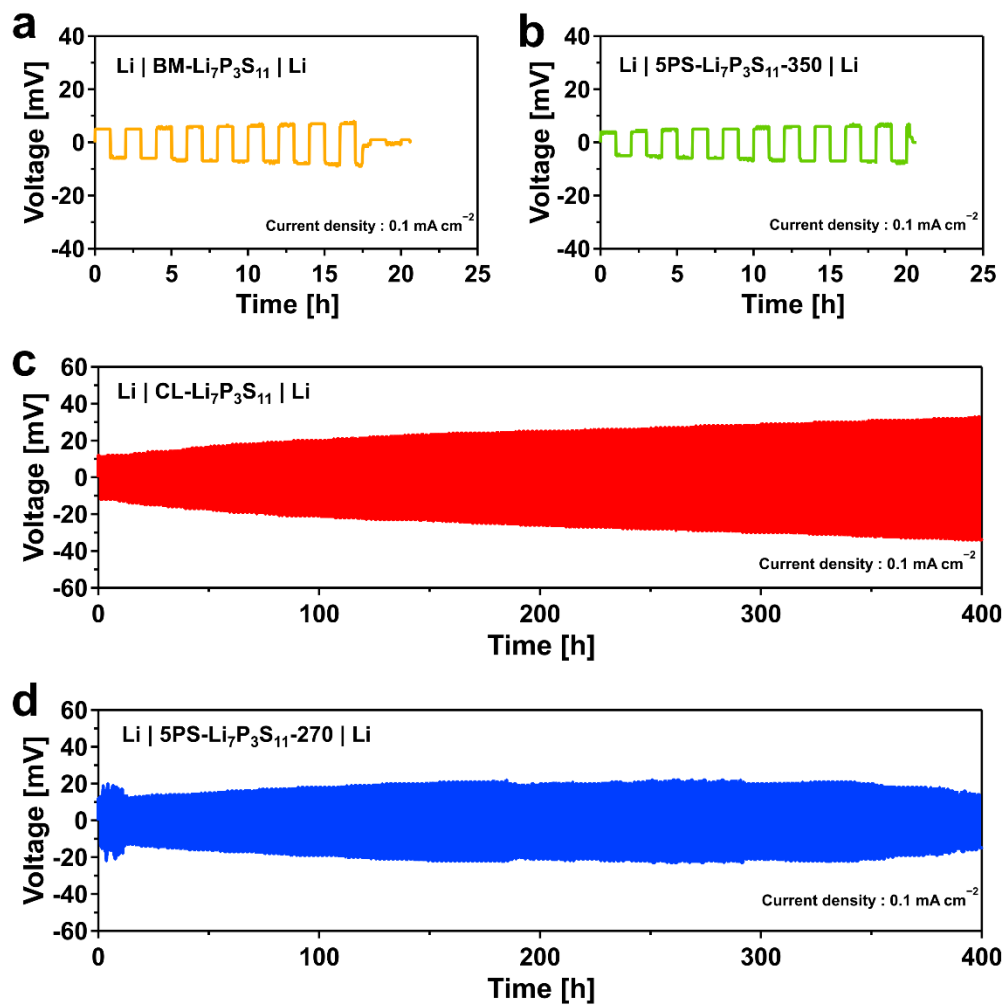
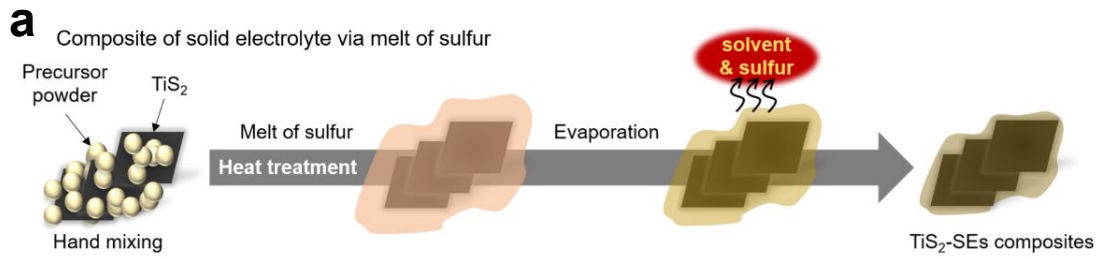
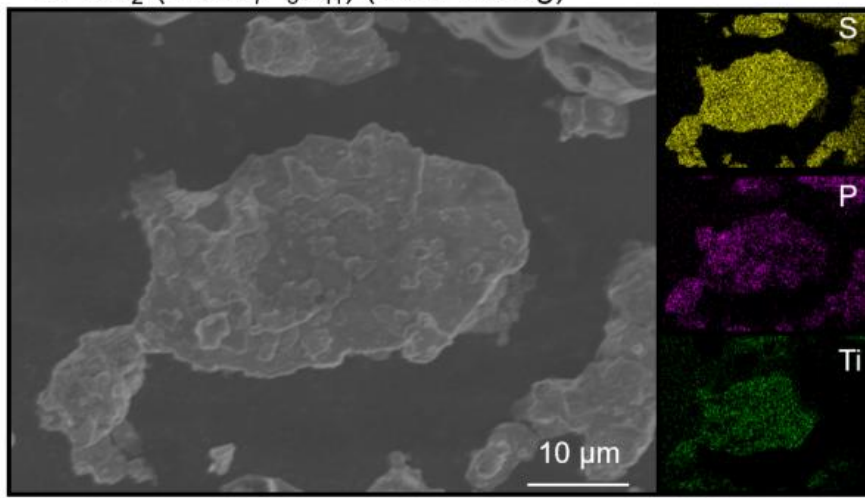


**Figure 2.3.11.** Voltage profiles during cycling of Li || (a) BM-Li<sub>7</sub>P<sub>3</sub>S<sub>11</sub>, (b) 5PS-Li<sub>7</sub>P<sub>3</sub>S<sub>11</sub>-350, (c) CL-Li<sub>7</sub>P<sub>3</sub>S<sub>11</sub>, and (d) 5PS-Li<sub>7</sub>P<sub>3</sub>S<sub>11</sub>-270 || Li in symmetric cells with a current density of  $0.1 \text{ mA cm}^{-2}$  at room temperature.



**b** TiS<sub>2</sub>-(BM-Li<sub>7</sub>P<sub>3</sub>S<sub>11</sub>) (hand mixing)



**c** TiS<sub>2</sub>-(5PS-Li<sub>7</sub>P<sub>3</sub>S<sub>11</sub>) (composite via melt)

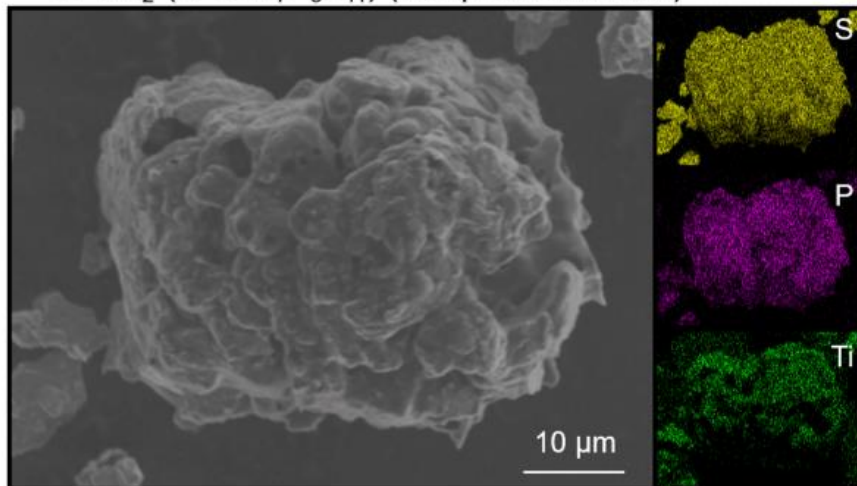


**Figure 2.3.12** (a) Schematic of the preparation of TiS<sub>2</sub>-5PS-Li<sub>7</sub>P<sub>3</sub>S<sub>11</sub> composites via the melt diffusion process of sulfur. SEM-EDS mapping of (b) TiS<sub>2</sub> composite mixed with BM-Li<sub>7</sub>P<sub>3</sub>S<sub>11</sub> by hand mixing and (c) TiS<sub>2</sub> composite coated with 5PS-Li<sub>7</sub>P<sub>3</sub>S<sub>11</sub> via molten sulfur.

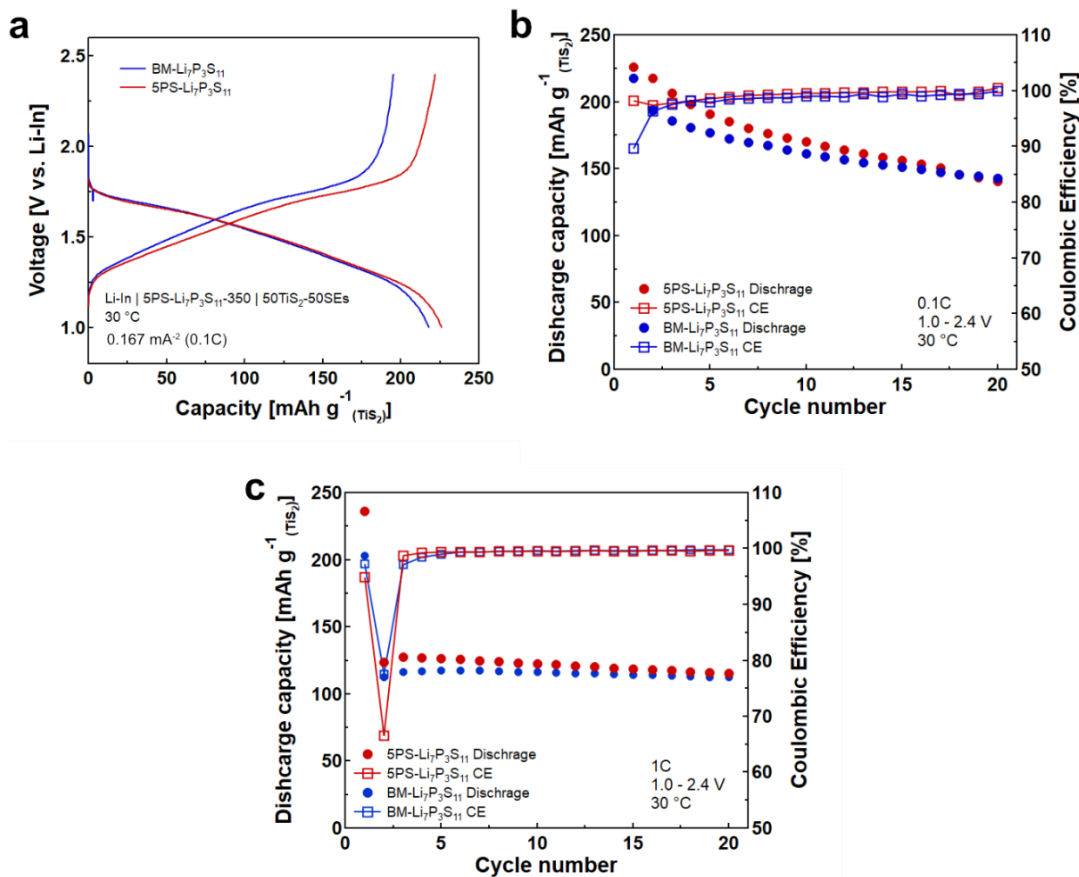


**Figure 2.3.13** (a) The voltage profiles at the first cycle of Li-In | 5PS-Li<sub>7</sub>P<sub>3</sub>S<sub>11</sub>-350 | TiS<sub>2</sub> composite coated with 5PS-Li<sub>7</sub>P<sub>3</sub>S<sub>11</sub> via molten sulfur and TiS<sub>2</sub> composite mixed with BM-Li<sub>7</sub>P<sub>3</sub>S<sub>11</sub> by hand mixing ASLB cells under a current density of 0.1C at 30 °C. Cycle performance under a current density of (b) 0.1C and (c) 1C at 30 °C. The theoretical capacity of TiS<sub>2</sub> is 239 mAh g<sup>-1</sup>.

## Chapter 3

# All-Solid-State Lithium Sulfur Batteries

### 3.1 Background

I described the novel solution synthesis of sulfide SEs for the large-scale manufacturing of ASLBs in Chapter 2. The improvement of energy storage devices requires not only the development of SEs but also active material. The active material which conventionally is used in liquid lithium-ion batteries has reached its theoretical capacity limit. The restricted performance motivated the development of active materials with high theoretical capacity. Lithium-sulfur batteries are promising candidates for next-generation batteries due to their high theoretical capacity, low cost, and resource abundance of S cathode materials.<sup>1</sup> However, the practical application of Li-S batteries faces several serious challenges: capacity loss with shuttling, sluggish kinetics of cathode materials, and low utilization because of electrically insulating of cathode materials (e.g. S and  $\text{Li}_2\text{S}$ ). The shuttling is caused by the dissolution of lithium polysulfides in organic liquid electrolytes during the charge/discharge. Replacing the organic liquid electrolytes with inorganic SEs, suppress the dissolution of lithium polysulfides, thereby resolving the cycle fade caused by self-discharge in Li-S batteries.<sup>2</sup> Nevertheless, the poor electronic and ionic conductivities of S and  $\text{Li}_2\text{S}$  cathodes still restrict the utilization of their high theoretical capacity. To improve the intrinsically electric cathode materials, the addition of heterogeneous elements, e.g., multivalent atoms and halogen, into  $\text{Li}_2\text{S}$  cathode materials was examined.<sup>3-5</sup> Several research groups have developed cathode composites mixed with highly conductive electron additives and SEs to improve the electric transport properties in cathode composites.<sup>6</sup> For instance, electron additives, such as mesoporous carbon<sup>7</sup>, carbon nanotube<sup>8-10</sup>, and reduced graphene oxide<sup>11</sup> were blended into cathode composites. Similarly, sulfide-based SEs such as  $\text{Li}_{10}\text{GeP}_2\text{S}_{12}$ <sup>11-13</sup>,  $\text{Li}_7\text{P}_3\text{S}_{11}$ <sup>14</sup>,  $\text{Li}_7\text{P}_2\text{S}_8\text{I}$ <sup>15</sup>, and  $\text{Li}_6\text{PS}_3\text{Cl}$ <sup>16-20</sup> are also used in the cathode composites. I describe the structural and electrochemical properties of  $\text{Li}_2\text{S}-\text{CaS}$  in Chapter 3.2,  $\text{Li}_2\text{S}-\text{CaX}_2$  ( $X = \text{F}, \text{Cl}, \text{Br}, \text{and I}$ ) in Chapter 3.3, and  $\text{Li}_2\text{S}-\text{AlI}_3$  in Chapter 3.4. Iodide-ion that occurs oxidation reaction at a slightly higher potential than the oxidation potential of  $\text{Li}_2\text{S}$  provides desirable redox activity in ASLSBs. The implication of such redox chemistry in the additive is expanded toward understanding the role of sulfide SEs as a redox mediator and the activation mechanism in ASLSBs. In Chapter 3.5, I unveil the effect of the decomposition of sulfide SEs on the cell performance in ASLSBs.

## 3.2 Lithium sulfide-calcium sulfide cathode nanocomposites

Herein,  $(100-x)\text{Li}_2\text{S}-x\text{CaS}$  nanocomposites are synthesized by high-energy ball milling, showing a higher ionic conductivity of  $1.4 \times 10^{-4} \text{ S cm}^{-1}$  at  $150 \text{ }^\circ\text{C}$  in  $x = 20$  than an ionic conductivity of  $2.1 \times 10^{-6} \text{ S cm}^{-1}$  in the milled  $\text{Li}_2\text{S}$ . A quantitative relationship between ion transport and relaxation behavior in the  $\text{Li}_2\text{S}-\text{CaS}$  nanocomposites is revealed based on complex conductivity and electric modulus formalism. The activation energy for relaxation is lower than the activation energy for conduction in  $\text{Li}_2\text{S}\cdot\text{CaS}$ . The long-range ion transport involves high activation energy compared to the hopping of carriers at the localized states. The cell with  $85\text{Li}_2\text{S}\cdot 15\text{CaS}$  cathode exhibits a higher capacity of  $819 \text{ mAh g}^{-1}$  after 15 cycles than the cell with the pristine  $\text{Li}_2\text{S}$ . The differential capacity curves of the cell using  $\text{Li}_2\text{S}-\text{CaS}$  demonstrate a large contribution of the degradation products from SEs during the charge/discharge cycle. The improved ionic conductivity of  $\text{Li}_2\text{S}-\text{CaS}$  and the large capacity contribution of SEs in cathode deliver high cell performance in ASLSBs.

### 3.2.1 Introduction

Lithium sulfide, as well as sulfur, is attractive as a cathode material for Li-S batteries owing to its high electrochemical capacity ( $1,167 \text{ mAh g}^{-1}$ ).<sup>21,22</sup> A Li-S battery based on a  $\text{Li}_2\text{S}$  cathode allows for coupling with a high-capacity anode such as Si and Sn; this is an appealing alternative to conventional Li-ion batteries.<sup>23</sup> However, the low electronic and ionic conductivity of  $\text{Li}_2\text{S}$  limits the complete utilization of its intrinsic capacity. Recently, multivalent cation doping to  $\text{Li}_2\text{S}$  improved its ionic conductivity and extracted a high battery performance as a cathode in all-solid-state Li-S batteries.<sup>24-26</sup> Both  $\text{Li}_2\text{S}-\text{Al}_2\text{S}_3$  and  $\text{Li}_2\text{S}-\text{MgS}$  solid solution demonstrated a higher conductivity (by two orders of magnitude of  $10^{-6} \text{ S cm}^{-1}$  at room temperature) than the milled  $\text{Li}_2\text{S}$  because of the nanoionics.  $\text{Li}_{1.50}\text{Al}_{0.167}\text{S}$  with improved ionic conductivity delivered a capacity of  $\sim 800 \text{ mAh g}^{-1}$  per the weight of  $\text{Li}_2\text{S}$  cathode material after 50 cycles.<sup>24,26</sup> Based on solid-state chemistry, the multiple unique nature of nanostructured materials containing  $\text{Li}_2\text{S}$  has inspired several devices that use rechargeable batteries. Calcium doping is an effective approach to improving ionic conductivity in inorganic materials. Interestingly, both ionic conductivity and activation energy of the  $\text{Na}_{2.730}\text{Ca}_{0.135}\text{PS}_4$  increased from a pristine  $\text{Na}_3\text{PS}_4$  solid electrolyte.<sup>27</sup> Calcium doping in Li-ion and Na-ion conductors is of considerable interest for expressing fast ionic conduction.<sup>28-30</sup>

Herein, I report the effect of  $\text{Ca}^{2+}$  doping on ion-transport properties in a  $\text{Li}_2\text{S}$  structure.  $(100-x)\text{Li}_2\text{S}\cdot x\text{CaS}$  (mol%) nanocomposites, prepared by high-energy ball milling, exhibit crystallite sizes ranging from 7 to 31 nm. The  $\text{Li}_2\text{S}-\text{CaS}$  nanocomposites demonstrate higher conductivity and

activation energy for conduction than the milled pure  $\text{Li}_2\text{S}$ . To understand the fundamental relationship between activation energy for conduction and relaxation in  $(100-x)\text{Li}_2\text{S}\cdot x\text{CaS}$ , I examined the complex conductivity and electric modulus formalism. The activation energy for electric relaxation is lower than the activation energy for conduction in  $80\text{Li}_2\text{S}\cdot 20\text{CaS}$ . The result indicates that long-range ion transport, including the contribution of a grain boundary, involves higher energy barriers than the hopping of carriers at localized states. The fabricated  $\text{Li}_2\text{S}\text{--CaS}$  cathode shows higher reversible capacities than the cathode using intrinsic  $\text{Li}_2\text{S}$ . The differential capacity curves in ASLSBs reveal the sulfide solid electrolyte in cathode composite as well as cathode materials shows electrochemical redox reaction and contributed to the high capacity.

### 3.2.2 Experimental methods

**Synthesis.** Lithium sulfide (99.9%, Mitsuwa) and CaS (99.99%, Kojundo Laboratory) were mixed at appropriate molar ratios. Then, the powders obtained were loaded in 45 ml of zirconia pots with  $\phi$  10 mm zirconia balls and subjected to high-energy ball milling with planetary ball milling (Fritsch Pulverisete 7 Premium line) at a rotation speed of 510 rpm for 10 h (1 h milling; 15 min pause).

$\text{Li}_{5.5}\text{PS}_{4.5}\text{Cl}_{1.5}$  SEs were prepared by mechanochemical reaction as follows. Lithium sulfide,  $\text{LiCl}$ , and  $\text{P}_2\text{S}_5$  were mixed at appropriate molar ratios. Then, the resultant powders were loaded in 45 ml of zirconia pots with  $\phi$  10 mm zirconia balls and subjected to ball milling with planetary ball milling (Fritsch Pulverisete 7 Premium line) at a rotation speed of 600 rpm for 20 h. The obtained precursor powders were heated at 450 °C for 2 h on a hot plate to form  $\text{Li}_{5.5}\text{PS}_{4.5}\text{Cl}_{1.5}$  SEs with an argyrodite structure.

The cathode composite electrodes were fabricated by ball milling. First, the cathode materials,  $\text{Li}_{5.5}\text{PS}_{4.5}\text{Cl}_{1.5}$  SEs, and Vapor grown carbon fiber (VGCF) were mixed by a mortar at a weight ratio 50:40:10, respectively. Then, the mixture powders were filled in 45 ml of zirconia pots with 35 g of zirconia balls ( $\phi$  4 mm) and subjected to ball milling with planetary ball milling (Fritsch Pulverisete 7 Premium line) at a rotation speed of 510 rpm for 10 h.

**Material characterization.** Powder XRD measurements were performed under  $2\theta = 10^\circ\text{--}80^\circ$  in a step interval of  $0.02^\circ$  at a scan rate of  $0.2^\circ \text{ min}^{-1}$  using a Rigaku Ultima IV diffractometer. An X-ray beam was generated using  $\text{CuK}\alpha$  radiation (40 kV, 30 mA). For XRD measurements, we used an XRD holder with a beryllium window (Rigaku). Subsequently, structural refinements were analyzed by the Rietveld method using the RIETAN-FP computer program.<sup>31</sup> The crystallite size,  $D$ , and the microstrain,  $\epsilon$ , for phases in the prepared nanocomposites were calculated from the Williamson–Hall method presented in Eq. 3.2.1:

$$\beta \cos \theta = C \epsilon \sin \theta + \frac{K \lambda}{D}, \quad (3.2.1)$$

where  $\beta$  is the integral breadth,  $K$  and  $C$  are constants (0.94 and 4), and  $\lambda$  is the wavenumber of X-rays. Note that instrumental broadening was corrected using crystalline  $\text{Li}_2\text{S}$  without ball milling. SEM characterization was carried out on a Hitachi-S4800 with an Energy dispersive X-ray spectroscopy (EDS; ULTIM MAX, Oxford Instrument).

**Electrochemical measurements.** The overall conductivities of prepared samples were determined by alternating current impedance spectroscopy (SI 1260, Solatron) in a frequency range of 1 MHz to 10 Hz under a dry Ar flow. To fabricate cells for EIS measurements, each sample (~80 mg) was filled in a holder made of PEEK with two stainless steel rods as blocking electrodes. I applied a uniaxial pressure of 256 MPa to pellets having diameters of ~10.0 mm at room temperature. The complex conductivity,  $\sigma^*$ , of samples was determined from the complex impedance,  $Z^*$ , obtained using EIS data and is reported as follows:

$$\sigma^* = \sigma' + j\sigma'' = \frac{l}{AZ^*} = \frac{l}{AZ'} + j \frac{l}{AZ''}, \quad (3.2.2)$$

where  $A$  and  $l$  are the contact area and the thickness of the pellets, respectively.

The complex electric modulus,  $M^*$ , was determined from Eqs. 3.2.3 and 3.2.4, which are related to complex conductivity and permittivity, respectively, as follows:

$$\epsilon^* = \epsilon'' - j\epsilon' = \frac{\sigma''}{\omega \epsilon_0} - j \frac{\sigma'}{\omega \epsilon_0} \quad (3.2.3)$$

$$M^* = \frac{1}{\epsilon^*} = \frac{1}{(\epsilon' - j\epsilon'')} = M' + jM'' = \frac{\epsilon'}{(\epsilon')^2 + (\epsilon'')^2} + j \frac{\epsilon''}{(\epsilon')^2 + (\epsilon'')^2}, \quad (3.2.4)$$

where  $\omega$  ( $= 2\pi f$ ) is a radial frequency expressed in radians/second parameter and  $\epsilon_0$  is the permittivity of free space.

For galvanostatic cycling tests, the Li-In |  $\text{Li}_{5.5}\text{PS}_{4.5}\text{Cl}_{1.5}$  | 50( $\text{Li}_2\text{S}$ -CaS)-40  $\text{Li}_{5.5}\text{PS}_{4.5}\text{Cl}_{1.5}$ -10VGCF cells were assembled as follows. First, 80 mg of  $\text{Li}_{5.5}\text{PS}_{4.5}\text{Cl}_{1.5}$  powder was filled with a PEEK with two stainless-steel rods, followed by a uniaxial pressure of 256 MPa to form pellets with diameters of ~10.0 mm at room temperature. Then, the cathodes were spread over one side of the SE layer and pressed under 256 MPa at room temperature. Indium and lithium foils were placed on the other side of the SE layer and pressed under 90 MPa at room temperature. The cells rested for 1 h before galvanostatic cycling testing. The fabricated ASLSBs were tested under 0.05C in a voltage range of 0.6-3.0 V (vs Li-In) at 30 °C. If not otherwise noted, capacities are given as values normalized by the weight of  $\text{Li}_2\text{S}$ .



### 3.2.3 Structural characterization

Figure 3.2.1a shows the XRD patterns of  $(100-x)\text{Li}_2\text{S}\cdot x\text{CaS}$  with Si powder as a standard. The XRD patterns for all samples show diffraction peaks attributed to a crystalline phase of  $\text{Li}_2\text{S}$  with the space group  $Fm-3m$ . These patterns show no change in peak position and no side reaction after adding CaS. The intensity of the peak at  $27^\circ$  decreases with an increasing CaS content, whereas the intensity of the most intense peak at  $31^\circ$  in the XRD pattern of the CaS phase increases. These experimental results indicate that  $\text{Li}_2\text{S}$ -CaS prepared by high-energy ball milling comprises a mixture of  $\text{Li}_2\text{S}$  and CaS phases. To examine lattice distortion and mean crystallite size of mechanically treated  $\text{Li}_2\text{S}$ -CaS, I performed Rietveld refinement based on XRD data. Figure 3.2.1b shows the Rietveld refinement pattern for  $80\text{Li}_2\text{S}\cdot 20\text{CaS}$ . A multi-phase crystal model, including  $\text{Li}_2\text{S}$  and CaS phases, offers R factors with good fitness, which are sufficiently low to support the extracted structural model.  $R_{\text{wp}}$ ,  $R_{\text{B}}$ , and  $R_{\text{F}}$  obtained for the  $\text{Li}_2\text{S}$  phase are 10.1%, 2.4%, and 2.0%, respectively. Figure 3.2.1c shows the mean crystallite sizes and the microstrain as a function of composition  $x$  in  $(100-x)\text{Li}_2\text{S}\cdot x\text{CaS}$ . Both the mean crystallite size and microstrain were estimated using the Williamson-Hall method. The Williamson-Hall plot for the sample with  $x = 50$  deviates from a linear relationship because of the anisotropic line broadening. The  $\text{Li}_2\text{S}$ -CaS prepared by high-energy ball milling forms nanocrystalline composites with crystallite sizes ranging from  $\sim 7$ – $31$  nm. The crystallite size shows a decreasing trend with an increasing CaS content. The microstrain of the  $\text{Li}_2\text{S}$  phase in the composites increases with the addition of CaS. Figure 3.2.2 shows FE-SEM images of  $(100-x)\text{Li}_2\text{S}\cdot x\text{CaS}$  particles ( $0 \leq x \leq 40$ ). The particle sizes of all samples are identical, which are estimated to be  $\sim 50$   $\mu\text{m}$ . The particle morphology is rougher with increasing CaS content. On the other hand, no calcium atoms were detected on the particle surface of the  $\text{Li}_2\text{S}$ -CaS doping from EDS mapping. This experimental result indicates that the  $\text{Li}_2\text{S}$ -CaS forms nanocomposite particles covered with the  $\text{Li}_2\text{S}$  phase.

### 3.2.4 Complex impedance spectroscopy

Figure 3.2.3a shows the real part  $\sigma'$  of the complex conductivity of  $80\text{Li}_2\text{S}\cdot 20\text{CaS}$  as a function of frequency. At lower frequencies, the impedance spectra of obtained nanocrystalline samples demonstrate an obvious DC plateau, which indicates long-range ion transport.<sup>32</sup> The electronic conductivity of  $\text{Li}_2\text{S}$  is lower than the ionic conductivity by at least two orders of magnitude in the temperature range from 30 to 450  $^\circ\text{C}$ ; thus, the observed DC plateau is attributed to ion transport.<sup>32</sup> The frequency-dependent dispersive region is observed at a higher frequency. Frequently, this observation has been interpreted as a fingerprint of the forward and backward jumps of carriers involving a short-length scale.<sup>33,34</sup> This suggests that the carrier repeats the polarization and its relaxation at a stable site for the carrier. A higher temperature allows for long-

range ion transport in samples over a broader frequency range. In the high-frequency region, the frequency dependence of conductivity obeys Jonscher's power law,<sup>35</sup> i.e.,  $\sigma \propto \omega^n$  where  $\omega$  is the angular frequency and exponent  $n$  is the degree of interaction between mobile ions as well as the lattice around them. Most ionic conducting compounds demonstrated no deviation from a value between 0.6 and 1.0 of exponent  $n$ .<sup>35</sup> However, the exponent  $n$  demonstrates a value of  $>1$  in 80Li<sub>2</sub>S·20CaS at lower temperatures than 90 °C. Furthermore, dispersive behavior in pure Li<sub>2</sub>S yields an exponent  $n$  of 1.2 at a temperature from 130 to 170 °C (Figure 3.2.3b). The higher exponent  $n$  may have originated from the migration of carriers from the occupied site to other sites via quantum mechanical tunneling between asymmetric double-well potentials.<sup>36,37</sup> This finding is consistent with the previous computational results that Li ions in the Li<sub>2</sub>S crystal exist in isolated tetrahedral sites in the face-centered cubic sulfur framework.<sup>38</sup> In contrast, the 80Li<sub>2</sub>S·20CaS demonstrates an exponent  $n$  of 0.63 at 110 °C. The power law exponent  $n$  is related to the effective dimension of ion diffusion pathways. The exponent of the 80Li<sub>2</sub>S·20CaS indicates the presence of 3D Li-ion pathways in the structure.<sup>39</sup> All samples follow the Arrhenius equation shown in Eq. 3.2.5:

$$\sigma_{DC}T = \sigma_0 \exp\left(-\frac{E_{a,DC}}{k_B T}\right), \quad (3.2.5)$$

where  $\sigma_{DC}$  is the DC conductivity of the samples,  $T$  is the temperature,  $\sigma_0$  is the pre-exponential,  $E_{a,DC}$  is the activation energy, and  $k_B$  is the Boltzmann constant. Figure 3.2.3c shows the DC conductivity of the dependence temperature in (100- $x$ )Li<sub>2</sub>S· $x$ CaS. The ionic conductivity for Li<sub>2</sub>S is highly dependent on the content of CaS, an insulator for Li ion. 80Li<sub>2</sub>S·20CaS demonstrates the highest conductivity of  $1.4 \times 10^{-4}$  S cm<sup>-1</sup> at 150 °C among the prepared samples; this value is two orders of magnitude higher than that of the milled pure Li<sub>2</sub>S ( $2.1 \times 10^{-6}$  S cm<sup>-1</sup>). This improvement could be attributed to the enhanced ion transport in the interface between the Li<sub>2</sub>S and CaS phases involving nanocrystallite sizes, i.e., the nanoionics.<sup>40-</sup>  
<sup>43</sup> The conductivity of (100- $x$ )Li<sub>2</sub>S· $x$ CaS demonstrates a decreasing trend in the sample with an increasing CaS content from 20 to 50 mol%, which is assumed to have caused a discontinuity in the conduction region in nanocomposites as the CaS insulator content increased. Therefore, the optimal composition for conductivity in nanocomposites is determined by the relationships between the enhancement of local conduction at the interface and the continuity of the conduction region. Figure 3.2.3d shows the activation energy and pre-exponential factor extracted from the Arrhenius plots in (100- $x$ )Li<sub>2</sub>S· $x$ CaS. Both the activation energy,  $E_a$ , and the pre-exponential factor,  $\sigma_0$ , increase in samples with the CaS content  $x$  between 0 and 20. Based on the hopping theory, the pre-exponential factor is expressed in Eq. 3.2.6:

$$\sigma_0 = \frac{nq^2 a_0^2 v_0 z}{6k_B T}, \quad (3.2.6)$$

where,  $n$  is the total density of charge carriers,  $q$  is the charge of the mobile ion,  $a_0$  is the jump distance, and geometrical factor  $z$  that considers the presence of possible cross-correlation in the diffusion (including the Haven ratio  $H_R$  which is the ratio between the tracer and charge diffusion coefficient), and  $v_0$  corresponds to the frequency where  $\sigma'(f)$  crosses over from power law to DC.<sup>39</sup> The pre-exponential factor of 90Li<sub>2</sub>S·10CaS is 26-fold that of pure Li<sub>2</sub>S, and  $v_0$  of 90Li<sub>2</sub>S·10CaS is 14-fold that of pure Li<sub>2</sub>S. This fact implies that the increase in  $v_0$  is the primary reason for the increase in the pre-exponential factor. Thus, the formation of the Li<sub>2</sub>S–CaS nanocomposites increases the rate of successful jumps in mobile cations, leading to the enhancement of the ionic conductivity. The conductivity for a broad range of inorganic materials often increases with a reduction in activation energy, whereas the conductivity of Li<sub>2</sub>S–CaS increases with increasing activation energy. This is consistent with the results observed in Na<sub>3–2x</sub>Ca<sub>x</sub>PS<sub>4</sub> and Li<sub>3–2x</sub>Ca<sub>x</sub>PS<sub>4</sub> as superionic conductors.<sup>27,30</sup> Moon et al. reported that high conductivities and activation energies in Na<sub>3–2x</sub>Ca<sub>x</sub>PS<sub>4</sub> were attributed to an impediment caused by the increased energy barriers close to Ca ions in the conduction pathways for the carrier.<sup>27</sup> Therefore, high activation energy and conductivity in Li<sub>2</sub>S–CaS nanocomposites can be described by the notion that the ion transport properties are governed by the conduction of mobile Li ions near the interface with the CaS nanocrystalline. In the sample with the CaS content  $x$  in the range between 20 and 50, the activation energy decreases. The decreased activation energy for ion conduction might be attributed to a strong amorphization for the Li<sub>2</sub>S phase, which is favorable for ion transport. The relative densities of the pellets of Li<sub>2</sub>S–CaS composites show a decreasing trend with the addition of CaS (Table 3.2.1). This result suggests that the CaS phase in Li<sub>2</sub>S–CaS composites shows poor mechanical deformability.

### 3.2.5 Electric modulus analysis

The investigation of dielectric peaks has long been an effective technique for examining microscopic motion in amorphous solids.<sup>36</sup> Recently, an electric modulus analysis revealed ion dynamics in crystalline solid electrolytes.<sup>44–46</sup> To establish quantitative relationships between the activation energy for conduction and relaxation in (100– $x$ )Li<sub>2</sub>S· $x$ CaS, I investigated based on complex electric modulus formalism. Figure 3.2.4a shows the imaginary part of electric modulus,  $M''$ , at different temperatures versus frequency in 90Li<sub>2</sub>S·10CaS. The relaxation peaks appear in all samples, and their positions shift toward higher frequencies with increasing temperature. The relaxation peak shows a transition from the overall averaged long-range to the short-range carrier migration, which corresponds to the relaxation frequency,  $f_{\max}$ . The mean relaxation time,  $\tau$ , is determined from the  $\tau = 1/2\pi f_{\max}$  relationship and follows the Arrhenius equation in Eq. 3.2.7 as

follows:

$$\tau = \tau_0 \exp\left(-\frac{E_{a,\tau}}{k_B T}\right), \quad (3.2.7)$$

where  $\tau_0$  is the relaxation time. Figure 3.2.4b shows the plot of the variation of  $\log(\tau_M^{-1})$  versus inverse temperature for the  $(100-x)\text{Li}_2\text{S} \cdot x\text{CaS}$ . Figure 3.2.4c shows activation energy for electrical relaxation and DC conductivity calculated from Arrhenius plots in Figure 3.2.3c and 3.2.4b. Despite an increase in activation energy,  $E_{a,DC}$ , for DC conductivity, the activation energy,  $E_{a,\tau}$ , for the relaxation time is maintained in the sample with CaS content  $x$  from 0 to 20. In  $80\text{Li}_2\text{S} \cdot 20\text{CaS}$ , the  $E_{a,\tau}$  value is observably lower than the  $E_{a,DC}$  value. The relaxation process indicates the hopping energy of carriers between localized states, whereas the conduction process is affected by long-range ion transport, including the contribution of the interface between  $\text{Li}_2\text{S}$  and CaS. Hence, long-range ion transport with high activation energy in  $80\text{Li}_2\text{S} \cdot 20\text{CaS}$  should be explained by the increase in the energy barrier near the interface between the  $\text{Li}_2\text{S}$  and CaS nanocrystallines.

### 3.2.6 Electrochemical redox reaction

I evaluated the electrochemical performance of the cell using the novel  $\text{Li}_2\text{S}$ -CaS cathode materials with improved ionic conductivity and revealed the effect of the unique conduction behavior of  $\text{Li}_2\text{S}$ -CaS on the redox reaction. Figure 3.2.5 shows voltage profiles of ASLSBs using  $(100-x)\text{Li}_2\text{S} \cdot x\text{CaS}$  cathode materials ( $x = 0, 5, 10, \text{ and } 15$ ). The first discharge capacities are  $441 \text{ mAh g}^{-1}$  for  $\text{Li}_2\text{S}$ ,  $518 \text{ mAh g}^{-1}$  for  $95\text{Li}_2\text{S} \cdot 5\text{CaS}$ ,  $509 \text{ mAh g}^{-1}$  for  $90\text{Li}_2\text{S} \cdot 10\text{CaS}$ , and  $651 \text{ mAh g}^{-1}$  for  $85\text{Li}_2\text{S} \cdot 15\text{CaS}$ . The cells using the  $\text{Li}_2\text{S}$  with the addition of CaS show higher capacity than the intrinsic  $\text{Li}_2\text{S}$ . This improvement with the addition of CaS should be originated from the increased ionic conductivity of cathode materials. The charge/discharge capacities of all cells increase with each cycle, showing  $529 \text{ mAh g}^{-1}$  for  $\text{Li}_2\text{S}$ ,  $750 \text{ mAh g}^{-1}$  for  $95\text{Li}_2\text{S} \cdot 5\text{CaS}$ ,  $621 \text{ mAh g}^{-1}$  for  $90\text{Li}_2\text{S} \cdot 10\text{CaS}$ , and  $819 \text{ mAh g}^{-1}$  for  $85\text{Li}_2\text{S} \cdot 15\text{CaS}$  after 15 cycles. In the cells using  $95\text{Li}_2\text{S} \cdot 5\text{CaS}$  and  $85\text{Li}_2\text{S} \cdot 15\text{CaS}$ , the capacity normalized by the weight of the cathode composite is higher than the  $\text{Li}_2\text{S}$ . The increased capacity during the initial charge/discharge process may be attributed to the reversible redox activity of the degradation product for SEs filled within the cathode composite.<sup>47-49</sup> The  $\text{Li}_{5.5}\text{PS}_{4.5}\text{Cl}_{1.5}$  SEs mixed with VGCF as an electron conductive additive offer the electrochemical activity at the operating voltage of ASLSBs (Figure 3.2.6a), although argyrodite-type SEs without carbon are kinetic stability within a wide range of electrode potentials.<sup>50</sup> This electrochemical reaction involves a reduction reaction at  $\sim 1.4 \text{ V}$  vs Li-In and two oxidation reactions at  $\sim 1.8$  and  $2.3 \text{ V}$  vs Li-In (Figure 3.2.6b). The finding is consistent with previous studies on electrochemical redox behaviors of  $\text{Li}_6\text{PS}_5\text{Cl}$  SEs.<sup>51,52</sup>

The redox reaction involving the decomposition of SEs will cause some confusion in the electrochemical redox reactions of ASLSBs. To clarify the redox reaction, I analyzed the differential capacity curves of ASLSBs using each cathode material (Figure 3.2.7). The calculated curves show a definite oxidation peak at  $\sim 1.8$  V vs Li-In, an oxidation peak observed in the first charge, and two reduction peaks. Additionally, a slight shoulder peak appears at  $\sim 2.3$  V vs Li-In in all of the samples, as seen in the magnified view. A conversion reaction from solid to solid in ASLSBs commonly provides a redox reaction with a single step of  $16\text{Li}^+ + \text{S}_8 + 16\text{e}^- \rightleftharpoons 8\text{Li}_2\text{S}$ . This is different from Li-S batteries using liquid electrolytes, in which a reduction reaction occurs with two steps through the solvation process of lithium polysulfides.<sup>53,54</sup> The reduction peak at  $\sim 1.3$  V vs Li-In and the oxidation shoulder peak at  $\sim 2.3$  V vs Li-In in the differential capacity curves should be delivered from the redox activity of the component other than the cathode material, that is the degradation product from SEs. The intensity of reduction peak at 1.3 V vs Li-In enhances with each cycle, which points to the emphasized contribution of the degradation product. Particularly, the cells using  $95\text{Li}_2\text{S}\cdot 5\text{CaS}$  and  $85\text{Li}_2\text{S}\cdot 15\text{CaS}$  show a huge contribution from the degradation product. This might lead to the improvement of overall electrochemical properties in these cells. On the other hand, the reduction peak at  $\sim 1.2$  V vs Li-In and the oxidation peak at  $\sim 1.8$  V vs Li-In are attributed to the electrochemical redox reaction of  $16\text{Li}^+ + \text{S}_8 + 16\text{e}^- \rightleftharpoons 8\text{Li}_2\text{S}$ . Sulfide SEs in the cathode decompose through the oxidation reaction; thus, the  $\text{Li}_2\text{S}$  and sulfide SEs in the cathode are simultaneously oxidated in the first charging process.

In addition to these redox peaks, a reduction peak at 1.7 V vs Li-In newly appears in the cell using  $90\text{Li}_2\text{S}\cdot 10\text{CaS}$  cathode material. Such reduction process with two steps is the same as a typical voltage profile of Li-S batteries using liquid electrolytes.<sup>54</sup> Galvanostatic cycling in Li-In |  $90\text{Li}_2\text{S}\cdot 10\text{CaI}_2$  |  $90\text{Li}_2\text{S}\cdot 10\text{CaS}$  cell shows the voltage profile as if the shuttle effect occurred, whereas Li-In |  $90\text{Li}_2\text{S}\cdot 10\text{CaI}_2$  |  $85\text{Li}_2\text{S}\cdot 15\text{CaS}$  cell shows a typical voltage profile of ASLSBs with a high overpotential (Figure 3.2.8). In short, the cell with the  $90\text{Li}_2\text{S}\cdot 10\text{CaS}$  cathode material shows a similar battery behavior as liquid Li-S batteries, characterized by the shuttle effect and the two discharging plateaus. Liquid Li-S batteries form the solvation structure that changes the  $\text{Li}^+\text{-S}^{2-}$  interaction for the electrochemical redox process. Based on a quantitative relationship between the activation energy for conduction and relaxation, I have revealed that the  $\text{Li}_2\text{S}\text{-CaS}$  composites shows higher activation energy for long-range ion transport than the hopping of carriers at localized states. This phenomenon was explained by the high activation barriers near the interface of the CaS nanocrystalline. This interface effect may vary the  $\text{Li}^+\text{-S}^{2-}$  interaction for the electrochemical redox process in the  $90\text{Li}_2\text{S}\cdot 10\text{CaS}$ , as in the liquid Li-S battery.

### 3.2.7 Conclusions

Our study reports the influence of CaS and  $\text{CaX}_2$  ( $X = \text{F}, \text{Cl}, \text{Br}, \text{and I}$ ) doping on the ion transport

properties of  $\text{Li}_2\text{S}$ . The  $\text{Li}_2\text{S}$ - $\text{CaS}$  composites involve crystallite sizes ranging from 7 to 31 nm, and demonstrated higher conductivity and activation energy for ion transport than the milled pure  $\text{Li}_2\text{S}$ . I demonstrate the quantitative relationship between the activation energy for conduction and relaxation in  $(100-x)\text{Li}_2\text{S}\cdot x\text{CaS}$ , based on complex conductivity and electric modulus formalism. In  $80\text{Li}_2\text{S}\cdot 20\text{CaS}$ ,  $E_{a,\tau}$  values are lower than  $E_{a,DC}$  values. This suggests that long-range ion transport in the sample involves higher activation energy compared with the hopping of carriers at localized states, which should be influenced by the increase in energy barriers near the interface between the  $\text{Li}_2\text{S}$  and  $\text{CaS}$  nanocrystallines. The fabricated  $\text{Li}_2\text{S}$ - $\text{CaS}$  cathodes exhibit improved cell performance over the intrinsic  $\text{Li}_2\text{S}$  and a high capacity of  $819 \text{ mAh g}^{-1}$  in the cell using  $85\text{Li}_2\text{S}\cdot 15\text{CaS}$  cathode after 15 cycles. The differential capacity curves of the cell using  $\text{Li}_2\text{S}$ - $\text{CaS}$  reveal the electrochemical redox reactions separating the contributions of sulfide solid electrolytes and cathode materials. These results indicate a large contribution of the degradation products from SEs during the charge/discharge cycle.

## References

- (1) Eftekhari, A.; Kim, D. W. Cathode Materials for Lithium-Sulfur Batteries: A Practical Perspective. *J. Mater. Chem. A* **2017**, *5*, 17734–17776.
- (2) Hayashi, A.; Ohtomo, T.; Mizuno, F.; Tadanaga, K.; Tatsumisago, M. All-Solid-State Li/S Batteries with Highly Conductive Glass-Ceramic Electrolytes. *Electrochem. Commun.* **2003**, *5*, 701–705.
- (3) Hakari, T.; Hayashi, A.; Tatsumisago, M. Li<sub>2</sub>S-Based Solid Solutions as Positive Electrodes with Full Utilization and Superlong Cycle Life in All-Solid-State Li/S Batteries. *Adv. Sustain. Syst.* **2017**, *1*, 1700017–1700023.
- (4) Fujita, Y.; Hakari, T.; Sakuda, A.; Deguchi, M.; Kawasaki, Y.; Tsukasaki, H.; Mori, S.; Tatsumisago, M.; Hayashi, A. Li<sub>2</sub>S-LiI Solid Solutions with Ionic Conductive Domains for Enhanced All-Solid-State Li/S Batteries. *ACS Appl. Energy Mater.* **2022**, *5*, 9429–9436.
- (5) Shigedomi, T.; Fujita, Y.; Kishi, T.; Motohashi, K.; Tsukasaki, H.; Nakajima, H.; Mori, S.; Tatsumisago, M.; Sakuda, A.; Hayashi, A. Li<sub>2</sub>S-V<sub>2</sub>S<sub>3</sub>-LiI Bifunctional Material as the Positive Electrode in the All-Solid-State Li/S Battery. *Chem. Mater.* **2022**, *34*, 9745–9752.
- (6) Wu, J.; Liu, S.; Han, F.; Yao, X.; Wang, C. Lithium/Sulfide All-Solid-State Batteries Using Sulfide Electrolytes. *Adv. Mater.* **2021**, *33*, 2000751–2000781.
- (7) Sakuda, A.; Sato, Y.; Hayashi, A.; Tatsumisago, M. Sulfur-Based Composite Electrode with Interconnected Mesoporous Carbon for All-Solid-State Lithium–Sulfur Batteries. *Energy Technol.* **2019**, *7*, 1900077–1900081.
- (8) Jiang, H.; Han, Y.; Wang, H.; Zhu, Y.; Guo, Q.; Jiang, H.; Zheng, C.; Xie, K. Facile Synthesis of a Mixed-Conductive Li<sub>2</sub>S Composites for All-Solid-State Lithium-Sulfur Batteries. *Ionics* **2020**, *26*, 4257–4265.
- (9) Zhang, W.; Zhang, Y.; Peng, L.; Li, S.; Wang, X.; Cheng, S.; Xie, J. Elevating Reactivity and Cyclability of All-Solid-State Lithium-Sulfur Batteries by the Combination of Tellurium-Doping and Surface Coating. *Nano Energy* **2020**, *76*, 105083–105090.
- (10) Nagao, M.; Hayashi, A.; Tatsumisago, M. High-Capacity Li<sub>2</sub>S-Nanocarbon Composite Electrode for All-Solid-State Rechargeable Lithium Batteries. *J. Mater. Chem.* **2012**, *22*, 10015–10020.
- (11) Yao, X.; Huang, N.; Han, F.; Zhang, Q.; Wan, H.; Mwizerwa, J. P.; Wang, C.; Xu, X. High-Performance All-Solid-State Lithium–Sulfur Batteries Enabled by Amorphous Sulfur-Coated Reduced Graphene Oxide Cathodes. *Adv. Energy Mater.* **2017**, *7*, 1602923–1602931.
- (12) Suzuki, K.; Mashimo, N.; Ikeda, Y.; Yokoi, T.; Hirayama, M.; Kanno, R. High Cycle Capability of All-Solid-State Lithium-Sulfur Batteries Using Composite Electrodes by Liquid-Phase and Mechanical Mixing. *ACS Appl. Energy Mater.* **2018**, *1* (6), 2373–2377.

- (13) Umeshbabu, E.; Zheng, B.; Zhu, J.; Wang, H.; Li, Y.; Yang, Y. Stable Cycling Lithium-Sulfur Solid Battery with Enhanced Li/Li<sub>10</sub>GeP<sub>2</sub>S<sub>12</sub> Solid Electrolyte Interface Stability **2019**, *11*, 18436–18447.
- (14) Han, Q.; Li, X.; Shi, X.; Zhang, H.; Song, D.; Ding, F.; Zhang, L. Outstanding Cycle Stability and Rate Capabilities of the All-Solid-State Li-S Battery with a Li<sub>7</sub>P<sub>3</sub>S<sub>11</sub> Glass-Ceramic Electrolyte and a Core-Shell S@BP2000 Nanocomposite. *J. Mater. Chem. A* **2019**, *7*, 3895–3902.
- (15) Wu, Z.; Chen, S.; Yu, C.; Wei, C.; Peng, L.; Wang, H. L.; Cheng, S.; Xie, J. Engineering High Conductive Li<sub>7</sub>P<sub>2</sub>S<sub>8</sub>I via Cl- Doping for All-Solid-State Li-S Batteries Workable at Different Operating Temperatures. *Chem. Eng. J.* **2022**, *442*, 136346–136355.
- (16) Wang, S.; Zhang, Y.; Zhang, X.; Liu, T.; Lin, Y. H.; Shen, Y.; Li, L.; Nan, C. W. High-Conductivity Argyrodite Li<sub>6</sub>PS<sub>5</sub>Cl Solid Electrolytes Prepared via Optimized Sintering Processes for All-Solid-State Lithium-Sulfur Batteries. *ACS Appl. Mater. Interfaces* **2018**, *10*, 42279–42285.
- (17) Wei, C.; Yu, C.; Peng, L.; Zhang, Z.; Xu, R.; Wu, Z.; Liao, C.; Zhang, W.; Zhang, L.; Cheng, S.; Xie, J. Tuning Ionic Conductivity to Enable All-Climate Solid-State Li-S Batteries with Superior Performances. *Mater. Adv.* **2022**, *3*, 1047–1054.
- (18) Ohno, S.; Koerver, R.; Dewald, G.; Rosenbach, C.; Titscher, P.; Steckermeier, D.; Kwade, A.; Janek, J.; Zeier, W. G. Observation of Chemomechanical Failure and the Influence of Cutoff Potentials in All-Solid-State Li-S Batteries. *Chem. Mater.* **2019**, *31*, 2930–2940.
- (19) Liu, M.; Wang, C.; Zhao, C.; van der Maas, E.; Lin, K.; Arszewski, V. A.; Li, B.; Ganapathy, S.; Wagemaker, M. Quantification of the Li-Ion Diffusion over an Interface Coating in All-Solid-State Batteries via NMR Measurements. *Nat. Commun.* **2021**, *12*, 5943–5952.
- (20) Han, F.; Yue, J.; Fan, X.; Gao, T.; Luo, C.; Ma, Z.; Suo, L.; Wang, C. High-Performance All-Solid-State Lithium-Sulfur Battery Enabled by a Mixed-Conductive Li<sub>2</sub>S Nanocomposite. *Nano Lett.* **2016**, *16*, 4521–4527.
- (21) Jiang, J.; Fan, Q.; Chou, S.; Guo, Z.; Konstantinov, K.; Liu, H.; Wang, J. Li<sub>2</sub>S-Based Li-Ion Sulfur Batteries: Progress and Prospects. *Small* **2021**, *17*, 1903934–1903957.
- (22) Kaiser, M. R.; Han, Z.; Liang, J.; Dou, S. X.; Wang, J. Lithium Sulfide-Based Cathode for Lithium-Ion/Sulfur Battery: Recent Progress and Challenges. *Energy Storage Mater.* **2019**, *19*, 1–15.
- (23) Nagata, H.; Akimoto, J. Excellent Deformable Oxide Glass Electrolytes and Oxide-Type All-Solid-State Li<sub>2</sub>S-Si Batteries Employing These Electrolytes. *ACS Appl. Mater. Interfaces* **2021**, *13*, 35785–35794.
- (24) Phuc, N. H. H.; Takaki, M.; Kazuhiro, H.; Hiroyuki, M.; Atsunori, M. Dual Effect of MgS



- Addition on Li<sub>2</sub>S Ionic Conductivity and All-Solid-State Li–S Cell Performance. *SN Appl. Sci.* **2020**, *2*, 1803–1811.
- (25) Takeuchi, T.; Kageyama, H.; Nakanishi, K.; Ogawa, M.; Ohta, T.; Sakuda, A.; Sakaebe, H.; Kobayashi, H.; Ogumi, Z. Preparation of Li<sub>2</sub>S-FeS<sub>x</sub> Composite Positive Electrode Materials and Their Electrochemical Properties with Pre-Cycling Treatments. *J. Electrochem. Soc.* **2015**, *162*, A1745–A1750.
- (26) Phuc, N. H. H.; Takaki, M.; Hiroyuki, M.; Atsunori, M. Preparation of Li<sub>2-3x</sub>Al<sub>x</sub>S for All-Solid-State Li-S Battery. *Front. Energy Res.* **2021**, *8*, 606023–606029.
- (27) Moon, C. K.; Lee, H.-J.; Kern, H.; Park, H.; Kwak, J. W.; Heo, K.; Choi, H.; Yang, M.-S.; Kim, S.-T.; Hong, H.; Lee, Y.; Seok, J. Vacancy-Driven Na<sup>+</sup> Superionic Conduction in New Ca-Doped Na<sub>3</sub>PS<sub>4</sub> for All-Solid-State Na-Ion Batteries. *ACS Energy Lett.* **2018**, *3*, 2504–2512.
- (28) Adeli, P.; Bazak, J. D.; Huq, A.; Goward, G. R.; Nazar, L. F. Influence of Aliovalent Cation Substitution and Mechanical Compression on Li-Ion Conductivity and Diffusivity in Argyrodite Solid Electrolytes. *Chem. Mater.* **2021**, *33*, 146–157.
- (29) Hikima, K.; Huy Phuc, N. H.; Tsukasaki, H.; Mori, S.; Muto, H.; Matsuda, A. High Ionic Conductivity of Multivalent Cation Doped Li<sub>6</sub>PS<sub>5</sub>Cl Solid Electrolytes Synthesized by Mechanical Milling. *RSC Adv.* **2020**, *10*, 22304–22310.
- (30) Phuc, N. H. H.; Kazuhiro, H.; Hiroyuki, M.; Atsunori, M. High Ionic Conductivity of Li<sub>3-2x</sub>M<sub>x</sub>PS<sub>4</sub> (M = Ca or Mg) at High Temperature. *Solid State Ionics* **2020**, *351*, 115324–115327.
- (31) Izumi, F.; Momma, K. Three-Dimensional Visualization in Powder Diffraction. *Solid State Phenomena.* **2007**, *130*, 15–20.
- (32) Lorgier, S.; Usiskin, R. E.; Maier, J. Transport and Charge Carrier Chemistry in Lithium Sulfide. *Adv. Funct. Mater.* **2019**, *29*, 1807688–1807698.
- (33) Preishuber-Pflügl, F.; Bottke, P.; Pregartner, V.; Bitschnau, B.; Wilkening, M. Correlated Fluorine Diffusion and Ionic Conduction in the Nanocrystalline F- Solid Electrolyte Ba<sub>0.6</sub>La<sub>0.4</sub>F<sub>2.4</sub> - <sup>19</sup>F T1(ρ) NMR Relaxation vs. Conductivity Measurements. *Phys. Chem. Chem. Phys.* **2014**, *16*, 9580–9590.
- (34) Funke, K. Jump relaxation in solid electrolytes. *Prog. Solid. State Chem.* **1993**, *22*, 111–195.
- (35) Jonscher, A. K. The ‘universal’ dielectric response. *Nature* **1977**, *267*, 673–679.
- (36) Gilkoy, K. S.; Phillips, W. A. An Asymmetric Double-Well Potential Model for Structural Relaxation Processes in Amorphous Materials. *Philosophical Magazine B: Physics of Condensed Matter; Statistical Mechanics, Electronic, Optical and Magnetic Properties* **1981**, *43*, 735–746.

- (37) Elliott, S. R. Frequency-Dependent Conductivity in Ionically and Electronically Conducting Amorphous Solids. *Solid State Ionics* **1994**, *70*, 27–40.
- (38) Wang, Y.; Richards, W. D.; Ong, S. P.; Miara, L. J.; Kim, J. C.; Mo, Y.; Ceder, G. Design Principles for Solid-State Lithium Superionic Conductors. *Nat. Mater.* **2015**, *14*, 1026–1031.
- (39) Sidebottom, D. L. Dimensionality Dependence of the Conductivity Dispersion in Ionic Materials. *Phys. Rev. Lett.*, **1999**, *83*, 983–986.
- (40) Jin-Phillipp, N. Y.; Sata, N.; Maier, J.; Scheu, C.; Hahn, K.; Kelsch, M.; Rühle, M. Structures of BaF<sub>2</sub>-CaF<sub>2</sub> Heterolayers and Their Influences on Ionic Conductivity. *J. Chem. Phys.* **2004**, *120*, 2375–2381.
- (41) Ruprecht, B.; Wilkening, M.; Steuernagel, S.; Heitjans, P. Anion Diffusivity in Highly Conductive Nanocrystalline BaF<sub>2</sub>:CaF<sub>2</sub> Composites Prepared by High-Energy Ball Milling. *J. Mater. Chem.* **2008**, *18*, 5412–5416.
- (42) Tsukasaki, H.; Mori, S.; Morimoto, H.; Hayashi, A.; Tatsumisago, M. Direct Observation of a Non-Crystalline State of Li<sub>2</sub>S-P<sub>2</sub>S<sub>5</sub> Solid Electrolytes. *Sci. Rep.* **2017**, *7*, 4142–4148.
- (43) Maier, J. Defect Chemistry and Ion Transport in Nanostructured Materials Part II. Aspects of Nanoionics. *Solid State Ionics*, **2003**, *157*, 327–334.
- (44) Gombotz, M.; Wilkening, H. M. R. Fast Li Ion Dynamics in the Mechanosynthesized Nanostructured Form of the Solid Electrolyte Li<sub>3</sub>YBr<sub>6</sub>. *ACS Sustain. Chem. Eng.* **2021**, *9*, 743–755.
- (45) Prutsch, D.; Gadermaier, B.; Brandstätter, H.; Pregartner, V.; Stanje, B.; Wohlmuth, D.; Epp, V.; Rettenwander, D.; Hanzu, I.; Wilkening, H. M. R. Nuclear Spin Relaxation in Nanocrystalline β-Li<sub>3</sub>PS<sub>4</sub> Reveals Low-Dimensional Li Diffusion in an Isotropic Matrix. *Chem. Mater.* **2018**, *30*, 7575–7586.
- (46) Hanghofer, I.; Brinek, M.; Eisbacher, S. L.; Bitschnau, B.; Volck, M.; Hennige, V.; Hanzu, I.; Rettenwander, D.; Wilkening, H. M. R. Substitutional Disorder: Structure and Ion Dynamics of the Argyrodites Li<sub>6</sub>PS<sub>5</sub>Cl, Li<sub>6</sub>PS<sub>5</sub>Br and Li<sub>6</sub>PS<sub>5</sub>I. *Phys. Chem. Chem. Phys.* **2019**, *21*, 8489–8507.
- (47) Ohno, S.; Zeier, W. G. Toward Practical Solid-State Lithium–Sulfur Batteries: Challenges and Perspectives. *Acc. Mater. Res.* **2021**, *2*, 869–880.
- (48) Ohno, S.; Rosenbach, C.; Dewald, G. F.; Janek, J.; Zeier, W. G. Linking Solid Electrolyte Degradation to Charge Carrier Transport in the Thiophosphate-Based Composite Cathode toward Solid-State Lithium-Sulfur Batteries. *Adv. Funct. Mater.* **2021**, *31*, 2010620–2010633.
- (49) Hakari, T.; Nagao, M.; Hayashi, A.; Tatsumisago, M. All-Solid-State Lithium Batteries with Li<sub>3</sub>PS<sub>4</sub> Glass as Active Material. *J. Power Sources* **2015**, *293*, 721–725.

- (50) Dewald, G. F.; Ohno, S.; Kraft, M. A.; Koerver, R.; Till, P.; Vargas-Barbosa, N. M.; Janek, J.; Zeier, W. G. Experimental Assessment of the Practical Oxidative Stability of Lithium Thiophosphate Solid Electrolytes. *Chem. Mater.* **2019**, *31* (20), 8328–8337.
- (51) Tan, D. H. S.; Wu, E. A.; Nguyen, H.; Chen, Z.; Marple, M. A. T.; Doux, J. M.; Wang, X.; Yang, H.; Banerjee, A.; Meng, Y. S. Elucidating Reversible Electrochemical Redox of  $\text{Li}_6\text{PS}_5\text{Cl}$  Solid Electrolyte. *ACS Energy Lett.* **2019**, *4*, 2418–2427.
- (52) Ohno, S.; Koerver, R.; Dewald, G.; Rosenbach, C.; Titscher, P.; Steckermeier, D.; Kwade, A.; Janek, J.; Zeier, W. G. Observation of Chemomechanical Failure and the Influence of Cutoff Potentials in All-Solid-State Li-S Batteries. *Chem. Mater.* **2019**, *31*, 2930–2940.
- (53) Chen, X.; Yuan, L.; Li, Z.; Chen, S.; Ji, H.; Qin, Y.; Wu, L.; Shen, Y.; Wang, L.; Hu, J.; Huang, Y. Realizing an Applicable “Solid  $\rightarrow$  Solid” Cathode Process via a Transplantable Solid Electrolyte Interface for Lithium-Sulfur Batteries. *ACS Appl. Mater. Interfaces* **2019**, *11*, 29830–29837.
- (54) Lin, Y.; Zheng, J.; Wang, C.; Qi, Y. The Origin of the Two-Plateaued or One-Plateaued Open Circuit Voltage in Li-S Batteries. *Nano Energy* **2020**, *75*, 104915–104924.

**Table 3.2.1.** Densities of pellets ( $d_1$ ), theoretical densities ( $d_2$ ), and relative densities ( $d_1/d_2$ ) of the  $(100-x)\text{Li}_2\text{S}-x\text{CaS}$  ( $x = 10, 20, 30,$  and  $50$ ) nanocomposites.  $d_1$  was calculated from the volume measured by the dimensions of the pellet.  $d_2$  was calculated from theoretical densities of an ideal  $\text{Li}_2\text{S}$  and  $\text{CaS}$  crystal phases.

$x$	$d_1$ ( $\text{g cm}^{-3}$ )	$d_2$ ( $\text{g cm}^{-3}$ )	$d_1/d_2$ (%)
0	1.54	1.66	93.0
10	1.40	1.75	79.6
20	1.59	1.85	86.3
30	1.64	1.94	84.5
50	1.64	2.13	77.4

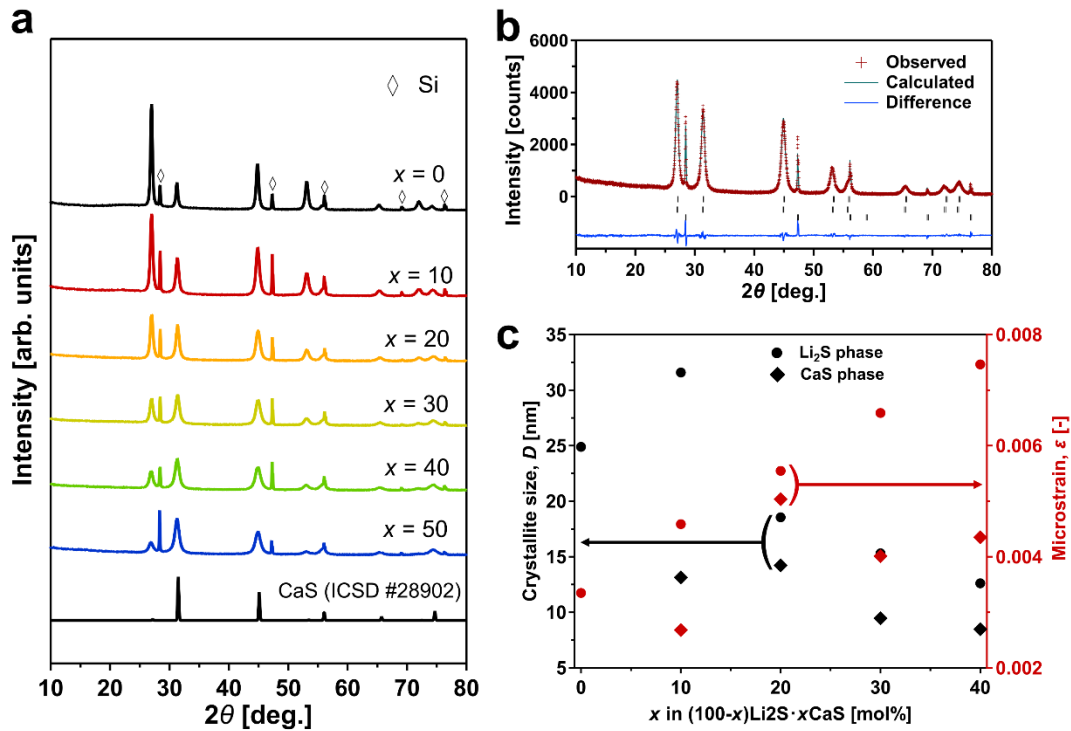


**Figure 3.2.1.** (a) The XRD patterns of  $(100-x)\text{Li}_2\text{S}\cdot x\text{CaS}$  with added Si powder. The bottom profile shows CaS as a reference. (b) The Rietveld refinement pattern for  $80\text{Li}_2\text{S}\cdot 20\text{CaS}$ . The observed diffraction intensities and calculated patterns are denoted by red plus signs and a solid green line, respectively. The blue trace at the bottom represents differences between calculated and experimental patterns. The short green bars below the observed and calculated profiles indicate the positions of the allowed Bragg reflections of Si, CaS, and  $\text{Li}_2\text{S}$  in order from the bottom. (c) The crystallite sizes and the microstrain of the  $\text{Li}_2\text{S}$  and CaS phases in  $(100-x)\text{Li}_2\text{S}\cdot x\text{CaS}$ . Circles and squares correspond to the  $\text{Li}_2\text{S}$  and CaS phases, respectively.

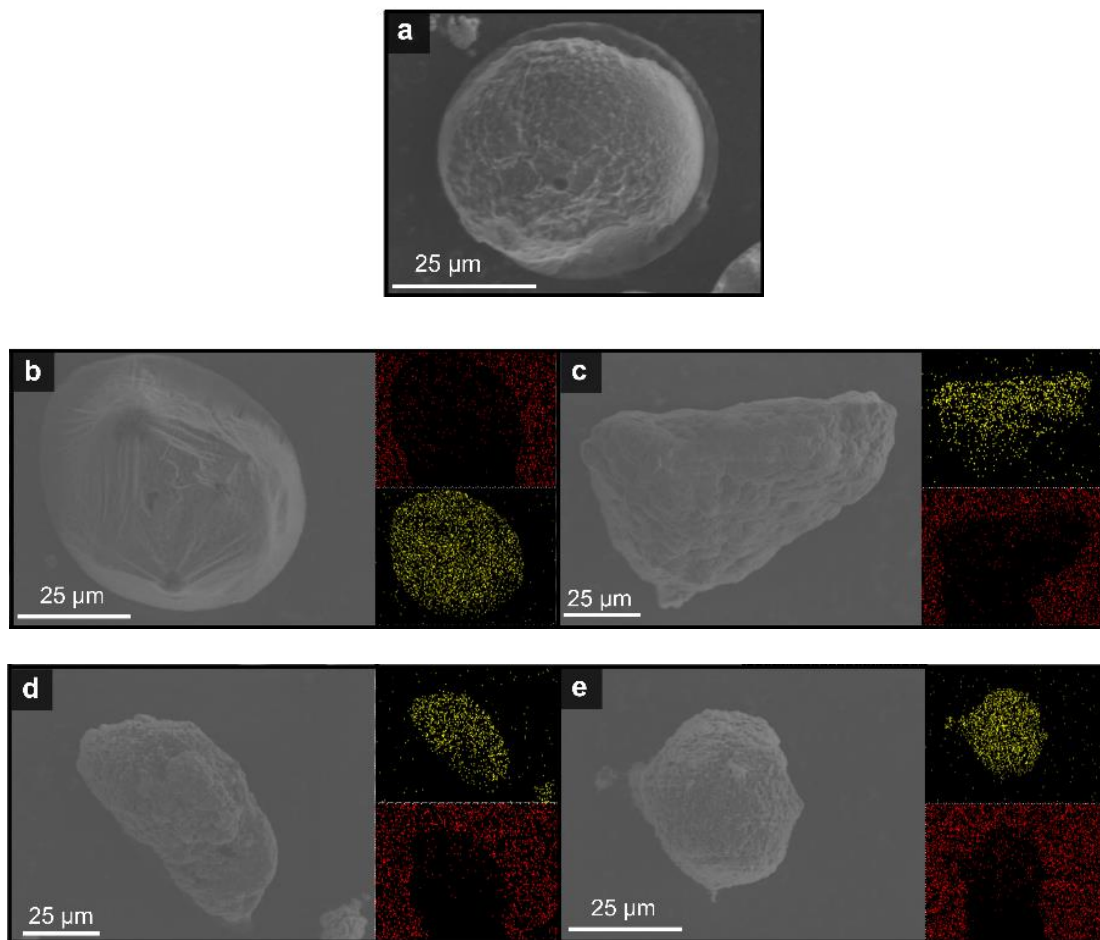


**Figure 3.2.2.** FE-SEM images of (a)  $\text{Li}_2\text{S}$ , (b)  $90\text{Li}_2\text{S}\cdot 10\text{CaS}$ , (c)  $80\text{Li}_2\text{S}\cdot 20\text{CaS}$ , (d)  $70\text{Li}_2\text{S}\cdot 30\text{CaS}$ , and (e)  $60\text{Li}_2\text{S}\cdot 40\text{CaS}$  particles.

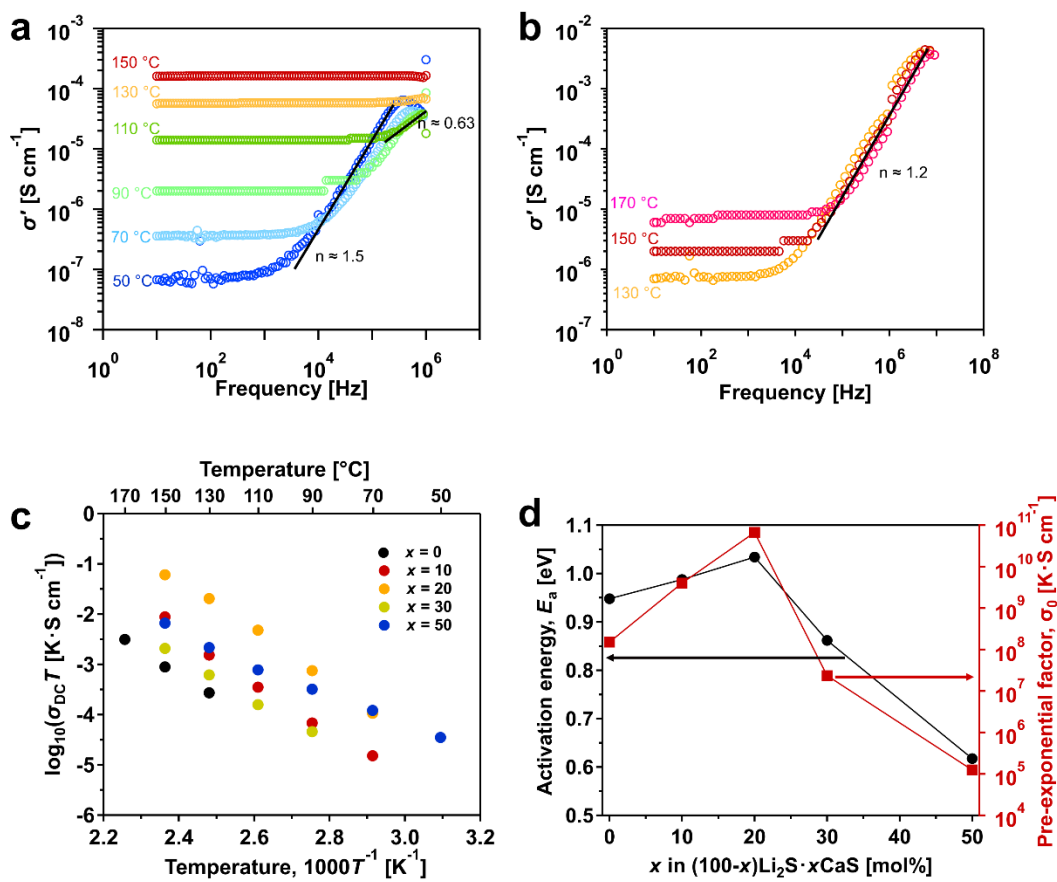


**Figure 3.2.3.** (a) Conductivity isotherms of  $80\text{Li}_2\text{S}:20\text{CaS}$  at different temperatures ranging from  $50\text{ }^\circ\text{C}$  to  $150\text{ }^\circ\text{C}$ . The solid lines represent fitting as per Jonscher's power law, i.e.,  $\sigma \propto \omega^n$  at the dispersive regime. (b) Arrhenius plots of the DC conductivities, (c) temperature dependence of ionic conductivity, and (d) activation energies and pre-exponential factors for  $(100-x)\text{Li}_2\text{S}:x\text{CaS}$  ( $0 \leq x \leq 50$ ).

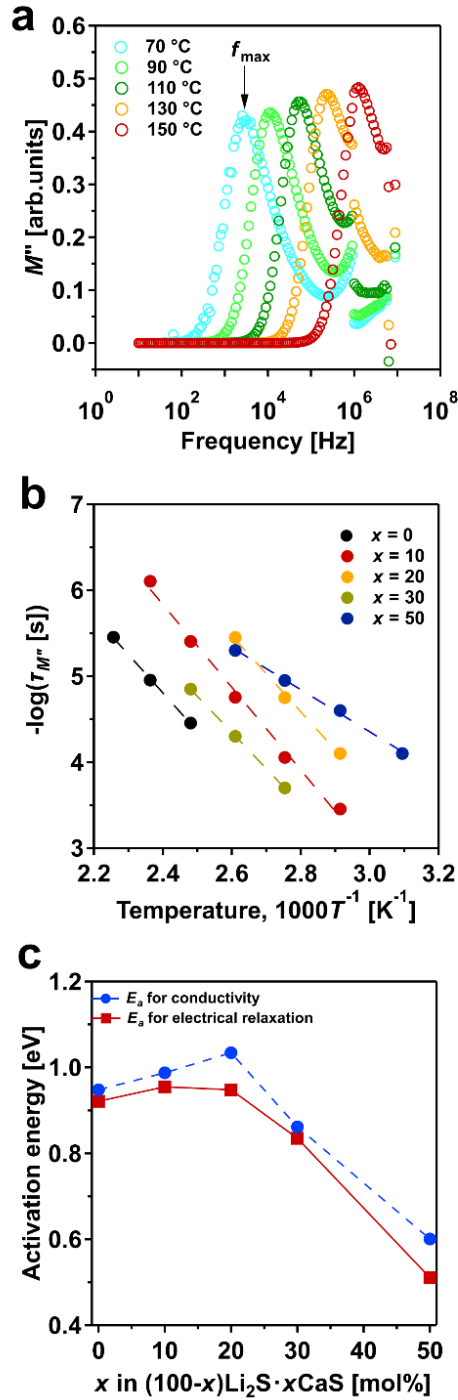


**Figure 3.2.4.** The imaginary part of the modulus,  $M''$ , versus the frequency of  $90\text{Li}_2\text{S}\cdot 10\text{CaS}$  at temperatures ranging from  $70\text{ }^\circ\text{C}$  to  $150\text{ }^\circ\text{C}$ . (b) The  $\tau_M^{-1}$  rate versus the inverse temperature of  $(100-x)\text{Li}_2\text{S}\cdot x\text{CaS}$ . Dashed lines represent the linear fit. (c) For comparison, the activation energy for electric relaxation and conduction as a function of composition  $x$  in  $(100-x)\text{Li}_2\text{S}\cdot x\text{CaS}$ .



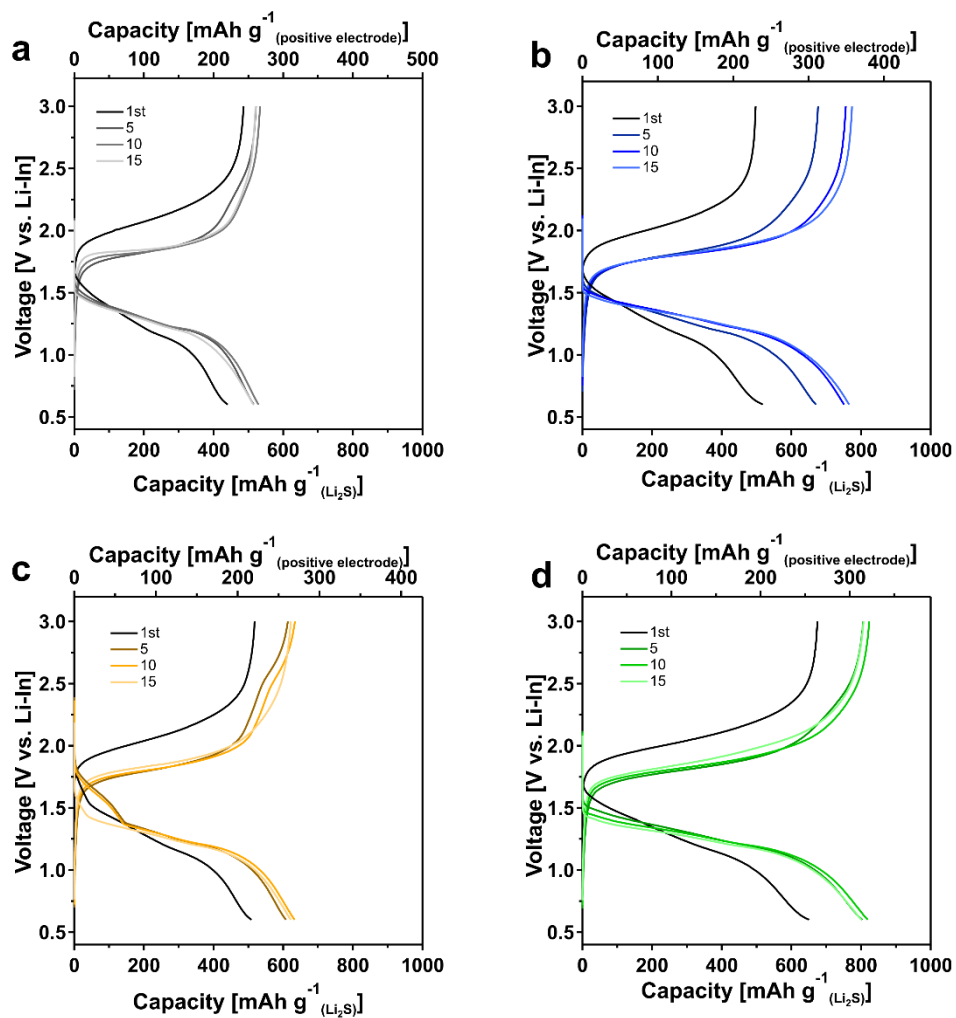


**Figure 3.2.5.** Voltage profiles of ASLSBs using (a)  $\text{Li}_2\text{S}$ , (b)  $95\text{Li}_2\text{S}\cdot 5\text{CaS}$ , (c)  $90\text{Li}_2\text{S}\cdot 10\text{CaS}$ , and (d)  $85\text{Li}_2\text{S}\cdot 15\text{CaS}$  cathode materials cycled under  $0.05\text{C}$  at  $30^\circ\text{C}$  in the voltage range of  $0.6\text{-}3.0\text{ V vs Li-In}$ .

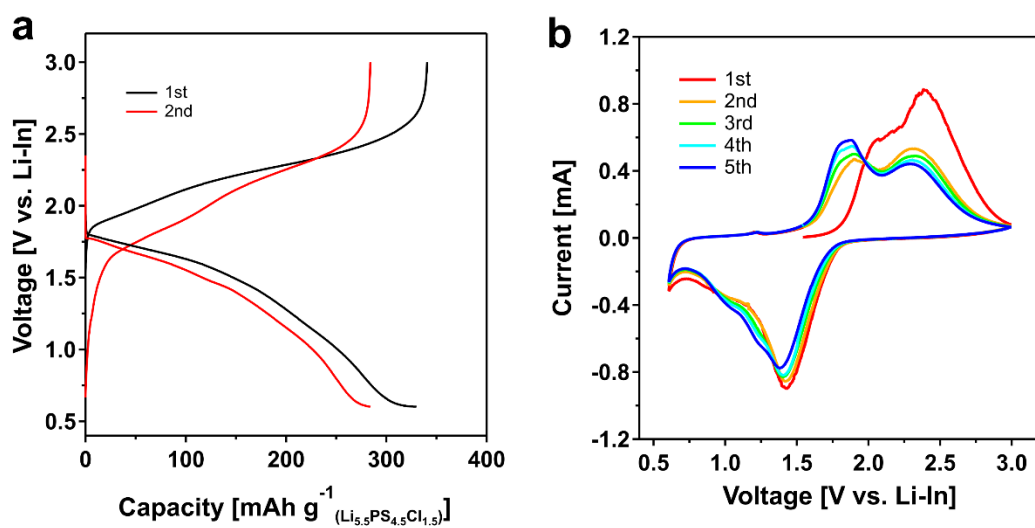


**Figure 3.2.6.** Differential capacity curves of ASLSBs using (a)  $\text{Li}_2\text{S}$ , (b)  $95\text{Li}_2\text{S}\cdot 5\text{CaS}$ , (c)  $90\text{Li}_2\text{S}\cdot 10\text{CaS}$ , and (d)  $85\text{Li}_2\text{S}\cdot 15\text{CaS}$  cathode materials cycled under 0.05C at 30 °C in the voltage range of 0.6-3.0 V vs Li-In.

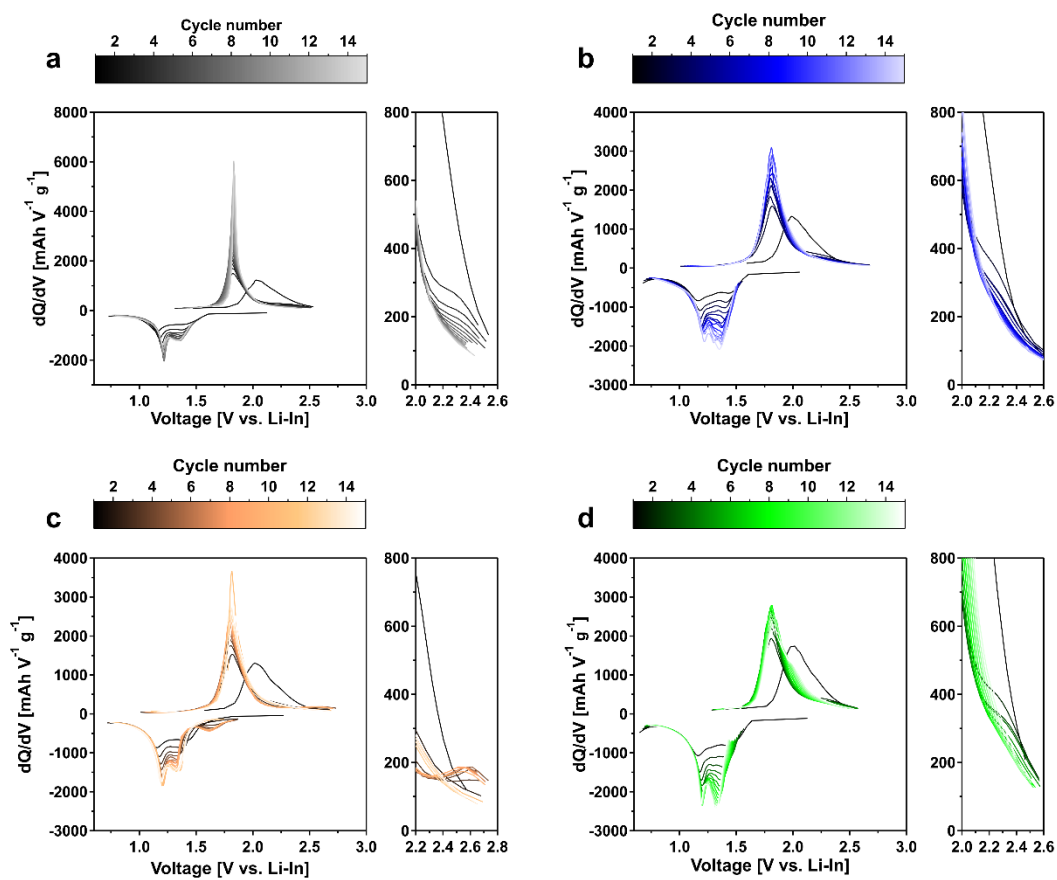


**Figure 3.2.7.** Differential capacity curves of ASLSBs using (a)  $\text{Li}_2\text{S}$ , (b)  $95\text{Li}_2\text{S} \cdot 5\text{CaS}$ , (c)  $90\text{Li}_2\text{S} \cdot 10\text{CaS}$ , and (d)  $85\text{Li}_2\text{S} \cdot 15\text{CaS}$  cathode materials cycled under 0.05C at 30 °C in the voltage range of 0.6-3.0 V vs Li-In.

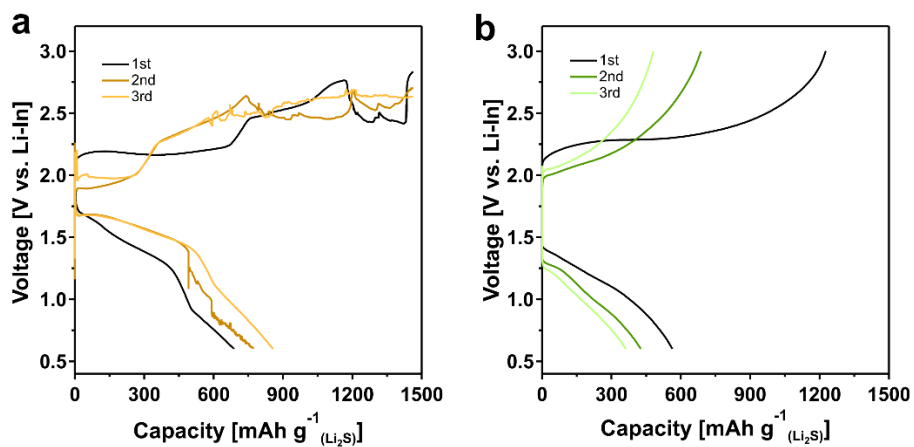


**Figure 3.2.8.** Galvanostatic voltage profiles of Li-In | 90Li<sub>2</sub>S·10CaI<sub>2</sub> | (a) 50(90Li<sub>2</sub>S·10CaS)- and (b) 50(85Li<sub>2</sub>S·15CaS)-40Li<sub>5.5</sub>PS<sub>4.5</sub>Cl<sub>1.5</sub>-10VGCF as a cathode under 0.05C at 60 °C in the voltage range of 0.6-3.0 V vs Li-In.

### 3.3 Lithium sulfide with dual-doping calcium halide

Herein, I report on the electrochemical properties of  $\text{Li}_2\text{S}-\text{CaX}_2$  ( $X = \text{F}, \text{Cl}, \text{Br}, \text{and I}$ ) prepared by high-energy ball milling. The dual doping of Ca and halogen reduces the activation energy for conduction and improves the ionic conductivity of  $\text{Li}_2\text{S}$ . The cells using the  $\text{Li}_2\text{S}-\text{CaX}_2$  ( $X = \text{Cl}, \text{Br}, \text{and I}$ ) show a higher utilization than the  $\text{Li}_2\text{S}$  cathode. Cyclic voltammetry at different scan rates demonstrated that the addition of  $\text{CaX}_2$  ( $X = \text{Cl}, \text{Br}, \text{and I}$ ) increases the Li-ion diffusion coefficient of cathode materials, which is the highest value for the  $90\text{Li}_2\text{S} \cdot 10\text{CaI}_2$  cathode material among the fabricated cathodes. In the electrochemical redox of the  $90\text{Li}_2\text{S} \cdot 10\text{CaI}_2$  cathode, an additional oxidation reaction appears at a slightly higher reaction potential than the oxidation potential of  $\text{Li}_2\text{S}$ . These electrochemical characteristics allow for excellent capacity, performance stability, and reversibility of the all-solid-state lithium-sulfur batteries using the  $90\text{Li}_2\text{S} \cdot 10\text{CaI}_2$  cathode material.

#### 3.3.1 Introduction

In Chapter 3.2, I developed the novel  $\text{Li}_2\text{S}-\text{CaS}$  cathode materials, which show improved overall cell performance than the pristine  $\text{Li}_2\text{S}$ . Nevertheless, these cathode materials have yet to achieve full utilization. The utilization is still limited by the sluggish electric conductivity of  $\text{Li}_2\text{S}$ -based cathode material. The substitution of halogen ions into  $\text{Li}_2\text{S}$  is an effective approach for delivering high utilization under a high C-rate (cycling rate) over long cycles.<sup>1</sup> Among halide-ion, I-substituted  $\text{Li}_2\text{S}$ -based cathode material achieved a high reversible capacity of  $> 1000 \text{ mAh g}^{-1}$  in ASLSBs. This superior capacity was explained by the high ionic conduction networks in  $\text{Li}_2\text{S}$  cathode. Additionally, the  $\text{Li}_2\text{S}$  with the addition of ductile  $\text{LiI}$  forms the solid phases with a high Li-ion diffusivity on the grain boundaries between the  $\text{Li}_2\text{S}$  and solid electrolyte, facilitating Li-ion transport.<sup>2</sup> Another study reported that a high catalyst activity of  $\text{LiI}$  allowed us to excellent redox kinetics and reversibility of  $\text{Li}_2\text{S}$  doped with  $\text{LiI}-\text{LiBr}$  in ASLSBs.<sup>3</sup> A systematic investigation revealed that  $\text{LiI}$  that have a higher onset oxidation voltage than that of  $\text{Li}_2\text{S}$  serve as an additive for increasing the electrochemical redox reaction kinetics.<sup>4</sup> Very recently,  $\text{Li}_2\text{S}-\text{V}_2\text{S}_3-\text{LiI}$  cathode materials prepared by a mechanochemical process show high ionic and electronic conductivity, delivering the high reversible capacity.

In this study, I prepared  $\text{Li}_2\text{S}-\text{CaX}_2$  ( $X = \text{F}, \text{Cl}, \text{Br}, \text{and I}$ ) cathode materials by high-energy ball milling and evaluated the cell performance of  $\text{Li}_2\text{S}-\text{CaX}_2$  ( $X = \text{Cl}, \text{Br}, \text{and I}$ ). Among each material system,  $90\text{Li}_2\text{S} \cdot 10\text{-CaI}_2$ ,  $80\text{Li}_2\text{S} \cdot 20\text{CaBr}_2$ ,  $85\text{Li}_2\text{S} \cdot 15\text{CaCl}_2$ , and  $95\text{Li}_2\text{S} \cdot 5\text{CaF}_2$  demonstrate the highest ionic conductivity of  $3.6 \times 10^{-5}$ ,  $1.3 \times 10^{-5}$ ,  $1.5 \times 10^{-5}$ , and  $1.8 \times 10^{-7} \text{ S cm}^{-1}$  at  $50 \text{ }^\circ\text{C}$ , respectively. These cathode materials improve the Li-ion diffusion coefficient and electronic

conductivity relative to intrinsic  $\text{Li}_2\text{S}$ , achieving high electrochemical utilization. The  $90\text{Li}_2\text{S}\cdot 10\text{CaI}_2$ , acting as a redox mediator, exhibits the highest capacity, cell stability, and reversibility of redox reactions at a high C-rate among the cathode materials examined.

### 3.3.2 Experimental methods

**Chemicals.** Lithium sulfide (99.9%, Mitsuwa),  $\text{CaF}_2$  (99.99%, Sigma-Aldrich),  $\text{CaCl}_2$  (99.99%, Sigma-Aldrich),  $\text{CaBr}_2$  (99.98%, Sigma-Aldrich),  $\text{CaI}_2$  (99.999%, Sigma-Aldrich),  $\text{LiCl}$  (99.99%, Wako Fujifilm),  $\text{P}_2\text{S}_5$  (99%, Merck), and VGCF (Vapor Grown Carbon Fiber; Showa Denko) were used without additional purification.

**Synthesis.**  $\text{Li}_2\text{S}-\text{CaX}_2$  ( $X = \text{F}, \text{Cl}, \text{Br}, \text{and I}$ ) cathode materials were prepared by high-energy ball milling. High-energy ball milling was conducted using planetary ball milling (Fritsch Pulverisete 7 Premium line) at a rotation speed of 510 rpm for 10 h.  $\text{Li}_{5.5}\text{PS}_{4.5}\text{Cl}_{1.5}$  SEs were prepared by mechanochemical reaction as follows. Lithium sulfide,  $\text{LiCl}$ , and  $\text{P}_2\text{S}_5$  were mixed at appropriate molar ratios. Then, the resultant powders were loaded in 45 ml of zirconia pots with  $\phi$  10 mm zirconia balls and subjected to ball milling with planetary ball milling (Fritsch Pulverisete 7 Premium line) at a rotation speed of 600 rpm for 20 h. The obtained precursor powders were heated at 450 °C for 2 h on a hot plate to form  $\text{Li}_{5.5}\text{PS}_{4.5}\text{Cl}_{1.5}$  SEs with an argyrodite structure.

The cathode composite electrodes were fabricated by ball milling. First, the cathode materials,  $\text{Li}_{5.5}\text{PS}_{4.5}\text{Cl}_{1.5}$  SEs, and VGCF were mixed by a mortar at a weight ratio 50:40:10, respectively. Then, the mixture powders were filled in 45 ml of zirconia pots with 35 g of zirconia balls ( $\phi$  4 mm) and subjected to ball milling with planetary ball milling (Fritsch Pulverisete 7 Premium line) at a rotation speed of 510 rpm for 10 h.

**Material characterization.** Powder XRD measurements were performed under  $2\theta = 10^\circ-80^\circ$  in a step interval of  $0.02^\circ$  at a scan rate of  $0.2^\circ \text{ min}^{-1}$  using a Rigaku Ultima IV diffractometer. An X-ray beam was generated using  $\text{CuK}\alpha$  radiation (40 kV, 30 mA). For XRD measurements, I used an XRD holder with a beryllium window (Rigaku).

**Electrochemical measurements.** The overall conductivities of the prepared  $\text{Li}_2\text{S}-\text{CaX}_2$  ( $X = \text{F}, \text{Cl}, \text{Br}, \text{and I}$ ) were determined by alternating current impedance spectroscopy (SI 1260, Solatron) in a frequency range of 1 MHz to 10 Hz under a dry Ar flow. To fabricate cells for EIS measurements, each sample (~80 mg) was filled in a holder made of PEEK with two stainless steel rods as blocking electrodes. I applied a uniaxial pressure of 256 MPa to pellets having diameters of ~10.0 mm at room temperature. For galvanostatic cycling tests, the  $\text{Li-In} \mid \text{Li}_{5.5}\text{PS}_{4.5}\text{Cl}_{1.5} \mid 50(\text{Li}_2\text{S}-\text{CaCl}_2, -\text{CaBr}_2, \text{and } -\text{CaI}_2)-40 \text{ Li}_{5.5}\text{PS}_{4.5}\text{Cl}_{1.5}-10\text{VGCF}$  cells were assembled as follow. First, 80 mg of  $\text{Li}_{5.5}\text{PS}_{4.5}\text{Cl}_{1.5}$  powder was filled with a PEEK with two

stainless-steel rods, followed by a uniaxial pressure of 256 MPa to form pellets with diameters of ~10.0 mm at room temperature. Then, the cathodes were spread over one side of the SE layer and pressed under 256 MPa at room temperature. Indium and lithium foils were placed on the other side of the SE layer and pressed under 90 MPa at room temperature. The cells rested for 1 h before galvanostatic cycling testing. The fabricated ASLSBs were tested under 0.05C in a voltage range of 0.6-3.0 V (vs Li-In) at 30 °C. If not otherwise noted, capacities are given as values normalized by the weight of Li<sub>2</sub>S. Cyclic voltammetry measurements were performed at a scan rate of 0.1-0.5 mV sec<sup>-1</sup> on an SI 1260, Solatron. Lithium-ion diffusion coefficients,  $D_{Li}$ , of the composite electrodes were determined from the Randles-Sevick equation as follows:

$$I_p = 268600n^{1.5}AD_{Li}^{\frac{1}{2}}Cv^{\frac{1}{2}} \quad (3.3.1)$$

Where,  $I_p$  is the peak current for redox reaction in the plotted CV curve,  $n$  is the number of electrons per reaction species (2 in the case of Li<sub>2</sub>S),  $A$  is the electrode area,  $C$  is the Li concentration of electrode (mol cm<sup>-3</sup>), and  $v$  is scan rate.

### 3.3.3 Structural characterization

Figure 3.3.1 shows the XRD patterns of (100- $x$ )Li<sub>2</sub>S· $x$ CaX<sub>2</sub> ( $X = F, Cl, Br, \text{ and } I$ ) added to Si power as a standard sample. The XRD patterns of (100- $x$ )Li<sub>2</sub>S· $x$ CaX<sub>2</sub> ( $X = F, Cl, Br, \text{ and } I$ ) show peaks attributed to Bragg reflection of Li<sub>2</sub>S crystalline phase with the space group  $Fm-3m$  in all the samples. The peak intensity decreases and the peak line-width broadens with an increase in CaX<sub>2</sub> ( $X = F, Cl, Br, \text{ and } I$ ) content. This suggests the disordered structure arising from the substitution of the anion. Note that lithium halide is formed in 80Li<sub>2</sub>S·20CaX<sub>2</sub> ( $X = Cl \text{ and } Br$ ) and 85Li<sub>2</sub>S·15CaI<sub>2</sub>. No change in the peak position following the addition of CaF<sub>2</sub> and CaCl<sub>2</sub> is observed, whereas the peak shifts toward a lower angle in the sample with the addition of CaBr<sub>2</sub> and CaI<sub>2</sub>. These peak shifts indicate that the lattice plane spacing increases due to the substitution of S<sup>2-</sup> in the Li<sub>2</sub>S structure by halogen with a larger ionic radius. Unsubstituted excess halogen reacted with Li ions, thus forming a lithium halide in the samples with high concentration halogen. There is no peak shift in Li<sub>2</sub>S following the addition of CaF<sub>2</sub>, despite the large difference between S<sup>2-</sup> and F<sup>-</sup> (1.84 versus 1.33 Å). Based on chemical defects, Lorget et al. reported that in Li<sub>2</sub>S doped with LiF, fluoride ions created comparatively large interstitial sites in the antifluorite structure of Li<sub>2</sub>S.<sup>5</sup>

### 3.3.4 Electrochemical impedance spectroscopy

Figure 3.3.2 plots the temperature dependence of conductivities for (100- $x$ )Li<sub>2</sub>S· $x$ CaX<sub>2</sub> ( $X = F, Cl, Br, \text{ and } I$ ). The ionic conductivities of the samples significantly improve than that of the milled Li<sub>2</sub>S. Among each material system, 90Li<sub>2</sub>S·10CaI<sub>2</sub>, 80Li<sub>2</sub>S·20CaBr<sub>2</sub>, 85Li<sub>2</sub>S·15CaCl<sub>2</sub>, and

95Li<sub>2</sub>S·5CaF<sub>2</sub> show the highest ionic conductivity of  $3.6 \times 10^{-5}$ ,  $1.3 \times 10^{-5}$ ,  $1.5 \times 10^{-5}$ , and  $1.8 \times 10^{-7}$  S cm<sup>-1</sup> at 50 °C, respectively. This is attributed to the creation of Li<sup>+</sup> vacancies following the substitution of halogen and the nanoionic effects. All of the samples follow the Arrhenius equation and present lower activation energy than intrinsic Li<sub>2</sub>S (Figure 3.3.3). The conduction properties at the applied temperature are determined by the electrostatic association that causes ionic charge carriers to be partially trapped at dopant sites.<sup>5</sup> The intrinsic high electron-attracting ability of F<sup>-</sup> and Cl<sup>-</sup> could affect the activation energy for ion transport. However, there is no correlation between the activation energy and the ionic radius of the introduced halogen in this study. The considerable difference in activation energy among material systems could not be explained only by the different trapping energies based on the dopant halogen species. A high electronegativity for F and Cl ions may cause a disordered local framework structure in Li<sub>2</sub>S crystals.<sup>6</sup> A systematic investigation reports that 90Li<sub>2</sub>S·10CaI<sub>2</sub> shows the highest ionic conductivity at 50 °C among the prepared samples. This should be originated from the presence of Li-ion vacancies and expansion of the Li-ion pathway when introducing I<sup>-</sup> with a larger ionic radius. Moreover, the ionic conductivity of 90Li<sub>2</sub>S·10CaI<sub>2</sub> is higher than 80Li<sub>2</sub>S·20LiI with identical I<sup>-</sup> doping levels, which may be described by the enhanced ion transport in the interface between the I-doped Li<sub>2</sub>S and CaS phases (Figure 3.3.4). The activation energy of 90Li<sub>2</sub>S·10CaI<sub>2</sub> is a higher value of 0.53 eV than that of 80Li<sub>2</sub>S·20LiI (0.48 eV). Given the electric modulus analysis for Li<sub>2</sub>S·CaS composites discussed in Chapter 3.2, the increase in ionic conductivity and activation energy is anticipated to originate from higher energy barriers near the interface of the CaS nanocrystallines.

### 3.3.5 Cell performance

Halogen doping plays an important role in the redox kinetics of Li<sub>2</sub>S cathode material.<sup>1-3</sup> The charge/discharge tests of Li<sub>2</sub>S–CaX<sub>2</sub> (X = Cl, Br, and I) cathode materials were conducted at 30 °C in the voltage range of 0.6–3.0 V vs Li-In (Figure 3.3.5a-c). For electrochemical tests, I used the Li<sub>2</sub>S–CaX<sub>2</sub> (X = Cl, Br, and I) cathode materials with the optimal composition that showed the highest ionic conductivity among each material system in comparison to conductivity at 50 °C. The capacities of the cells using 85Li<sub>2</sub>S·15CaCl<sub>2</sub>, 85Li<sub>2</sub>S·15CaBr<sub>2</sub>, and 90Li<sub>2</sub>S·10CaI<sub>2</sub> cathode materials improve from that of the cell using Li<sub>2</sub>S, showing 732 mAh g<sup>-1</sup>, 908 mAh g<sup>-1</sup>, and 971 mAh g<sup>-1</sup> at the first cycle, respectively. These capacities decrease with each cycle, which is in disagreement with the redox behavior of the cell using Li<sub>2</sub>S and Li<sub>2</sub>S·CaS after the initial charge/discharge process observed in Chapter 3.2. After 30 cycles, the discharge capacity shows 448 mAh g<sup>-1</sup> for Li<sub>2</sub>S, 649 mAh g<sup>-1</sup> for 85Li<sub>2</sub>S·15CaCl<sub>2</sub>, 646 mAh g<sup>-1</sup> for 85Li<sub>2</sub>S·15CaBr<sub>2</sub>, and 855 mAh g<sup>-1</sup> for 90Li<sub>2</sub>S·10CaI<sub>2</sub>, involving 98.7%, 98.5%, 96.9%, and 98.5% of Coulombic efficiency, respectively. The addition of CaX<sub>2</sub> (X = Cl, Br, and I) to Li<sub>2</sub>S reduces an overpotential, enhancing cell performance. Figure 3.3.6 plots the charge/discharge capacities of ASLSBs cells



using  $\text{Li}_2\text{S}-\text{CaX}_2$  ( $X = \text{Cl}, \text{Br}, \text{and I}$ ) cathode materials at various C-rates. The cells using  $\text{Li}_2\text{S}$ ,  $85\text{Li}_2\text{S}\cdot 15\text{CaCl}_2$ , and  $85\text{Li}_2\text{S}\cdot 15\text{CaBr}_2$  show significant capacity reduction under high C-rates. In contrast, the cell using  $90\text{Li}_2\text{S}\cdot 10\text{CaI}_2$  shows the best capacity, performance stability, and reversibility of redox reactions at high C-rates among the cathode materials examined in this study.

Figure 3.3.7 displays cyclic voltammograms of ASLSBs using the  $\text{Li}_2\text{S}-\text{CaX}_2$  ( $X = \text{Cl}, \text{Br}, \text{and I}$ ) cathode materials cycled at a scan rate of  $0.1 \text{ mV sec}^{-1}$  in the voltage range of  $0.6-3.0 \text{ V vs Li-In}$ . The initial charging for all cells appears a high oxidation voltage called the activation process. The  $90\text{Li}_2\text{S}\cdot 10\text{CaI}_2$  shows the same reduction peak at  $1.7 \text{ V vs Li-In}$  as the  $90\text{Li}_2\text{S}\cdot 10\text{CaS}$  cathode material and an apparent new oxidation peak at a higher voltage ( $2.3 \text{ V vs Li-In}$ ) than the voltage of the oxidation reaction from  $\text{Li}_2\text{S}$  to  $\text{S}$ .  $80(90\text{Li}_2\text{S}\cdot 10\text{CaI}_2)\text{-}20\text{VGCF}$  (wt%) cathode composite without SEs provides an oxidation reaction with two steps and a reduction reaction with a single step (Figure 3.3.8). Lithium iodide oxidizes to  $\text{LiI}_3$  at  $\sim 2.3 \text{ V vs Li-In}$ .<sup>2,7</sup> Thus, the new oxidation peak at  $\sim 2.3 \text{ V vs Li-In}$  would correspond to the oxidation reaction from  $\text{I}^-$  to  $\text{I}_3^-$  in the  $90\text{Li}_2\text{S}\cdot 10\text{CaI}_2$  cathode material. Moreover, the cell using the  $90\text{Li}_2\text{S}\cdot 10\text{CaI}_2$  cathode without SEs shows no reduction peak observed at  $1.7 \text{ V vs Li-In}$  in the  $90\text{Li}_2\text{S}\cdot 10\text{CaI}_2$  cathode with SEs. This reduction reaction could result from a change in bonding energy at the interface between the cathode material and solid electrolyte. Figure 3.3.9a-d shows CV curves of the cells with the  $\text{Li}_2\text{S}-\text{CaX}_2$  ( $X = \text{Cl}, \text{Br}, \text{and I}$ ) cathode materials cycled at different scan rates. Preoperation of 5 cycles was carried out to exclude the activation process of cathode material. Increasing scan rate  $\nu$  shifts cathodic peaks to lower potential and anodic peaks to higher potential in each cell, and highlights the magnitude of  $I_p$ . Figure 3.3.9e shows the peak current,  $I_p$ , estimated by the CV curve as a function of the square root of the scan rate,  $\sqrt{\nu}$ , for each cathode. The proportionality between peak currents and the  $\sqrt{\nu}$  indicates a reversible electrochemical reaction, which means faster electrochemical reaction kinetics of the redox species than the diffusion rate of Li ions.<sup>8</sup> I calculated the lithium-ion diffusion coefficient for each cathode from the slope of the linear fit (Table 1).<sup>8,9</sup> The lithium-ion diffusion coefficients for  $\text{Li}_2\text{S}-\text{CaX}_2$  ( $X = \text{Cl}, \text{Br}, \text{and I}$ ) cathodes improve from that of the intrinsic  $\text{Li}_2\text{S}$  cathode. The  $90\text{Li}_2\text{S}\cdot 10\text{CaI}_2$  cathode shows the highest lithium-ion diffusion coefficient among the fabricated cathodes, which is probably attributed to the high ionic conductivity for  $90\text{Li}_2\text{S}\cdot 10\text{CaI}_2$ . Each of these electrodes leads to a higher Li-ion diffusion coefficient for a cathodic reaction than an anodic reaction because of strong  $\text{Li}^+\text{-S}^{2-}$  interaction. The  $85\text{Li}_2\text{S}\cdot 15\text{CaCl}_2$  cathode exhibits a higher Li-ion diffusion coefficient for the cathodic reaction than the intrinsic  $\text{Li}_2\text{S}$ , but the Li-ion diffusion coefficient for the anodic reaction is identical to the intrinsic  $\text{Li}_2\text{S}$  cathode. A high electronegativity of Cl ion should cause a strong interaction with Li-ions, increasing the activation barrier during anodic reactions. I additionally examined electronic conductivities for cathode materials by direct polarization test. The electronic conductivities for  $\text{Li}_2\text{S}$ ,  $85\text{Li}_2\text{S}\cdot 15\text{CaCl}_2$ ,  $85\text{Li}_2\text{S}\cdot 15\text{CaBr}_2$ , and  $90\text{Li}_2\text{S}\cdot 10\text{CaI}_2$  show  $2.1 \times 10^{-10}$ ,

$28 \times 10^{-10}$ ,  $15 \times 10^{-10}$ , and  $35 \times 10^{-10}$  S cm<sup>-1</sup> at room temperature, respectively. The enhanced Li-ion diffusion coefficient and electronic conductivity for Li<sub>2</sub>S–CaX<sub>2</sub> (X = Cl, Br, and I) cathode materials will result in high electrochemical utilization. The 85Li<sub>2</sub>S·15CaCl<sub>2</sub> and 85Li<sub>2</sub>S·15CaBr<sub>2</sub> show the capacities of less than 100 mAh g<sup>-1</sup> under 1C as well as the intrinsic Li<sub>2</sub>S as seen in Figure 3.3.6, although they show higher conductivity than the intrinsic Li<sub>2</sub>S. Factors other than the ion transport properties of the cathode may be responsible for the high capacity under a high C-rate in the cell using the 90Li<sub>2</sub>S·10CaI<sub>2</sub>. One possible factor that contributes to achieving high capacity at high C-rates could be the redox activity of additives as redox mediators.<sup>3,10</sup> The additive with a slightly higher oxidation reaction voltage than the Li<sub>2</sub>S cathode effectively acts as a redox mediator for Li<sub>2</sub>S activation.<sup>11</sup> The oxidation reaction of LiI can be leveraged as an electrochemical redox mediator that facilitates the redox reaction because occurs at a slightly higher oxidation reaction voltage than Li<sub>2</sub>S. The 90Li<sub>2</sub>S · 10CaI<sub>2</sub>, which exhibits the electrochemical redox reaction including the oxidation of I-substituted Li<sub>2</sub>S, thereby, may deliver high capacity at high C-rates. These findings report here provide insight into the design of Li<sub>2</sub>S-based cathode materials for achieving high capacity under high C-rates.

### 3.3.6 Conclusions

In this study, I evaluated the conductivity properties of the Li<sub>2</sub>S–CaX<sub>2</sub> (X = F, Cl, Br, and I) cathode materials prepared by high-energy ball milling and the cell performance of the Li<sub>2</sub>S–CaX<sub>2</sub> (X = Cl, Br, and I) with the optimal composition. The addition of CaX<sub>2</sub> (X = F, Cl, Br, and I) allows for increasing the ionic conductivity of Li<sub>2</sub>S. The 85Li<sub>2</sub>S · 15CaCl<sub>2</sub>, 85Li<sub>2</sub>S · 15CaBr<sub>2</sub>, and 90Li<sub>2</sub>S·10CaI<sub>2</sub> cathode materials show a higher utilization than the cell using the intrinsic Li<sub>2</sub>S. The cell using the 90Li<sub>2</sub>S·10CaI<sub>2</sub> cathode shows an excellent capacity of 855 mAh g<sup>-1</sup> after 30 cycles (448 mAh g<sup>-1</sup> for Li<sub>2</sub>S cathode). CV measurements at different scan rates demonstrate that the addition of CaX<sub>2</sub> (X = Cl, Br, and I) improves the Li-ion diffusion coefficient of the cathode materials; this is the highest in the 90Li<sub>2</sub>S·10CaI<sub>2</sub> cathode among the fabricated cells. The enhanced Li-ion diffusion coefficient should lead to the improvement of cell performance in Li<sub>2</sub>S-based cathode. However, the cells using the 85Li<sub>2</sub>S·15CaCl<sub>2</sub> and 85Li<sub>2</sub>S·15CaBr<sub>2</sub> show almost identical capacity as the cell using the intrinsic Li<sub>2</sub>S under a high C-rate. These experimental results suggest that factors other than the transport properties of the cathode materials may be responsible for the high capacity under a high C-rate. The 90Li<sub>2</sub>S·10CaI<sub>2</sub> shows electrochemical redox behavior that oxidation reaction occurs at a slightly higher potential than the oxidation potential of Li<sub>2</sub>S, which will provide desirable redox activity in ASLSBs. Thus, the 90Li<sub>2</sub>S·10CaI<sub>2</sub> cathode material demonstrates excellent capacity, performance stability, and reversibility of redox reactions at high C-rates.

## References

- (1) Hakari, T.; Hayashi, A.; Tatsumisago, M. Li<sub>2</sub>S-Based Solid Solutions as Positive Electrodes with Full Utilization and Superlong Cycle Life in All-Solid-State Li/S Batteries. *Adv. Sustain. Syst.* **2017**, *1*, 1700017–1700023.
- (2) Liu, M.; Wang, C.; Zhao, C.; van der Maas, E.; Lin, K.; Arszewska, V. A.; Li, B.; Ganapathy, S.; Wagemaker, M. Quantification of the Li-Ion Diffusion over an Interface Coating in All-Solid-State Batteries via NMR Measurements. *Nat. Commun.* **2021**, *12*, 5943–5952.
- (3) Wan, H.; Zhang, B.; Liu, S.; Zhang, J.; Yao, X.; Wang, C. Understanding LiI-LiBr Catalyst Activity for Solid State Li<sub>2</sub>S/S Reactions in an All-Solid-State Lithium Battery. *Nano Lett.* **2021**, *21*, 8488–8494.
- (4) Hakari, T.; Fujita, Y.; Deguchi, M.; Kawasaki, Y.; Otoyama, M.; Yoneda, Y.; Sakuda, A.; Tatsumisago, M.; Hayashi, A. Solid Electrolyte with Oxidation Tolerance Provides a High-Capacity Li<sub>2</sub>S-Based Positive Electrode for All-Solid-State Li/S Batteries. *Adv. Funct. Mater.* **2022**, *32*.
- (5) Lorger, S.; Usiskin, R. E.; Maier, J. Transport and Charge Carrier Chemistry in Lithium Sulfide. *Adv. Funct. Mater.* **2019**, *29*.
- (6) Choi, Y. S.; Lee, J. C. Electronic and Mechanistic Origins of the Superionic Conductivity of Sulfide-Based Solid Electrolytes. *J. Power Sources* **2019**, *415*, 189–196.
- (7) Zhao, Q.; Lu, Y.; Zhu, Z.; Tao, Z.; Chen, J. Rechargeable Lithium-Iodine Batteries with Iodine/Nanoporous Carbon Cathode. *Nano Lett.* **2015**, *15*, 5982–5987.
- (8) Huang, X.; Wang, Z.; Knibbe, R.; Luo, B.; Ahad, S. A.; Sun, D.; Wang, L. Cyclic Voltammetry in Lithium–Sulfur Batteries—Challenges and Opportunities. *Energy Technol.* **2019**, *7*, 1801001–1801013.
- (9) Das, S. R.; Majumder, S. B.; Katiyar, R. S. Kinetic Analysis of the Li<sup>+</sup> Ion Intercalation Behavior of Solution Derived Nano-Crystalline Lithium Manganate Thin Films. *J. Power Sources* **2005**, *139*, 261–268.
- (10) Li, M.; Bai, Z.; Li, Y.; Ma, L.; Dai, A.; Wang, X.; Luo, D.; Wu, T.; Liu, P.; Yang, L.; Amine, K.; Chen, Z.; Lu, J. Electrochemically Primed Functional Redox Mediator Generator from the Decomposition of Solid State Electrolyte. *Nat. Commun.* **2019**, *10*, 1890–1898.

**Table 3.3.1.** Lithium ion diffusion coefficient for the electrode using the  $\text{Li}_2\text{S}$ ,  $85\text{Li}_2\text{S}\cdot 15\text{CaCl}_2$ ,  $85\text{Li}_2\text{S}\cdot 15\text{CaBr}_2$ , and  $90\text{Li}_2\text{S}\cdot 10\text{CaI}_2$  cathode materials calculated from Randles-Sevick equation.

Cathode	Li ion diffusion coefficient ( $\times 10^{-11} \text{ cm}^2 \text{ s}^{-1}$ )	
	Anodic	Cathodic
$\text{Li}_2\text{S}$	3.6	6.8
$85\text{Li}_2\text{S}\cdot 15\text{CaCl}_2$	3.5	12
$85\text{Li}_2\text{S}\cdot 15\text{CaBr}_2$	7.7	20
$90\text{Li}_2\text{S}\cdot 10\text{CaI}_2$	19	28

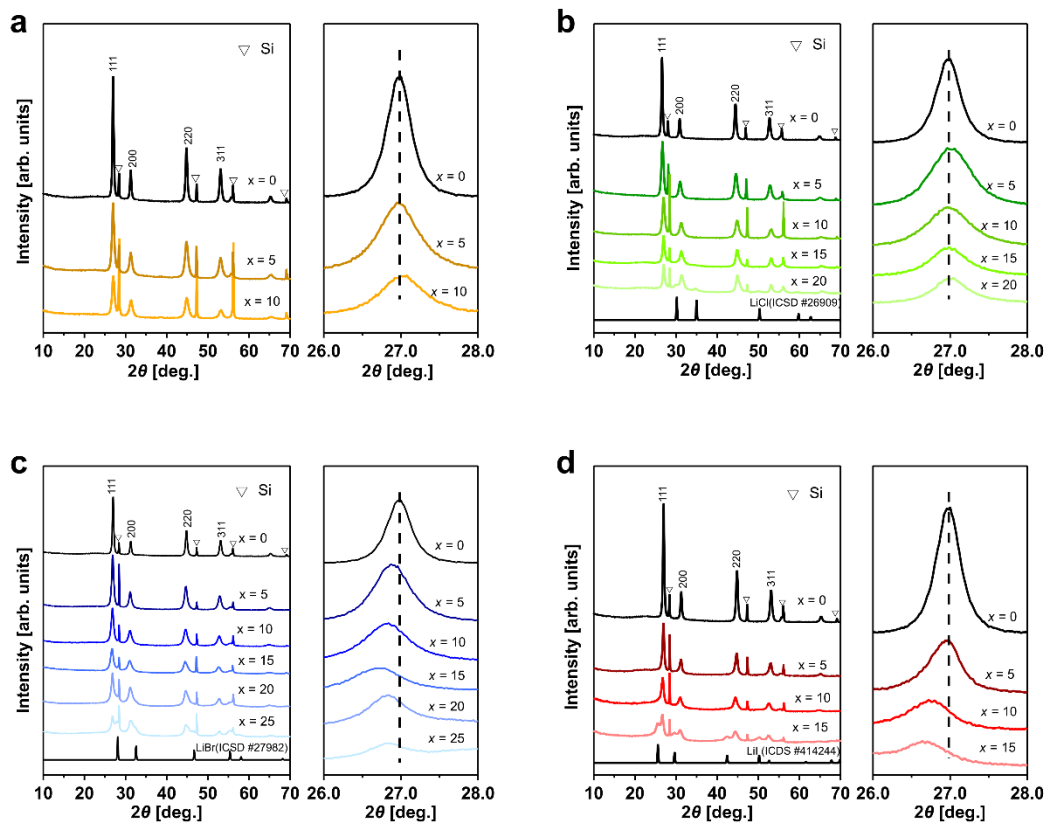


**Figure 3.3.1.** The XRD patterns of (a)  $(100-x)\text{Li}_2\text{S}\cdot x\text{CaF}_2$ , (b)  $(100-x)\text{Li}_2\text{S}\cdot x\text{CaCl}_2$ , (c)  $(100-x)\text{Li}_2\text{S}\cdot x\text{CaBr}_2$ , and (d)  $(100-x)\text{Li}_2\text{S}\cdot x\text{CaI}_2$  with added Si powder as a standard sample.

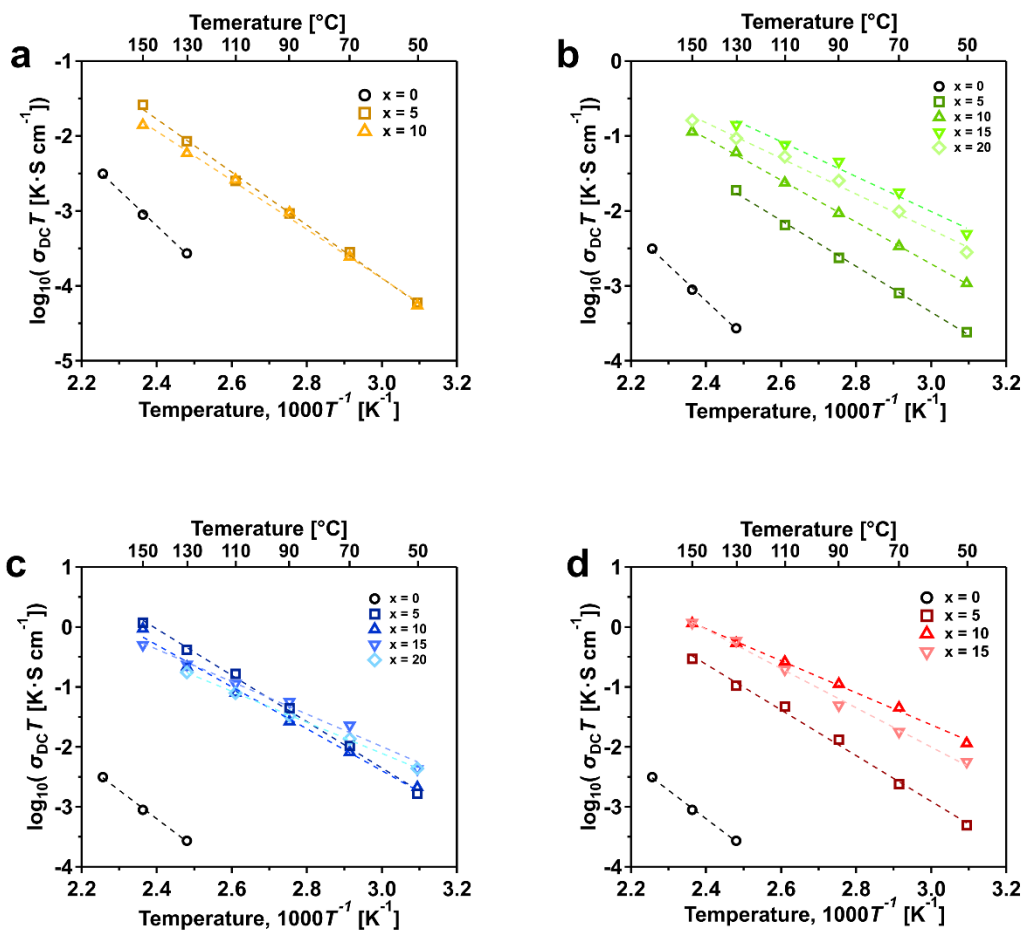


**Figure 3.3.2.** Arrhenius plots of the DC conductivities for (a)  $(100-x)\text{Li}_2\text{S} \cdot x\text{CaF}_2$ , (b)  $(100-x)\text{Li}_2\text{S} \cdot x\text{CaCl}_2$ , (c)  $(100-x)\text{Li}_2\text{S} \cdot x\text{CaBr}_2$ , and (d)  $(100-x)\text{Li}_2\text{S} \cdot x\text{CaI}_2$ .

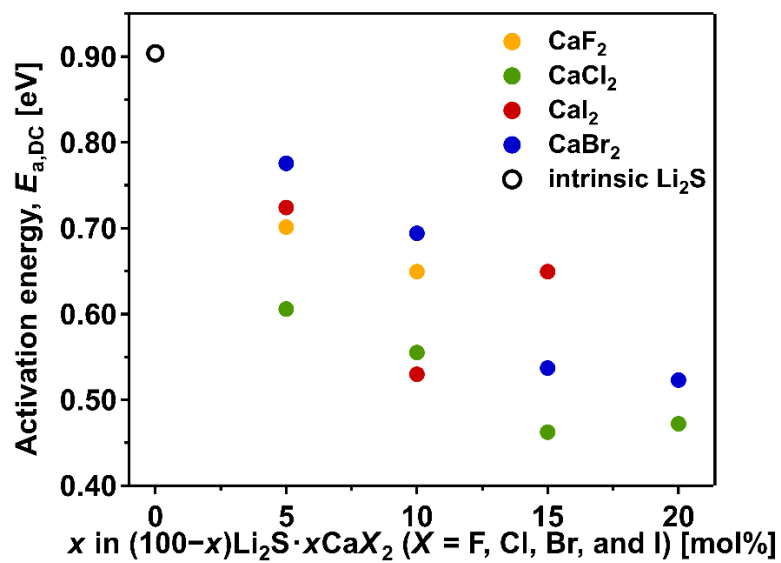


**Figure 3.3.3.** Activation energy for conduction in  $(100-x)\text{Li}_2\text{S}\cdot x\text{CaX}_2$  ( $X = \text{F, Cl, Br, and I}$ ).

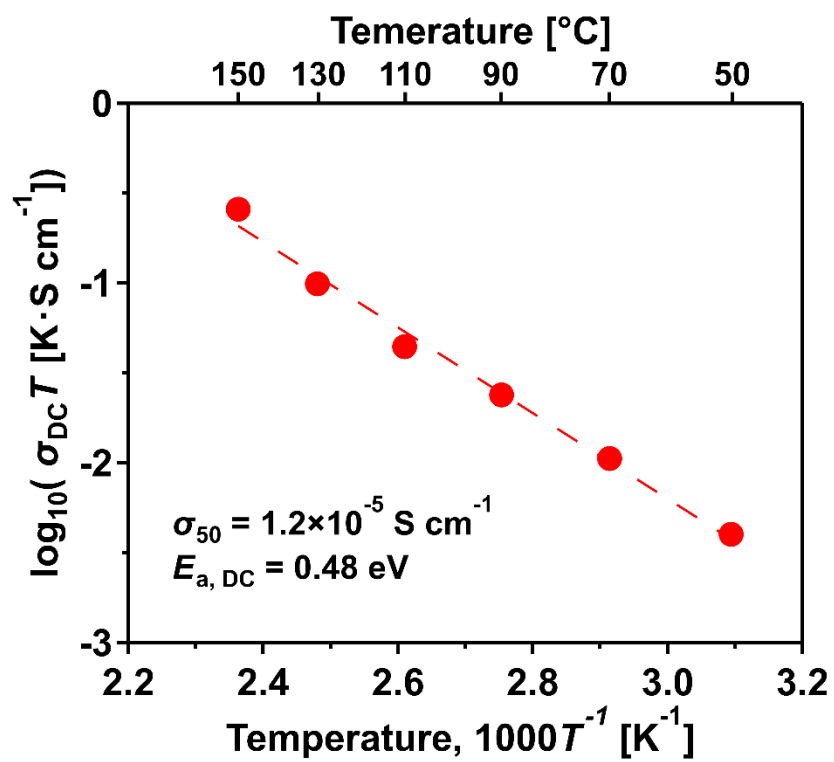
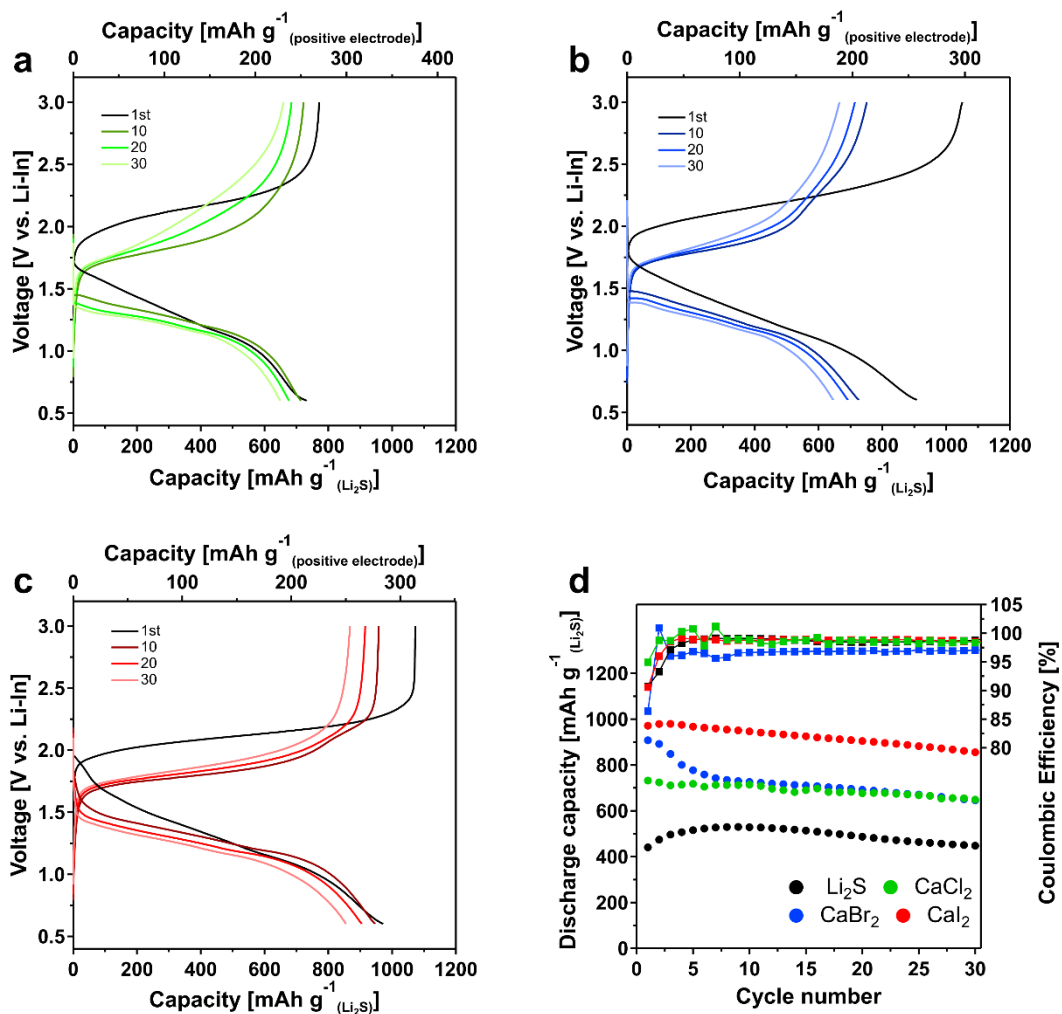
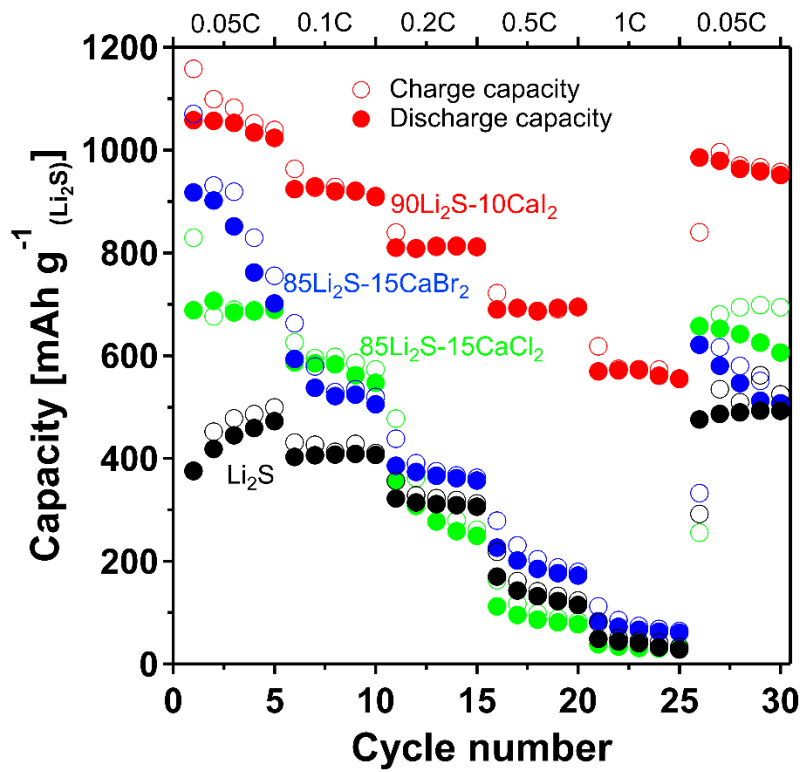


Figure 3.3.4. An Arrhenius plot of the DC conductivities for 80Li<sub>2</sub>S·20LiI.





**Figure 3.3.5.** Voltage profiles of ASLSB using (a) 85Li<sub>2</sub>S·15CaCl<sub>2</sub>, (b) 85Li<sub>2</sub>S·15CaBr<sub>2</sub>, and (c) 90Li<sub>2</sub>S·10CaI<sub>2</sub> cathode materials cycled under 0.05C at 30 °C in the voltage range of 0.6-3.0 V vs Li-In. (d) Discharge capacities and Coulombic efficiencies of Li<sub>2</sub>S·CaX<sub>2</sub> (X = Cl, Br, and I) cathode materials cycled under 0.05C at 30 °C in the voltage range of 0.6-3.0 V vs Li-In.



**Figure 3.3.6.** Charge/discharge capacities and Coulombic efficiencies of  $\text{Li}_2\text{S}\cdot\text{CaX}_2$  ( $X = \text{Cl}$ ,  $\text{Br}$ , and  $\text{I}$ ) cathode materials cycled under C-rates of 0.05, 0.1, 0.2, 0.5, and 1C at 30 °C in the voltage range of 0.6-3.0 V vs Li-In.

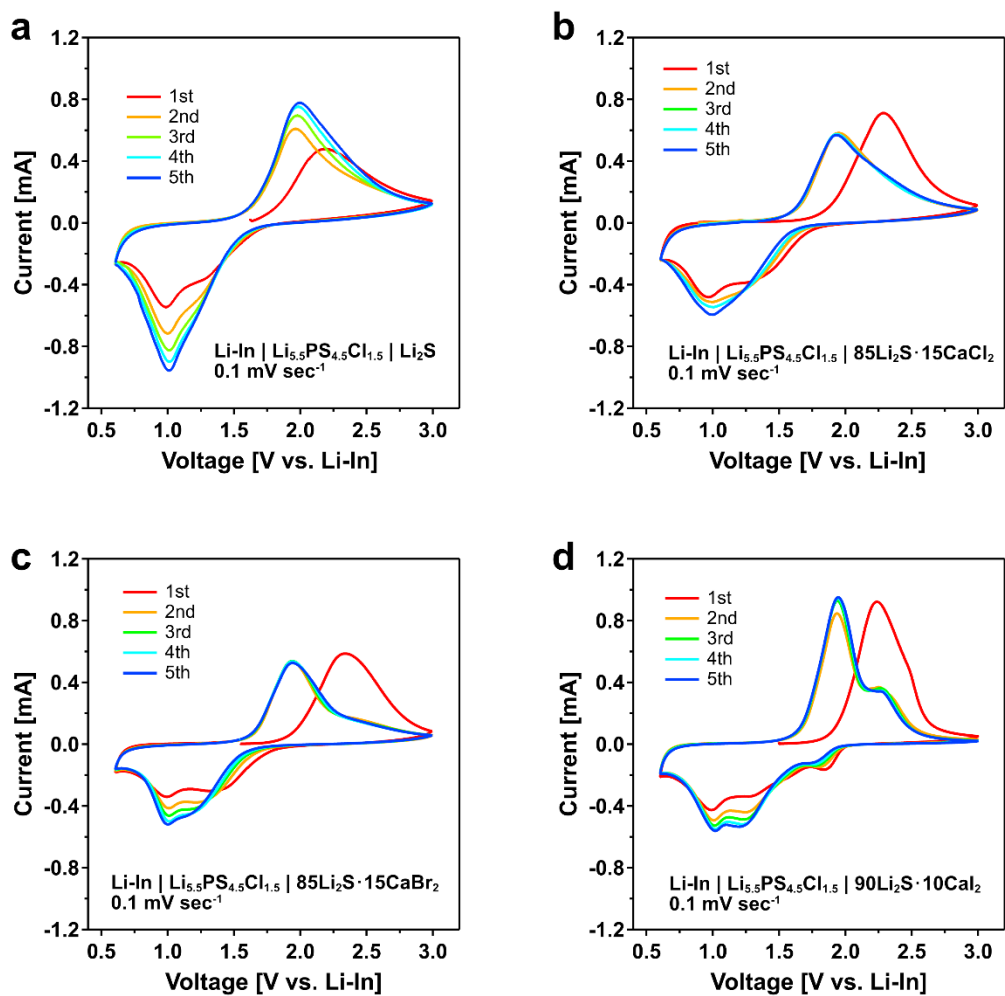


**Figure 3.3.7.** Cyclic voltammetry profiles of ASLSB using (a) Li<sub>2</sub>S, (b) 85Li<sub>2</sub>S·15CaCl<sub>2</sub>, (c) 85Li<sub>2</sub>S·15CaBr<sub>2</sub>, and (d) 90Li<sub>2</sub>S·10CaI<sub>2</sub> cathode materials cycled at 30 °C in the voltage range of 0.6-3.0 V vs Li-In under a scan rate of 0.1 mV sec<sup>-1</sup>.

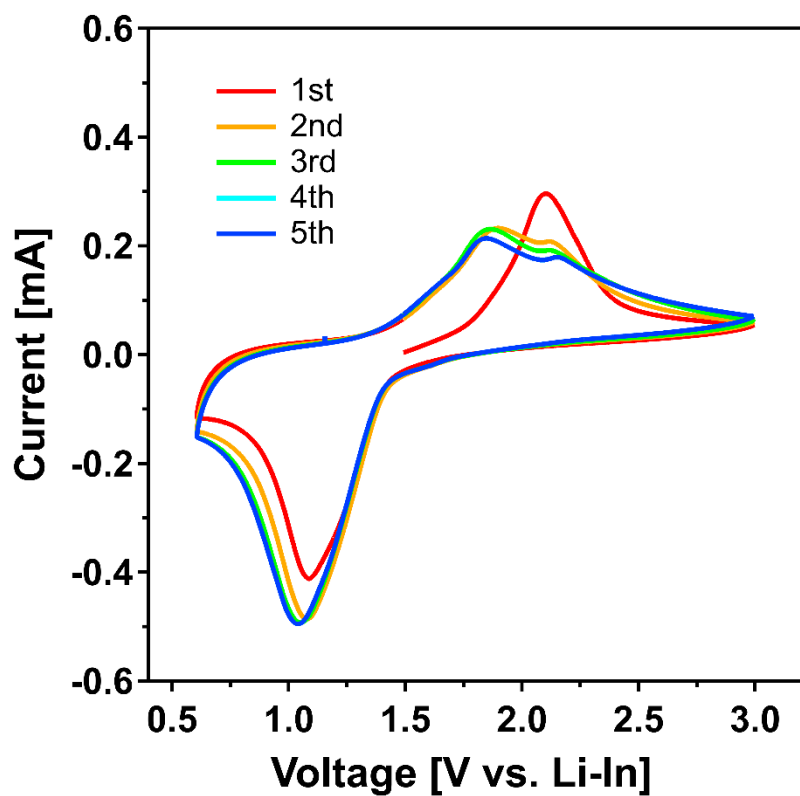


**Figure 3.3.8.** Cyclic voltammetry profiles of Li-In | 90Li<sub>2</sub>S·10CaI<sub>2</sub> | 80(90Li<sub>2</sub>S·10CaI<sub>2</sub>)-20VGCF cell cycled at 60 °C in the voltage range of 0.6-3.0 V vs Li-In under a scan rate of 0.1 mV sec<sup>-1</sup>.

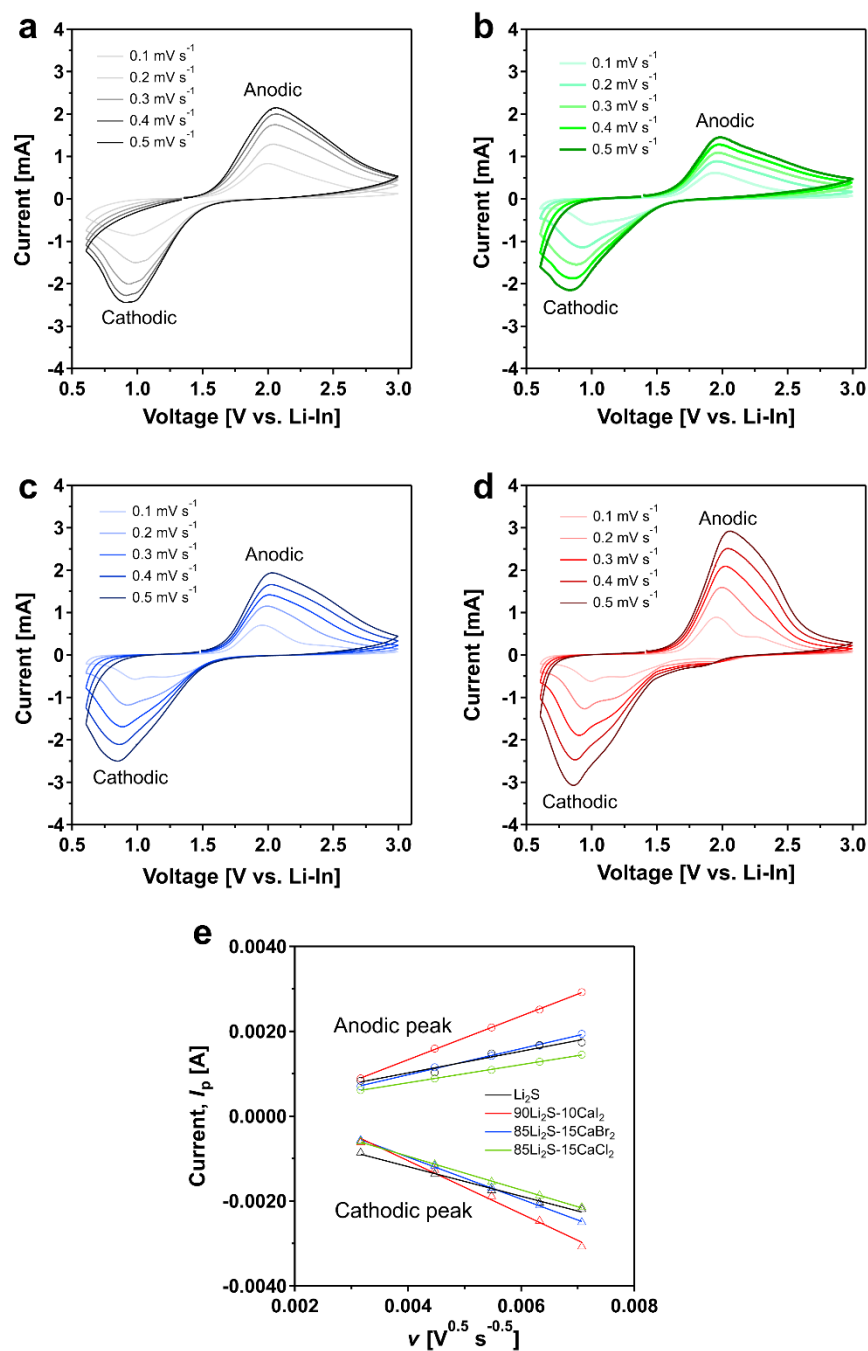


**Figure 3.3.9.** Cyclic voltammetry profiles of ASLSB using (a)  $\text{Li}_2\text{S}$ , (b)  $85\text{Li}_2\text{S}\cdot 15\text{CaCl}_2$ , (c)  $85\text{Li}_2\text{S}\cdot 15\text{CaBr}_2$ , and (d)  $90\text{Li}_2\text{S}\cdot 10\text{CaI}_2$  cathode materials cycled at  $30^\circ\text{C}$  in the voltage range of 0.6-3.0 V vs Li-In under a scan rate of 0.1-0.5  $\text{mV sec}^{-1}$ . (e) The maximum anodic and cathodic peaks,  $I_p$ , as a function of square root of scan rate in (a-d).

### 3.4 Lithium sulfide cathode materials doped with aluminum iodide

In this chapter, I discuss the structural and electrochemical features of  $(100 - x)\text{Li}_2\text{S} \cdot x\text{AlI}_3$  ( $0 \leq x \leq 5$ ) solid solutions for ASLSBs. XRD and UV-Vis studies demonstrate that  $\text{AlI}_3$  is dissolved in the  $\text{Li}_2\text{S}$  matrix during the preparation process. The change in the electronic structures of  $\text{Li}_2\text{S}$  following the addition of  $\text{AlI}_3$  is found based on X-ray photoelectron spectroscopy (XPS) results. This change increases both ionic and electronic conductivities of  $\text{Li}_2\text{S}$ . The cell with 99.5  $\text{Li}_2\text{S} \cdot 0.5\text{AlI}_3$  exhibits better initial capacity, Coulombic efficiency, and capacity retention than the one employing pristine  $\text{Li}_2\text{S}$ . The cathode developed here shows superior specific capacity per gram of cathode composite to other  $\text{Li}_2\text{S}$ -based cathode composites reported in the literature. This work offers a useful strategy to improve the electrochemical performance of materials for ASLSBs.

#### 3.4.1 Introduction

In Chapter 3.3, I unveiled that the iodide doped into  $\text{Li}_2\text{S}$  plays a significant role in cell performance at high C-rates. The capacity normalized by the weight of  $\text{Li}_2\text{S}$  in the cell with  $90\text{Li}_2\text{S} \cdot 10\text{CaI}_2$  showed an excellent value of  $971 \text{ mAh g}^{-1}$ . However, as normalized by the weight of the cathode composite, the capacity is  $250 \text{ mAh g}^{-1}$ . Thus, the addition of large amounts of I-ion in  $\text{Li}_2\text{S}$  cathode enhances the utilization but limits capacity per the weight of the cathode composite. Namely, this leads to a decrease in the energy density of ASLSBs. An  $80\text{Li}_2\text{S} \cdot 20\text{LiI}$  cathode material remarkably improved  $\text{Li}_2\text{S}$  utility and cyclic stability, whereas the capacity normalized by the weight of the cathode composite was  $325 \text{ mAh g}^{-1}$ .<sup>1</sup> The achievement of intrinsically high cell performance of ASLSBs requires high utilization of  $\text{Li}_2\text{S}$  while maintaining high loads of  $\text{Li}_2\text{S}$  in the electrode layer. Recent work reported an electrode without SEs and conductive carbon in the cathode to deliver high energy density. The  $\text{Li}_2\text{S} \cdot \text{V}_2\text{S}_3 \cdot \text{LiI}$  cathode designed by Sakuda et al. showed a high capacity of  $370 \text{ mAh}$  per the weight of the cathode layer at  $25^\circ\text{C}$  after 100 cycles.<sup>2</sup> Furthermore, the addition of a catalyst and redox mediator is a useful approach for improving the capacity per the weight of cathode composite. Transition metal sulfides and oxides serve as a catalyst that enhances the redox reaction kinetics of  $\text{Li}_2\text{S}$  cathode in liquid Li-S batteries.<sup>3-5</sup> Similarly, the addition of the multivalence cations  $\text{Al}^{3+}$  emphasized the redox reaction kinetics of ASLSBs, allowing us superior cell performance.<sup>6</sup>

In this study, I have developed an  $\text{AlI}_3$ -doped  $\text{Li}_2\text{S}$  cathode material that shows high capacity per the weight of the cathode composite. Dual doping  $\text{Al}^{3+}$  and  $\text{I}^-$  enables the increase in the redox reaction kinetics owing to high catalytic effect of these dopants. XRD, UV-Vis, and XPS measurements were employed to analyze the structure of prepared  $(100 - x)\text{Li}_2\text{S} \cdot x\text{AlI}_3$ . The

capacity of the cell using  $99.5\text{Li}_2\text{S}\cdot 0.5\text{AlI}_3$  remains at  $449\text{ mAh g}^{-1}$  (normalized by the weight of cathode composite), which is higher than  $282\text{ mAh g}^{-1}$  for the pristine  $\text{Li}_2\text{S}$  after 60 cycles.

### 3.4.2 Experimental methods

**Chemical.**  $\text{Li}_2\text{S}$  (99.9%) and  $\text{P}_2\text{S}_5$  (99%) were purchased from Mitsuwa Chemical and Merck Group, respectively, and used without purification.  $\text{AlI}_3$  (99.9%) and  $\text{LiI}$  (99.9%) were received from Kojundo Chemical Laboratory and Aldrich, respectively.

**Synthesis.**  $(100 - x)\text{Li}_2\text{S}\cdot x\text{AlI}_3$  ( $0 \leq x \leq 30$ ) was prepared via planetary ball milling.  $\text{Li}_2\text{S}$  and  $\text{AlI}_3$  were mixed for 10 min using an agate mortar and then put into a 45-ml zirconia pot with zirconia balls (10 mm, 15 balls). The pots were rotated at 500 rpm for 12 h using a Pulverisette 7 (Fritsch). The obtained samples were recovered and used without any further heat treatment.  $\text{Li}_{10}\text{P}_3\text{S}_{12}\text{I}$  glass-ceramic solid electrolyte was prepared by solid-state reaction. Amounts of 1.5 g of  $\text{Li}_2\text{S}$ ,  $\text{P}_2\text{S}_5$ , and  $\text{LiI}$  with a molar ratio of  $\text{Li}_2\text{S}:\text{P}_2\text{S}_5:\text{LiI} = 9:3:2$  were weighed, mixed well with an agate mortar, and then put into a 45-ml zirconia pot with 70 g of zirconia balls (4 mm). The pots were rotated at 510 rpm for 15 h using a Pulverisette 7 (Fritsch). The obtained glassy powder was then sintered at  $190^\circ\text{C}$  for 1 h in an Ar atmosphere to obtain  $\text{Li}_{10}\text{P}_3\text{S}_{12}\text{I}$  glass-ceramic solid electrolyte with an ionic conductivity of approximately  $1.0\text{ mS cm}^{-1}$  at room temperature.

A composite cathode composed of  $(100 - x)\text{Li}_2\text{S}\cdot x\text{AlI}_3$ ,  $\text{Li}_{10}\text{P}_3\text{S}_{12}\text{I}$  glass ceramic, and KB with a weight ratio of 50:40:10 was prepared via two-step planetary ball milling. An amount of 0.3 g of  $(100 - x)\text{Li}_2\text{S}\cdot x\text{AlI}_3$  and KB (weight ratio of 5:1) was put into a zirconia pot with 30 g of zirconia balls (4 mm) and the pot was rotated at 510 rpm for 10 h. Then 0.2 g of  $\text{Li}_{10}\text{P}_3\text{S}_{12}\text{I}$  glass-ceramic was added to the pots and they were rotated at 400 rpm for 2 h to obtain the cathode composites.

**Material characterization.** The structure of the prepared  $(100 - x)\text{Li}_2\text{S}\cdot x\text{AlI}_3$  powders was characterized via XRD (Ultima IV, Rigaku) and diffuse reflection UV-Vis (V-670, Jasco). For analysis, the samples were sealed in special holders in an Ar-filled glove box to avoid exposure to humidity. The electronic structure was characterized using XPS (K-Alpha, Thermo Fisher Scientific) with a monochromatic Al  $K\alpha$  source (1486.6 eV).<sup>7</sup> Calibration of the observed binding energies was performed with respect to the advantageous C 1s peak at 284.7 eV after etching.  $\text{Ar}^+$  ion-etching was carried out using Ar gas cluster ion beams with the energy of 6 keV for 30 min to suppress damage to the samples. The etching rate was  $1\text{ nm min}^{-1}$ . The sample was characterized without exposure to air by using an Ar-filled transfer vessel.

**Electrochemical measurements.** The temperature dependence of the ionic conductivity of the prepared  $(100 - x)\text{Li}_2\text{S}\cdot x\text{AlI}_3$  samples was investigated using alternating current impedance spectroscopy (SI 1260, Solatron) in a frequency range of 1 MHz to 10 Hz under a dry Ar flow.

The electronic conductivity at room temperature was measured via the direct current polarization method. Prior to the measurements, the samples were pressed into pellets of ~10 mm in diameter at a pressure of 550 MPa at room temperature. The pellets were then placed in a PEEK holder with two stainless steel rods as blocking electrodes. Voltages of 0.1–2.0 V were then applied to the prepared cells for 60 min and the currents were measured. The experiments were carried out using a potentiostat (SI 1287; Solatron). ASLSB cells were fabricated with a structure resembling one reported elsewhere.<sup>5</sup> The current density was ~0.25 mA cm<sup>-2</sup>. The cut-off voltages of all batteries were 0.9–3.0 V vs. Li-In for the first cycle and 0.9–2.25 V vs. Li-In for subsequent cycles. The charge-discharge test after the first charge was carried out at constant current-constant voltage mode. The normalized Li<sub>2</sub>S loading in each cell was 1.8–2.2 mg. ASLSB cells were cycled under about applied external pressure of 36 MPa at 30 °C. All the experiments were conducted in an Ar-filled glove box (water <0.1 ppm) or an airtight sample holder to avoid direct exposure of the samples to ambient humidity.

### 3.4.3 Structural characterization

Figure 3.4.1 illustrates the XRD patterns of  $(100 - x)\text{Li}_2\text{S} \cdot x\text{AlI}_3$  samples. The XRD patterns of  $(100 - x)\text{Li}_2\text{S} \cdot x\text{AlI}_3$  show the peaks originated from Li<sub>2</sub>S crystal until  $x = 10$ , which shift to lower angles until  $x = 5$  compared with  $x = 0$  (pristine Li<sub>2</sub>S). These facts prove that the lattice volume of the Li<sub>2</sub>S structure increases because I<sup>-</sup> in AlI<sub>3</sub> are dissolved into the Li<sub>2</sub>S structure. Calculating the lattice parameters from the diffraction angles corresponding to the (111), (200), (220), and (311) lattice plane, the lattice parameters for samples with  $x = 0, 0.5, 3,$  and  $5$  are 5.718, 5.741, 5.752, and 5.777 Å, respectively. The lattice parameters of the Li<sub>2</sub>S structure increase with an increasing AlI<sub>3</sub> doping level in Li<sub>2</sub>S. In the sample above  $x = 7$ , the peaks of LiI are detected and the peaks of Li<sub>2</sub>S disappear in the sample with  $x = 20$ . Li<sub>2</sub>S·AlS<sub>1.5</sub> prepared by high-energy mechanical milling shows an XRD halo pattern and no diffraction peak at a specific composition with high Al-ion concentration.<sup>8</sup> Thus, AlI<sub>3</sub> in  $(100 - x)\text{Li}_2\text{S} \cdot x\text{AlI}_3$  samples with higher  $x$  can dissolve into the Li<sub>2</sub>S glass matrix to form a solid solution. Figure 3.4.2 illustrates the UV-Vis spectra of  $(100 - x)\text{Li}_2\text{S} \cdot x\text{AlI}_3$  ( $x \leq 5$ ). UV-Vis spectrum of Li<sub>2</sub>S exhibits one small shoulder centered at 270 nm and a large shoulder in the range of 250–190 nm. Aluminum iodide shows a large absorption shoulder ranging from ~320 nm to 190 nm. Doping a small amount of AlI<sub>3</sub> into the Li<sub>2</sub>S structure ( $x \leq 2$ ) results in the appearance of a small absorption shoulder centered at approximately 350 nm whereas the absorption bands centered at 270 nm and 290 nm of Li<sub>2</sub>S and AlI<sub>3</sub> are disappeared. At higher doping levels of  $2 < x \leq 5$ , the band at 350 nm is replaced by a new absorption band centered at 307 nm. This is consistent with the change of UV-Vis spectra observed in Li<sub>2</sub>S·Al<sub>2</sub>S<sub>3</sub> solid solution<sup>6</sup>, indicating that Al-ions in AlI<sub>3</sub> are well dispersed in the Li<sub>2</sub>S glass matrix. Thus, the  $(100 - x)\text{Li}_2\text{S} \cdot x\text{AlI}_3$  ( $x \leq 5$ ) solid solution formation drastically



changes the electronic structure.

Figure 3.4.3a-d shows the XPS spectra (envelope after background subtraction) of S 2p, I 3d, Li 1s, and Al 2p, respectively, for the prepared samples and standard materials Li<sub>2</sub>S (ball milled), AlI<sub>3</sub> (ball milled), LiI, and 80Li<sub>2</sub>S–20LiI for comparison. The two peaks at 160.1 eV and 161.3 eV of Li<sub>2</sub>S are assigned to the binding energies of S 2p<sub>3/2</sub> and 2p<sub>1/2</sub> (Figure 3.4.3a).<sup>9</sup> Those of 80Li<sub>2</sub>S·20LiI are 160.6 eV and 161.8 eV. Doping Li<sub>2</sub>S with a small amount of AlI<sub>3</sub> ( $x = 0.5$ ) results in the peaks shifting to higher binding energies, 160.5 eV and 161.6 eV. The peaks shift to 160.8 eV and 162.0 eV for both the higher doping levels,  $x = 3$  and  $x = 5$ . The higher binding energy of S<sup>2-</sup> can attribute to the bond of Al<sup>3+</sup> with the higher electronegativity of 1.61 than Li<sup>+</sup> (0.98). The I 3d XPS data is provided in Figure 3.4.3b. The two peaks located at 619.0 eV and 630.4 eV are assigned to 3d<sub>5/2</sub> and 3d<sub>3/2</sub> of I<sup>-</sup>.<sup>10,11</sup> Those values for I<sup>-</sup> in AlI<sub>3</sub> are 619.7 eV and 631.2 eV. The 80Li<sub>2</sub>S–20LiI expresses the peaks of I<sup>-</sup> at 619.1 eV and 630.5 eV. Peaks of I<sup>-</sup> in all the prepared samples ( $x = 0.5, 3, 5$ ) appear in the region of I<sup>-</sup> in 80Li<sub>2</sub>S–20LiI instead of AlI<sub>3</sub>. This observation indicates that I-ion dissolves into the Li<sub>2</sub>S structure. The signal of Li 1s in LiI appears at 56.3 eV while that of Li<sub>2</sub>S is at 54.5 eV.<sup>10,12</sup> The peak of Li 1s in 80Li<sub>2</sub>S–20LiI is detected at 55.1 eV, which is in between the values of those in LiI and Li<sub>2</sub>S. Doping AlI<sub>3</sub> to Li<sub>2</sub>S results in the peak-shifting of Li 1s from 54.5 eV in Li<sub>2</sub>S to 54.8 eV, 55.2 eV, and 55.4 eV with  $x = 0, 3$ , and  $5$ , respectively. The Al 2p of AlI<sub>3</sub> shows a peak at 75.0 eV.<sup>13</sup> The addition of AlI<sub>3</sub> into Li<sub>2</sub>S at  $x = 0.5$  leads to a drastic peak-shifting to 73.6 eV. With  $x = 3$  and  $x = 5$ , the signal of Al 2p appears at 73.9 eV and 74.0 eV. The peak-shifting observed in  $(100 - x)\text{Li}_2\text{S} \cdot x\text{AlI}_3$  ( $0 < x \leq 5$ ) demonstrates that the Al<sup>3+</sup> is bound to S with low electronegativity in comparison with that of I<sup>-</sup>. Therefore, these XPS results also confirm that the Al<sup>3+</sup> in AlI<sub>3</sub> dissolved into the Li<sub>2</sub>S matrix. These results are also in good agreement with those obtained from XRD and UV–Vis measurements. The formation of the Li<sub>2</sub>S·AlI<sub>3</sub> solid solution should dramatically change the electronic structures in both Li<sub>2</sub>S and AlI<sub>3</sub>. It should be noted that the obtained XPS spectrum is reflected from the chemical binding state from the surface to a depth of 10 nm in Li<sub>2</sub>S·AlI<sub>3</sub>.

### 3.4.4 Electric conductivity

The temperature dependence of ionic conductivity and polarized I–V correlation (electronic current) of  $(100 - x)\text{Li}_2\text{S} \cdot x\text{AlI}_3$  ( $0 \leq x \leq 5$ ) samples are shown in Figure 3.4.4. The reported ionic conductivity of Li<sub>2</sub>S at room temperature was reported  $10^{-9}$ – $10^{-8}$  S cm<sup>-1</sup>.<sup>1</sup> However, the value obtained in this study is lower than  $10^{-12}$  S cm<sup>-1</sup>, which is in agreement with the value reported by Z. Lin et al.<sup>14</sup> A 99Li<sub>2</sub>S·1AlI<sub>3</sub> solid solution exhibits ionic conductivity approximately three orders of magnitude higher than that of Li<sub>2</sub>S. 95Li<sub>2</sub>S·5AlI<sub>3</sub> expresses an ionic conductivity of  $4.5 \times 10^{-6}$  S cm<sup>-1</sup> at room temperature, which are comparable to that of 80Li<sub>2</sub>S·20LiI.<sup>15</sup> A slight increase in the amount of AlI<sub>3</sub> from 5 to 7 improves an ionic conductivity from  $4.5 \times 10^{-6}$  S cm<sup>-1</sup>

to  $2.8 \times 10^{-5} \text{ S cm}^{-1}$ . The highest conductivity at room temperature is obtained with  $80\text{Li}_2\text{S}\cdot 20\text{AlI}_3$ , which is approximately  $6.0 \times 10^{-5} \text{ S cm}^{-1}$ . The values of ionic conductivity obtained in this study are much higher than that of any  $\text{Li}_2\text{S}$ -based substances reported so far.<sup>16</sup> Hayashi et al. reported that the  $60\text{Li}_2\text{S}\cdot 40\text{AlI}_3$  amorphous solid electrolyte prepared by mechanical milling showed an ionic conductivity of  $3.4 \times 10^{-5} \text{ S cm}^{-1}$  at room temperature as a pure Li ion conductor.<sup>7</sup> Thus, aluminum ions in the  $\text{Li}_2\text{S}$  matrix spatially localize to occupied sites, and the  $\text{Li}_2\text{S}\text{-AlI}_3$  system is most likely a pure Li ion conductor. The results of the I-V correlation measurements using blocking electrodes for evaluation of electron conductivity are shown in Figure 3.4.4b. The results confirm that  $\text{Li}_2\text{S}$  is nearly insulating toward electrons at applied voltages up to 1 V. Adding  $\text{AlI}_3$  increases the electronic conductivity by one order of magnitude compared to the pristine  $\text{Li}_2\text{S}$ .

### 3.4.5 Cell performance

Figure 3.4.5a shows the charge-discharge curves at the 1<sup>st</sup>, 10<sup>th</sup>, and 50<sup>th</sup> cycle of the cell using samples  $x = 0$  and  $x = 0.5$  as active materials. The overpotential of the cell drastically reduces with 0.5 mol%  $\text{AlI}_3$  doping. The overpotentials of both cells decrease during the first 10 cycles. Figure 3.4.5b plots the cyclic properties of ASLSBs employing electrode composites with  $x = 0, 0.5, 1.5,$  and  $2$ . The capacity and stability of cells with  $x = 0.5$  and  $x = 1.5$  are better than those of  $x = 0$  and  $x = 2$ . The initial Coulombic efficiency of  $x = 0.5$  and  $x = 1.5$  are 91.0% and 82.3% but those of  $x = 0$  and  $x = 2$  were 79.1% and 76.8 %, respectively. The highest capacities of the cells  $x = 0, 0.5, 1.5,$  and  $2$  are 880, 1059, 1006, and 869 mAh g<sup>-1</sup>, respectively. The capacity retention of the cells  $x = 0, 0.5, 1.5,$  and  $2$  after 60 cycles is 64.0%, 88.4%, 69.6%, and 71.2%, respectively. Thus, doping  $\text{AlI}_3$  into  $\text{Li}_2\text{S}$  improves not only initial capacity and initial Coulombic efficiency but also capacity retention. The cell with  $99.5\text{Li}_2\text{S}\cdot 0.5\text{AlI}_3$  demonstrates the best cell performance among the cell with the prepared cathode materials even though the ionic and electronic conductivity of  $\text{Li}_2\text{S}\text{-AlI}_3$  increases with increasing  $\text{AlI}_3$  content. The fact indicates no correlation between the electric conductivity and the cell performance in the  $\text{Li}_2\text{S}\text{-AlI}_3$  system. The enhanced cell performance of  $99.5\text{Li}_2\text{S}\cdot 0.5\text{AlI}_3$  cannot be described only by the improved electric conductivity properties. The reaction kinetics in Li-S battery depends on the surface reaction of  $\text{Li}_2\text{S}$  or S particles. In Chapter 3.3, I found that the  $\Gamma^-$  facilitates the redox reaction of  $\text{Li}_2\text{S}$  through its oxidation reaction to  $\text{I}_3^-$ , enhancing the cell performance. Thus, the reaction of  $\text{Li}_2\text{S}$  may be promoted by two joint effects: the catalytic effect of  $\text{Al}^{3+}$ , and activation by  $\Gamma^-$  as a redox mediator. In addition, Augustyn et al. revealed that LiI coating on  $\text{Li}_2\text{S}$  particles lowers the barrier for grain boundary diffusion between the  $\text{Li}_2\text{S}$  and  $\text{Li}_6\text{PS}_5\text{Cl}$  based on NMR analysis.<sup>17</sup>  $\text{AlI}_3$  doping could enhance the grain boundary diffusion between the electrode and solid electrolyte because of the high polarization of I-ion. These experimental results suggest the importance of interface design to establish high redox reaction kinetics of  $\text{Li}_2\text{S}$  in ASLSBs. It is believed that the solid electrolyte

in the cathode composite is activated by the high-energy ball milling employed to prepare the cathode composite in this study. A comparison of battery performance including cell design and operating conditions is listed in Table 1. The cathode composite reported here is more attractive among other  $\text{Li}_2\text{S}$ -based cathode composites reported in the recent literature in terms of high specific capacity per gram of cathode composite, as well as areal  $\text{Li}_2\text{S}$  loading and cycling stability.

### 3.4.6 Conclusions

In summary, this work has demonstrated  $(100 - x)\text{Li}_2\text{S}-x\text{AlI}_3$  ( $0 \leq x \leq 5$ ) solid solutions for ASLSBs. The  $\text{AlI}_3$  doped  $\text{Li}_2\text{S}$  cathode materials were prepared by the planetary ball-milling method. XRD and UV-Vis studies demonstrate that  $\text{AlI}_3$  is dissolved in the  $\text{Li}_2\text{S}$  matrix during the preparation process. XPS results point out that the electronic structures of  $\text{Li}_2\text{S}$  are changed by the addition of  $\text{AlI}_3$ . This change leads to the formation of new UV-Vis absorption bands, increasing both ionic and electronic conductivities. Better initial capacity, Coulombic efficiency, and capacity retention are also obtained with the cells using  $\text{Li}_2\text{S}-\text{AlI}_3$  solid solution compared with the one employing bare  $\text{Li}_2\text{S}$ . This work provides a facile strategy to improve the electrochemical performance of materials for ASLSBs.

## References

- (1) Hakari, T.; Hayashi, A.; Tatsumisago, M. Li<sub>2</sub>S-Based Solid Solutions as Positive Electrodes with Full Utilization and Superlong Cycle Life in All-Solid-State Li/S Batteries. *Adv. Sustain. Syst.* **2017**, *1*, 1700017–1700023.
- (2) Shigedomi, T.; Fujita, Y.; Kishi, T.; Motohashi, K.; Tsukasaki, H.; Nakajima, H.; Mori, S.; Tatsumisago, M.; Sakuda, A.; Hayashi, A. Li<sub>2</sub>S-V<sub>2</sub>S<sub>3</sub>-LiI Bifunctional Material as the Positive Electrode in the All-Solid-State Li/S Battery. *Chem. Mater.* **2022**, *34*, 9745–9752.
- (3) Mwizerwa, J. P.; Zhang, Q.; Han, F.; Wan, H.; Cai, L.; Wang, C.; Yao, X. Sulfur-Embedded FeS<sub>2</sub> as a High-Performance Cathode for Room Temperature All-Solid-State Lithium-Sulfur Batteries. *ACS Appl. Mater. Interfaces* **2020**, *12*, 18519–18525.
- (4) Chung, S. H.; Manthiram, A. A Li<sub>2</sub>S-TiS<sub>2</sub>-Electrolyte Composite for Stable Li<sub>2</sub>S-Based Lithium-Sulfur Batteries. *Adv Energy Mater* **2019**, *9*, 1901397–1901405.
- (5) Chung, S. H.; Luo, L.; Manthiram, A. TiS<sub>2</sub>-Polysulfide Hybrid Cathode with High Sulfur Loading and Low Electrolyte Consumption for Lithium-Sulfur Batteries. *ACS Energy Lett.* **2018**, *3*, 568–573.
- (6) Phuc, N. H. H.; Takaki, M.; Hiroyuki, M.; Atsunori, M. Preparation of Li<sub>1-3x</sub>Al<sub>x</sub>S for All-Solid-State Li-S Battery. *Front. Energy Res.* **2021**, *8*, 606023–606029.
- (7) Yubuchi, S.; Uematsu, M.; Deguchi, M.; Hayashi, A.; Tatsumisago, M. Lithium-Ion-Conducting Argyrodite-Type Li<sub>6</sub>PS<sub>5</sub>X (X = Cl, Br, I) Solid Electrolytes Prepared by a Liquid-Phase Technique Using Ethanol as a Solvent. *ACS Appl. Energy Mater.* **2018**, *1*, 3622–3629.
- (8) Hayashi, A.; Fukuda, T.; Morimoto, H.; Minami, T.; Tatsumisago, M. Amorphous Solid Electrolytes in the System Li<sub>2</sub>S-Al<sub>2</sub>S<sub>3</sub>-SiS<sub>2</sub> Prepared by Mechanical Milling. *J. Mater. Sci.* **2004**, *39*, 5125–5127.
- (9) Kawasaki, Y.; Tsukasaki, H.; Ayama, T.; Mori, S.; Deguchi, M.; Tatsumisago, M.; Sakuda, A.; Hayashi, A. Synthesis and Electrochemical Properties of Li<sub>3</sub>CuS<sub>2</sub> as a Positive Electrode Material for All-Solid-State Batteries. *ACS Appl. Energy Mater.* **2021**, *4*, 20–24.
- (10) Kim, S.; Kim, S.-K.; Sun, P.; Oh, N.; Braun, P. v. Reduced Graphene Oxide/LiI Composite Lithium Ion Battery Cathodes. *Nano Lett.* **2017**, *17*, 6893–6899.
- (11) Lin, Y.; Wen, Z.; Liu, J.; Wu, D.; Zhang, P.; Zhao, J. Constructing a Uniform Lithium Iodide Layer for Stabilizing Lithium Metal Anode. *J. Energy Chem.* **2021**, *55*, 129–135.
- (12) Seh, Z. W.; Wang, H.; Liu, N.; Zheng, G.; Li, W.; Yao, H.; Cui, Y. High-Capacity Li<sub>2</sub>S-Graphene Oxide Composite Cathodes with Stable Cycling Performance. *Chem. Sci.* **2014**, *5*, 1396–1400.
- (13) Yu, L.; Liu, F.-C.; Fu, Z.-W. Electrochemical Features of Al/I<sub>2</sub> Batteries in Water and Non-Aqueous Solution. *Electrochim. Acta* **2009**, *54*, 2818–2822.

- (14) Lin, Z.; Liu, Z.; Dudney, N. J.; Liang, C. Lithium Superionic Sulfide Cathode for All-Solid Lithium–Sulfur Batteries. *ACS Nano* **2013**, *7*, 2829–2833.
- (15) Jiao, Z.; Chen, L.; Si, J.; Xu, C.; Jiang, Y.; Zhu, Y.; Yang, Y.; Zhao, B. Core-Shell  $\text{Li}_2\text{S}@\text{Li}_3\text{PS}_4$  Nanoparticles Incorporated into Graphene Aerogel for Lithium-Sulfur Batteries with Low Potential Barrier and Overpotential. *J. Power Sources* **2017**, *353*, 167–175.
- (16) Lorger, S.; Usiskin, R. E.; Maier, J. Transport and Charge Carrier Chemistry in Lithium Sulfide. *Adv. Funct. Mater.* **2019**, *29*, 1807688–1807698.
- (17) Liu, M.; Wang, C.; Zhao, C.; van der Maas, E.; Lin, K.; Arszewska, V. A.; Li, B.; Ganapathy, S.; Wagemaker, M. Quantification of the Li-Ion Diffusion over an Interface Coating in All-Solid-State Batteries via NMR Measurements. *Nat. Commun.* **2021**, *12*, 5943–5952.
- (18) Yan, H.; Wang, H.; Wang, D.; Li, X.; Gong, Z.; Yang, Y. In Situ Generated  $\text{Li}_2\text{S}-\text{C}$  Nanocomposite for High-Capacity and Long-Life All-Solid-State Lithium Sulfur Batteries with Ultrahigh Areal Mass Loading. *Nano Lett.* **2019**, *19*, 3280–3287.
- (19) Jiang, H.; Han, Y.; Wang, H.; Zhu, Y.; Guo, Q.; Jiang, H.; Zheng, C.; Xie, K.  $\text{Li}_2\text{S}-\text{Li}_3\text{PS}_4$  (LPS) Composite Synthesized by Liquid-Phase Shaking for All-Solid-State Lithium–Sulfur Batteries with High Performance. *Energy Technol.* **2020**, *8*, 2000023–2000029.
- (20) Liang, J.; Sun, Q.; Zhao, Y.; Sun, Y.; Wang, C.; Li, W.; Li, M.; Wang, D.; Li, X.; Liu, Y.; Adair, K.; Li, R.; Zhang, L.; Yang, R.; Lu, S.; Huang, H.; Sun, X. Stabilization of All-Solid-State Li–S Batteries with a Polymer–Ceramic Sandwich Electrolyte by Atomic Layer Deposition. *J. Mater. Chem. A* **2018**, *6*, 23712–23719.
- (21) Eom, M.; Son, S.; Park, C.; Noh, S.; Nichols, W. T.; Shin, D. High Performance All-Solid-State Lithium-Sulfur Battery Using a  $\text{Li}_2\text{S}-\text{VGCF}$  Nanocomposite. *Electrochim. Acta* **2017**, *230*, 279–284.

**Table 3.4.1.** Comparison of all-solid-state cells with Li<sub>2</sub>S-based cathode composites.

Active material	Content of active materials	Loading [mg cm <sup>-2</sup> ]	Current density [mA cm <sup>-2</sup> ]	Cycle number	Specific capacity [mA g <sup>-1</sup> (active materials)]	Specific capacity [mA g <sup>-1</sup> (composite cathode)]	Operating temperature [°C]	Ref.
Li <sub>2</sub> S	30.6%	0.2-0.5	0.04	30	720	220	60	14
Li <sub>2</sub> S	28.9%	0.9-1.1	0.58	60	1100	318	25	1
Li <sub>2</sub> S	38.0%	3.5	0.2	10	1047	398	RT	18
Li <sub>2</sub> S	50.0%	3.84	0.2	30	674	337	60	19
Li <sub>2</sub> S	35.8%	3.6	0.13	60	830	297	RT	20
Li <sub>2</sub> S	30.0%	2.24	0.044	50	525	161	RT	21
Li <sub>2</sub> S	48.0%	2.45	0.285	60	936	449	30	This work

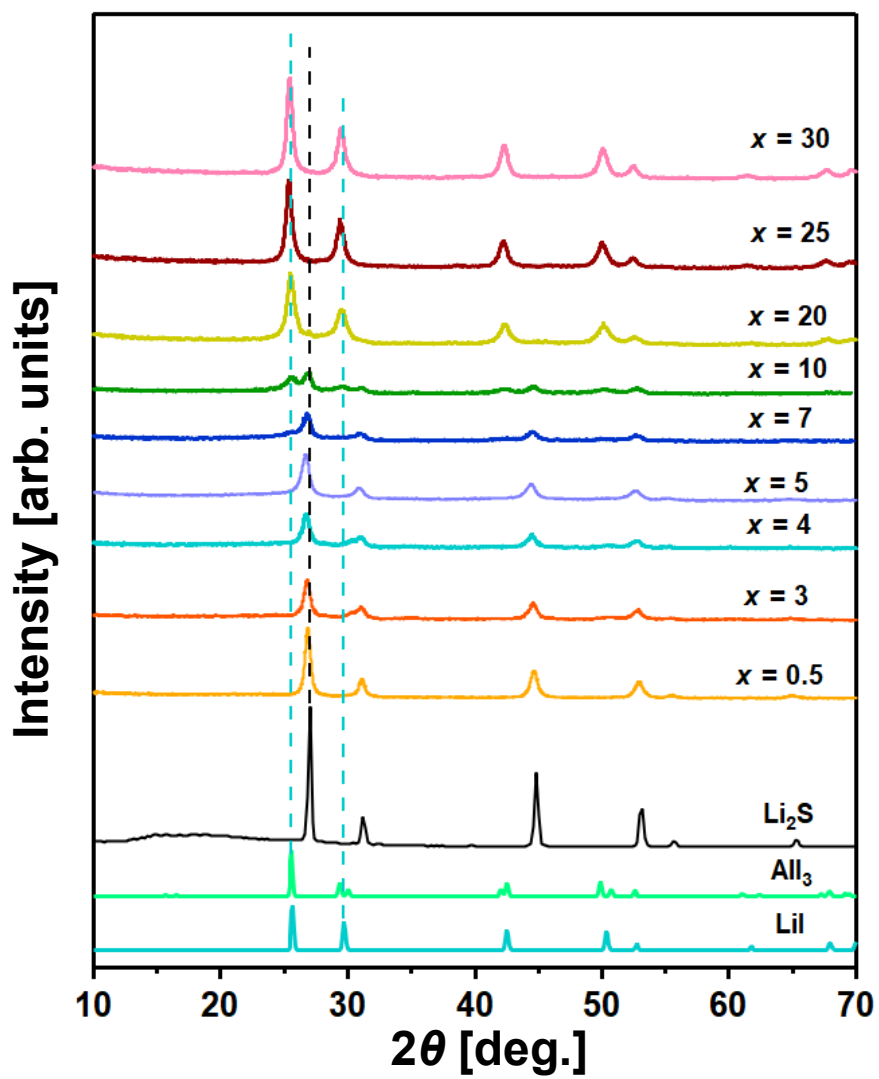


Figure 3.4.1. XRD patterns of  $(100-x)\text{Li}_2\text{S}-x\text{AlI}_3$  prepared by high-energy ball milling.

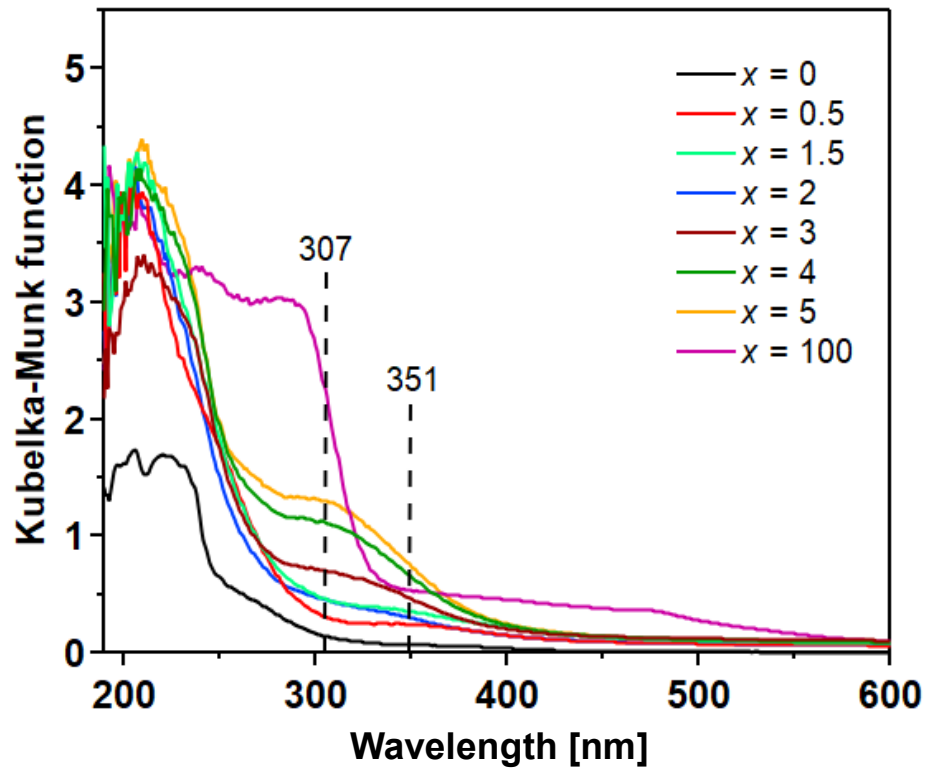
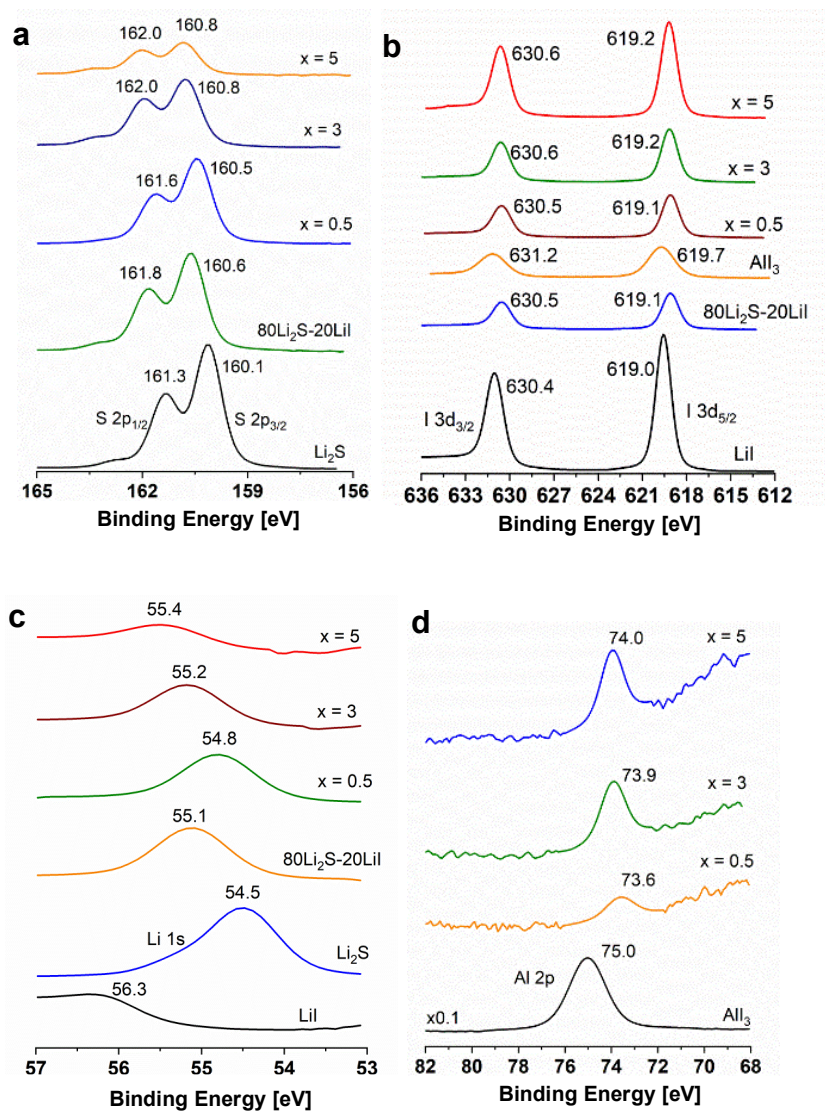
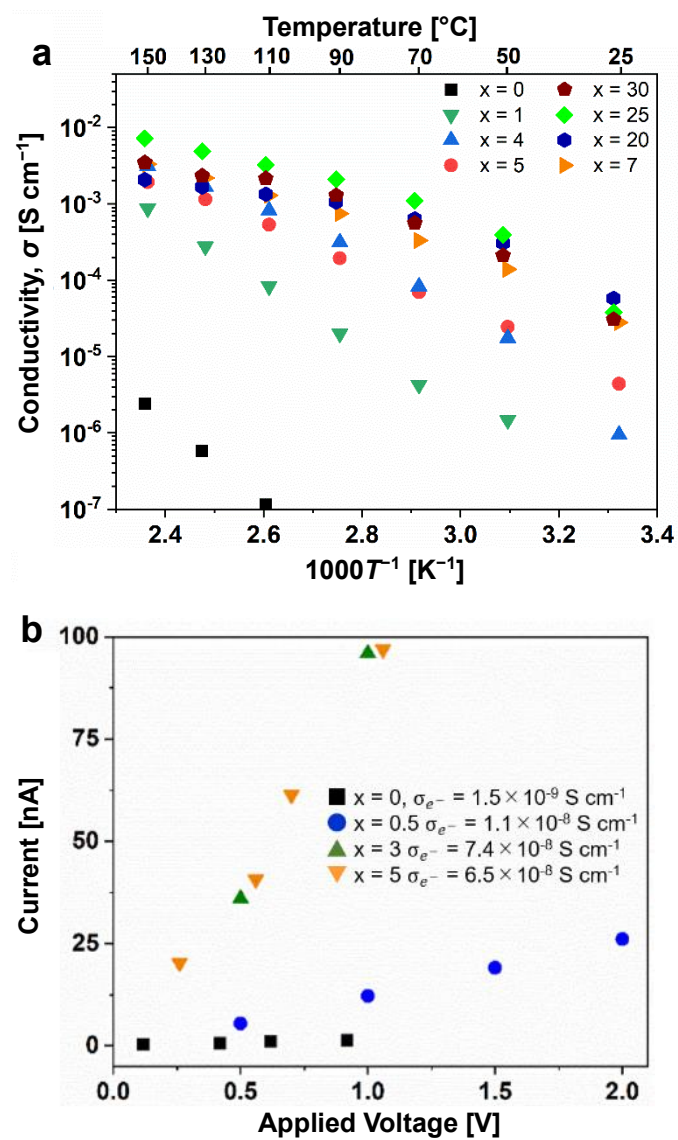


Figure 3.4.2. UV-Vis spectra of  $\text{Li}_2\text{S}$  ( $x = 0$ ),  $\text{AlI}_3$  ( $x = 100$ ), and  $(100-x)\text{Li}_2\text{S}-x\text{AlI}_3$ .





**Figure 3.4.3.** XPS spectra of the prepared samples and standard materials. (a) S 2p; (b) I 3d; (c) Li 1s; (d) Al 2p.



**Figure 3.4.4.** (a) Temperature dependence of ionic conductivity and (b) I–V correlation (polarized electronic current) of  $(100-x)\text{Li}_2\text{S}-x\text{AlI}_3$ .

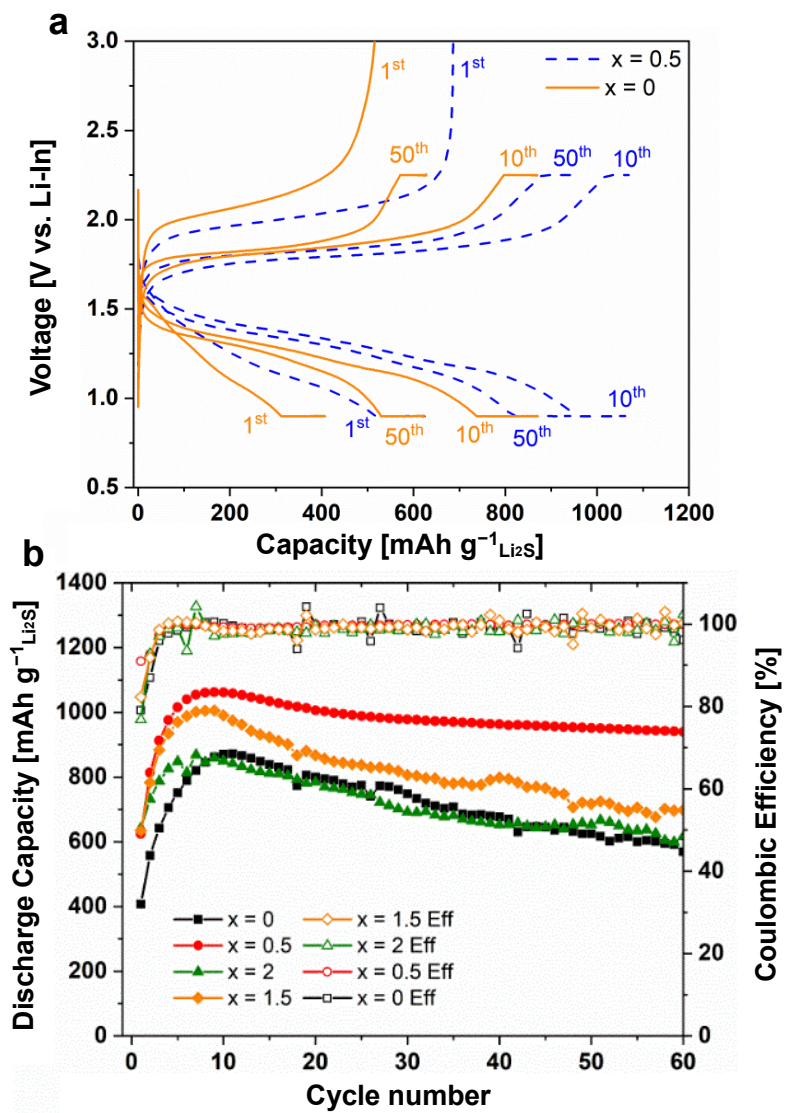


**Figure 3.4.5.** (a) Charge–discharge curves of ASLSBs employing electrode composites with  $x = 0$  and  $0.5$ ; (b) cyclic properties of ASLSBs employing electrode composites with  $x = 0, 0.5, 1.5,$  and  $2$ .

## 3.5 Understanding Decomposition of Electrolytes in All-Solid-State Lithium–Sulfur Batteries

In this chapter, I unveil the redox chemistry related to  $\text{Li}_2\text{S}/\text{S}$  conversion reaction, electrolyte decomposition, and redox reaction of the decomposition product, based on differential capacity curves. The oxidation reaction of  $\text{Li}_2\text{S}$  proceeds simultaneously with a continuous oxidative decomposition of sulfide SEs. Raman spectroscopy of the cell after cycling shows that SEs in the cathode convert the thiophosphates with a S-S bond via the decomposition behavior of the electrolytes. The implication of this reaction chemistry is expanded toward understanding the  $\text{Li}_2\text{S}$  activation process in ASSLSBs.  $\text{Li}_2\text{S}/\text{SE}$  interface modification by different rotation speeds of ball milling in SE mixing allows us to control the decomposition kinetics of electrolytes. The severe decomposition of electrolytes causes cycle fading instead of increasing the electrochemical redox activity in the early period. The findings of this work highlight the need for interface engineering to avoid severe degradation of electrolytes in the cathode and enhance the ability of SEs as a redox mediator.

### 3.5.1 Introduction

In Chapter 3.2 to 3.4, I discussed the development of the novel  $\text{Li}_2\text{S}$  cathode materials for improved redox reaction kinetics in ASLSBs. In contrast to this, Ohno et al. pointed out that the conduction properties of SEs blended in cathode composites hold a key to improving the utilization of sulfur cathodes because sluggish ionic transport properties in the cathode limit the battery performance of ASLSBs.<sup>1</sup> The sulfide SEs in the cathode decompose into chemical species with electrochemical redox activity at the highly electrochemically conductive surfaces with a carbon additive in the charging process.<sup>2–8</sup> The decomposition of electrolytes results in the loss of ionic conduction pathways, degrading the overall cell performance.<sup>2</sup> Thus, the understanding of the electrolyte decomposition in the charge/discharge process must be taken into account. In contrast, the redox-active chemical species produced through the oxidative decomposition of sulfide SE decreases the charge overpotential of  $\text{Li}_2\text{S}$  in liquid Li-S batteries.<sup>9</sup> Thus, sulfide SEs can serve as a redox mediator in ASLSBs owing to their electrolyte decomposition behavior, in addition to their role as conduction pathways. However, there is a lack of fundamental studies on the electrochemical redox-active decomposition product produced from sulfide SEs in ASLSBs. This is because the onset potential of the oxidative decomposition of SEs is close to the oxidation potential of  $\text{Li}_2\text{S}$ . In addition, the voltage profile of ASLSBs shows a single discharge plateau compared to the two-plateaued discharging voltage profile in liquid Li-S batteries.<sup>10</sup> These electrochemical behaviors have resulted in misinterpretation of redox reactions among many

researchers. In fact, the reported voltage profiles of ASLSBs involve multistep plateaus in the discharge process, whereas such reaction steps have been obscure so far.<sup>11–20</sup> A recent study reported that the  $\text{Li}_2\text{S}$  cathode composites fabricated by mixing  $\text{Li}_3\text{PS}_4$  (LPS) in a mortar did not show any electrochemical activity of LPS, excluding the capacity contribution of SEs in ASLSBs.<sup>21</sup> Nevertheless, the voltage profiles seem to involve reduction reactions with multisteps in the aforementioned reports; the reason for these reactions is still unclear. In addition, such an ambiguous reaction mechanism brings a limited understanding of the  $\text{Li}_2\text{S}$  activation process: a high activation barrier in the first charge process and increased capacity during the early cycle, observed in the galvanostatic charge/discharge tests of  $\text{Li}_2\text{S}$ ,  $\text{Li}_2\text{S-CaS}$ ,  $\text{Li}_2\text{S-CaX}$  ( $X = \text{Cl, Br, and I}$ ), and  $\text{Li}_2\text{S-AlI}_3$  (see Chapter 3.2-3.4).

In the present work, I identify the electrochemical decomposition behavior of SEs in ASLSBs using galvanostatic charge-discharge tests and their differential capacity curves. These fundamental experiments provide insight into the ASLSBs electrochemistry involving the  $\text{Li}_2\text{S}$  redox reaction, oxidative decomposition of sulfide SEs, and redox reaction of the decomposition product in ASLSBs. This redox chemistry contributes to the understanding of the  $\text{Li}_2\text{S}$  activation process in ASLSBs. Additionally, I investigate the effect of different  $\text{Li}_2\text{S/SE}$  interfaces, which are designed by altering the rotation speeds (250 and 510 rpm) in LPS SE mixing, on cell performance. Engineering the  $\text{Li}_2\text{S/SE}$  interface controls the electrolyte decomposition kinetics governing the ability of SEs as a redox mediator and cycle stability. This gives insight into an optimized design of ASLSBs that can suppress cycle fading and enhance the electrochemical redox activity owing to the decomposition of SEs.

### 3.5.2 Experimental methods

**Chemicals.** Lithium sulfide (99.9%, Mitsuwa),  $\text{LiCl}$  (99.99%, Wako Fujifilm),  $\text{P}_2\text{S}_5$  (99%, Merck), and VGCF (Showa Denko) were procured and used without additional purification.

**Synthesis of cathode materials and SEs.** For the synthesis of the  $\text{Li}_2\text{S}$  cathode material, 1 g of  $\text{Li}_2\text{S}$  particles was ball-milled using planetary ball milling (Fritsch Pulverisette 7 Premium line) and 45 ml of zirconia pots containing 15 zirconia balls with a diameter of  $\phi$  10 mm at a rotation speed of 510 rpm for 10 h. Amorphous LPS SEs were prepared by ball milling a mixture powder (1 g) of  $\text{Li}_2\text{S}$  and  $\text{P}_2\text{S}_5$  at a molar ratio of 3:1 under identical conditions, as described above.  $\text{Li}_{5.5}\text{PS}_{4.5}\text{Cl}_{1.5}$  SEs were prepared for the electrolyte layer by ball milling a mixture (2 g) of  $\text{Li}_2\text{S}$ ,  $\text{P}_2\text{S}_5$ , and  $\text{LiCl}$  with a stoichiometric ratio at a rotation speed of 600 rpm for 20 h followed by heat treatment at 450 °C for 2 h.

**Synthesis of cathode composites.** For the synthesis of cathode composites, 0.4 g of  $\text{Li}_2\text{S}$  and VGCF powders with a weight ratio of 5:1 was first ball-milled with 45 ml of zirconia pots

containing 35 g of  $\phi$  4 mm zirconia balls at a rotation speed of 510 rpm for 10 h. 0.4 g of the  $\text{Li}_2\text{S}$ -VGCF and amorphous LPS powders with a weight ratio of 6:4 was then ball-milled with 45 ml of zirconia pots containing 35 g of  $\phi$  4 mm zirconia balls at a rotation speed of 250 or 510 rpm for 2 h. The obtained  $\text{Li}_2\text{S}$ -LPS-VGCF cathode composites milled at 250 and 510 rpm were denoted as  $\text{Li}_2\text{S}$ -250 and  $\text{Li}_2\text{S}$ -510, respectively. For the synthesis of LPS-VGCF cathode composites, 0.4 g of amorphous LPS and VGCF powders a weight ratio of 9:1 was ball-milled at a rotation speed of 250 and 510 rpm for 2 h.

**Cell assembly.** For galvanostatic cycling tests, the  $\text{Li-In} \mid \text{Li}_{5.5}\text{PS}_{4.5}\text{Cl}_{1.5} \mid \text{Li}_2\text{S}$ -250 and -510 cells were assembled as follows. First, 80 mg of  $\text{Li}_{5.5}\text{PS}_{4.5}\text{Cl}_{1.5}$  powder was filled with a PEEK with two stainless-steel rods, followed by the application of a uniaxial pressure of 256 MPa to form pellets with diameters of  $\sim 10.0$  mm at room temperature. The cathode composites were spread over one side of the SE layer and pressed under 256 MPa at room temperature. The  $\text{Li}_2\text{S}$  cathode material loading in  $\text{Li}_2\text{S}$ -250 and -510 is  $3.2 \text{ mg cm}^{-2}$ . Indium and Li foils were placed on the other side of the SE layer and pressed under 90 MPa at room temperature. The assembled cell was sandwiched between two stainless steel rods under a pressure of approximately 50 MPa for electrochemical measurement. The cells were rested for 1 h before performing the galvanostatic cycling test for alloying. In the case of LPS-VGCF cathode composites, the LPS material loading is  $5.7 \text{ mg cm}^{-2}$ .

**Electrochemical measurements.** The fabricated cells were cycled under 0.1C (corresponding to the current density of approximately  $0.292 \text{ mA cm}^{-2}$ ) in a voltage range of 0.6–3.0 V (vs Li-In) at 30 °C using a charge-discharge device (Nagano, BST-2004H). EIS was performed for the cell with  $\text{Li}_2\text{S}$ -250 and -510 at the state of full charge and discharge using an electrochemical measurement system HZ-Pro (Hokuto Denko) in the frequency range of 1 MHz to 1 mHz and an applied voltage of 10 mV.

**Material characterization.** Powder XRD measurements were conducted with Cu  $K\alpha$  radiation and a scan rate of  $5^\circ \text{ min}^{-1}$  using Rigaku SmartLab SE. Structural refinements were analyzed by the Rietveld method using RIETAN-FP computer program.<sup>22</sup> The crystalline size,  $D$ , of  $\text{Li}_2\text{S}$  in the prepared cathode composite was calculated from the Halder-Wagner method presented in Eq. 3.5.1:

$$\left( \frac{\beta}{\tan\theta} \right)^2 = \frac{K\lambda}{D} \frac{\beta}{\tan\theta \sin\theta} + 16\epsilon^2 \quad (3.5.1)$$

Where  $\beta$  is the integral breadth,  $K$  is constant (0.94),  $\epsilon$  is the microstrain, and  $\lambda$  is the wavenumber of X-rays. The field-emission SEM was performed using Hitachi-S4800 with an EDS (Ultim Max, Oxford Instrument). The sample for SEM characterization was directly prepared from powder.

### 3.5.3 Structural properties of pulverized SEs

Engineering the cathode/SE interface using the ball milling treatment allows us to modify the electrochemical redox kinetics of SEs and sulfur cathodes.<sup>23-25</sup> To gain insights into the effect of the structural properties of LPS SEs on the electrochemical activity, I evaluated the structural properties of the LPS SEs milled at rotation speeds of 250 and 510 rpm (denoted as LPS-250 and LPS-510). Figure 3.5.1a-c shows the SEM images of LPS, LPS-250, and LPS-510, respectively. The average secondary particle sizes of LPS-250 and -510 were calculated to be  $62.2 \pm 24.0 \mu\text{m}$  and  $42.0 \pm 15.9 \mu\text{m}$ , respectively. These surface morphologies are similar to pristine LPS particles. Figure 3.5.2a shows the XRD patterns of pristine LPS, LPS-250, and LPS-510. A halo pattern is observed in all of the samples, indicating that they form an amorphous structure. Raman spectroscopy was performed on pristine LPS, LPS-250, and LPS-510 to investigate the modification of the local structure induced by ball milling (Figure 3.5.2b). Raman spectra of the pristine LPS have three Raman peaks at 280, 405, and  $436 \text{ cm}^{-1}$ . Raman spectroscopy study in previous work reported that amorphous  $\text{Li}_3\text{PS}_4$  consists of the  $\text{PS}_4^{3-}$  assigned to the Raman peak at  $420 \text{ cm}^{-1}$  and  $\text{P}_2\text{S}_6^{4-}$  assigned to the Raman peak at  $386 \text{ cm}^{-1}$  anion units.<sup>26</sup> Thus, the obvious peak at  $436 \text{ cm}^{-1}$  corresponds to the symmetric stretching vibration of the P-S covalent bond in the isolated  $\text{PS}_4^{3-}$  anion units and the peak at  $405 \text{ cm}^{-1}$  corresponds to  $\text{P}_2\text{S}_6^{4-}$  anion units. In addition, the broad peak at  $280 \text{ cm}^{-1}$  is attributed to the bending vibration of the intramolecular S-S repulsion in the isolated  $\text{PS}_4^{3-}$  anion units.<sup>27</sup> In LPS-250 and -510, the peaks corresponding to the  $\text{P}_2\text{S}_6^{4-}$  ( $393 \text{ cm}^{-1}$ ) and P-S covalent bond in the  $\text{PS}_4^{3-}$  ( $428 \text{ cm}^{-1}$ ) are observed. These peaks shift toward the lower wavenumber (i.e., red shifting) in comparison with the pristine LPS, which indicates a softening of the lattice.<sup>28</sup> In contrast to these peak shifts, no shift of the peak corresponding to the S-S bond in the  $\text{PS}_4^{3-}$  is detected. The spectra of LPS-510 are broader than those of the pristine LPS and LPS-250. This observation implies that the  $\text{PS}_4^{3-}$  tetrahedra are distorted by ball milling treatment with a higher rotation speed. These experimental results highlight that ball milling treatment leads to the loose P-S covalent bond in the  $\text{PS}_4^{3-}$  of amorphous LPS and distortion of the  $\text{PS}_4^{3-}$  tetrahedra in LPS-510. Therefore, ball milling with a higher rotation speed for the pulverization leads to a decrease in the secondary particle size and the distorted local structure of LPS SEs.

### 3.5.4 Decomposition Behavior of SEs

Figure 3.5.3a plots the ionic conductivity versus inverse temperature of the pelletized pristine LPS, LPS-250, and LPS-510. These samples exhibit the ionic conductivities of  $4.8 \times 10^{-4}$ ,  $4.1 \times 10^{-4}$ , and  $2.8 \times 10^{-4} \text{ S cm}^{-1}$  at  $30 \text{ }^\circ\text{C}$ , respectively. The change in the ionic conductivity may be caused by the distortion of the  $\text{PS}_4^{3-}$  anion unit observed in the Raman spectra. Additionally, Ates et al. reported that  $\beta$ -LPS SE pellets with higher porosity and a larger particle size show higher

ionic conductivity. This observation demonstrates the major effect of grain boundary resistance on the ionic conductivity of  $\beta$ -LPS.<sup>29</sup> The pelletized pristine LPS, LPS-250, and LPS-510 have pellet densities of 1.82, 1.93, and 2.22 g cm<sup>-3</sup>, which are calculated from the volume measured by the dimensions of the pellets, respectively. The LPS with the lower pellet density and larger particle size shows higher ionic conductivity. The decrease in ionic conductivity induced by ball milling may be originated not only from the modified local structure but also the grain boundary resistance. Figure 3.5.3b depicts galvanostatic charge-discharge profiles of 90LPS-10VGCF (wt%) milled at rotation speeds of 250 rpm and 510 rpm (denoted as 90LPS-10VGCF-250 and -510, respectively) under a current density of 0.13 mA cm<sup>-2</sup> at 30 °C. Compared to the cell with 90LPS-10VGCF-250, the cell with 90LPS-10VGCF-510 exhibits a higher capacity for 50 cycles. The particle size of the component in the electrode dictates electronic and/or ionic contact, affecting the electrochemical reaction kinetics of active materials in all-solid-state Li-ion batteries.<sup>23,30</sup> The high capacity of the 90LPS-10VGCF-510 is attributed to a larger interfacial contact area between the smaller SEs and VGCF but not the effective ionic conductivity of SEs in the cathode. This larger contact area can be explained by the higher pellet density of LPS-510 than that of LPS-250. Figure 3.5.3c shows the differential charge capacity curves of the cell with 90LPS-10VGCF-510. The curves involve an oxidation peak at 2.27 V in the first charge process, and its intensity declines with each cycle. After the initial oxidation reaction, a new oxidation peak appears at 1.76 V in the second cycle. Sulfide SEs decompose into redox-active chemical species containing the complex  $-P-[S_n]-P-$  species and sulfur.<sup>1,4-6,8,9,31-35</sup> In other words, once the LPS is oxidized, it cannot return to its pristine electron structure. The oxidation peaks at 2.27 V and 1.76 V correspond to the decomposition reaction of LPS and oxidation reaction of the decomposition product, respectively. In contrast to the oxidation at 2.27 V, the oxidation peak observed at 1.76 V is maintained throughout the cycle, which indicates that the decomposition product has reversible redox activity.<sup>31</sup> Figure 3.5.3d shows Raman spectra of LPS-VGCF-250 and -510 after the first cycle. No change in the local structure is detected in LPS-VGCF-250 before and after the cycle. In LPS-VGCF-510, the Raman peak of the  $PS_4^{3-}$  anion unit becomes sharp after the cycle, which indicates that the reorientation of  $PS_4^{3-}$  occurs through the charge/discharge process. Given that the LPS-VGCF-510, in which the reorientation of  $PS_4^{3-}$  occurs, shows a higher capacity than LPS-VGCF-250, the modified local structure of amorphous LPS leads to no significant impact on the electrochemical redox activity.

### 3.5.5 Impact of the Li<sub>2</sub>S/LPS Interface on Battery Performance

The oxidative decomposition of LPS results in redox activity, which can improve the battery performance limited by the sluggish kinetics of Li<sub>2</sub>S cathode materials. The Li<sub>2</sub>S reaction chemistry with contributions from the interfacial reaction between LPS and Li<sub>2</sub>S (or VGCF) must



be taken into account. The cathode composites with different interface designs were fabricated as shown in Figure 3.5.4a. The Li<sub>2</sub>S-VGCF composite shows broader Bragg peaks than milled Li<sub>2</sub>S, which is attributed to the smaller crystalline size of Li<sub>2</sub>S in Li<sub>2</sub>S-VGCF composites (Figure 3.5.4b). Ball milling treatment for VGCF mixing further pulverizes the Li<sub>2</sub>S particles. Using the Halder-Wagner method, the average crystalline size of the Li<sub>2</sub>S crystal was calculated to be 16.1 nm for Li<sub>2</sub>S-250 and 11.1 nm for Li<sub>2</sub>S-510. The milled Li<sub>2</sub>S involves rough secondary particles of over 50 μm in diameter (Figure 3.5.4c). As can be seen in Figure 3.5.4d and e, the SEM-EDS images reveal that each particle in Li<sub>2</sub>S-250 and -510 is aggregated and is in close contact with the others. Phosphorus and sulfur atoms are evenly distributed across the entire particle. The electrochemical redox activity of Li<sub>2</sub>S is affected by its microstructure.<sup>24,36–38</sup> Based on the structural properties of LPS SEs and Li<sub>2</sub>S cathode composites, I believe that Li<sub>2</sub>S-250 and -510 were fabricated, in which Li<sub>2</sub>S shows similar redox activity and LPS has different secondary particle sizes. Figure 3.5.5a and b presents the galvanostatic charge-discharge profiles of the cells with Li<sub>2</sub>S-250 and -510, respectively. Both cells show a high activation barrier in the first charge process. The capacity of these cells is ~350 mAh g<sup>-1</sup> in the first discharge and increases with each cycle (Figure 3.5.5c). This increase of capacity in the early period and the high activation barrier in the initial cycle are called the activation process.<sup>15,18,24,39</sup> The capacity of the cell with Li<sub>2</sub>S-510 reaches a maximum of 564 mAh g<sup>-1</sup> after 16 cycles and then decreases to 212 mAh g<sup>-1</sup> with a low capacity retention of 59% after 100 cycles. This decrease in capacity should be caused by the degradation of electrolytes.<sup>2,40</sup> In contrast, the cell with Li<sub>2</sub>S-250 shows a maximum capacity of 496 mAh g<sup>-1</sup>, achieving relatively stable battery performance in long-term cycles.

The Coulombic and conversion efficiencies were calculated to uncover the evolution of electrolyte degradation during the charge-discharge cycle (Figure 3.5.5d). The conversion efficiency  $\phi_C$  can be determined by dividing the discharge capacity  $Q_{d,n}$  by the charge capacity  $Q_{c,n-1}$ , where  $n$  is the cycle number.<sup>2</sup> The Coulombic efficiency  $\phi_Q$  can be determined by dividing the discharge capacity  $Q_{d,n}$  by the charge capacity  $Q_{c,n}$  in the same cycle. The efficiency is dominated by three contributions: the cathode material, decomposition of SEs, and redox-active decomposition product. The  $\phi_Q$  values of Li<sub>2</sub>S-250 and -510 show 82 and 94% in the first cycle, respectively. The  $\phi_Q$  stabilizes at 100% for Li<sub>2</sub>S-250 and 98.4% for Li<sub>2</sub>S-510 after a few cycles. The low  $\phi_Q$  can originate from the irreversibility associated with the chemo-mechanical failure and/or decomposition reaction of LPS. This chemomechanical failure should be caused by the volume change of the cathode material involving a redox reaction. The drastic drops in capacity and efficiency are observed in the 67th cycle, which can be attributed to the chemomechanical failure. Given that severe oxidative decomposition occurs at LPS milled at 510 rpm, as can be seen in Figure 3.5.3c, the low  $\phi_Q$  of Li<sub>2</sub>S-510 observed in long-term cycles should originate from the continuous decomposition reaction of SEs. The conversion efficiency of both Li<sub>2</sub>S-250 and -

510 is ~115% in the initial cycle and converged to 100% after several cycles. The efficiency of over 100% implies an additional capacity contribution of the LPS and increase in the electrochemical redox activity through the oxidation decomposition of LPS.

### 3.5.6 Reaction Chemistry of ASSLSBs

The differential capacity curves of the cells with Li<sub>2</sub>S-250 and -510 are shown in Figure 3.5.6a and b. The calculated differential curves show an oxidation peak(○) at ~2.3 V, a pronounced oxidation peak(☆) that appears after the second cycle, and two reduction peaks(□ & ◇). The first oxidation reaction occurs at the same potential as the oxidative decomposition of LPS, as confirmed in Figure 3.5.3c. However, the initial charge capacity of the cells with Li<sub>2</sub>S-250 and -510 is significantly different from that of 90LPS-10VGCF-510. This shows that the oxidation reaction of Li<sub>2</sub>S participates simultaneously with the oxidative decomposition of LPS. A Li<sub>2</sub>S electrode blended with LPS in liquid Li-S batteries is activated by a redox mediator generated from the delithiation of LPS, decreasing the charging potential in the first cycle.<sup>9</sup> Hence, LPS should serve as the redox mediator through the oxidative decomposition in ASSLSBs. The oxidative decomposition of LPS is observed even after the second cycle, which implies the dynamic evolution of the interface between LPS and Li<sub>2</sub>S (or VGCF, electron additive). To clarify the effect of the redox mediator of sulfide SEs, I evaluated the cell performance of a cathode composite blended with Li<sub>3</sub>YCl<sub>6</sub> SEs, which show oxidative stability in the operating voltage range of ASSLSBs.<sup>41</sup> The cell exhibits an extremely low capacity of less than 100 mAh g<sup>-1</sup>, although the ionic conductivity of Li<sub>3</sub>YCl<sub>6</sub> ( $\sigma_{30} = 2.9 \times 10^{-4}$  S cm<sup>-1</sup>) is similar to that of LPS Figure 3.5.7a-c. The cathode composite shows no oxidation decomposition of Li<sub>3</sub>YCl<sub>6</sub> in the charging process, as shown in Figure 3.5.7d of the differential charge capacity curves. In a recent study, Li<sub>3</sub>HoBr<sub>6</sub> having a high ionic conductivity of ~1 mS cm<sup>-1</sup> and oxidative stability was applied to ASSLSBs, resulting in a reversible capacity of 582 mAh g<sup>-1</sup> at 0.1C.<sup>42</sup> Here, the weight percentage of the sulfur cathode in cathode composites is only 8% and the operating temperature is 60 °C. These findings highlight that the redox behavior of SEs that are oxidated at a slightly higher oxidation reaction potential than Li<sub>2</sub>S enhances the redox reaction kinetics of Li<sub>2</sub>S in ASSLSBs. Hakari et al. have reported that the Li<sub>2</sub>S cathode blended with SEs or additives (such as lithium halide) with a slightly higher onset oxidation potential than Li<sub>2</sub>S shows a high reversible capacity of >1000 mAh g<sup>-1</sup> in ASSLSBs.<sup>21</sup> This high capacity was explained by the high ionic conduction networks in Li<sub>2</sub>S cathodes.<sup>21,43</sup> Unlike this notion, this work points out that those SEs can act as a redox mediator and accelerate the redox reaction kinetics of the Li<sub>2</sub>S cathode. As mentioned in Chapter 3.3, I-substituted Li<sub>2</sub>S-based cathode materials have achieved a superior higher discharge capacity under high C-rates compared to other halide-ion substituted Li<sub>2</sub>S-based cathode materials due to the redox behavior of I<sup>-</sup>, which involves the oxidation to I<sup>3-</sup> at a slightly

higher potential than the oxidation potential of  $\text{Li}_2\text{S}$ . In some cases of sulfide ASSLSBs, increasing the ionic conductivity of sulfide SEs by a factor of two leads to no significant improvement in the battery performance of ASSLSBs in the early cycle.<sup>12,14,52</sup> In contrast, the use of  $\text{Li}_7\text{P}_3\text{S}_{11}$  introduced  $\text{MoS}_2$  with high catalytic activity allows for significantly enhanced reversible capacity in the early cycle.<sup>45</sup> I believe that the development of SEs with inherent high catalytic activity can guide the advancement of ASSLSBs.

Distinguishable reduction peaks are observed at  $\sim 1.1$  ( $\square$ ) and  $\sim 1.3$  V ( $\diamond$ ) vs Li-In. A conversion reaction from solid to solid in Li-S batteries commonly occurs through a single step.<sup>46</sup> In addition, the reduction reaction of sulfur in ASSLSBs occurs at a potential of  $\sim 1.1$  V (vs Li-In).<sup>47</sup> Therefore, the reduction peaks at higher ( $\diamond$ ) and lower voltages ( $\square$ ) attribute to the decomposition products of LPS and S cathode material, respectively. The reduction peak corresponding to the conversion reaction of S ( $\square$ ) disappears completely after 50 cycles. In other words, the  $\text{Li}_2\text{S}$  cathode is inactivated through long-term cycling. The loss of redox activity indicates that the discharge capacity of  $\text{Li}_2\text{S}$ -250 and -510 after 50 cycles is entirely responsible for the reduction reaction of the decomposition product. Nevertheless, the capacities of  $\text{Li}_2\text{S}$ -250 and -510 are significantly higher than the capacity of the cell with 90LPS-10VGCF-510 after 50 cycles (Figure 3.5.3b). This implies that the decomposition product from LPS converts to compounds with higher redox activity through the charge/discharge process. To investigate the structural evolution of LPS in the cathode during charge/discharge, Raman analysis was performed on  $\text{Li}_2\text{S}$ -250 and -510 without treatment and after the 20th cycle (Figure 3.5.8). For the pristine  $\text{Li}_2\text{S}$ -250, two peaks are detected at 428 and 280  $\text{cm}^{-1}$ , which correspond to P-S and S-S bonds in the  $\text{PS}_4^{3-}$  anion unit, respectively. Raman spectra of  $\text{Li}_2\text{S}$ -250 after the 20th cycle show a weak peak related to the S-S bond at 241  $\text{cm}^{-1}$ . For the pristine  $\text{Li}_2\text{S}$ -510, a weak peak corresponding to the P-S the  $\text{PS}_4^{3-}$  anion unit is observed at 427  $\text{cm}^{-1}$ . After the 20th cycle, an obvious peak corresponding to P-S bonds in the  $\text{PS}_4^{3-}$  is detected, which suggests that the reorientation of  $\text{PS}_4^{3-}$  occurs through the charge/discharge process. Additionally, the peaks related to the symmetry species of the S-S bonds appear at 156, 224, 250, 440, and 476  $\text{cm}^{-1}$ . These Raman spectra are consistent with those of thiophosphates with S-S thiol bond,  $\text{P}_4\text{S}_{10+n}$  molecules; this compound is generated from a series of reactions of tetraphosphorus decasulfide with disulfides, showing a high reversible capacity of over 500  $\text{mAh g}^{-1}$ .<sup>48-52</sup> Therefore, the amorphous LPS SEs in the cathode should react with polysulfides produced by the delithiation of  $\text{Li}_2\text{S}$  in the charging process to form complex  $-\text{P}-[\text{S}_n]-\text{P}-$  polyanions that contain long-chain cross-linked sulfur. The high capacity obtained after the inactivation of  $\text{Li}_2\text{S}$  can be described by the formation of sulfur-rich thiophosphates with redox activity. The redox peak corresponding to the decomposition products in the cell with  $\text{Li}_2\text{S}$ -510 shifts to the low potential side during the long-term cycle. This can be attributed to the decrease in chain length for cross-linked sulfur in the decomposition product.<sup>48</sup> This decomposition

behavior should cause an irreversible redox reaction, fading cycle stability. This work points out that the overall performance of ASSLSBs discussed in previous studies may have been dominated by the electrochemical activity of the decomposition products. The decomposition behavior of SEs relates to the activation process: the initial oxidation reaction with a higher activation barrier, and an increase in capacity during dozens of cycles. Lithium sulfide cathode is activated by the onset of electrochemical redox-active decomposition products generated through the oxidative decomposition of SEs in the initial charge. In the activation process, sulfide SEs in the cathode react with sulfur through continuous oxidative decomposition to form thiophosphates with a S-S thiol bond. This reaction chemistry of ASSLSBs enhances the cell performance in the early cycles. Figure 3.5.9 plots the overvoltage calculated from the potential difference between the maximum oxidation and reduction peaks in the differential capacity curves of the galvanostatic cycling test, as shown in Figure 3.5.6a and b. The cells with Li<sub>2</sub>S-250 and -510 show a high overvoltage in the first cycle because of the activation process. The overvoltage significantly reduces in the second cycle and again after subsequent cycles. The second decrease means that the dominant redox of the Li<sub>2</sub>S switches to the dominant redox of the decomposition products. The cell with Li<sub>2</sub>S-510 exhibits an apparent lower overvoltage after several cycles compared to the cell with Li<sub>2</sub>S-250. This could originate from the larger contact area between the Li<sub>2</sub>S cathode material and LPS SEs in Li<sub>2</sub>S-510.

### 3.5.7 Electrochemical Impedance Spectroscopy of ASLSBs

Figure 3.5.10a and b shows the electrochemical impedance spectra of cells with Li<sub>2</sub>S-250 and -510 at open circuit voltage until 10 cycles. The Nyquist plots show a straight 45° line and a sharp capacitive tail at the low-frequency regime, which are characterized by a typical non-Faradaic transmission line model (TLM) behavior (Figure 3.5.10c). A TLM for impedance analysis can determine the effective ionic transport property in ASSLSBs.<sup>1</sup> The ion transport resistance  $R_{ion}$  is identified from the low-frequency limit in the real part of the impedance spectrum if the electronic resistance is negligible, as follow<sup>53-55</sup>:

$$Z'_{overall, \omega \rightarrow 0} = R_{electrolyte} + \frac{1}{3}R_{ion} \quad (3.5.2)$$

The extracted  $R_{ion}$  in the pristine cell without treatment was calculated to be 680 Ω for Li<sub>2</sub>S-250 and 975 Ω for Li<sub>2</sub>S-510 based on the resistance of ~34 Ω in the electrolyte layer. Compared to the cell with Li<sub>2</sub>S-250, the cell with Li<sub>2</sub>S-510 shows a higher resistance. No correlation is found between the resistance obtained from the EIS measurement of the pristine cell and the overvoltage of galvanostatic charge-discharge; this observation is consistent with the EIS study in liquid Li-S batteries.<sup>9</sup> This difference between the measurements could be because EIS measurement treats responses in equilibrium potentials theoretically by linearized current-potential characteristics but

not electrochemical responses in dynamic equilibrium. In the Nyquist plot of the fully discharged cell with Li<sub>2</sub>S-510 at the 10th cycle, a part of the circle emerges at the low-frequency regime. This represents the charge transfer resistance resulting from the decomposition products of LPS SEs.<sup>54</sup>

EIS measurements of the cells with Li<sub>2</sub>S-250 and -510 after the 1st and 10th charging were conducted. The obtained electrochemical impedance spectra were fitted using the equivalent circuit (see Figure 3.5.11a). The experimental and simulated Nyquist plots of Li<sub>2</sub>S-250 and -510 in the state of full charge are shown in Figure 3.5.11b and c. The model is based on the equivalent circuit ( $R_{SE}(R_{int,anode/SE}Q_1)(R_{int,cathode/SE}Q_2)(R_{ct,decomposition}Q_3)$ ) that was applied to Li<sub>6</sub>PS<sub>5</sub>Cl SEs following the oxidative decomposition, with the addition of charge transfer resistance,  $R_{ct,cathode}$ , and capacitance components connected in parallel ( $Q$  is a constant phase element, CPE, which represents a pseudocapacitance).<sup>6</sup> A good fitness for this model supports the validity of the equivalent circuit. The extracted values for  $R$  and CPE are summarized in Table S1. Four resistance components located in the high-frequency ( $\geq 100$  kHz), mid-frequency ( $\sim 200$  Hz), low-frequency ( $\sim 30$  mHz), and further lower-frequency ( $\leq 5$  mHz) regions correspond to the Li-In/SE interface, SE/cathode interface, charge transfer of the decomposition product in the cathode, and charge transfer of the cathode material, respectively. The bulk resistance of both cells decreased through cycling (Figure 3.5.11d). This reduction in resistance could be derived from consuming SEs in the electrolyte layer by the evolution of the interfacial degradation at the Li-In/SE (Figure 3.5.11e).<sup>56</sup> The interfacial resistance of the cathode/SE in the cells with Li<sub>2</sub>S-250 and -510 increases through cycling, which should be caused by the detrimental volume changes of the cathode material in the lithiation and delithiation processes (Figure 3.5.11f). The cell with Li<sub>2</sub>S-510 shows a lower interfacial resistance of the cathode/SE than the cell with Li<sub>2</sub>S-250 due to the intimate contact between LPS with small secondary particle size and the cathode material (or carbon additive) in Li<sub>2</sub>S-510. The charge transfer resistance related to the decomposition product in the cell with Li<sub>2</sub>S-510 is twice that of the cell with Li<sub>2</sub>S-250 in the 10th cycle because the pulverized SEs facilitate electrolyte decomposition (Figure 3.5.11g). This is consistent with the existence of the large circle component observed in the Nyquist plots of Li<sub>2</sub>S-510 in the state of full discharge (see Figure 3.5.10b). Figure 3.5.11h shows the charge transfer resistance of the cathode material. The resistance in the first cycle is approximately the same as the charge transfer resistance of the fully charged sulfur cathode in liquid Li-S batteries reported in the past.<sup>9</sup> The resistance increases through cycling, inducing the inactivation of Li<sub>2</sub>S. The comprehensive electrochemical analysis and Raman measurement reveal that the Li<sub>3</sub>PS<sub>4</sub> in the cathode converts the phosphorus compound with a S-S thiol bond through the decomposition reaction, which dominates the overall cell performance of ASSLSBs. This reaction chemistry improves the electrochemical redox activity in the early period, whereas the severe decomposition of the electrolyte negatively affects cycle stability in long-term cycles. Thus, the variability in cell

performance that occurs simply by altering the rotation speed in the mixing with SEs highlights the need for interface engineering, not only avoiding severe degradation of electrolytes in the cathode but also enhancing the ability of SEs as a redox mediator.

### 3.5.8 Conclusions

Here, I investigated the decomposition reactions of LPS SEs in  $\text{Li}_2\text{S}$  cathode composites with different interface designs and examined their effects on cell performance. The findings of this study have contributed to the understanding of the reaction chemistry in ASSLSBs involving the decomposition reaction of sulfide-based SEs. Galvanostatic charge-discharge tests and their differential capacity curves demonstrated that the  $\text{Li}_2\text{S}$  cathode material participates simultaneously in the oxidation reaction as the decomposition reaction of LPS in the initial charge process. The decomposition product produced through the oxidative decomposition of LPS shows a reversible redox reaction. Namely,  $\text{Li}_2\text{S}$  is activated by the electrochemical redox-active decomposition products of SEs. Such oxidation decomposition of LPS occurs continuously even after the initial charge process. Raman spectroscopy of the cell after the 20th cycle unveils that the  $\text{Li}_3\text{PS}_4$  in the cathode converts into the thiophosphate compound with the S-S bond through the charge/discharge process. This reaction chemistry involving continuous electrolyte decomposition enhances the cell performance of ASSLSBs in the early cycles. In contrast, the  $\text{Li}_2\text{S}$  cathode causes inactivation through long-term cycles. The capacities after the inactivation are entirely attributed to the contribution of the decomposition products. This demonstrates that the decomposition behavior of electrolytes dominates the entire cell performance in ASSLSBs. The increasing rotation speed in SE mixing gains a larger effective contact area at the  $\text{Li}_2\text{S}/\text{SE}$  interface and thus facilitates the decomposition reaction of SEs. This leads to an increase in the charge transfer resistance corresponding to the decomposition products. The increasing decomposition kinetics dramatically enhances the capacity in the early cycle but degrades cycle stability. Therefore, this ASSLSB reaction chemistry indicates the need for interface engineering and rational SE selection to control the decomposition kinetics of SEs.

## References

- (1) Ohno, S.; Rosenbach, C.; Dewald, G. F.; Janek, J.; Zeier, W. G. Linking Solid Electrolyte Degradation to Charge Carrier Transport in the Thiophosphate-Based Composite Cathode toward Solid-State Lithium-Sulfur Batteries. *Adv. Funct. Mater.* **2021**, *31*, 2010620–2010633.
- (2) Ohno, S.; Koerver, R.; Dewald, G.; Rosenbach, C.; Titscher, P.; Steckermeier, D.; Kwade, A.; Janek, J.; Zeier, W. G. Observation of Chemomechanical Failure and the Influence of Cutoff Potentials in All-Solid-State Li-S Batteries. *Chem. Mater.* **2019**, *31*, 2930–2940.
- (3) Dewald, G. F.; Ohno, S.; Kraft, M. A.; Koerver, R.; Till, P.; Vargas-Barbosa, N. M.; Janek, J.; Zeier, W. G. Experimental Assessment of the Practical Oxidative Stability of Lithium Thiophosphate Solid Electrolytes. *Chem. Mater.* **2019**, *31*, 8328–8337.
- (4) Swamy, T.; Chen, X.; Chiang, Y. M. Electrochemical Redox Behavior of Li Ion Conducting Sulfide Solid Electrolytes. *Chem. Mater.* **2019**, *31*, 707–713.
- (5) Banerjee, A.; Wang, X.; Fang, C.; Wu, E. A.; Meng, Y. S. Interfaces and Interphases in All-Solid-State Batteries with Inorganic Solid Electrolytes. *Chem. Rev.* **2020**, *120*, 6878–6933.
- (6) Tan, D. H. S.; Wu, E. A.; Nguyen, H.; Chen, Z.; Marple, M. A. T.; Doux, J. M.; Wang, X.; Yang, H.; Banerjee, A.; Meng, Y. S. Elucidating Reversible Electrochemical Redox of  $\text{Li}_6\text{PS}_5\text{Cl}$  Solid Electrolyte. *ACS Energy Lett.* **2019**, *4*, 2418–2427.
- (7) Walther, F.; Randau, S.; Schneider, Y.; Sann, J.; Rohnke, M.; Richter, F. H.; Zeier, W. G.; Janek, J. Influence of Carbon Additives on the Decomposition Pathways in Cathodes of Lithium Thiophosphate-Based All-Solid-State Batteries. *Chem. Mater.* **2020**, *32*, 6123–6136.
- (8) Hakari, T.; Deguchi, M.; Mitsuhara, K.; Ohta, T.; Saito, K.; Orikasa, Y.; Uchimoto, Y.; Kowada, Y.; Hayashi, A.; Tatsumisago, M. Structural and Electronic-State Changes of a Sulfide Solid Electrolyte during the Li Deinsertion-Insertion Processes. *Chem. Mater.* **2017**, *29*, 4768–4774.
- (9) Li, M.; Bai, Z.; Li, Y.; Ma, L.; Dai, A.; Wang, X.; Luo, D.; Wu, T.; Liu, P.; Yang, L.; Amine, K.; Chen, Z.; Lu, J. Electrochemically Primed Functional Redox Mediator Generator from the Decomposition of Solid State Electrolyte. *Nat. Commun.* **2019**, *10*, 1890–1898.
- (10) Lin, Y.; Zheng, J.; Wang, C.; Qi, Y. The Origin of the Two-Plateaued or One-Plateaued Open Circuit Voltage in Li-S Batteries. *Nano Energy* **2020**, *75*, 104915–104924.
- (11) Jiang, H.; Han, Y.; Wang, H.; Zhu, Y.; Guo, Q.; Jiang, H.; Zheng, C.; Xie, K. Facile Synthesis of a Mixed-Conductive  $\text{Li}_2\text{S}$  Composites for All-Solid-State Lithium-Sulfur Batteries. *Ionics* **2020**, *26*, 4257–4265.
- (12) Wu, Z.; Chen, S.; Yu, C.; Wei, C.; Peng, L.; Wang, H. L.; Cheng, S.; Xie, J. Engineering

- High Conductive  $\text{Li}_7\text{P}_2\text{S}_8\text{I}$  via Cl- Doping for All-Solid-State Li-S Batteries Workable at Different Operating Temperatures. *Chem. Eng. J.* **2022**, *442*, 136346–136355.
- (13) Wang, S.; Zhang, Y.; Zhang, X.; Liu, T.; Lin, Y. H.; Shen, Y.; Li, L.; Nan, C. W. High-Conductivity Argyrodite  $\text{Li}_6\text{PS}_5\text{Cl}$  Solid Electrolytes Prepared via Optimized Sintering Processes for All-Solid-State Lithium-Sulfur Batteries. *ACS Appl. Mater. Interfaces* **2018**, *10*, 42279–42285.
- (14) Wei, C.; Yu, C.; Peng, L.; Zhang, Z.; Xu, R.; Wu, Z.; Liao, C.; Zhang, W.; Zhang, L.; Cheng, S.; Xie, J. Tuning Ionic Conductivity to Enable All-Climate Solid-State Li-S Batteries with Superior Performances. *Mater. Adv.* **2022**, *3*, 1047–1054.
- (15) Jiang, H.; Han, Y.; Wang, H.; Zhu, Y.; Guo, Q.; Jiang, H.; Sun, W. W.; Zheng, C.; Xie, K. In-Situ Generated  $\text{Li}_2\text{S}$ -Based Composite Cathodes with High Mass and Capacity Loading for All-Solid-State Li-S Batteries. *J. Alloys Compd.* **2021**, *874*, 159763 –159768.
- (16) Wang, D.; Wu, Y.; Zheng, X.; Tang, S.; Gong, Z.; Yang, Y.  $\text{Li}_2\text{S}@\text{NC}$  Composite Enable High Active Material Loading and High  $\text{Li}_2\text{S}$  Utilization for All-Solid-State Lithium Sulfur Batteries. *J. Power Sources* **2020**, *479*, 228792 –228798.
- (17) Chang, G. H.; Oh, Y. S.; Kang, S.; Park, J. Y.; Lim, H. T. Single-Step Prepared  $\text{Li}_2\text{S}-\text{P}_2\text{S}_5-\text{C}$  Composite Cathode for High Areal Capacity All-Solid-State Lithium Ion Batteries. *Electrochim. Acta* **2020**, *358*, 136884–136892.
- (18) Jiang, H.; Han, Y.; Wang, H.; Zhu, Y.; Guo, Q.; Jiang, H.; Zheng, C.; Xie, K.  $\text{Li}_2\text{S}-\text{Li}_3\text{PS}_4$  (LPS) Composite Synthesized by Liquid-Phase Shaking for All-Solid-State Lithium–Sulfur Batteries with High Performance. *Energy Technol.* **2020**, *8*, 2000023–2000029.
- (19) Yi, J.; Chen, L.; Liu, Y.; Geng, H.; Fan, L. Z. High Capacity and Superior Cyclic Performances of All-Solid-State Lithium-Sulfur Batteries Enabled by a High-Conductivity  $\text{Li}_{10}\text{SnP}_2\text{S}_{12}$  Solid Electrolyte. *ACS Appl. Mater. Interfaces* **2019**, *11*, 36774–36781.
- (20) Hakari, T.; Hayashi, A.; Tatsumisago, M.  $\text{Li}_2\text{S}$ -Based Solid Solutions as Positive Electrodes with Full Utilization and Superlong Cycle Life in All-Solid-State Li/S Batteries. *Adv. Sustain. Syst.* **2017**, *1*, 1700017–1700023.
- (21) Hakari, T.; Fujita, Y.; Deguchi, M.; Kawasaki, Y.; Otoyama, M.; Yoneda, Y.; Sakuda, A.; Tatsumisago, M.; Hayashi, A. Solid Electrolyte with Oxidation Tolerance Provides a High-Capacity  $\text{Li}_2\text{S}$ -Based Positive Electrode for All-Solid-State Li/S Batteries. *Adv. Funct. Mater.* **2022**, *32*, 2106174–2106186.
- (22) Izumi, F.; Momma, K. Three-Dimensional Visualization in Powder Diffraction. *Solid State Phenomena.* **2007**, *130*, 15–20.
- (23) Nagao, M.; Hayashi, A.; Tatsumisago, M. Sulfur-Carbon Composite Electrode for All-Solid-State Li/S Battery with  $\text{Li}_2\text{S}-\text{P}_2\text{S}_5$  Solid Electrolyte. *Electrochim. Acta* **2011**, *56*, 6055–6059.



- (24) Yu, C.; Ganapathy, S.; Eck, E. R. H. V.; Wang, H.; Basak, S.; Li, Z.; Wagemaker, M. Accessing the Bottleneck in All-Solid State Batteries, Lithium-Ion Transport over the Solid-Electrolyte-Electrode Interface. *Nat. Commun.* **2017**, *8*, 1086–1094.
- (25) Liu, M.; Wang, C.; Zhao, C.; van der Maas, E.; Lin, K.; Arszewska, V. A.; Li, B.; Ganapathy, S.; Wagemaker, M. Quantification of the Li-Ion Diffusion over an Interface Coating in All-Solid-State Batteries via NMR Measurements. *Nat. Commun.* **2021**, *12*, 5943–5952.
- (26) Stöffler, H.; Zinkevich, T.; Yavuz, M.; Hansen, A. L.; Knapp, M.; Bednarčík, J.; Randau, S.; Richter, F. H.; Janek, J.; Ehrenberg, H.; Indris, S. Amorphous versus Crystalline Li<sub>3</sub>PS<sub>4</sub>: Local Structural Changes during Synthesis and Li Ion Mobility. *J. Phys. Chem. C* **2019**, *123*, 10280–10290.
- (27) Famprikis, T.; Bouyanfif, H.; Canepa, P.; Zbiri, M.; Dawson, J. A.; Suard, E.; Fauth, F.; Playford, H. Y.; Dambournet, D.; Borkiewicz, O. J.; Courty, M.; Clemens, O.; Chotard, J. N.; Islam, M. S.; Masquelier, C.; Famprikis, T.; Islam, M. S. Insights into the Rich Polymorphism of the Na<sup>+</sup> Ion Conductor Na<sub>3</sub>PS<sub>4</sub> from the Perspective of Variable-Temperature Diffraction and Spectroscopy. *Chem. Mater.* **2021**, *33*, 5652–5667.
- (28) Krauskopf, T.; Muy, S.; Culver, S. P.; Ohno, S.; Delaire, O.; Shao-Horn, Y.; Zeier, W. G. Comparing the Descriptors for Investigating the Influence of Lattice Dynamics on Ionic Transport Using the Superionic Conductor Na<sub>3</sub>PS<sub>4-x</sub>Se<sub>x</sub>. *J. Am. Chem. Soc.* **2018**, *140*, 14464–14473.
- (29) Ates, T.; Neumann, A.; Danner, T.; Latz, A.; Zarrabeitia, M.; Stepien, D.; Varzi, A.; Passerini, S. Elucidating the Role of Microstructure in Thiophosphate Electrolytes – a Combined Experimental and Theoretical Study of  $\beta$ -Li<sub>3</sub>PS<sub>4</sub>. *Adv. Sci.* **2022**, *9*, 2105234–2105244.
- (30) Strauss, F.; Bartsch, T.; de Biasi, L.; Kim, A. Y.; Janek, J.; Hartmann, P.; Brezesinski, T. Impact of Cathode Material Particle Size on the Capacity of Bulk-Type All-Solid-State Batteries. *ACS Energy Lett.* **2018**, *3*, 992–996.
- (31) Ohno, S.; Zeier, W. G. Toward Practical Solid-State Lithium-Sulfur Batteries: Challenges and Perspectives. *Acc Mater. Res.* **2021**, *2*, 869–880.
- (32) Schwietert, T. K.; Arszewska, V. A.; Wang, C.; Yu, C.; Vasileiadis, A.; de Klerk, N. J. J.; Hageman, J.; Hupfer, T.; Kerkamm, I.; Xu, Y.; van der Maas, E.; Kelder, E. M.; Ganapathy, S.; Wagemaker, M. Clarifying the Relationship between Redox Activity and Electrochemical Stability in Solid Electrolytes. *Nat. Mater.* **2020**, *19*, 428–435.
- (33) Koerver, R.; Walther, F.; Aygün, I.; Sann, J.; Dietrich, C.; Zeier, W. G.; Janek, J. Redox-Active Cathode Interphases in Solid-State Batteries. *J. Mater. Chem. A* **2017**, *5*, 22750–22760.

- (34) Wang, S.; Tang, M.; Zhang, Q.; Li, B.; Ohno, S.; Walther, F.; Pan, R.; Xu, X.; Xin, C.; Zhang, W.; Li, L.; Shen, Y.; Richter, F. H.; Janek, J.; Nan, C. W. Lithium Argyrodite as Solid Electrolyte and Cathode Precursor for Solid-State Batteries with Long Cycle Life. *Adv. Energy Mater.* **2021**, *11*, 2101370–2101379.
- (35) Wang, S.; Zhang, W.; Chen, X.; Das, D.; Ruess, R.; Gautam, A.; Walther, F.; Ohno, S.; Koerver, R.; Zhang, Q.; Zeier, W. G.; Richter, F. H.; Nan, C. W.; Janek, J. Influence of Crystallinity of Lithium Thiophosphate Solid Electrolytes on the Performance of Solid-State Batteries. *Adv. Energy Mater.* **2021**, *11*, 2100654–2100664.
- (36) Tan, G.; Xu, R.; Xing, Z.; Yuan, Y.; Lu, J.; Wen, J.; Liu, C.; Ma, L.; Zhan, C.; Liu, Q.; Wu, T.; Jian, Z.; Shahbazian-Yassar, R.; Ren, Y.; Miller, D. J.; Curtiss, L. A.; Ji, X.; Amine, K. Burning Lithium in CS<sub>2</sub> for High-Performing Compact Li<sub>2</sub>S–Graphene Nanocapsules for Li–S Batteries. *Nat. Energy* **2017**, *2*, 17090–17100.
- (37) Takeuchi, T.; Kageyama, H.; Nakanishi, K.; Tabuchi, M.; Sakaebe, H.; Ohta, T.; Senoh, H.; Sakai, T.; Tatsumi, K. All-Solid-State Lithium Secondary Battery with Li<sub>2</sub>S–C Composite Positive Electrode Prepared by Spark-Plasma-Sintering Process. *J. Electrochem. Soc.* **2010**, *157*, A1196–A1201.
- (38) Nagao, M.; Hayashi, A.; Tatsumisago, M.; Ichinose, T.; Ozaki, T.; Togawa, Y.; Mori, S. Li<sub>2</sub>S Nanocomposites Underlying High-Capacity and Cycling Stability in All-Solid-State Lithium-Sulfur Batteries. *J. Power Sources* **2015**, *274*, 471–476.
- (39) Nagao, M.; Hayashi, A.; Tatsumisago, M. High-Capacity Li<sub>2</sub>S-Nanocarbon Composite Electrode for All-Solid-State Rechargeable Lithium Batteries. *J. Mater. Chem.* **2012**, *22*, 10015–10020.
- (40) Han, Q.; Li, X.; Shi, X.; Zhang, H.; Song, D.; Ding, F.; Zhang, L. Outstanding Cycle Stability and Rate Capabilities of the All-Solid-State Li-S Battery with a Li<sub>7</sub>P<sub>3</sub>S<sub>11</sub> Glass-Ceramic Electrolyte and a Core-Shell S@BP2000 Nanocomposite. *J. Mater. Chem. A* **2019**, *7* (8), 3895–3902.
- (41) Asano, T.; Sakai, A.; Ouchi, S.; Sakaida, M.; Miyazaki, A.; Hasegawa, S. Solid Halide Electrolytes with High Lithium-Ion Conductivity for Application in 4 V Class Bulk-Type All-Solid-State Batteries. *Adv. Mater.* **2018**, *30*, 1803075–1803081.
- (42) Shi, X.; Zeng, Z.; Sun, M.; Huang, B.; Zhang, H.; Luo, W.; Huang, Y.; Du, Y.; Yan, C. Fast Li-Ion Conductor of Li<sub>3</sub>HoBr<sub>6</sub> for Stable All-Solid-State Lithium-Sulfur Battery. *Nano Lett.* **2021**, *21*, 9325–9331.
- (43) Fujita, Y.; Hakari, T.; Sakuda, A.; Deguchi, M.; Kawasaki, Y.; Tsukasaki, H.; Mori, S.; Tatsumisago, M.; Hayashi, A. Li<sub>2</sub>S–LiI Solid Solutions with Ionic Conductive Domains for Enhanced All-Solid-State Li/S Batteries. *ACS Appl. Energy Mater.* **2022**, *5* (8), 9429–9436.

- (44) Ahmad, N.; Zhou, L.; Faheem, M.; Tufail, M. K.; Yang, L.; Chen, R.; Zhou, Y.; Yang, W. Enhanced Air Stability and High Li-Ion Conductivity of  $\text{Li}_{6.988}\text{P}_{2.994}\text{Nb}_{0.2}\text{S}_{10.934}\text{O}_{0.6}$  Glass-Ceramic Electrolyte for All-Solid-State Lithium-Sulfur Batteries. *ACS Appl. Mater. Interfaces* **2020**, *12*, 21548–21558.
- (46) Xu, R. C.; Xia, X. H.; Wang, X. L.; Xia, Y.; Tu, J. P. Tailored  $\text{Li}_2\text{S-P}_2\text{S}_5$  Glass-Ceramic Electrolyte by  $\text{MoS}_2$  Doping, Possessing High Ionic Conductivity for All-Solid-State Lithium-Sulfur Batteries. *J. Mater. Chem. A* **2017**, *5*, 2829–2834.
- (47) Chen, X.; Yuan, L.; Li, Z.; Chen, S.; Ji, H.; Qin, Y.; Wu, L.; Shen, Y.; Wang, L.; Hu, J.; Huang, Y. Realizing an Applicable “Solid  $\rightarrow$  Solid” Cathode Process via a Transplantable Solid Electrolyte Interface for Lithium-Sulfur Batteries. *ACS Appl. Mater. Interfaces* **2019**, *11*, 29830–29837.
- (48) Li, X.; Liang, J.; Lu, Y.; Hou, Z.; Cheng, Q.; Zhu, Y.; Qian, Y. Sulfur-Rich Phosphorus Sulfide Molecules for Use in Rechargeable Lithium Batteries. *Angew. Chem.* **2017**, *129*, 2983–2987.
- (49) Li, X.; Liang, J.; Banis, M. N.; Luo, J.; Wang, C.; Li, W.; Li, X.; Sun, Q.; Hu, Y.; Xiao, Q.; Sham, T. K.; Zhang, L.; Zhao, S.; Lu, S.; Huang, H.; Li, R.; Sun, X. Totally Compatible  $\text{P}_4\text{S}_{10+n}$  Cathodes with Self-Generated  $\text{Li}^+$  Pathways for Sulfide-Based All-Solid-State Batteries. *Energy Storage Mater.* **2020**, *28*, 325–333.
- (50) Tanibata, N.; Tsukasaki, H.; Deguchi, M.; Mori, S.; Hayashi, A.; Tatsumisago, M. A Novel Discharge-Charge Mechanism of a  $\text{S-P}_2\text{S}_5$  Composite Electrode without Electrolytes in All-Solid-State Li/S Batteries. *J. Mater. Chem. A* **2017**, *5*, 11224–11228.
- (51) Ozturk, T.; Ertas, E.; Mert, O. A Berzelius Reagent, Phosphorus Decasulfide ( $\text{P}_4\text{S}_{10}$ ), in Organic Syntheses. *Chem Rev* **2010**, *110*, 3419–3478.
- (52) Nizamov, I. S.; Al’Metkina, L.; Garifzyanova, G. G.; Batyeva, E. S.; Al’Fonsov, V. A.; Pudovik, A. N. Reactions of Tetraphosphorus Decasulfide and 2, 4-Bis(Alkylthio)- 2, 4-Dithioxo-1, 3,  $2\lambda^5$ ,  $4\lambda^5$ -Dithiadiphosphetanes with Disulfides and Thioacetals. *Phosphorus Sulfur Silicon Relat. Elem.* **1993**, *83*, 191–201.
- (53) Kato, Y.; Shiotani, S.; Morita, K.; Suzuki, K.; Hirayama, M.; Kanno, R. All-Solid-State Batteries with Thick Electrode Configurations. *J. Phys. Chem. Lett.* **2018**, *9*, 607–613.
- (54) Siroma, Z.; Sato, T.; Takeuchi, T.; Nagai, R.; Ota, A.; Ioroi, T. AC Impedance Analysis of Ionic and Electronic Conductivities in Electrode Mixture Layers for an All-Solid-State Lithium-Ion Battery. *J. Power Sources* **2016**, *316*, 215–223.
- (55) Kaiser, N.; Spannenberger, S.; Schmitt, M.; Cronau, M.; Kato, Y.; Roling, B. Ion Transport Limitations in All-Solid-State Lithium Battery Electrodes Containing a Sulfide-Based Electrolyte. *J. Power Sources* **2018**, *396*, 175–181.
- (56) Luo, S.; Wang, Z.; Li, X.; Liu, X.; Wang, H.; Ma, W.; Zhang, L.; Zhu, L.; Zhang, X.

Growth of Lithium-Indium Dendrites in All-Solid-State Lithium-Based Batteries with Sulfide Electrolytes. *Nat. Commun.* **2021**, *12*, 6968–6977.

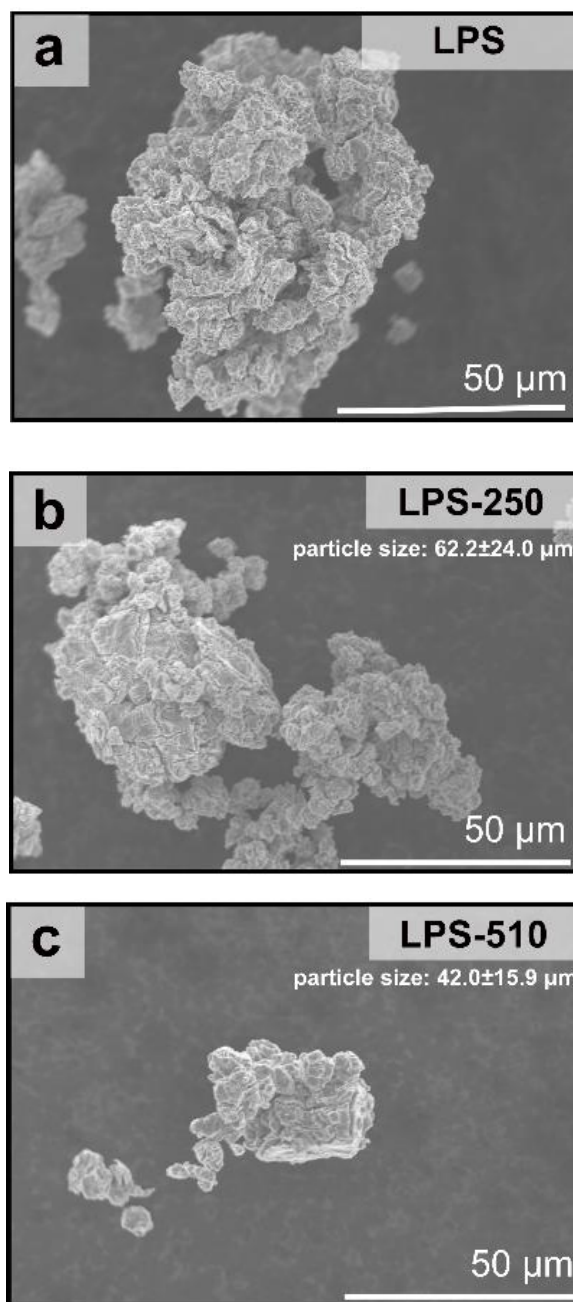


**Figure 3.5.1.** SEM images of (a) LPS, (b) LPS-250, and (c) LPS-510 particles.

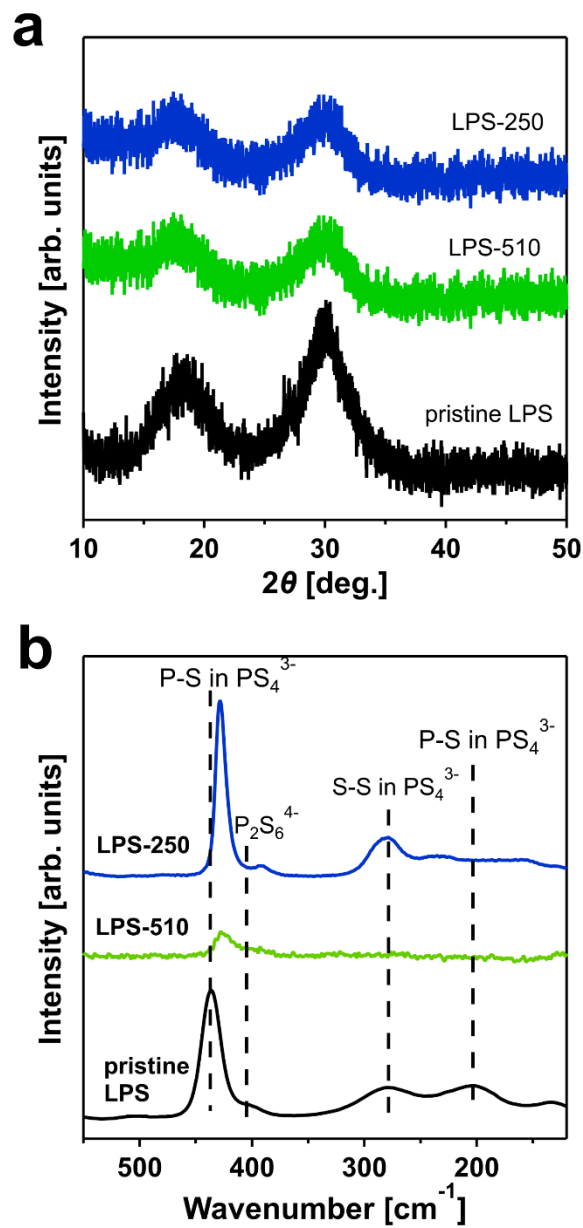


**Figure 3.5.2.** (a) XRD patterns and (b) Raman spectra of pristine LPS, LPS-250, and LPS-510.

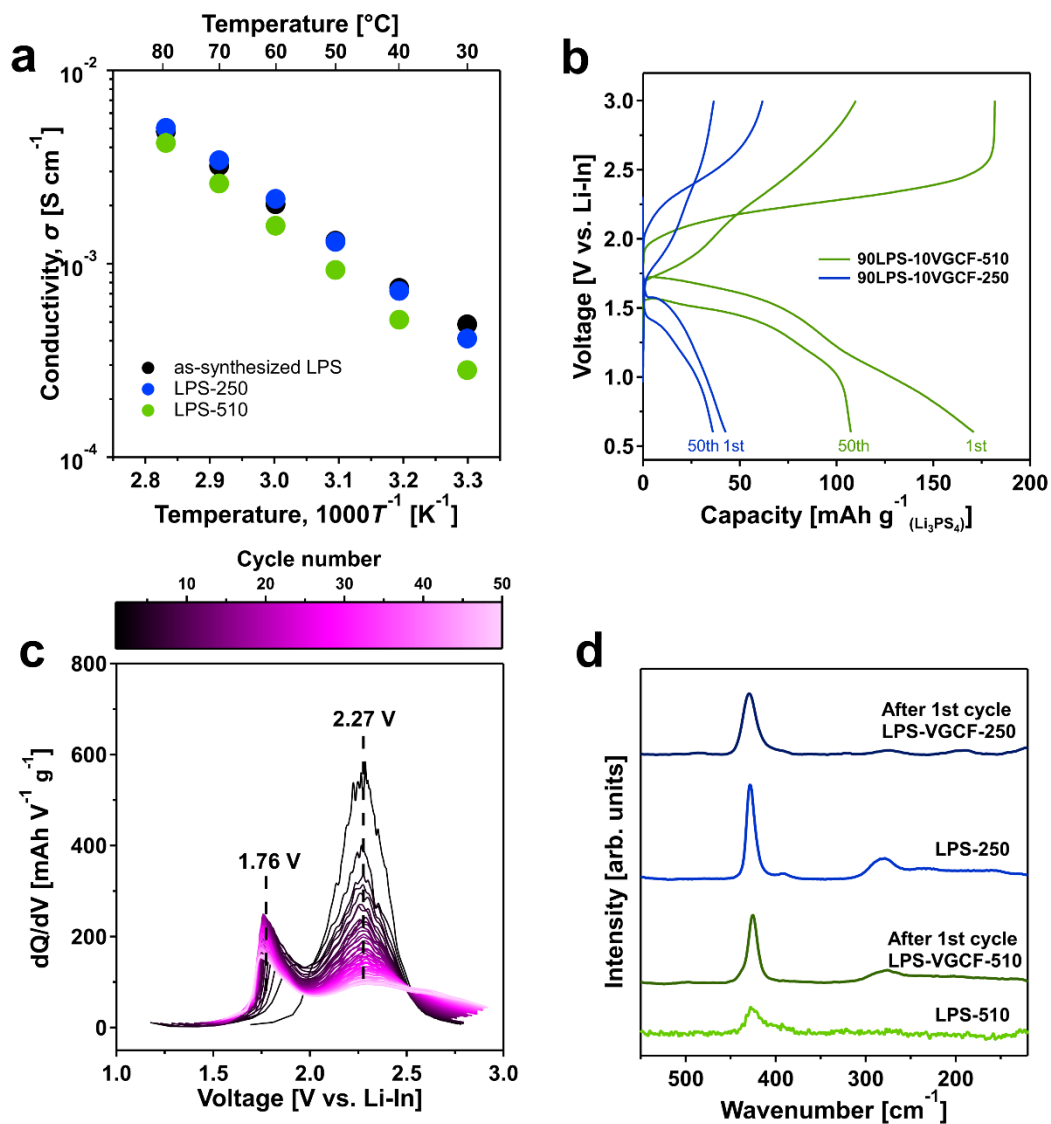


**Figure 3.5.3.** (a) Ionic conductivity for LPS, LPS-250, and LPS-510 as a function of inverse temperature. (b) Galvanostatic charge-discharge profiles of Li-In | Li<sub>5.5</sub>PS<sub>4.5</sub>Cl<sub>1.5</sub> | 90LPS-10VGCF-250 and -510 cycled in the voltage range of 0.6–3.0 V (vs Li-In) under 0.13 mA cm<sup>-2</sup> at 30 °C. (c) Differential charge capacity curves of the cell with 90LPS-10VGCF-510. (d) Raman spectra of LPS-VGCF-250 and -510 after the first cycle.

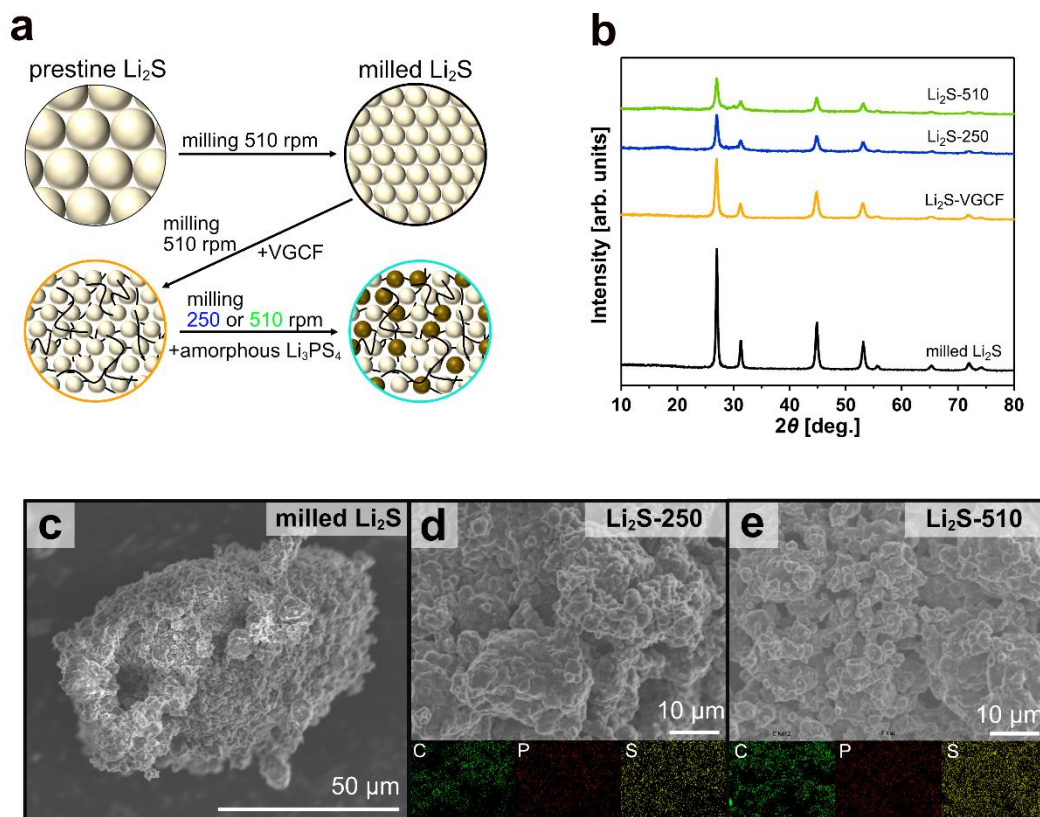


**Figure 3.5.4.** The structural properties of  $\text{Li}_2\text{S}$  cathode composites. (a) Experimental procedure of the synthesis of  $\text{Li}_2\text{S}$  cathode composites. (b) The XRD patterns of the prepared  $\text{Li}_2\text{S}$  cathode composites. (c) SEM image of milled  $\text{Li}_2\text{S}$ . SEM-EDS images of  $\text{Li}_2\text{S}$ -LPS-VGCF cathode composites milled at rotation speeds of (d) 250 rpm and (e) 510 rpm for 2 h.



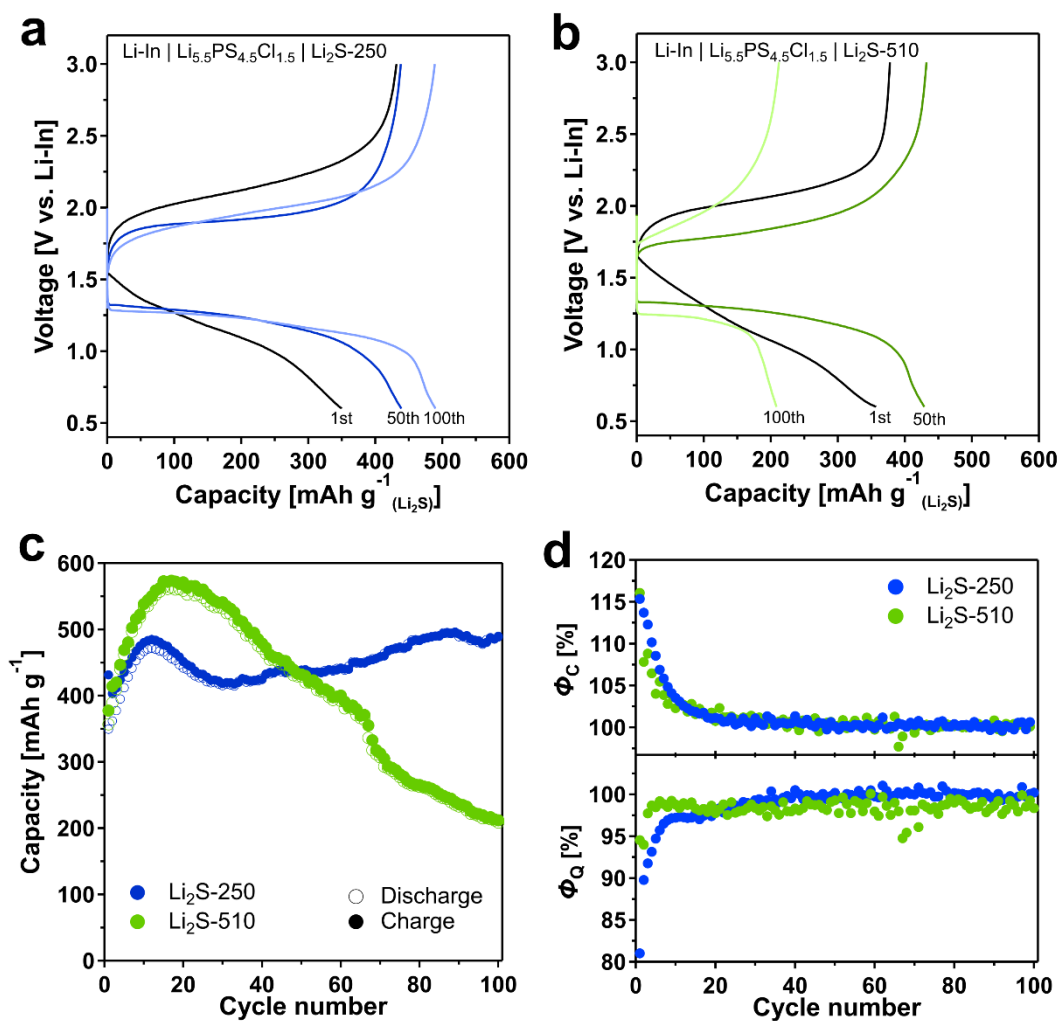


**Figure 3.5.5.** Electrochemical properties of  $\text{Li}_2\text{S}$ -LPS-VGCF cathode composites milled at rotation speeds of 250 rpm and 510 rpm. Galvanostatic charge-discharge profiles of Li-In |  $\text{Li}_{5.5}\text{PS}_{4.5}\text{Cl}_{1.5}$  | (a)  $\text{Li}_2\text{S-250}$  and (b)  $\text{Li}_2\text{S-510}$  cells cycled in the voltage range of 0.6–3.0 V vs. Li-In under 0.1C at 30 °C. (c) Cycle stabilities, and (d) Coulombic efficiency ( $\phi_Q$ ) and conversion efficiency ( $\phi_C$ ) of  $\text{Li}_2\text{S-250}$  and -510.

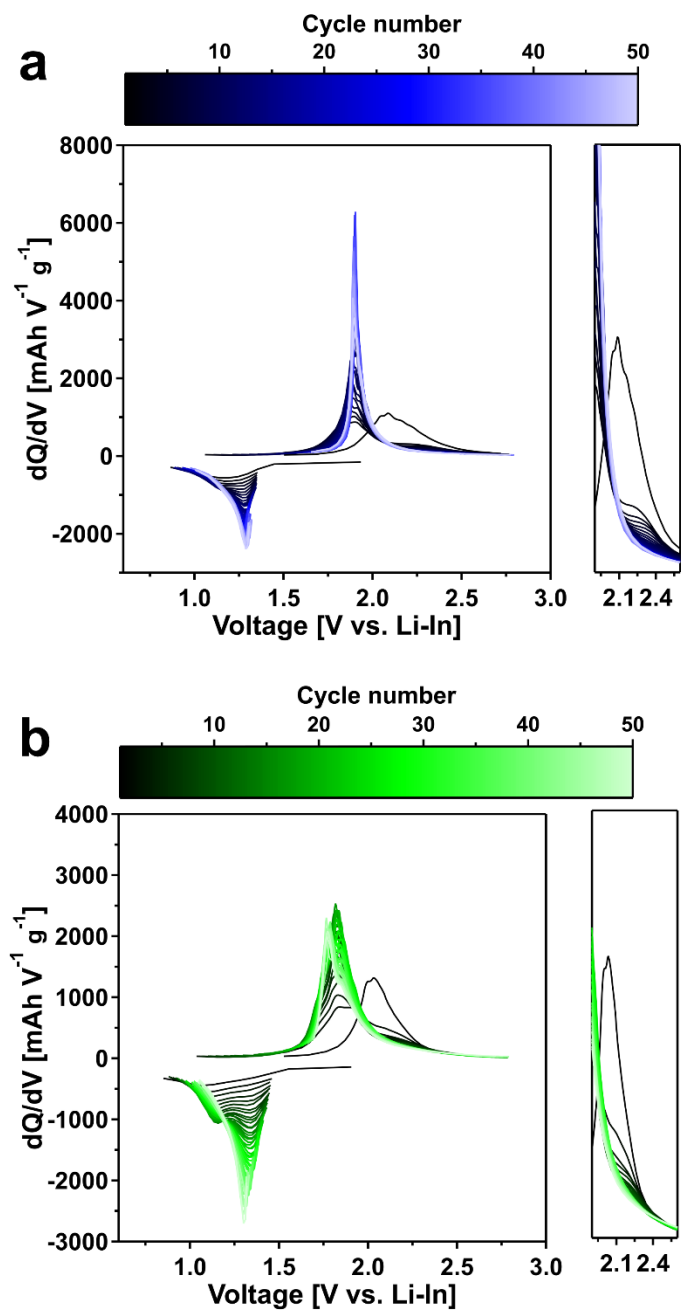


**Figure 3.5.6.** Differential capacity curves of cells with (a)  $\text{Li}_2\text{S}$ -250 and (b) -510.

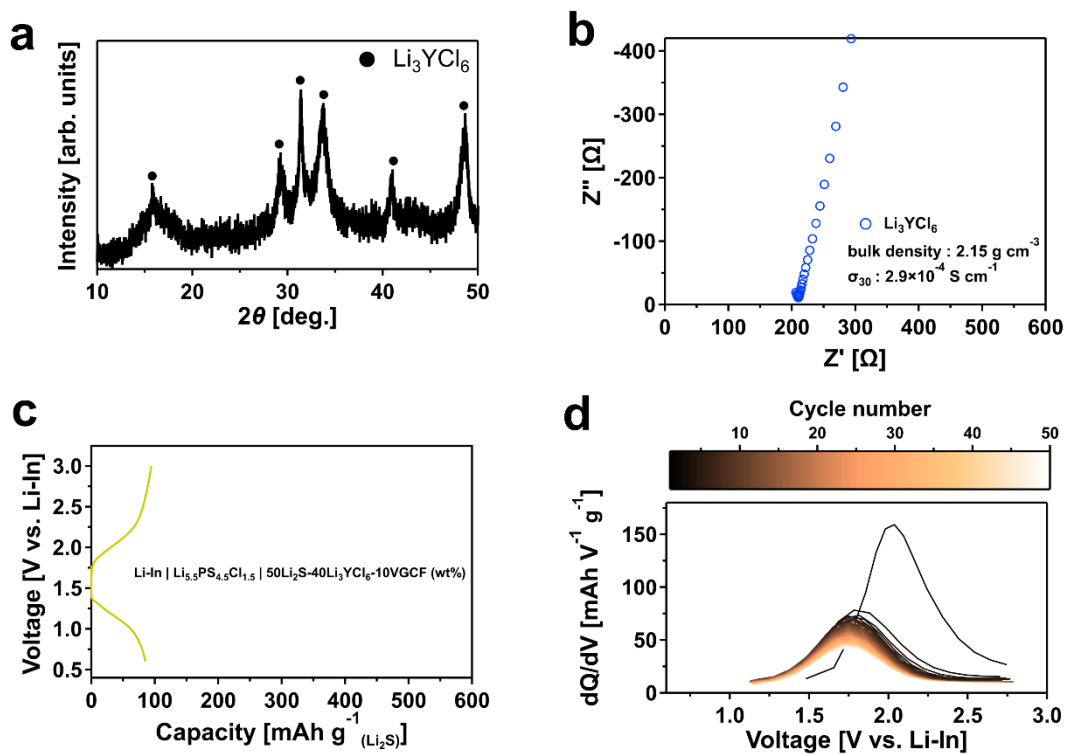


**Figure 3.5.7.** (a) The XRD pattern and (b) Nyquist plot at  $30^\circ\text{C}$  of  $\text{Li}_3\text{YCl}_6$  prepared by mechanical milling. (c) The first galvanostatic charge-discharge voltage profiles of the cells using  $50\text{Li}_2\text{S}-40\text{Li}_3\text{YCl}_6-10\text{VGCF}$  (wt%) cathode composites that are mixed at rotation speeds of 510 rpm. The cells were cycled in the voltage range of 0.6-3.0 V vs Li-In under 0.1C at  $30^\circ\text{C}$ . (d) Differential capacity curves of cells with  $50\text{Li}_2\text{S}-40\text{Li}_3\text{YCl}_6-10\text{VGCF}$  cathode composites.

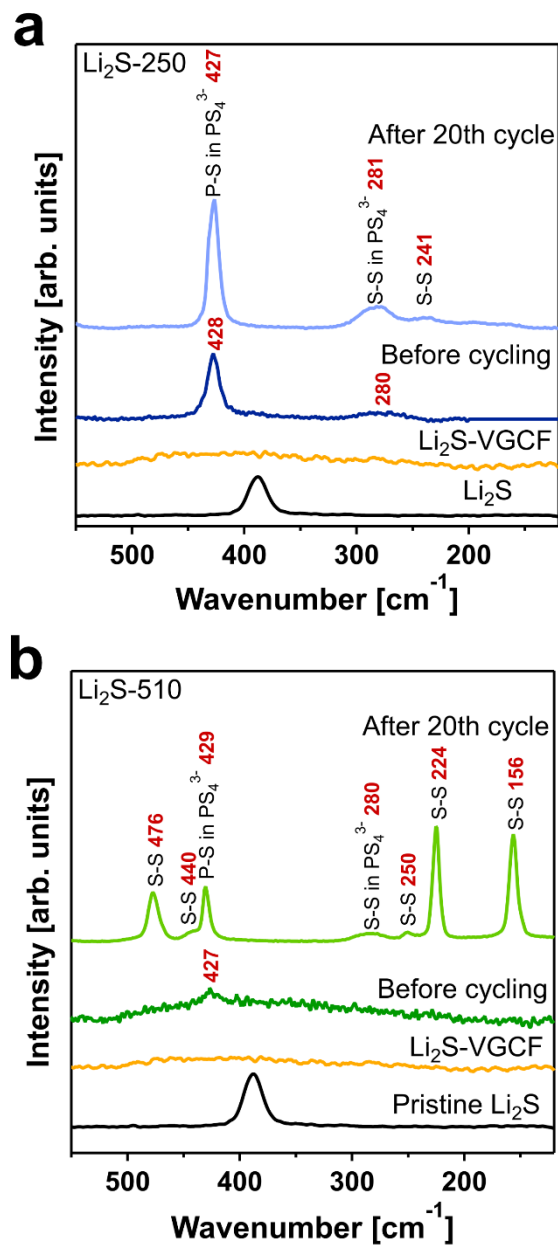


**Figure 3.5.8.** Raman spectra of the (a) Li<sub>2</sub>S-250 and (b) Li<sub>2</sub>S-510 without treatment and after the 20th cycle.

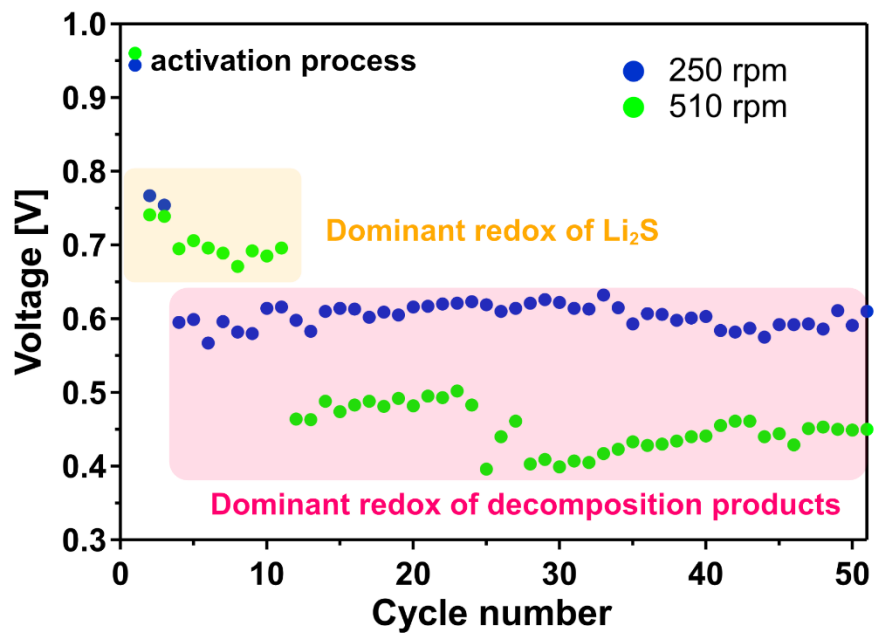
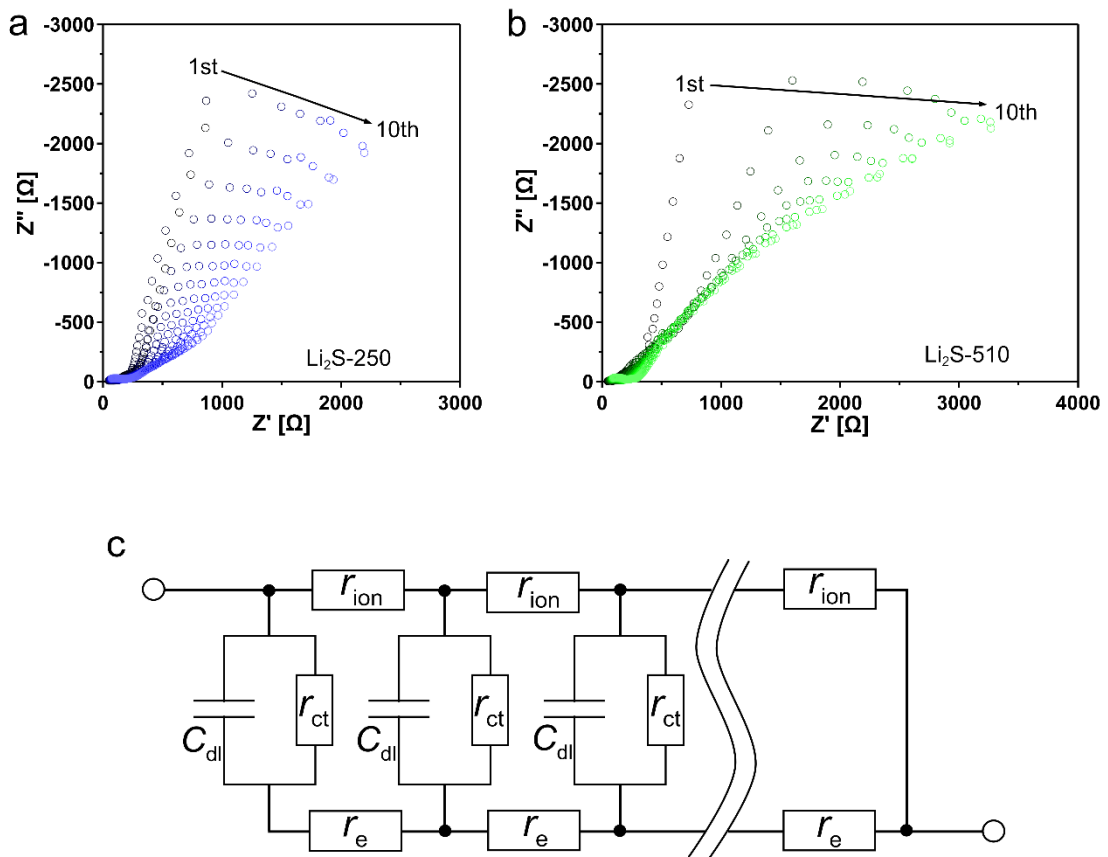
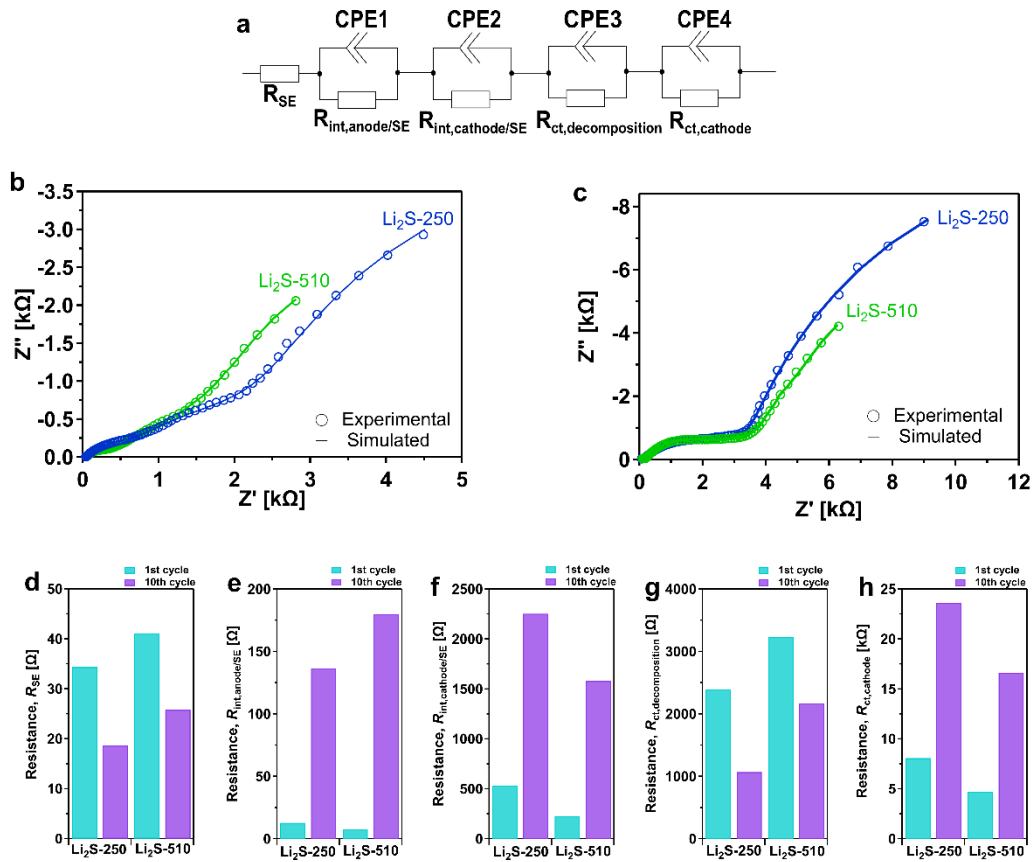


Figure 3.5.9. Overvoltage of galvanostatic cycling test.



**Figure 3.5.10.** Nyquist plots of the fully discharged cells using (a) the  $\text{Li}_2\text{S}$ -250 and (b)  $\text{Li}_2\text{S}$ -510 in from before cycling to the 10th cycle. (c) Schematic diagram of the equivalent circuit for a typical non-Faradaic transmission line model.  $r_{\text{ion}}$  is the ionic resistance,  $r_e$  is the electronic resistance,  $C_{\text{dl}}$  is the double-layer capacitance.



**Figure 3.5.11.** (a) Equivalent circuit for simulation. Experimental and simulated impedance spectra of Li<sub>2</sub>S-250 and -510 in the state of full charge after (b) the 1st cycle and (c) 10th cycle. (d–h) Extracted resistance of the cells with Li<sub>2</sub>S-250 and -510 in the state of full charge after the 1st and 10th cycles. (d) Bulk resistance of an electrolyte layer, (e) interfacial resistance between anode and SEs, (f) interfacial resistance between cathode and SEs, (g) charge transfer resistance of decomposition products, and (h) charge transfer resistance of cathode materials.

## Chapter 4

# Sodium-Ion Solid Electrolyte for All-Solid-State Sodium-Ion Batteries

### 4.1 Background

The growing demand for large-scale energy storage has accelerated research into the next-generation battery that offers low-cost and low load on the environment. However, conventional Li-based batteries have the resource challenge that Li is a limited resource in the Earth's crust and has a geologically uneven distribution.<sup>1</sup> Rechargeable sodium ion battery holds a bright future as an energy storage device and large-scale system owing to the abundance and low cost of sodium resources.<sup>2</sup> Sodium has a reasonable electrochemical window ( $E_{\text{Na}^+/\text{Na}} = -2.71$  V vs SHE), just above that of lithium ( $E_{\text{Li}^+/\text{Li}} = -3.04$  V vs SHE). Technology involving fast ion conduction in solids has attracted significant interest with respect to its application in ASSBs, as well as ASLBs.<sup>3</sup> The development of super Na ion conductors is crucial for the practical application of ASSBs. Sulfide solid electrolytes have demonstrated the potential to realize high ionic conductivity at room temperature. In 2012, Hayashi et al. described a crystalline sulfide-based Na ion solid electrolyte,  $\text{Na}_3\text{PS}_4$ , with high ionic conductivity and distinct properties compared with previously reported Na-based conductors.<sup>4</sup>  $\text{Na}_3\text{PS}_4$  with  $\text{Si}^{4+}$  substituted for a part of  $\text{P}^{5+}$  was reported to exhibit an ionic conductivity of  $0.74 \text{ mS cm}^{-1}$  at room temperature. Additionally, substitutions of various atoms, e.g.,  $\text{As}^{5+}$ , and  $\text{Cl}^-$ , into the  $\text{Na}_3\text{PS}_4$  framework improved the ionic conductivity.<sup>5-9</sup> Since the development of  $\text{Na}_3\text{PS}_4$ , material development has mainly focused on  $\text{Na}_3\text{PS}_4$ . However, these  $\text{Na}_3\text{PS}_4$ -based SEs react with  $\text{H}_2\text{O}$  in the air atmosphere to generate highly toxic  $\text{H}_2\text{S}$  gas based on Hard and soft acid/base (HSAB) theory. Sodium-ion SE with not only high ionic conductivity but also air stability is required.

### 4.2 $\text{Na}_3\text{SbS}_4$ substituted with Cl solid electrolytes

In this chapter, I report on  $\text{Na}_{3-x}\text{SbS}_{4-x}\text{Cl}_x$  ( $0 \leq x \leq 0.1$ ) SEs prepared by a liquid-phase method that is suitable for large-scale manufacturing. A maximum ionic conductivity of  $9.0 \times 10^{-4} \text{ S cm}^{-1}$  at room temperature is achieved in the  $\text{Na}_{2.95}\text{SbS}_{3.95}\text{Cl}_{0.05}$ , which is three times in comparison with the pristine  $\text{Na}_3\text{SbS}_4$ . Rietveld analysis based on the XRD data indicates that the altered structure due to Cl substitution involves looser local bonding between Na and S (or Cl) around the Na1 site (Wyckoff  $4d$  position), which comprises a 3D ion-transport network that promoted fast ion



transport. A BVS mapping technique reveals that the specific crystal structure formed following Cl substitution enables the expansion of bottlenecks for Na<sup>+</sup> conduction, especially along the c-axis. These crystal structure features lead to the enhanced ionic conductivity of Na<sub>3</sub>SbS<sub>4</sub>. To investigate the effect of Cl doping in Na<sub>3</sub>SbS<sub>4</sub> on the overall cell performance, the electrochemical performances of symmetric Na<sub>15</sub>Sn<sub>4</sub>/Na<sub>2.95</sub>SbS<sub>3.95</sub>Cl<sub>0.05</sub> and Na<sub>2.90</sub>SbS<sub>3.90</sub>Cl<sub>0.10</sub>/Na<sub>15</sub>Sn<sub>4</sub> cells were evaluated and compared with that of Na<sub>3</sub>SbS<sub>4</sub>. The introduction of NaCl into Na<sub>3</sub>SbS<sub>4</sub> suppresses the increase in interfacial resistance that accompanies stripping/plating, thereby enhancing the cell's electrochemical stability at 0 V vs Na/Na<sup>+</sup>.

#### 4.2.1 Introduction

Na<sub>3</sub>SbS<sub>4</sub> prepared via a solid-phase synthetic method has attracted interest as a potential superionic conductor for ASSBs because it exhibits high conductivity ( $\geq 1.0 \text{ mS cm}^{-1}$  at room temperature),<sup>10</sup> excellent air stability,<sup>10</sup> and low activation energy for ion conduction.<sup>11</sup> Based on HSAB theory, Na<sub>3</sub>SbS<sub>4</sub> is tractable in liquid-phase processes, unlike Na<sub>3</sub>PS<sub>4</sub>.<sup>10,12-14</sup> In fact, Na<sub>3</sub>SbS<sub>4</sub> can be prepared in aqueous solution using Na<sub>2</sub>S, Sb<sub>2</sub>S<sub>3</sub>, and S as starting materials.<sup>15,16</sup> Previous efforts achieved the development of Na<sub>3</sub>SbS<sub>4</sub>-based SEs with the improved ionic conductivity<sup>16-19</sup>, for example, Se-substituted Na<sub>3</sub>SbS<sub>4</sub>.<sup>20,21</sup> Substituting S with larger ions weakened the electrostatic interactions between the diffusion ions and the counter ions, often leading to increased ionic conductivity. In addition, Na<sub>3</sub>SbS<sub>4</sub> analogs substituted with aliovalent ions, such as  $\Gamma$  or W<sup>6+</sup>, have demonstrated high ionic conductivity.<sup>16,22,23</sup> Remarkably, Na<sub>2.88</sub>Sb<sub>0.88</sub>W<sub>0.12</sub>S<sub>4</sub> achieved an ionic conductivity of  $32 \text{ mS cm}^{-1}$  at room temperature, which was higher than the best value demonstrated by Li<sub>19.54</sub>Si<sub>1.74</sub>P<sub>1.44</sub>S<sub>11.7</sub>Cl<sub>0.3</sub> ( $25 \text{ mS cm}^{-1}$ ).<sup>24</sup>

Among the potential elemental substitutions, Cl substitution provides desirable properties for excellent performance in all-solid-state batteries. This is an effective strategy for creating vacancies in sulfide-based materials and often enhances the ionic conductivity of various inorganic materials.<sup>24-27</sup> Moreover, this approach to developing a high-performance ionic conductor plays an important role in developing anodic stability. Na<sub>3</sub>SbS<sub>4</sub> will continue to react while in contact with Na metal, thus exhibiting kinetic instability at the interface between Na<sub>3</sub>SbS<sub>4</sub> and Na metal, because Na<sub>3</sub>Sb, which is a decomposition product of Na<sub>3</sub>SbS<sub>4</sub>, is an ionically- and electronically conductive interphase. However, solid electrolytes containing chlorine decompose to generate chloride, which is an electronic insulator that can suppress a dynamic interface evolution.<sup>28</sup>

In this work, I synthesized Cl-doped Na<sub>3</sub>SbS<sub>4</sub> from an aqueous solution and evaluated its properties and performance. The obtained SEs demonstrate high conductivity and excellent

compatibility with a Na anode compared with pristine Na<sub>3</sub>SbS<sub>4</sub>. The Cl-substituted Na<sub>3</sub>SbS<sub>4</sub> contains relatively longer bonds between Na and S (or Cl) ions at the Na1 sites (Wyckoff 2a position) and shorter bonds between Na ions. Chloride substitution modifies the structural characteristics by creating Na vacancies within the lattice, inducing a 3D conduction network. Moreover, the introduction of NaCl into Na<sub>3</sub>SbS<sub>4</sub> suppresses the increasing interfacial resistance between the Na anode and the solid electrolyte layer. The results indicate that the developed solid electrolytes exhibit suitable reactivity with Na anodes for long-term cell cycling.

#### 4.2.2 Experimental methods

**Synthesis.** Na<sub>2</sub>S (Wako, 1.0 g, 98%), Sb<sub>2</sub>S<sub>3</sub> (Kojundo Laboratory, 1.065 g, 99.99%), and elemental S (Wako, 0.3 g, 98%) were dissolved in deionized water (30 mL) and stirred at 70 °C for 2 h to obtain an aqueous Na<sub>3</sub>SbS<sub>4</sub> solution, which was then filtered. After adding acetone (10 mL) to the Na<sub>3</sub>SbS<sub>4</sub> solution, the resulting solution was stored at approximately 20 °C for two days. The generated precipitates were collected by filtration and dried in ambient air to obtain the Na<sub>3</sub>SbS<sub>4</sub> precursor.

Na<sub>3-x</sub>SbS<sub>4-x</sub>Cl<sub>x</sub> precursors were prepared by dissolving stoichiometric amounts of the Na<sub>3</sub>SbS<sub>4</sub> precursor and NaCl in deionized water (10 mL), followed by freeze-drying for two days. The resulting precursors were then heated to 150 °C under vacuum conditions for 1 h to obtain Na<sub>3-x</sub>SbS<sub>4-x</sub>Cl<sub>x</sub> (0 ≤ x ≤ 0.1) solid electrolytes.

**Material characterization.** TG-DTA (EVO II, Rigaku) was performed under a flow of Ar (industrial gas, 99.997%) with a temperature ramp of 5 K min<sup>-1</sup>. Powder XRD measurements were carried out using a Rigaku Ultima IV diffractometer and an XRD holder with a beryllium window (Rigaku). The XRD data were acquired from 2θ = 10–120° with a step interval of 0.02° and a scan rate of 0.2° min<sup>-1</sup>. The X-ray beam was generated by CuKα radiation (40 kV, 30 mA). Structural refinements were analyzed by the Rietveld method using the computer program, RIETAN-FP,<sup>29</sup> and the crystallographic images were illustrated using VESTA 3.<sup>30</sup> I also performed BVS calculations to investigate the influence of the ion arrangement on Na ion diffusion. A BVS map was calculated using the program PyAbstantia.

**Electrochemical measurements.** Total conductivity measurements were performed using alternating-current impedance spectroscopy (SI 1260, Solatron) in the frequency range from 1 MHz to 10 Hz under a dry Ar flow. To assemble the cell for impedance measurements, each sample (~150 mg) was loaded into a holder made of PEEK with two stainless-steel rods as blocking electrodes, and the sample was pressed (pressure = 256 MPa at room temperature) into a pellet with a diameter of ~10.0 mm.

To fabricate the symmetric  $\text{Na}_{15}\text{Sn}_4$  cells,  $\sim 80$  mg of  $\text{Na}_{3-x}\text{SbS}_{4-x}\text{Cl}_x$  powder was cold-pressed (pressure = 160 MPa at room temperature) in a 10-mm-diameter PEEK die. A  $\text{Na}_{15}\text{Sn}_4$ -VGCF (Showa Denko) composite was prepared as previously reported<sup>32</sup> and loaded into both sides of the  $\text{Na}_{3-x}\text{SbS}_{4-x}\text{Cl}_x$  pellet; the resulting cells were pressed into the pellets at a pressure of 256 MPa at room temperature. The electrochemical performances of the symmetric cells were evaluated by cycling at a current density of  $0.1 \text{ mA cm}^{-2}$  during each 1-h cycle at room temperature using an SI 1260 (Solatron) impedance analyzer.

### 4.2.3 Structural characterization

Figure 4.2.1 shows the XRD patterns of  $\text{Na}_{3-x}\text{SbS}_{4-x}\text{Cl}_x$  ( $0 \leq x \leq 0.1$ ) solid electrolytes. Throughout the range of fabricated compositions, I identify the crystalline phase of  $\text{Na}_3\text{SbS}_4$  as the tetragonal structure reported by Banerjee et al.<sup>19</sup> The XRD patterns for the samples with  $x \geq 0.05$  contains Bragg peak originating from NaCl crystals, as shown in the enlarged view between 31 and 32 degrees. No apparent peak shifts are detected in the Cl-doped samples because the ionic radii of S (183 pm) and Cl (181 pm) are nearly identical.<sup>31</sup> As highlighted in the enlarged view between 34.5 and 36 degrees, the pristine sample ( $x = 0$ ) clearly has a peak corresponding to the Bragg reflection of the (220) lattice plane. In contrast, the Cl-doped samples show slightly combined peaks corresponding to Bragg reflections of the (202) and (220) lattice planes, indicating higher structural symmetry. To examine the structure of  $\text{Na}_{3-x}\text{SbS}_{4-x}\text{Cl}_x$  in detail, the average structures of  $\text{Na}_{3-x}\text{SbS}_{4-x}\text{Cl}_x$  are studied using the Rietveld method. Figure 4.2.2 and Table 1 present the Rietveld refinement pattern and the crystallographic parameters, respectively, of  $\text{Na}_{2.95}\text{SbS}_{3.95}\text{Cl}_{0.05}$  (Cl content = 1.25%). The Cl-doped samples are refined using the  $\text{Na}_3\text{SbS}_4$  phase with trace amounts of NaCl. A crystal structure model of  $\text{Na}_3\text{SbS}_4$  with space group  $P-4 2_1 c$  was applicable as the main phase for the refinement. Virtual chemical species that mixed S and Cl in finite amounts were applied within the structural model to obtain the refined  $\text{Na}_{3-x}\text{SbS}_{4-x}\text{Cl}_x$  structures because it is extremely difficult to distinguish S atoms from Cl atoms in XRD measurements. Given the larger BVS difference of Na2 compared with that of Na1, it was assumed that vacancies were created at the Na2 sites upon Cl doping because it is unfavorable for the Na2 site in  $\text{Na}_3\text{SbS}_4$  to be occupied.<sup>19</sup> The atomic displacement parameter values ( $B_{\text{iso}}$ ) in the Cl-doped samples were fixed at an identical value to that of unsubstituted  $\text{Na}_3\text{SbS}_4$ . The  $R$  factors obtained from the refinement of  $\text{Na}_{2.95}\text{SbS}_{3.95}\text{Cl}_{0.05}$  are  $R_{\text{wp}} = 7.8\%$ ,  $R_e = 5.3\%$ ,  $R_p = 5.8\%$ ,  $R_B = 3.5\%$ , and  $R_F = 1.9\%$ , which are sufficiently low to support the structural model. In the structure of  $\text{Na}_{2.95}\text{SbS}_{3.95}\text{Cl}_{0.05}$ , S (or Cl) atoms forms tetrahedrons with antimony in the center, and these tetrahedra are arranged into a body-centered cubic structure (Figure 4.2.3a). The Na ions are distributed over two sites at the Wyckoff  $4d$  and  $2a$  positions, and each Na ion is coordinated with six or eight S (or Cl) atoms (Figure 4.2.3b). The Na ion diffusion along the  $c$ -axis involves ion

migration between stable sites within a  $\text{NaS}_6$  octahedron, and diffusion along the  $ab$ -plane involves ion migration between stable sites within  $\text{NaS}_8$  dodecahedra and  $\text{NaS}_6$  octahedra.

Figure 4.2.4a shows the lattice parameters and cell volumes for  $\text{Na}_{3-x}\text{SbS}_{4-x}\text{Cl}_x$  ( $0 \leq x \leq 0.1$ ) extracted from the Rietveld refinements. The lattice parameters of the crystallographic  $a$ - and  $b$ -axes increases slightly upon Cl doping, whereas those of the  $c$ -axis decrease. As a result of these lattice parameter changes, the tetragonal lattice distortion is reduced (Figure 4.2.4b). The higher structural symmetry obtained with Cl substitution is consistent with the trend observed in  $\text{Na}_{3-x}\text{Sb}_{1-x}\text{W}_x\text{S}_4$ <sup>22</sup> and  $\text{Na}_{3-2x}\text{Ca}_x\text{PS}_4$ <sup>9</sup> superionic conductors, wherein the formation of a cubic phase structure is detected following aliovalent substitution into tetragonal  $\text{Na}_3\text{PnS}_4$  ( $\text{Pn} = \text{Sb}, \text{P}$ ). The structural symmetry of tetragonal  $\text{Na}_3\text{SbS}_4$  can be associated with the rotation of  $\text{SbS}_4^{3-}$  tetrahedra and the redistribution of Na ions, as previously observed in the case of  $\text{Na}_3\text{PS}_4$ .<sup>32</sup> Thus, the reduction in tetragonal lattice distortion may be attributed to the slight reorientation of tetrahedral anions due to the Cl substitution and the reduction in the interatomic distance between Na ions (see Figure 4.2.4c-e). However, Chu et al. determined that Cl substitution into  $\text{Na}_3\text{PS}_4$ , which is isostructural with  $\text{Na}_3\text{SbS}_4$ , promotes the formation of a tetragonal structure along with slight lattice expansion; the synthesis of Cl-doped  $\text{Na}_3\text{PS}_4$  with cubic phase was unsuccessful. Their observation contrasts with the trend observed in this study. The average bond length between Na2 and S (or Cl) decreases slightly upon Cl doping, whereas that between Na1 and S (or Cl) increases, as illustrated in Figure 4.2.4f. The Na vacancies created by the Cl substitutions likely weaken the Coulombic repulsion between Na ions, thereby modifying the local environment around the Na ions. Additionally, the high electronegativity of Cl (3.16) exerts a strong electrostatic attractive force on counter cations, which should alter the structural parameters in Cl-substituted  $\text{Na}_3\text{SbS}_4$  despite the nearly identical ionic radii of S and Cl.<sup>33</sup> The doped Cl reaches the solid solubility limit around  $x = 0.05$ , which is evident based on the detection of residual NaCl and the trends of structural parameters as a function of composition. As a result, Cl ions are successfully introduced as substitutes for S in the  $\text{Na}_3\text{SbS}_4$  structure; this verifies the validity of the structural model containing Na ion vacancies. The structural characterization of Cl-substituted  $\text{Na}_3\text{SbS}_4$  is reasonably supported by the Rietveld refinements based on XRD data.

#### 4.2.4 Ionic conductivity properties

Figure 4.2.5a shows the temperature dependence of the conductivities for  $\text{Na}_{3-x}\text{SbS}_{4-x}\text{Cl}_x$  ( $0 \leq x \leq 0.1$ ). The total conductivity, including bulk and grain boundary contributions, was calculated from the resistance value determined by the real axis intercept at high frequency in the Nyquist plot. For all samples, the conductivities versus temperature follow the Arrhenius equivalent presented in Eq. 4.2.1,

$$\sigma T = \sigma_0 \exp\left(-\frac{E_a}{k_B T}\right), \quad (4.2.1)$$

where  $\sigma$  is the total conductivity of the pellet,  $T$  is the temperature,  $E_a$  is the activation energy, and  $\sigma_0$  is the pre-exponential factor. Figure 4.2.5b illustrates the dependence of the solid electrolytes' conductivities on the  $\text{Na}_{3-x}\text{SbS}_{4-x}\text{Cl}_x$  ( $0 \leq x \leq 0.1$ ) composition at 25 °C. The ionic conductivity of Cl-doped  $\text{Na}_3\text{SbS}_4$  increases with an increasing Cl content up to  $x = 0.05$  and reaches a maximum value of  $9.0 \times 10^{-4} \text{ S cm}^{-1}$  in  $\text{Na}_{2.95}\text{SbS}_{3.95}\text{Cl}_{0.05}$ . As the Cl content increases further, the conductivity decreases to  $2.0 \times 10^{-4} \text{ S cm}^{-1}$  in the sample with  $x = 0.10$  because of the precipitation of insulating-phase NaCl. The existence of NaCl induces a high activation energy for Na ion diffusion. Defects in  $\text{Na}_3\text{PS}_4$  and  $\text{Na}_3\text{PSe}_4$  play a significant role in enabling fast Na ion conduction.<sup>32,34,35</sup> A computational study revealed that Na ion vacancies corresponding to only 2% in  $\text{Na}_3\text{PS}_4$  resulted in a one-order-of-magnitude increase in ionic conductivity compared with pure  $\text{Na}_3\text{PS}_4$ .<sup>34</sup> Therefore, the observed improvement in conductivity following Cl substitution into  $\text{Na}_3\text{SbS}_4$  is most likely a result of the vacancies created in the structure. The relative densities of the pellets of  $\text{Na}_{3-x}\text{SbS}_{4-x}\text{Cl}_x$  ( $0 \leq x \leq 0.1$ ) were all very similar (ranging from 80.5 to 83.2%). Thus, the microstructure of the Cl-doped samples should not significantly affect the observed trends in terms of conductivity. Figure 4.2.5c displays the activation energy and pre-exponential factor of  $\text{Na}_{3-x}\text{SbS}_{4-x}\text{Cl}_x$  solid electrolytes as a function of their Cl content. For Cl-substituted  $\text{Na}_3\text{SbS}_4$  with  $x$  in the range of 0–0.05, the activation energy decreases from  $34.0 \text{ kJ mol}^{-1}$  to  $26.2 \text{ kJ mol}^{-1}$ , and the pre-exponential factor decreases by one order of magnitude. The maximum ionic conductivity ( $9.0 \times 10^{-4} \text{ S cm}^{-1}$  at room temperature) is achieved for  $\text{Na}_{2.95}\text{SbS}_{3.95}\text{Cl}_{0.05}$ , which exhibits the most favorable combination of activation energy and pre-exponential factor among the tested Cl-substituted  $\text{Na}_3\text{SbS}_4$  structures. The ion conduction properties of  $\text{Na}_{3-x}\text{SbS}_{4-x}\text{Cl}_x$  ( $0 \leq x \leq 0.1$ ) are applicable to the Meyer-Neldel rule for all compositions (Figure 4.2.5d).

#### 4.2.5 Ionic conduction pathways

Figure 4.2.6a presents the crystal structure overlaid on the 3D BVS map of  $\text{Na}_{2.95}\text{SbS}_{3.95}\text{Cl}_{0.05}$  with the isosurface of BVS difference = 0.3 v.u. The BVS maps in Figure 4.2.6a depict a simple ion conduction path with an isosurface of  $\Delta|V_B|$ , which represents the difference between the ideal and actual valence of Na ions. The regions with smaller  $\Delta|V_B|$  values correspond to more stable positions for Na ions. Sodium ion diffusion channels constitute a 3D network containing the open pathways along the *ab*-plane through Na1 and Na2 sites and along the *c*-axis through Na1 and Na1 sites. Figure 4.2.6b shows a BVS map that depicts the isosurfaces of the BVS difference  $\Delta|V_B|$  at each level on the (100) and (001) planes in  $\text{Na}_{3-x}\text{SbS}_{4-x}\text{Cl}_x$  ( $0 \leq x \leq 0.10$ ). The Na ion conduction pathways along the *c*-axis in  $\text{Na}_{2.95}\text{SbS}_{3.95}\text{Cl}_{0.05}$  involves an isosurface with smaller  $\Delta|V_B|$  compared with that of pristine  $\text{Na}_3\text{SbS}_4$ . The results of these calculations indicate

that Na ion conduction along the *c*-axis in  $\text{Na}_{3-x}\text{SbS}_{4-x}\text{Cl}_x$  is enhanced with an increasing Cl doping. This is consistent with a previous report that found that the bottleneck of Na diffusion along the *c*-axis in  $\text{Na}_3\text{PS}_4$  expands with the phase transition from tetragonal ( $\alpha$ -phase) to cubic ( $\beta$ -phase).<sup>35</sup> The 3D network of ion-transport channels in  $\text{Na}_3\text{SbS}_4$ , especially along the *c*-axis, is governed by the migration of Na ions through the Na1 lattice site (see Figure 4.2.3b). Therefore, the local environment around the underlying Na1 site in the 3D network dominates the overall ion-transport properties of  $\text{Na}_3\text{SbS}_4$  and its analogs. The longer bond length between Na1 and S (or Cl) in  $\text{Na}_{2.95}\text{SbS}_{3.95}\text{Cl}_{0.05}$  relative to that in pristine  $\text{Na}_3\text{SbS}_4$  indicates weaker  $\text{Na}^+-\text{S}^{2-}$  (or Cl<sup>-</sup>) Coulombic attraction around the Na1 site (Figure 4.2.4f). The loose local bonding of Na–S (or Cl) at the Na1 site induces the three-dimensionally accessible site and encouraged ion transport, especially along the *c*-axis.<sup>36</sup> The smaller interatomic distances between Na ions should also effectively promote ion transport. A larger cell volume, which allows a broad diffusion pathway for ion transport, is desirable for achieving high ionic conductivity in a variety of materials. Despite decreasing the cell volume of  $\text{Na}_3\text{SbS}_4$  through Cl substitution, the activation energy determined based on EIS data decreases, and the ion-transport bottleneck size determined from the BVS map is enlarged. These results indicate that the overall structural features (e.g., the cell volume, the Na2–S (or Cl) bond lengths, and the structural symmetry) are critical factors influencing the ionic conductivity of  $\text{Na}_3\text{SbS}_4$  structures. This finding is consistent with a previous study involving  $\text{Na}_3\text{SbSe}_{4-x}\text{S}_x$  superionic conductors.<sup>20</sup>

#### 4.2.6 Anode stability

Symmetric  $\text{Na}_{15}\text{Sn}_4/\text{Na}_3\text{SbS}_4$ ,  $\text{Na}_{2.95}\text{SbS}_{3.95}\text{Cl}_{0.05}$ , and  $\text{Na}_{2.90}\text{SbS}_{3.90}\text{Cl}_{0.10}/\text{Na}_{15}\text{Sn}_4$  cells were cycled at a constant current of  $0.1 \text{ mA cm}^{-2}$  (Figure 4.2.7a). The rapidly increasing overpotential appears at 68 h in the cell with pristine  $\text{Na}_3\text{SbS}_4$ , indicating an unstable interface between the Na–Sn alloy and  $\text{Na}_3\text{SbS}_4$ .<sup>45</sup>  $\text{Na}_3\text{SbS}_4$  decomposes into  $\text{Na}_2\text{S}$  and  $\text{Na}_3\text{Sb}$  at the interface with Na metal, rendering the SEI unsuitable for long-term cell cycling.<sup>37,38</sup> However, the cells with  $\text{Na}_{2.95}\text{SbS}_{3.95}\text{Cl}_{0.05}$  and  $\text{Na}_{2.90}\text{SbS}_{3.90}\text{Cl}_{0.10}$  shows increased overpotential through stripping/plating, but importantly, they operate for over 300 h of cycling without a rapid increase in overpotential. As shown in Figure 4.2.7b, the cells with  $\text{Na}_{2.90}\text{SbS}_{3.90}\text{Cl}_{0.10}$  and  $\text{Na}_{2.95}\text{SbS}_{3.95}\text{Cl}_{0.05}$  shows almost identical overpotentials after 50 h. The difference in overpotential gradually becomes apparent during long-term cycling, and the cell comprising  $\text{Na}_{2.90}\text{SbS}_{3.90}\text{Cl}_{0.10}$  demonstrates a lower overpotential relative to that with  $\text{Na}_{2.95}\text{SbS}_{3.95}\text{Cl}_{0.05}$  after 250 h (Figure 4.2.7c). This indicates that  $\text{Na}_3\text{SbS}_4$  solid electrolytes with higher Cl contents exhibit improved electrochemical stability at 0 V vs Na/Na<sup>+</sup>. This improvement is consistent with the previous observation regarding the electrochemical stability of the interface between Na anodes and  $\text{Na}_3\text{PS}_4$ , 6.25% Cl-doped  $\text{Na}_3\text{PS}_4$ , and 12.5% Cl-doped  $\text{Na}_3\text{PS}_4$ .<sup>39</sup> In another recent study, the electrochemical stability window of

Na<sub>3</sub>SbS<sub>4</sub> is enhanced by the formation of NaH and Na<sub>2</sub>O as a passivating product via electrolyte hydration.<sup>37</sup> There is a continuous increase in the overpotential during each individual cycle; this increase highlights the pronounced change in longer-term cell cycling (Figure 4.2.7b,c). This may have been caused by stripping from the original Na alloy beneath the SEI with a higher energy barrier. Lin et al. proposed that in a symmetric cell with Li metal and an argyrodite-type SE, the overpotential could increase during stripping/plating when the freshly deposited Li metal was exhausted and then stripping from the Li foil beneath the SEI was required.<sup>40</sup> The Nyquist plots constructed from the EIS data of the symmetric cells with Na<sub>3</sub>SbS<sub>4</sub> and Na<sub>2.90</sub>SbS<sub>3.90</sub>Cl<sub>0.10</sub> during direct current polarization tests are shown in Figure 4.2.8a and b, respectively. The Nyquist plots for both of the cells without treatment show part of a semicircle in the high-frequency region. This semicircle is related to the resistance (*R*<sub>1</sub>) of the solid electrolyte layer and the Na alloy layer, except for the diffusion resistance, according to a previous study.<sup>41</sup> The slope in the low-frequency region corresponds to the diffusion resistance of the Na alloy layer. After 20 h, the cells each exhibit a second semicircle with response frequencies distinct from *R*<sub>1</sub> at around 100 kHz, which corresponds to the interfacial resistance (*R*<sub>2</sub>) associated with the formation of the SEI. Based on the allocation of these resistance components, I fitted the impedance data using the equivalent circuit depicted in Figure 4.2.8c, and the calculated resistance components, *R*<sub>1</sub> and *R*<sub>2</sub>, are plotted in Figure 4.2.8d. The interfacial resistance (*R*<sub>2</sub>) initially appears to be almost identical for the cells with *x* = 0 and *x* = 0.10, and this parameter increases with repeated stripping/plating in both cells. The interfacial resistance of the cell with *x* = 0.10 increases from 1847 to 3822 Ω between 60 and 80 h, whereas the interfacial resistance of the cell with *x* = 0 drastically increases from 2268 to 6279 Ω between 60 and 80 h. These observations correspond to the rapidly increasing overpotential observed in the direct current polarization test (Figure 4.2.7). The long-term cycling of the cell containing Cl-doped Na<sub>3</sub>SbS<sub>4</sub> suggests that the passivating NaCl layers formed at the Na–Sn alloy surface act as a barrier against further reaction. The Cl-doped Na<sub>3</sub>SbS<sub>4</sub> solid electrolytes, which demonstrate good compatibility with Na anodes, have the potential to improve the performances of ASSBs by coupling with well-established liquid-phase coating technology.

#### 4.2.7 Conclusions

In this report, I synthesized Na<sub>3-x</sub>SbS<sub>4-x</sub>Cl<sub>x</sub> (0 ≤ *x* ≤ 0.1) solid electrolytes from an aqueous solution and discussed their structural and electrochemical characteristics. The conductivity of the prepared Na<sub>3-x</sub>SbS<sub>4-x</sub>Cl<sub>x</sub> solid electrolytes (0 ≤ *x* ≤ 0.1) reaches a maximum value of 9.0 × 10<sup>-4</sup> S cm<sup>-1</sup> for Na<sub>2.95</sub>SbS<sub>3.95</sub>Cl<sub>0.05</sub>. The Cl substitution creates Na vacancies within the lattice, which decreases the activation energy and benefits the Na ion conduction properties. Applying Rietveld analysis and a BVS mapping technique, I demonstrate that 3D ion-transport bottlenecks, especially along the *c*-axis, expanded with increasing levels of Cl doping. The excellent ionic

transport properties of Cl-substituted  $\text{Na}_3\text{SbS}_4$  are explained by the Na lattice vacancies as well as the relatively looser local bonding between Na and S (or Cl) at the Na1 site (Wyckoff  $4d$  position), which was the underlying site supporting a 3D network. The results presented herein suggest that the major role of Cl substitution is to introduce Na vacancies within the structure and to generate a specific crystal structural framework with weaker electrostatic interactions between mobile ions and counter ions. In addition, symmetric cells containing Cl-doped  $\text{Na}_3\text{SbS}_4$  operated for over 300 h of cycling without a rapid increase in overpotential, thus exhibiting good compatibility with Na anodes compared with pure  $\text{Na}_3\text{SbS}_4$ .  $\text{Na}_3\text{SbS}_4$  with a significant amount of Cl demonstrated good electrochemical stability at 0 V vs  $\text{Na}/\text{Na}^+$ . This work provides insights relevant for the rational design of optimal Na-based solid electrolytes with desirable properties, such as high ionic conductivity at room temperature and good stability in contact with Na metal.



## References

- (1) Yabuuchi, N.; Kubota, K.; Dahbi, M.; Komaba, S. Research Development on Sodium-Ion Batteries. *Chem. Rev.* **2014**, *114*, 11636–11682.
- (2) Pan, H.; Hu, Y. S.; Chen, L. Room-Temperature Stationary Sodium-Ion Batteries for Large-Scale Electric Energy Storage. *Energy Environ. Sci.* **2013**, *6*, 2338–2360.
- (3) Takada, K. Progress and Prospective of Solid-State Lithium Batteries. *Acta Mater.* **2013**, *61*, 759–770.
- (4) Hayashi, A.; Noi, K.; Sakuda, A.; Tatsumisago, M. Superionic Glass-Ceramic Electrolytes for Room-Temperature Rechargeable Sodium Batteries. *Nat. Commun.* **2012**, *3*, 856–860.
- (5) Yu, Z.; Shang, S. L.; Seo, J. H.; Wang, D.; Luo, X.; Huang, Q.; Chen, S.; Lu, J.; Li, X.; Liu, Z. K.; Wang, D. Exceptionally High Ionic Conductivity in  $\text{Na}_3\text{P}_{0.62}\text{As}_{0.38}\text{S}_4$  with Improved Moisture Stability for Solid-State Sodium-Ion Batteries. *Adv. Mater.* **2017**, *29*, 1605561–1605567.
- (6) Chu, I. H.; Kompella, C. S.; Nguyen, H.; Zhu, Z.; Hy, S.; Deng, Z.; Meng, Y. S.; Ong, S. P. Room-Temperature All-Solid-State Rechargeable Sodium-Ion Batteries with a Cl-Doped  $\text{Na}_3\text{PS}_4$  Superionic Conductor. *Sci. Rep.* **2016**, *6*, 33733–33742.
- (7) Tanibata, N.; Noi, K.; Hayashi, A.; Kitamura, N.; Idemoto, Y.; Tatsumisago, M. X-Ray Crystal Structure Analysis of Sodium-Ion Conductivity in  $\text{Na}_3\text{PS}_4 \cdot 6\text{Na}_4\text{SiS}_4$  Glass-Ceramic Electrolytes. *ChemElectroChem* **2014**, *1*, 1130–1132.
- (8) Tanibata, N.; Noi, K.; Hayashi, A.; Tatsumisago, M. Preparation and Characterization of Highly Sodium Ion Conducting  $\text{Na}_3\text{PS}_4\text{-Na}_4\text{SiS}_4$  Solid Electrolytes. *RSC Adv* **2014**, *4*, 17120–17123.
- (9) Moon, C. K.; Lee, H.-J.; Kern, H.; Park, H.; Kwak, J. W.; Heo, K.; Choi, H.; Yang, M.-S.; Kim, S.-T.; Hong, H.; Lee, Y.; Seok, J. Vacancy-Driven  $\text{Na}^+$  Superionic Conduction in New Ca-Doped  $\text{Na}_3\text{PS}_4$  for All-Solid-State Na-Ion Batteries. *ACS Energy Lett.* **2018**, *3*, 2504–2512.
- (10) Wang, H.; Chen, Y.; Hood, Z. D.; Sahu, G.; Pandian, A. S.; Keum, J. K.; An, K.; Liang, C. An Air-Stable  $\text{Na}_3\text{SbS}_4$  Superionic Conductor Prepared by a Rapid and Economic Synthetic Procedure. *Angew. Chem.* **2016**, *128*, 8693–8697.
- (11) Wang, H.; Chen, Y.; Hood, Z. D.; Keum, J. K.; Pandian, A. S.; Chi, M.; An, K.; Liang, C.; Sunkara, M. K. Revealing the Structural Stability and Na-Ion Mobility of 3D Superionic Conductor  $\text{Na}_3\text{SbS}_4$  at Extremely Low Temperatures. *ACS Appl. Energy Mater.* **2018**, *1*, 7028–7034.
- (12) Atsunori, M.; Hirotsuda, G.; Phuc, N. H. H. Preparation of Cubic  $\text{Na}_3\text{PS}_4$  by Liquid-Phase Shaking in Methyl Acetate Medium. *Heliyon* **2019**, *5*, e02760–e02764.

- (13) Uematsu, M.; Yubuchi, S.; Noi, K.; Sakuda, A.; Hayashi, A.; Tatsumisago, M. Preparation of Na<sub>3</sub>PS<sub>4</sub> Electrolyte by Liquid-Phase Process Using Ether. *Solid State Ionics* **2018**, *320*, 33–37.
- (14) Yubuchi, S.; Hayashi, A.; Tatsumisago, M. Sodium-Ion Conducting Na<sub>3</sub>PS<sub>4</sub> Electrolyte Synthesized via a Liquid-Phase Process Using N-Methylformamide. *Chem. Lett.* **2015**, *44*, 884–886.
- (15) Kim, T. W.; Park, K. H.; Choi, Y. E.; Lee, J. Y.; Jung, Y. S. Aqueous-Solution Synthesis of Na<sub>3</sub>SbS<sub>4</sub> Solid Electrolytes for All-Solid-State Na-Ion Batteries. *J. Mater. Chem. A* **2018**, *6*, 840–844.
- (16) Park, K. H.; Kim, D. H.; Kwak, H.; Jung, S. H.; Lee, H. J.; Banerjee, A.; Lee, J. H.; Jung, Y. S. Solution-Derived Glass-Ceramic NaI·Na<sub>3</sub>SbS<sub>4</sub> Superionic Conductors for All-Solid-State Na-Ion Batteries. *J. Mater. Chem. A* **2018**, *6*, 17192–17200.
- (17) Zhang, D.; Cao, X.; Xu, D.; Wang, N.; Yu, C.; Hu, W.; Yan, X.; Mi, J.; Wen, B.; Wang, L.; Zhang, L. Synthesis of Cubic Na<sub>3</sub>SbS<sub>4</sub> Solid Electrolyte with Enhanced Ion Transport for All-Solid-State Sodium-Ion Batteries. *Electrochim. Acta* **2018**, *259*, 100–109.
- (18) Zhang, L.; Zhang, D.; Yang, K.; Yan, X.; Wang, L.; Mi, J.; Xu, B.; Li, Y. Vacancy-Contained Tetragonal Na<sub>3</sub>SbS<sub>4</sub> Superionic Conductor. *Adv. Sci.* **2016**, *3*, 1600089–1600094.
- (19) Banerjee, A.; Park, K. H.; Heo, J. W.; Nam, Y. J.; Moon, C. K.; Oh, S. M.; Hong, S. T.; Jung, Y. S. Na<sub>3</sub>SbS<sub>4</sub>: A Solution Processable Sodium Superionic Conductor for All-Solid-State Sodium-Ion Batteries. *Angew. Chem.* **2016**, *55*, 9634–9638.
- (20) Xiong, S.; Liu, Z.; Rong, H.; Wang, H.; McDaniel, M.; Chen, H. Na<sub>3</sub>SbSe<sub>4-x</sub>S<sub>x</sub> as Sodium Superionic Conductors. *Sci. Rep.* **2018**, *8*, 9146–9152.
- (21) Wan, H.; Mwiszerwa, J. P.; Han, F.; Weng, W.; Yang, J.; Wang, C.; Yao, X. Grain-Boundary-Resistance-Less Na<sub>3</sub>SbSe<sub>4-x</sub>S<sub>x</sub> Solid Electrolytes for All-Solid-State Sodium Batteries. *Nano Energy* **2019**, *66*, 104109–10416.
- (22) Hayashi, A.; Masuzawa, N.; Yubuchi, S.; Tsuji, F.; Hotehama, C.; Sakuda, A.; Tatsumisago, M. A Sodium-Ion Sulfide Solid Electrolyte with Unprecedented Conductivity at Room Temperature. *Nat. Commun.* **2019**, *10*, 5266–5271.
- (23) Yubuchi, S.; Ito, A.; Masuzawa, N.; Sakuda, A.; Hayashi, A.; Tatsumisago, M. Aqueous Solution Synthesis of Na<sub>3</sub>SbS<sub>4</sub>-Na<sub>2</sub>WS<sub>4</sub> Superionic Conductors. *J. Mater. Chem. A* **2020**, *8*, 1947–1954.
- (24) Kato, Y.; Hori, S.; Saito, T.; Suzuki, K.; Hirayama, M.; Mitsui, A.; Yonemura, M.; Iba, H.; Kanno, R. High-Power All-Solid-State Batteries Using Sulfide Superionic

- Conductors. *Nat. Energy* **2016**, *1*, 16030–16026.
- (25) Chen, B.; Xu, C.; Wang, H.; Zhou, J. Insights into Interfacial Stability of Li<sub>6</sub>PS<sub>5</sub>Cl Solid Electrolytes with Buffer Layers. *Current Appl. Phys.* **2019**, *19*, 149–154.
- (26) Hanghofer, I.; Brinek, M.; Eisbacher, S. L.; Bitschnau, B.; Volck, M.; Hennige, V.; Hanzu, I.; Rettenwander, D.; Wilkening, H. M. R. Substitutional Disorder: Structure and Ion Dynamics of the Argyrodites Li<sub>6</sub>PS<sub>5</sub>Cl, Li<sub>6</sub>PS<sub>5</sub>Br and Li<sub>6</sub>PS<sub>5</sub>I. *Phys. Chem. Chem. Phys.* **2019**, *21*, 8489–8507.
- (27) Xuan, M.; Xiao, W.; Xu, H.; Shen, Y.; Li, Z.; Zhang, S.; Wang, Z.; Shao, G. Ultrafast Solid-State Lithium Ion Conductor through Alloying Induced Lattice Softening of Li<sub>6</sub>PS<sub>5</sub>Cl. *J. Mater. Chem. A* **2018**, *6*, 19231–19240.
- (28) Banerjee, A.; Wang, X.; Fang, C.; Wu, E. A.; Meng, Y. S. Interfaces and Interphases in All-Solid-State Batteries with Inorganic Solid Electrolytes. *Chem. Rev.* **2020**, *120*, 6878–6933.
- (29) Izumi, F.; Momma, K. Three-Dimensional Visualization in Powder Diffraction. In *Solid State Phenomena*. **2007**, *130*, 15–20.
- (30) Momma, K.; Izumi, F. VESTA: A Three-Dimensional Visualization System for Electronic and Structural Analysis. *J. Appl. Crystallogr.* **2008**, *41*, 653–658.
- (31) Shannon, R. D. Revised Effective Ionic Radii and Systematic Studies of Interatomic Distances in Halides and Chalcogenides. *Acta Crystallographica. Section A* **1976**, *32*, 751–767.
- (32) Bo, S.-H.; Wang, Y.; Ceder, G. Structural and Na-Ion Conduction Characteristics of Na<sub>3</sub>PS<sub>x</sub>Se<sub>4-x</sub>. *J. Mater. Chem. A* **2016**, *4*, 9044–9053.
- (33) Bo, S.-H.; Wang, Y.; Kim, J. C.; Richards, W. D.; Ceder, G. Computational and Experimental Investigations of Na-Ion Conduction in Cubic Na<sub>3</sub>PSe<sub>4</sub>. *Chem. Mater.* **2016**, *28*, 252–258.
- (34) de Klerk, N. J. J.; Wagemaker, M. Diffusion Mechanism of the Sodium-Ion Solid Electrolyte Na<sub>3</sub>PS<sub>4</sub> and Potential Improvements of Halogen Doping. *Chem. Mater.* **2016**, *28*, 3122–3130.
- (35) Nishimura, S.; Tanibata, N.; Hayashi, A.; Tatsumisago, M.; Yamada, A. The Crystal Structure and Sodium Disorder of High-Temperature Polymorph β-Na<sub>3</sub>PS<sub>4</sub>. *J. Mater. Chem. A* **2017**, *5*, 25025–25030.
- (36) Ramos, E. P.; Zhang, Z.; Assoud, A.; Kaup, K.; Lalère, F.; Nazar, L. F. Correlating Ion Mobility and Single Crystal Structure in Sodium-Ion Chalcogenide-Based Solid State Fast Ion Conductors: Na<sub>11</sub>Sn<sub>2</sub>PnS<sub>12</sub> (Pn = Sb, P). *Chem. Mater.* **2018**, *30*, 7413–7417.
- (37) Tian, Y.; Sun, Y.; Hannah, D. C.; Xiao, Y.; Liu, H.; Chapman, K. W.; Bo, S.-H.;

- Ceder, G. Reactivity-Guided Interface Design in Na Metal Solid-State Batteries. *Joule* **2019**, *3*, 1037–1050.
- (38) Wu, E. A.; Kompella, C. S.; Zhu, Z.; Lee, J. Z.; Lee, S. C.; Chu, I.-H.; Nguyen, H.; Ong, S. P.; Banerjee, A.; Meng, Y. S. New Insights into the Interphase between the Na Metal Anode and Sulfide Solid-State Electrolytes: A Joint Experimental and Computational Study. *ACS Appl. Mater. Interfaces* **2018**, *10*, 10076–10086.
- (39) Wenzel, S.; Leichtweiss, T.; Weber, D. A.; Sann, J.; Zeier, W. G.; Janek, J. Interfacial Reactivity Benchmarking of the Sodium Ion Conductors Na<sub>3</sub>PS<sub>4</sub> and Sodium β-Alumina for Protected Sodium Metal Anodes and Sodium All-Solid-State Batteries. *ACS Appl. Mater. Interfaces* **2016**, *8*, 28216–28224.
- (40) Lin, D.; Zhao, J.; Sun, J.; Yao, H.; Liu, Y.; Yan, K.; Cui, Y. Three-Dimensional Stable Lithium Metal Anode with Nanoscale Lithium Islands Embedded in Ionically Conductive Solid Matrix. *Proc. Natl. Acad. Sci.* **2017**, *114*, 4613–4618.
- (41) Tanibata, N.; Deguchi, M.; Hayashi, A.; Tatsumisago, M. All-Solid-State Na/S Batteries with a Na<sub>3</sub>PS<sub>4</sub> Electrolyte Operating at Room Temperature. *Chem. Mater.* **2017**, *29*, 5232–5238.

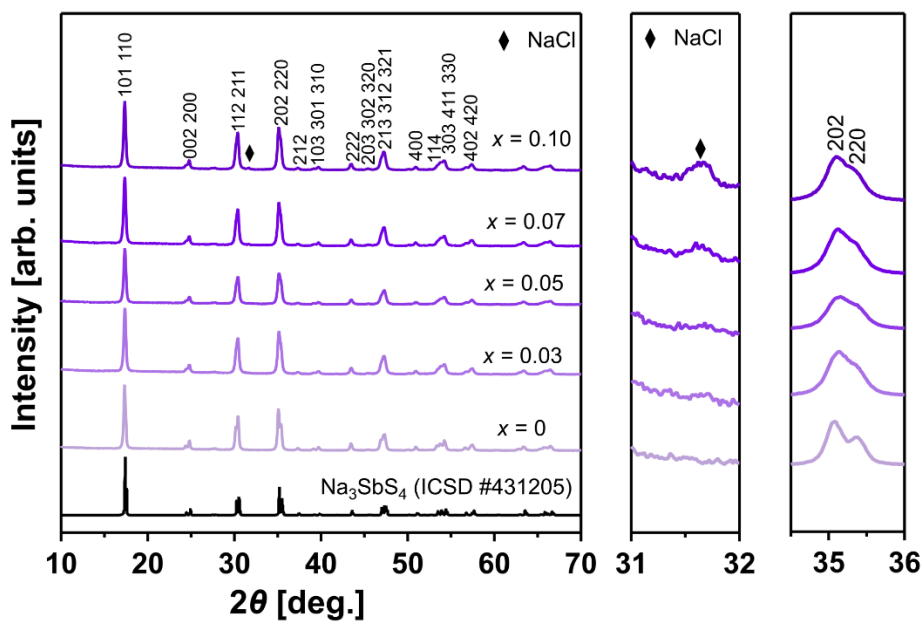


**Figure 4.2.1.** XRD patterns of  $\text{Na}_{3-x}\text{Sb}_{4-x}\text{Cl}_x$  ( $0 \leq x \leq 0.10$ ) and enlarged views of selected regions.

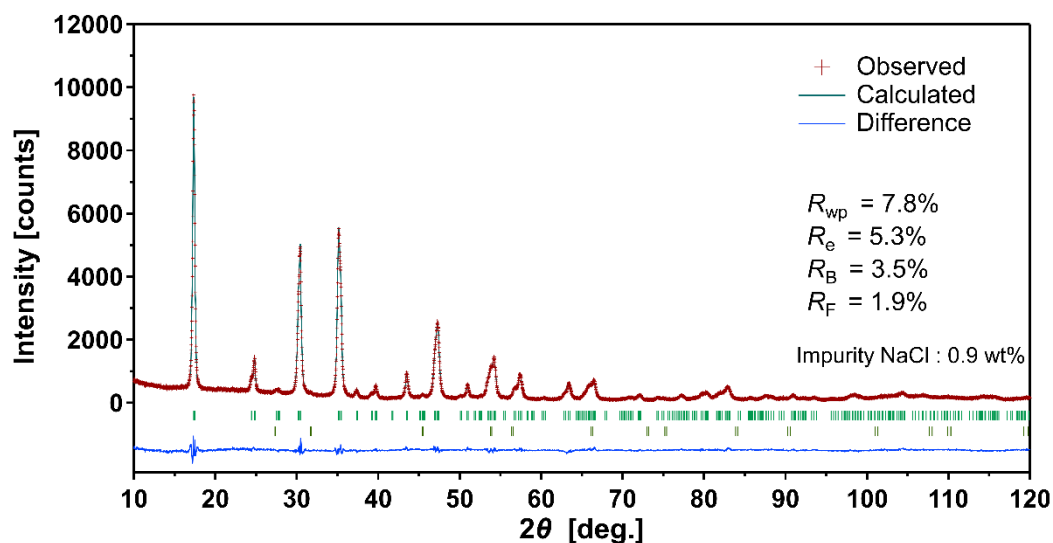


**Figure 4.2.2.** Reitveld refinement pattern for  $\text{Na}_{2.95}\text{SbS}_{3.95}\text{Cl}_{0.05}$ . The observed diffraction intensities and calculated patterns are denoted by red plus signs and a green solid line, respectively. The blue trace at the bottom represents the differences between the calculated and experimental patterns. The short green bars below the observed and calculated profiles indicate the positions of the allowed Bragg reflections of NaCl and tetragonal  $\text{Na}_3\text{SbS}_4$  in order from the bottom.

**Table 4.2.1.** Fractional coordinates, Occupancies ( $g$ ), and Atomic displacement parameters ( $B_{\text{iso}}$ ) for  $\text{Na}_{2.95}\text{SbS}_{3.95}\text{Cl}_{0.05}^a$

atom	site	$x$	$y$	$z$	$g$	$B_{\text{iso}}$
Na1	$4d$	0	0	0.0567(7)	1	3.1
Na2	$2b$	0	0	0	0.95	2.8
X	$8e$	0.2032(4)	0.1723(4)	0.1848(4)	1	1
Sb	$2a$	0	0	0	1	0.6

$a$ ;  $\text{Na}_{2.95}\text{SbX}_4$  [X: S = 0.9875, Cl = 0.0125; space group  $P\bar{4}2_1c$  (no. 114); crystal system: tetragonal].

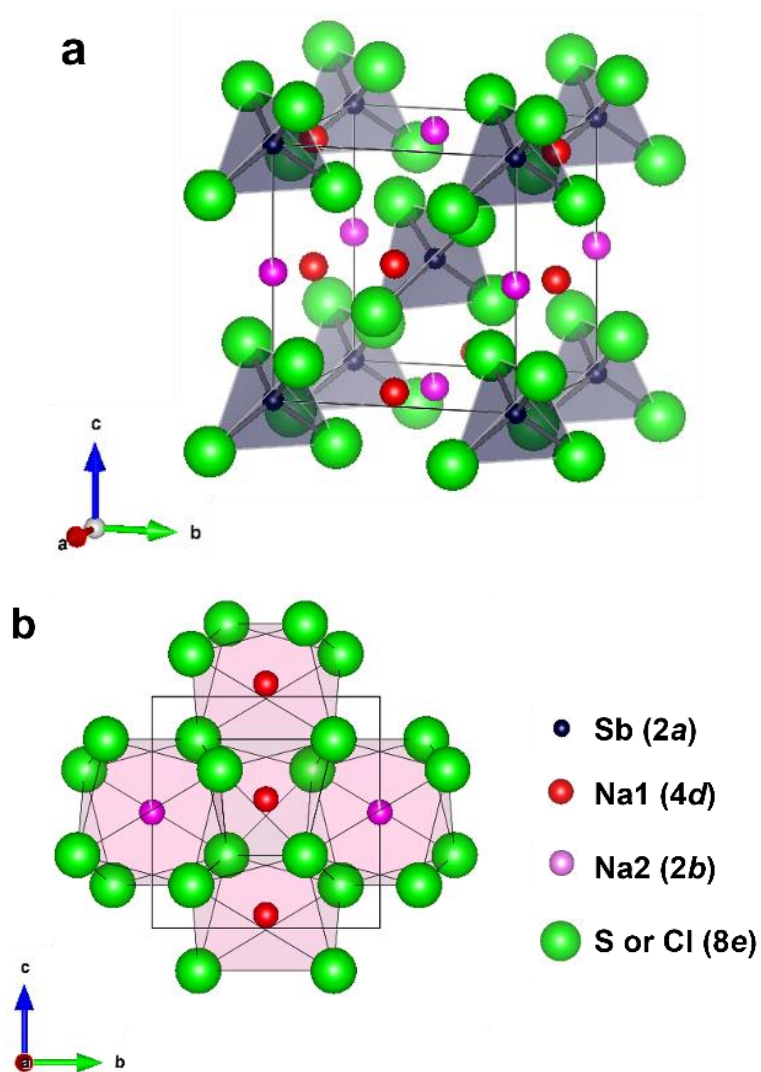


**Figure 4.2.3.** (a) Tetragonal  $\text{Na}_{2.95}\text{SbS}_{3.95}\text{Cl}_{0.05}$  unit cell with the building blocks of  $\text{SbS}_4^{3-}$  tetrahedra and (b) crystal structure of tetragonal  $\text{Na}_{2.95}\text{SbS}_{3.95}\text{Cl}_{0.05}$  with a polyhedral framework related to Na-ion conduction along the *c*-axis and the *ab*-plane.

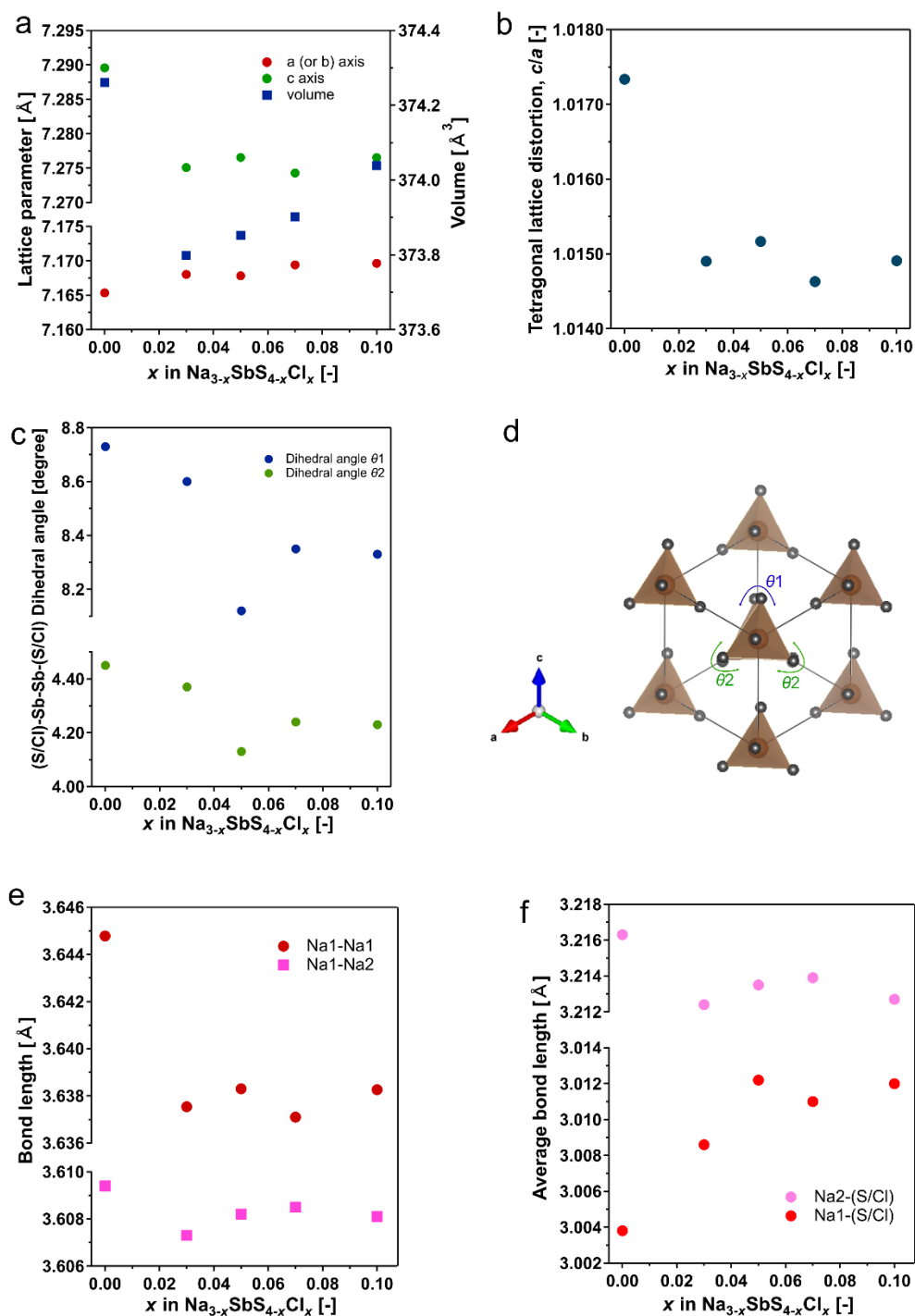


**Figure 4.2.4.** Structural properties of Na<sub>3-x</sub>SbS<sub>4-x</sub>Cl<sub>x</sub> (0 ≤ x ≤ 0.10) SEs. (a) Lattice parameters and cell volumes as a function of Cl content, (b) tetragonal lattice distortion of Na<sub>3-x</sub>SbS<sub>4-x</sub>Cl<sub>x</sub> (0 ≤ x ≤ 0.10) SEs. (c) (S/Cl)-Sb-Sb-(S/Cl) dihedral angle and (d) tetragonal modification in the projection of the (111) plane of Na<sub>3-x</sub>SbS<sub>4-x</sub>Cl<sub>x</sub>. (e) Na1-Na1 and Na1-Na2 bond lengths and (f) average bond lengths of Na1-(S/Cl) and Na2-(S/Cl).



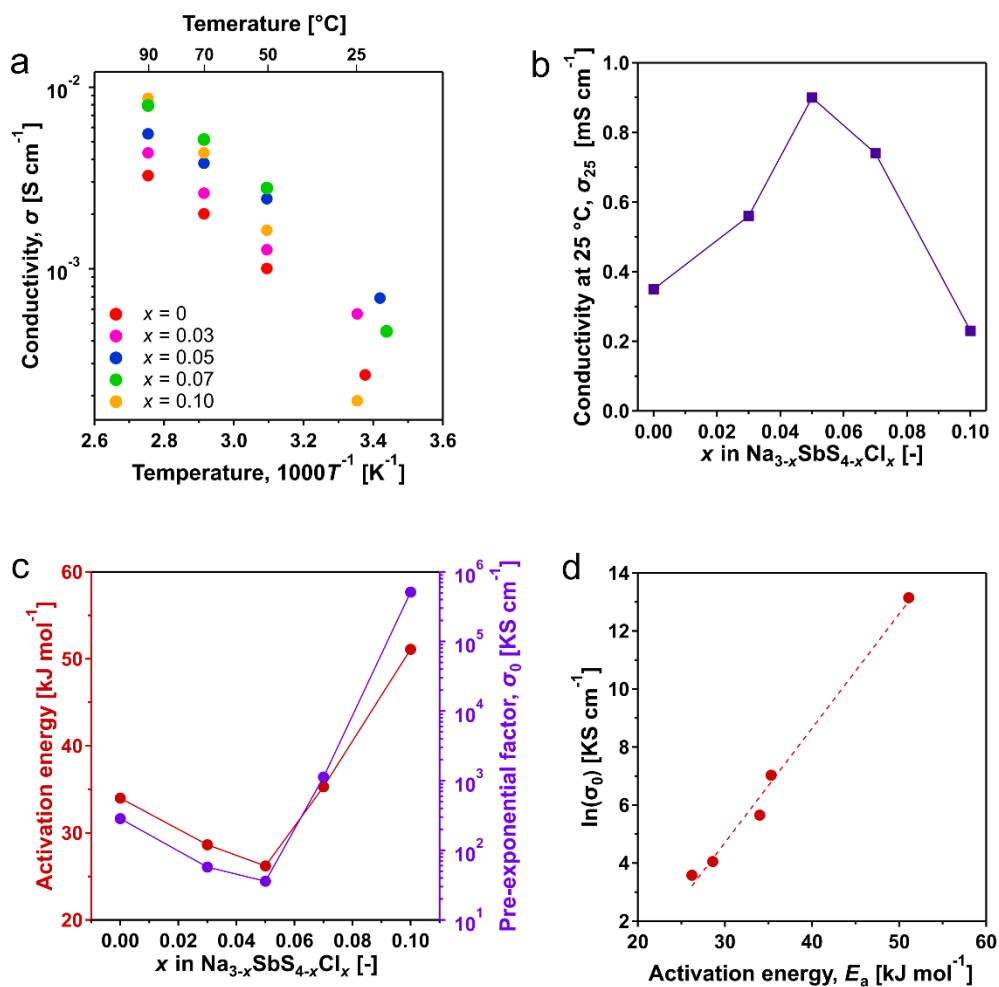


**Figure 4.2.5.** Electrochemical properties obtained from electrochemical impedance spectroscopy of  $\text{Na}_{3-x}\text{SbS}_{4-x}\text{Cl}_x$  ( $0 \leq x \leq 0.10$ ) SEs. (a) Temperature dependence of ionic conductivities of the  $\text{Na}_{3-x}\text{SbS}_{4-x}\text{Cl}_x$  ( $0 \leq x \leq 0.10$ ). (b) Dependence of conductivities on the  $\text{Na}_{3-x}\text{SbS}_{4-x}\text{Cl}_x$  ( $0 \leq x \leq 0.10$ ) composition at 25 °C. (c) Activation energies and pre-exponential factors of  $\text{Na}_{3-x}\text{SbS}_{4-x}\text{Cl}_x$  ( $0 \leq x \leq 0.10$ ). (d) Meyer-Neldel rule applied to  $\text{Na}_{3-x}\text{SbS}_{4-x}\text{Cl}_x$  ( $0 \leq x \leq 0.10$ ).

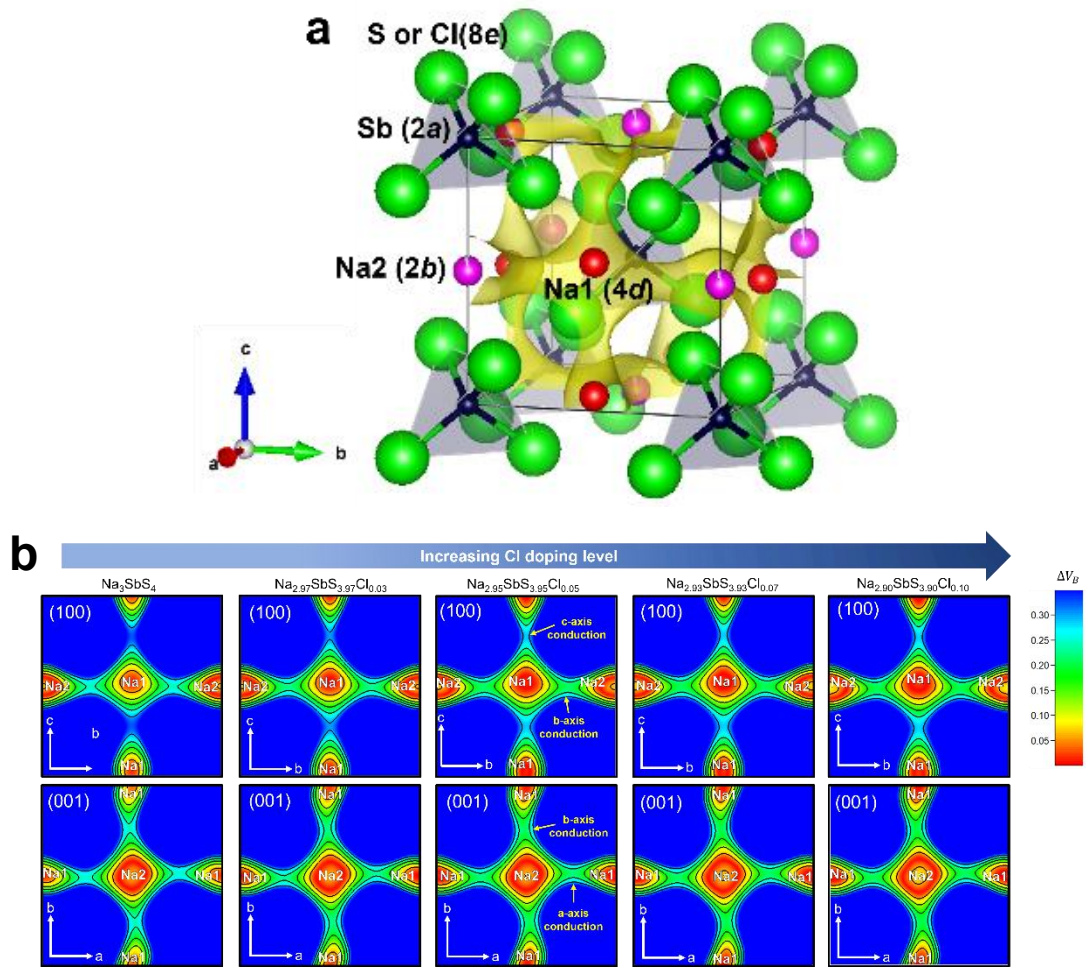


**Figure 4.2.6.** (a) Crystal structure of  $\text{Na}_{2.95}\text{SbS}_{3.95}\text{Cl}_{0.05}$  overlapped with its 3D BVS map with the isosurface of the BVS difference,  $\Delta|V_B|$ , showing a representative composition and (b) BVS maps of  $\text{Na}_{3-x}\text{SbS}_{4-x}\text{Cl}_x$  ( $0 \leq x \leq 0.10$ ) with the isosurfaces of the BVS differences,  $\Delta|V_B|$ , at each level of the (100) and (001) planes. Contour lines are shown with BVS differences between 0.3 and 0.05 v.u. at intervals of 0.05 v.u.

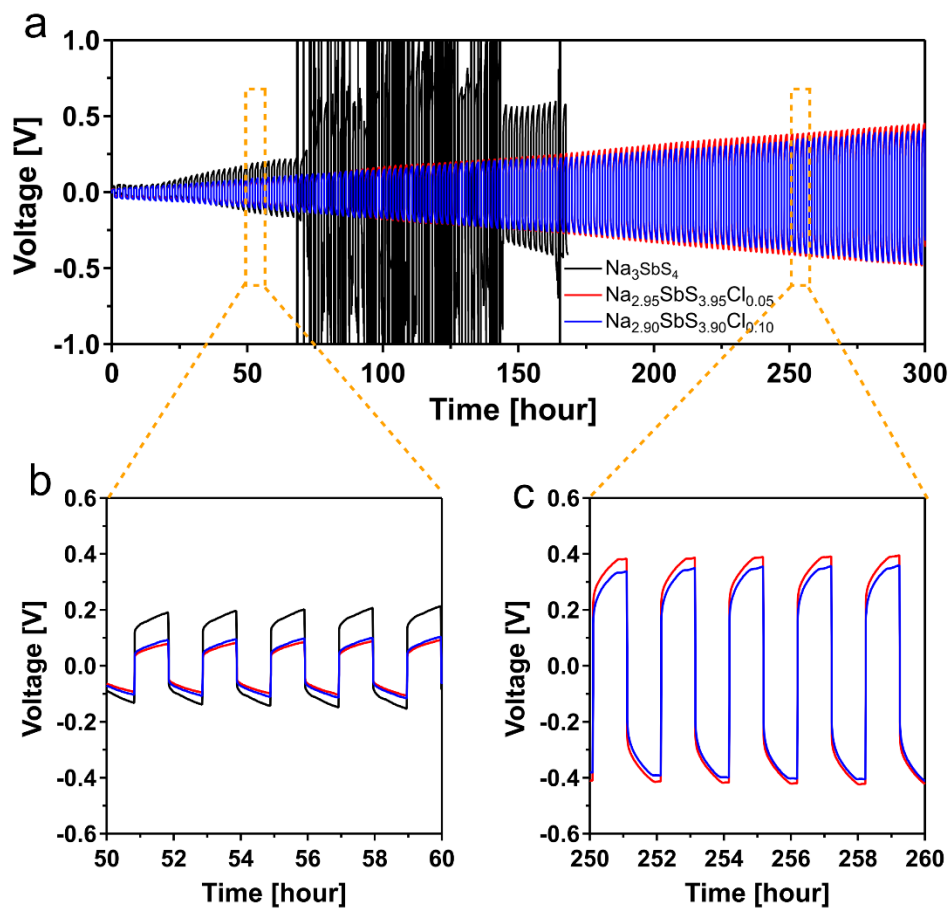


**Figure 4.2.7.** (a) Voltage profiles during cycling of  $\text{Na}_{15}\text{Sn}_4 \parallel \text{Na}_3\text{SbS}_4$ ,  $\text{Na}_{2.95}\text{SbS}_{3.95}\text{Cl}_{0.05}$ ,  $\text{Na}_{2.90}\text{SbS}_{3.90}\text{Cl}_{0.10} \parallel \text{Na}_{15}\text{Sn}_4$  in symmetric cells with an intrinsic current density of  $0.1 \text{ mA cm}^{-2}$  at room temperature. Enlargements of (b) 50-60 and (c) 250-260 h.

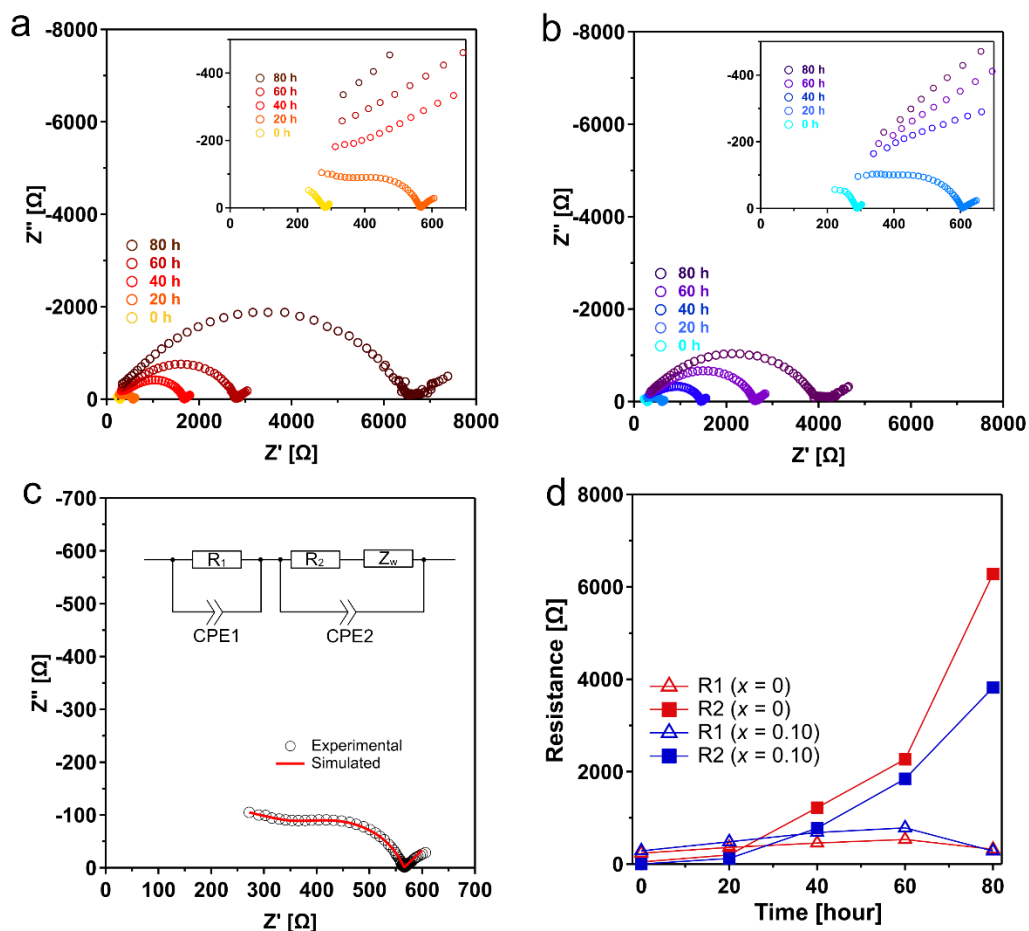


**Figure 4.2.8.** Nyquist plots obtained from EIS data during direct current polarization tests involving symmetric cells comprising (a)  $\text{Na}_3\text{SbS}_4$  and (b)  $\text{Na}_{2.90}\text{SbS}_{3.90}\text{Cl}_{0.10}$ . (c) Experimental and simulated Nyquist plots of the symmetric cell containing  $\text{Na}_{15}\text{Sn}_4 \parallel \text{Na}_3\text{SbS}_4 \parallel \text{Na}_{15}\text{Sn}_4$  after 20 h and a schematic diagram of the equivalent circuit employed in the simulation. (d) Resistance ( $R1$ ) of the Na alloy and solid electrolyte (including bulk and grain boundary contributions) and the interfacial resistance ( $R2$ ) between the Na alloy and the solid electrolyte.

## Chapter 5

### General Conclusions and Future works

This thesis has focused on all-solid-state Li-ion battery, all-solid-state Li-S battery, and all-solid-state Na-ion battery and presented solutions of their critical challenges. First, I have identified the nature of organic solvent that determines reactivity of lithium thiophosphates in wet-chemical reactions and established a novel rapid solution synthesis method of sulfide SEs. Dielectric constant of organic solvent is an essential indicator for the strength of chemical bond between the organic solvent molecule and lithium thiophosphate in liquid-phase synthesis. Thus, polarity of the organic solvent is characterized by its dielectric constant. In contrast, previous work proposed that donor number of organic solvent is a key indicator for liquid-phase synthesis. These various parameters complicate understanding the wet chemistry of lithium thiophosphates. The findings obtained here offer the leading theory on the wet-chemical reaction of sulfide SEs that has been empirically studied so far. Recently, it is demonstrated that organic solvents other than ACN, for instance, ethyl acetate and ethylene diamine with high nucleophilicity, are useful choice. The use of these organic solvents allows to the dissolution of raw materials for sulfide SEs that are insoluble in almost of aprotic solvent, leading to the kinetically beneficial reaction. The fact indicates that chemical and physical understanding of the solvent's nature dominating the solubility of lithium thiophosphates would advance highly scalable solution synthesis method. The solution synthesis developed in this thesis gives a great opportunity to well-establish a universal synthesis method. This thesis provides guidelines on the role of organic solvent in solution process where excess sulfur is introduced. This process involves the reaction mechanism that is difference from previously reported liquid synthesis. Previous studies on liquid Li-S batteries unveiled the chemical stability of  $\text{Li}_2\text{S}$  and lithium polysulfides. I believe that integrating the results enables to the further progress of liquid-phase synthesis method. Additionally, our work suggests the promise of hybrid solvents, though most conventional liquid-phase synthesis has been used a single organic solvent. The findings regarding organic solvent accumulated in the study on the traditional LIBs help the solution synthesis of sulfide SEs. In the future, the development of solution processing technology that overcomes the following two challenges will be required: minimizing the drying process, which involves high energy consumption and using solvents with low environmental impact.

Second, I have developed novel  $\text{Li}_2\text{S}$ -based cathode materials for ASLSBs. The addition of  $\text{CaS}$ ,  $\text{CaX}_2$  ( $X = \text{Cl}, \text{Br}, \text{and I}$ ),  $\text{AlI}_3$  increases the ionic conductivity, improving the cell performance. More importantly, iodide-ion participates the redox reaction of cathode materials via its redox reaction, thus and serves as a redox mediator that enhances redox reaction kinetics. This role of

redox mediator can be observed in cathode blended with sulfide SEs. The sulfide SEs in cathode react with the cathode active materials in the charge/discharge process and convert the decomposition product with the S-S bond. Such decomposition behavior dominates the overall cell performance of ASLSBs. Thus, the design of cathode in ASLSBs should take into account the electrolyte decomposition related to their capability as redox mediators. The development of sulfide SEs that show high catalytic activity may be an effective strategy for achieving excellent battery performance.

Third, Cl-doped  $\text{Na}_3\text{SbS}_4$  was successfully synthesized using liquid-phase method, showing a higher ionic conductivity of  $0.9 \text{ mS cm}^{-1}$  at room temperature than the pristine  $\text{Na}_3\text{SbS}_4$ . Rietveld analysis reveals that the structural transformation of cubic phase induced Cl doping facilitates the ion conduction along 3D networks. Cl substitution enhances the ionic conductivity of  $\text{Na}_3\text{SbS}_4$  based on not only defect chemistry but also anionic frameworks.

As mentioned above, the results of these studies are likely to offer pathways towards development of excellent performing material alternatives for SEs and cathode materials, scalable and low-cost processing for all-solid-state lithium-ion and sodium-ion batteries.

## List of Publications

The following publications cover part of the work presented in this thesis.

- [1] H. Gamo, N. H. H. Phuc, H. Muto, and A. Matsuda, “Effects of Substituting S with Cl on the Structural and Electrochemical Characteristics of  $\text{Na}_3\text{SbS}_4$  Solid Electrolytes” *ACS Applied Energy Materials*, **4**, 6125–6134, 2021.
- [2] H. Gamo, A. Nagai, and A. Matsuda, “The Effect of Solvent on Reactivity of the  $\text{Li}_2\text{S}$ – $\text{P}_2\text{S}_5$  System in Liquid-Phase Synthesis of  $\text{Li}_7\text{P}_3\text{S}_{11}$  Solid Electrolyte” *Scientific Reports*, **11**, 1–8, 2021.
- [3] H. Gamo, T. Maeda, K. Hikima, M. Deguchi, Y. Fujita, Y. Kawasaki, A. Sakuda, H. Muto, N. H. H. Phuc, A. Hayashi, M. Tatsumisago, and A. Matsuda, “Synthesis of  $\text{AlI}_3$ -doped  $\text{Li}_2\text{S}$  Positive Electrode with Superior Performance in All-Solid-State Battery” *Materials Advances*, **3**, 2488–2494, 2022.
- [4] H. Gamo, J. Nishida, A. Nagai, K. Hikima, and A. Matsuda, “Solution Processing via Dynamic Sulfide Radical Anions for Sulfide Solid Electrolytes”, *Advanced Energy and Sustainability Research*, **3**, 2200019–2200028, 2022.
- [5] H. Gamo, N. H. H. Phuc, M. Ikari, K. Hikima, H. Muto, and A. Matsuda, “Ionic conduction and electric modulus in  $\text{Li}_2\text{S}$ - $\text{CaS}$  and  $\text{CaX}_2$  ( $X = \text{F}, \text{Cl}, \text{Br}, \text{and I}$ ) nanocomposites”, *Electrochemistry*, **90**, 067005–067011, 2022.
- [6] H. Gamo, N. H. H. Phuc, M. Ikari, K. Hikima, H. Muto, and A. Matsuda, “Electrochemical Redox of  $\text{Li}_2\text{S}$ – $\text{CaS}$  and  $-\text{CaX}_2$  ( $X = \text{Cl}, \text{Br}, \text{and I}$ ) Cathode Materials for All-Solid-State Lithium-Sulfur Batteries”, *Electrochimica Acta*, **431**, 141149–141156, 2022.
- [7] H. Gamo, K. Hikima, and A. Matsuda, “Understanding Decomposition of Electrolytes in All-Solid-State Lithium-Sulfur Batteries”, *Chemistry of Materials*, **34**, 10952–10963, 2022.

## Acknowledgements

I would like to express my sincere thanks to my advisors, laboratory members, colleagues, friend, family, and many others for their guidance, help, and support. Without them, I would never have been able to complete this dissertation.

I would like to sincerely express my gratitude to my advisor Professor, Dr. Atsunori Matsuda for his continuous guidance and encouragement. He showed his enthusiasm for my research mentoring me for six years, starting when I was a senior undergraduate student. Along with technical guidance for my work, he involved me in many research projects that helped me broaden my skill set in many fields of battery research.

I would also express my deepest gratitude to Dr. Nguyen Huu Huy Phuc of Hochiminh City University of Technology for his support of my research as my co-advisor. He has provided great insight and vision into my research. He shared with me his vast knowledge and experience in my research field. I am most fortunate in my research life to have such a great mentor who has given me a wonderful guiding light in my research life.

I would like to thank Dr. Atsushi Nagai of Ensemble3 at next-generation energy systems group for giving me great support. He showed me an example of how to be a good researcher. His support has made me a better researcher.

I would like to thank Dr. Kazuhiro Hikima of Toyohashi University of Technology for always kindly guiding me in my work. He has given me tremendous support to make my research run smoothly.

I thank Dr. Fujio Izumi, who is a developer of RIETAN-FP used in this thesis, for teaching me important knowledge about Rietveld analysis. He was always attentive to answering my questions. My work would not have been possible without their advice. I am sorry to hear of the passing of Dr. Fujio Izumi last year. I would like to express my sincere gratitude for the guidance he gave me and pray that he rests in peace.

I would like to thank of my dissertation committee members, Dr Hiroyuki Muto and Dr. Ryoji Inada of Toyohashi University of Technology. I would particularly thank Dr. Hiroyuki Muto for his support of my research as my co-advisor. I would also like to express my sincere gratitude to Dr. Go Kawamura, Dr. Wai Kian Tan, Dr. Jin Nishida, Dr. Atsushi Yokoi of Toyohashi University of Technology, Dr. Masahiro Tatsumisago, Dr. Akitoshi Hayashi, and Dr. Atsushi Sakuda of Osaka Metropolitan University for their support, guidance, and valuable comments on my research.

I would like to thank everyone in the lab, the colleagues I worked with, many friends from my



hometown, and everyone in the light music club with for their unconditional support and friendship. I feel lucky to have Dr. Keiichiro Maekawa as a colleague with whom I could engage in friendly competition. It has been a great pleasure working with him.

More importantly, none of this would have been possible without the love and support of my family. I would like to thank the family members. My grandpa, my grandma, my father, my mother, my twin brother, and my sisters have given me love, concern, support, and strength all these years. In particular, my twin brother, Hironori Gamo, gave me great encouragement to me in my research. To all my family, I would like to express my deepest gratitude for all the love and support they have given me.